U.S. Department
of Transportation
Federal Railroad
Administration

Office of Research,
Development and Technology
Washington, DC 20590

# Full-scale Grade Crossing Impact of a Single-frame Highway Truck into an LNG Tender

## APPENDICES

DOT/FRA/ORD-24/14

Final Report | March 2024

## Appendix A.
## Camera and Target Positions

Figure A 1 and Figure A 2 show schematics of the camera position setup. The high-speed cameras were set up to view the impact from the side with both a focused and wide-angle view.

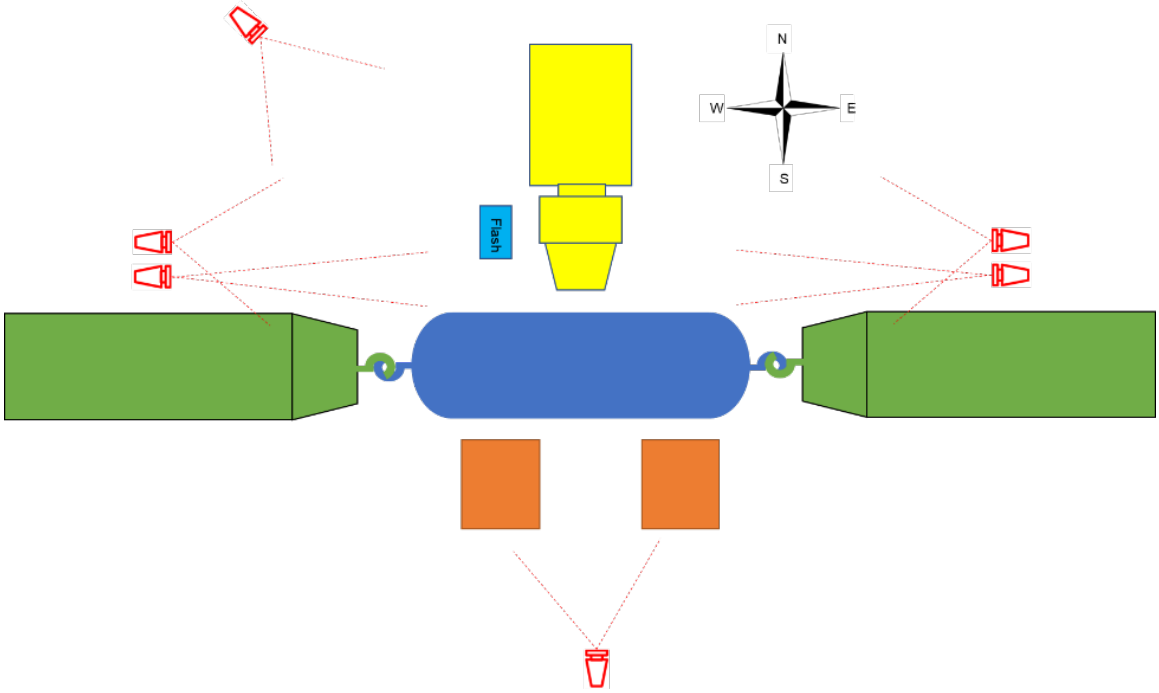


**Figure A 1. Locations and Approximate Views of the High-Speed Cameras**

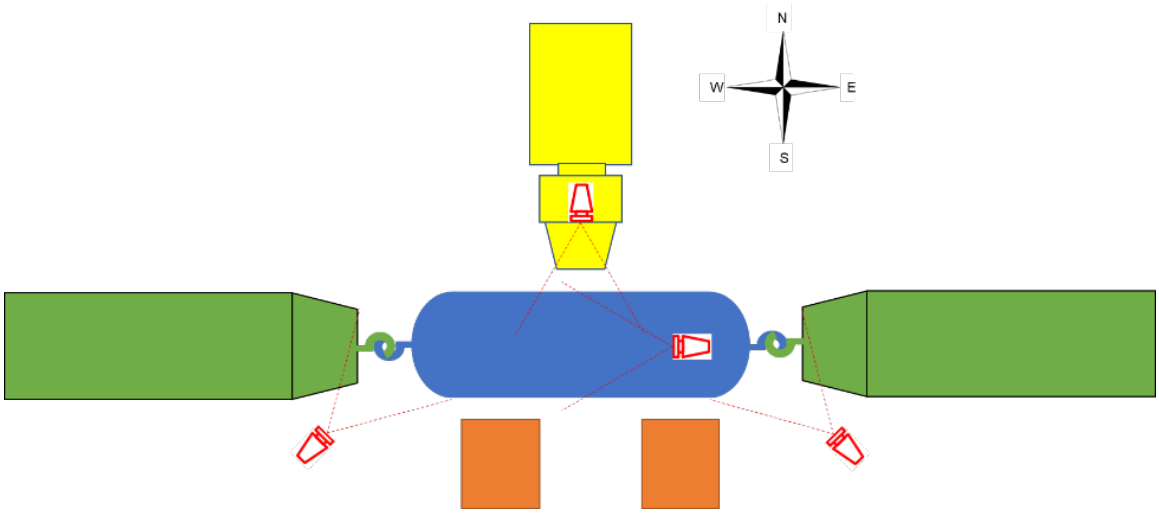


**Figure A 2. Locations and Approximate Views of the Real-Time High-Definition Cameras**

The other high-speed cameras were set up to provide an overview of the impact both from an angled view and from the far side of the impact. The real-time high-definition video cameras

were set up to have views of the underside of the LNG fuel tender. These cameras were set up mainly to view the behavior of the couplers and cabinet. A fourth real-time high-definition camera was attached to the dump truck to provide a view from the dump truck as it impacted the fuel tender. The camera was dislodged from its mounting during impact, and the video from this camera was subsequently lost. An electronic flash was added to the ground near the LNG fuel tender to show the triggering of the data acquisition systems as recorded by the high-speed camera system.

A grid of 5-inch (127-mm) by 5-inch (127-mm) black squares bordered by a 1-inch (25.4 mm) gap were stuck to the hood of the dump truck to facilitate the high-speed analysis. Figure A 3 shows this grid pattern on the dump truck.

**Figure A 3. Black Square Grid Applied to the Dump Truck Hood**

## Appendix B.
## Test Data

Although all the data acquisition systems recorded for at least seven seconds, the bulk of the impact event was over in 0.8 seconds (see the Main Report). When the data are plotted for the entire seven seconds, the short impact event becomes obscured by recorded data of little value. Therefore, the data for all the measured channels are plotted from -0.1 second to 0.8 second in Figure B 1 to Figure B 11. Only the acceleration channels were filtered at 60 Hz according to SAE J211 [1]. It should further be noted that some of the data channels failed shortly after the impact. This is indicated by the sharp drop in value going into a steady value for a large portion of the total 0.9 seconds of the plot.

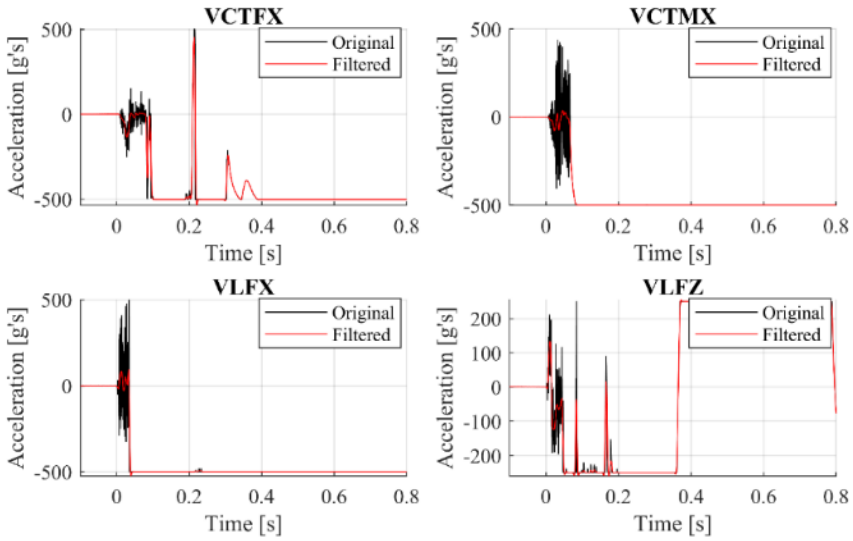


**Figure B 1. Plots of Measured Channels VCTFX, VCTMX, VLFX, and VLFZ**

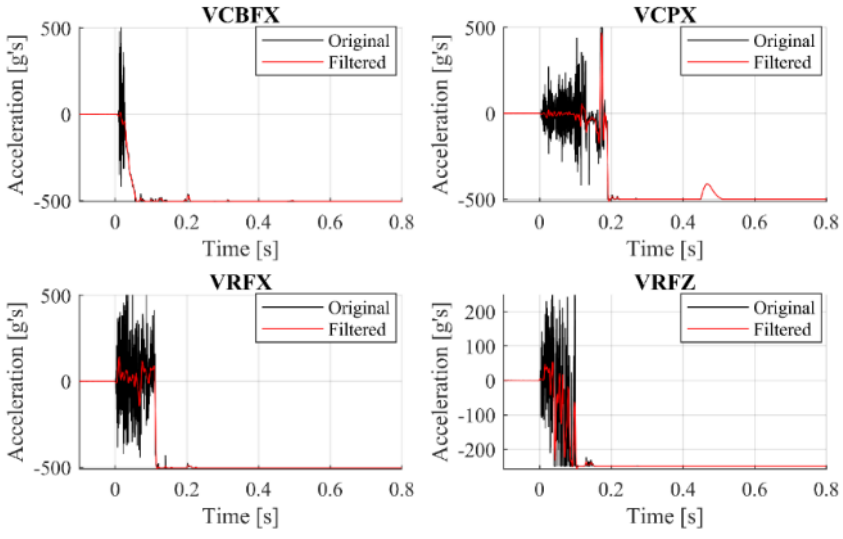


**Figure B 2. Plots of Measured Channels VCBFX, VCPX, VRFX, and VRFZ**

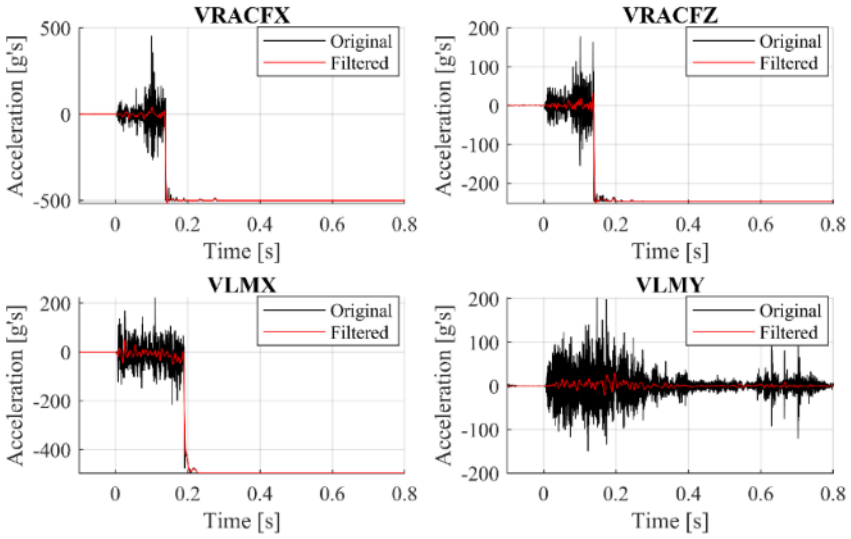


**Figure B 3. Plots of Measured Channels VRACFX, VRACFZ, VLMX, and VLMY**

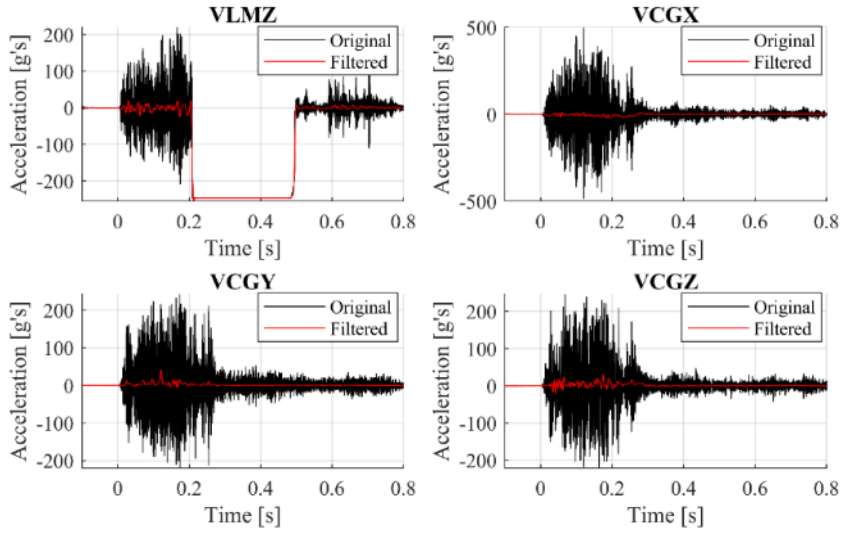


**Figure B 4. Plots of Measured Channels VLMZ, VCGX, VCGY, and VCGZ**

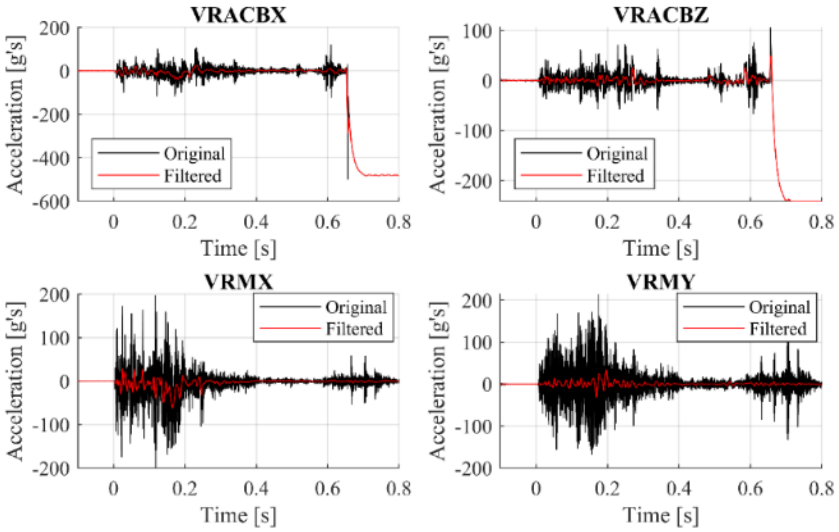


**Figure B 5. Plots of Measured Channels VRACBX, VRACBZ, VRMX, and VRMY**

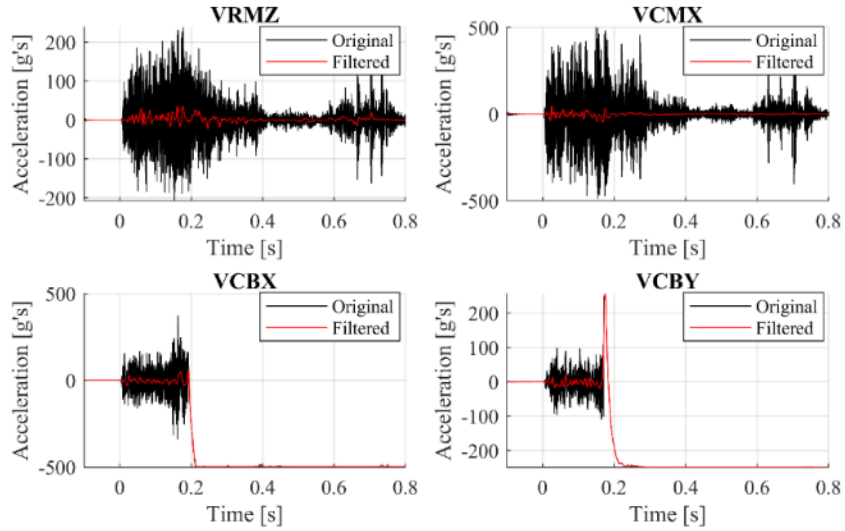


**Figure B 6. Plots of Measured Channels VRMZ, VCMX, VCBX, and VCBY**

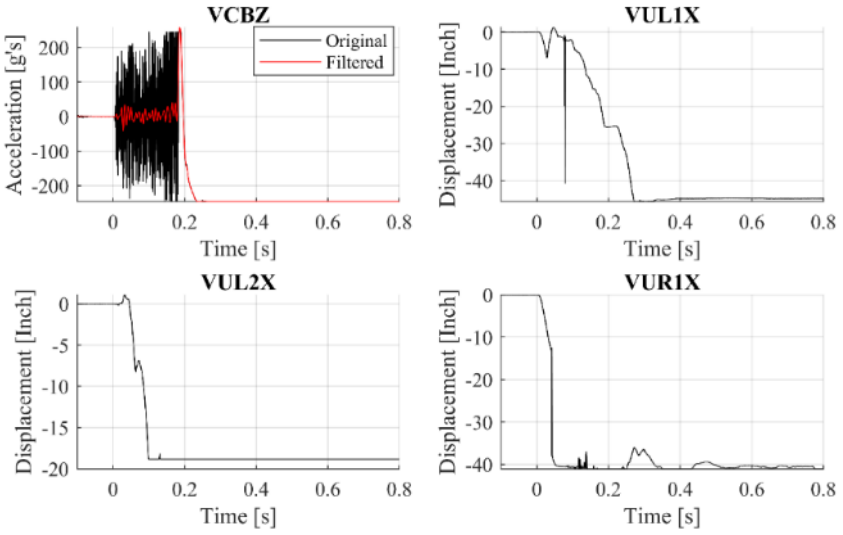


**Figure B 7. Plots of Measured Channels VCBZ, VUL1X, VUL2X, and VUR1X**

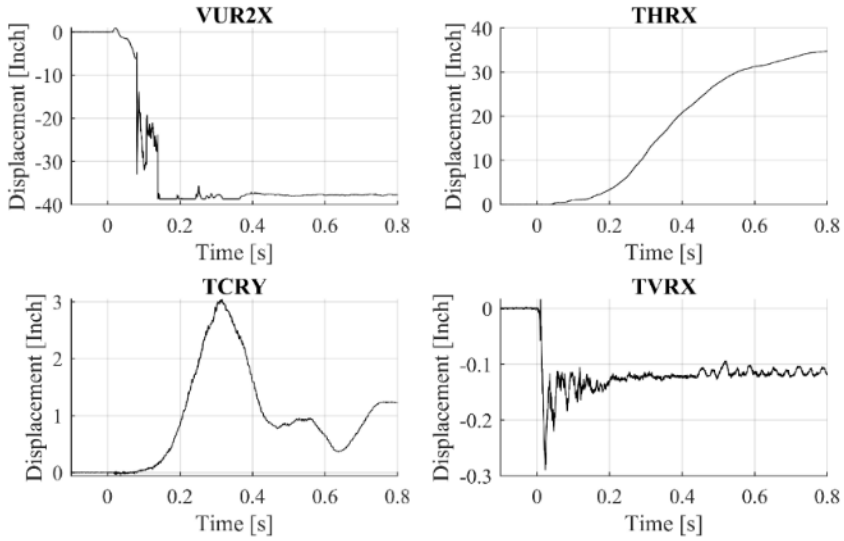


**Figure B 8. Plots of Measured Channels VUR2X, THRX, TCRY, and TVRX**

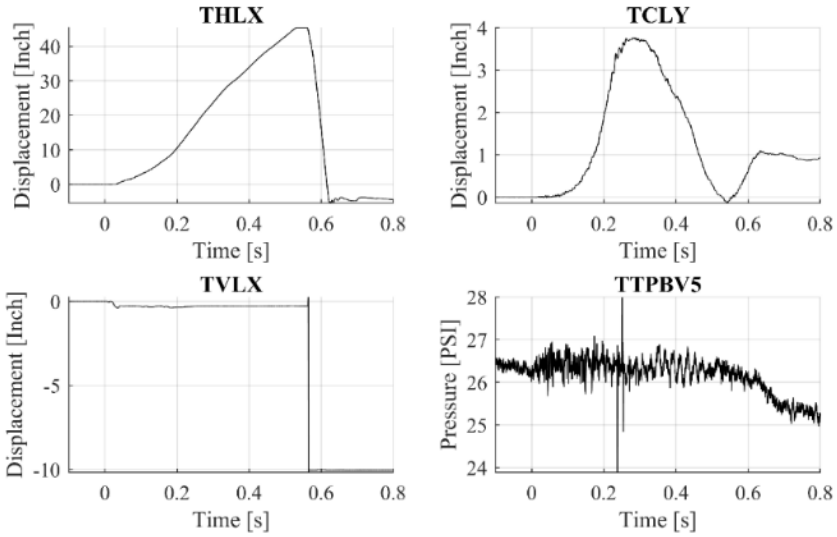


**Figure B 9. Plots of Measured Channels THLX, TCLY, TVLX, and TTPBV5**

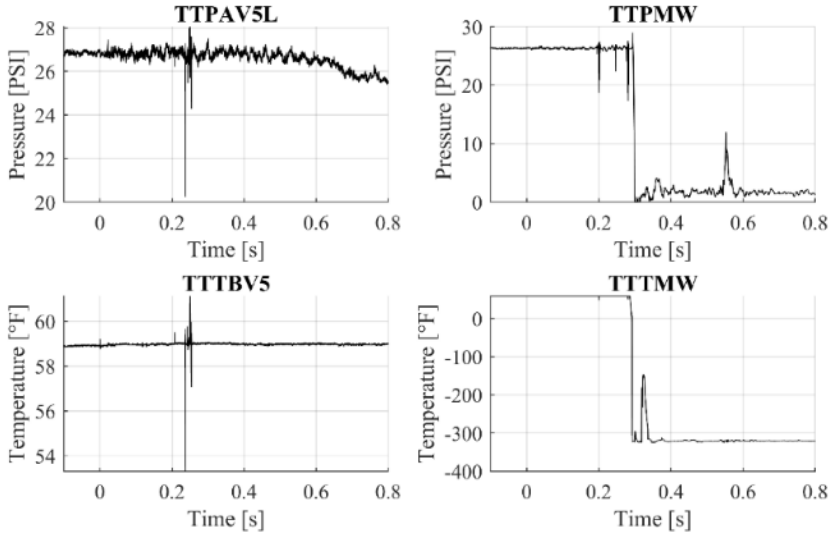


**Figure B 10. Plots of Measured Channels TTPAV5L, TTPMW, TTTBV5, and TTTMW**

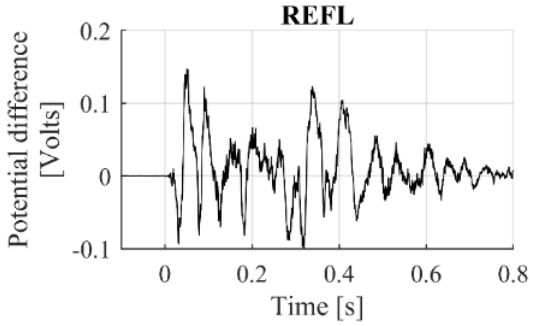


**Figure B 11. Plots of Measured Channels REFL**

## Appendix C.
## Design of the Dump Truck Suspension

A dump truck was converted to a hi-rail vehicle for the impact test. The team initially planned to fit the railway wheelsets directly to the dump truck to minimize the amount of work required in the conversion. A NUCARS® simulation was used to assess the performance of the dump truck as it ran on the existing track after being fitted with the railway wheelsets without additional suspension. The dump truck simulation was run at 40 mph and used the measured track geometry of the existing track as track input. The vertical force results of this assessment are shown in Figure C 1. The results show several wheel unloading events. Wheel unloading is undesirable since it may result in a wheel lift derailment of the dump truck.

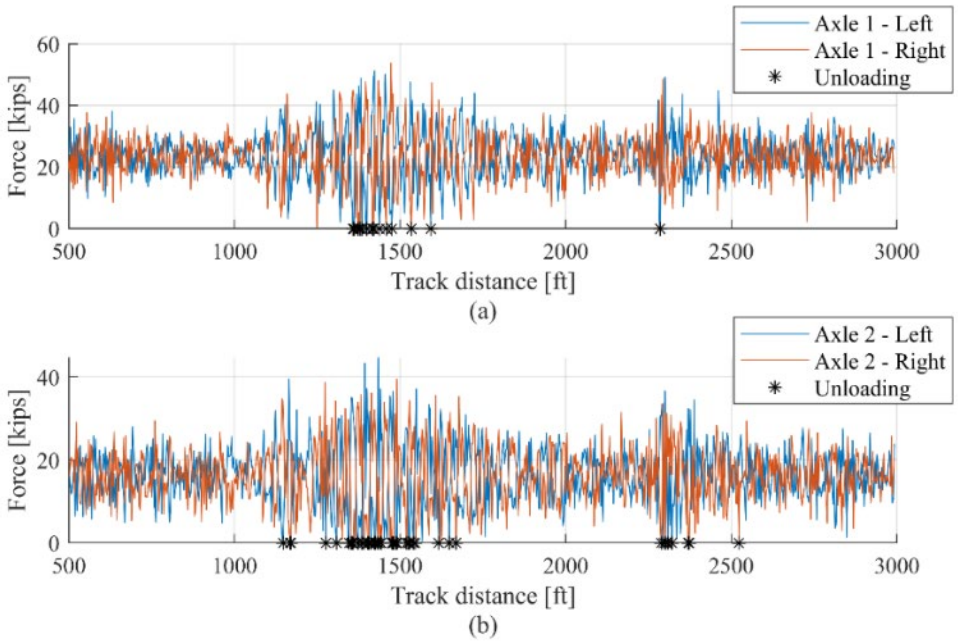


**Figure C 1. Vertical Wheel Forces on (a) Axle 1 and (b) Axle 2 for the Dump Truck with a Rigid Underframe, Without Suspension**

To determine if the dump truck was flexible and potentially capable of providing the flexibility required to negotiate the track safely, the torsional stiffness of the dump truck was determined through a series of tests. Four hydraulic jacks were placed roughly at the center of the wheelset attachment to the dump truck underframe. Four load cells and four displacement transducers were used to record the force input and displacement during loading. Opposite ends of the dump truck underframe were jacked up to create twist load effect on the dump truck body. The torsional stiffness of the dump truck underframe was determined and applied in the model. The vertical force results from the NUCARS assessment performed using the dump truck with the flexible underframe are shown in Figure C 2. The results show that although there were fewer wheel unloading events due to the flexibility modeled in the body, the probability of a wheel lift derailment of the dump truck was still high.

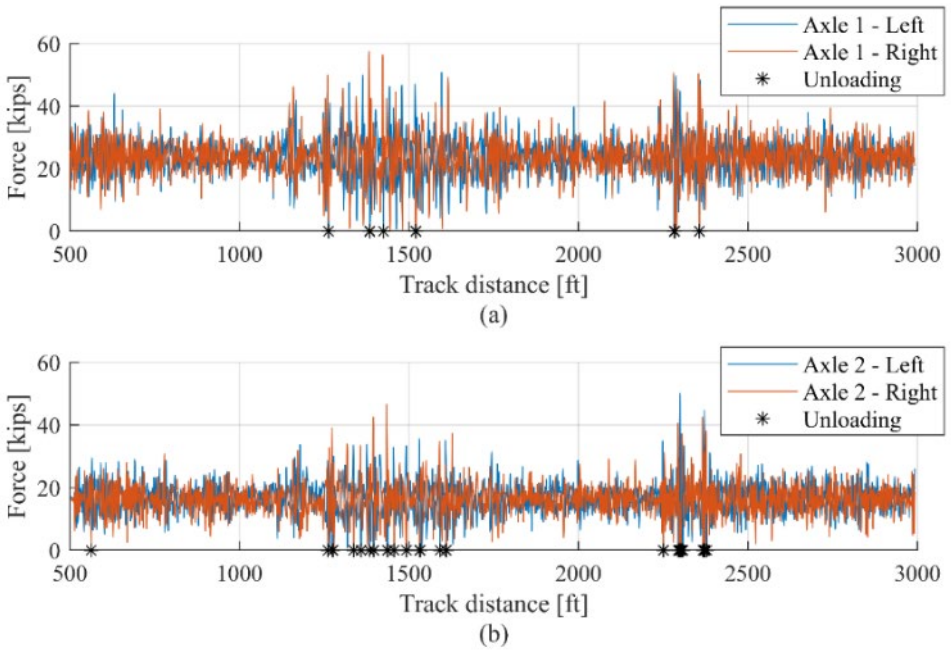


**Figure C 2. Vertical Wheel Forces on (a) Axle 1 and (b) Axle 2 for the Dump Truck with a Flexible Underframe, Without Suspension**

Suspension was added to the NUCARS model, and the team determined the vertical stiffness of the suspension that would not result in wheel unloading. The vertical force results for the suspension-fitted dump truck are shown in Figure C 4. There were no wheel unloading events for the suspension-fitted dump truck, and the vertical forces remained below 42 kips.

A leaf spring suspension with a stiffness of approximately 25,000 lbf/inch was sourced to create a structural design that would allow the attachment of the wheelset through the leaf spring to the underframe of the dump truck. The final design of the structure is shown in Figure C 3. The main structural component requiring design was the structure below the side frame of the axle which attached to the bottom of the leaf spring. A half section of this structural component is shown in Figure C 5.

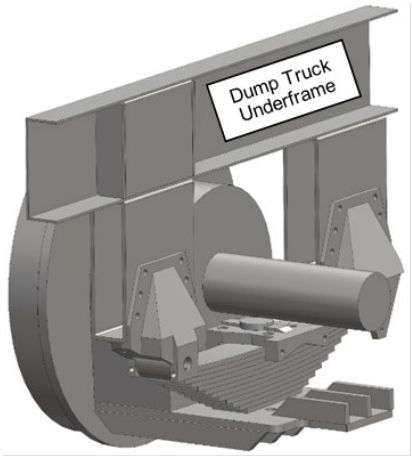


**Figure C 3. Sectioned View of Suspension Attachment Between the Railway Wheelset and Dump Truck Underframe**

The model shown in Figure C 5 was imported into ANSYS, a FE modeling package, and structural design was performed. The boundary conditions that were applied to the FE model is shown in Figure C 6. The 99th percentile of the vertical forces shown in Figure C 4 was determined and applied as a vertical force to the structure between the four bolt holes in a FE model as shown by the red area and red arrow in Figure C 6. Mirror boundary conditions were applied to the three gussets and plate as shown in yellow and marked with the "C" arrow in Figure C 6. A rigid constraint was applied to the left side where the side frame would attach as marked by the blue "B" arrow in Figure C 6. The area shown in yellow and marked by the "D" arrow is the attachment between the side frame and the structure. This area was fixed in the vertical direction but allowed to move in the longitudinal and lateral directions.

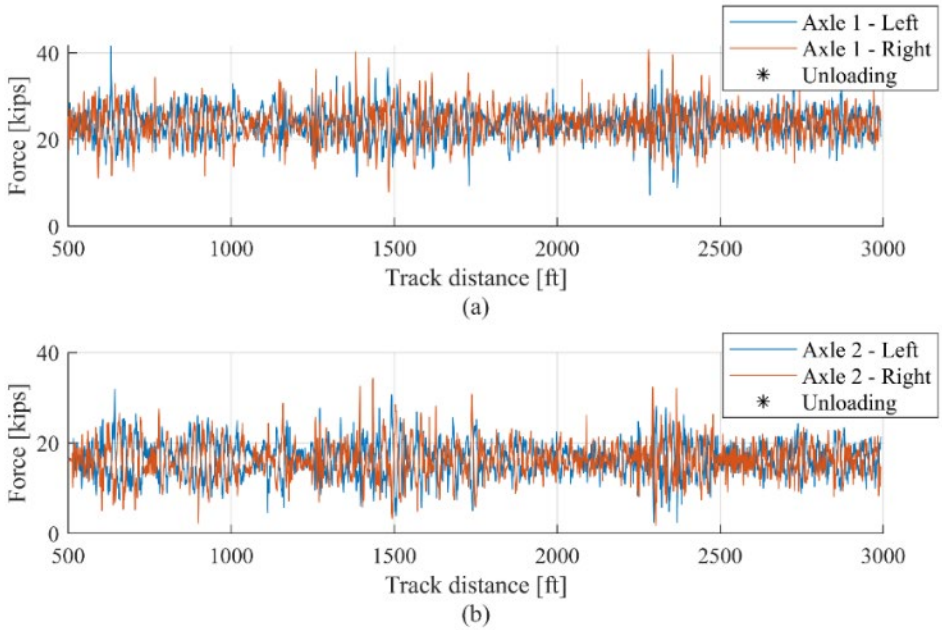


**Figure C 4. Vertical Wheel Forces on (a) Axle 1 and (b) Axle 2 for the Dump Truck with a Flexible Underframe and Suspension**

The FE model was used to determine the stresses at the outer top and bottom faces of the gussets to ensure that the material would not yield. A yield strength of 36.26 ksi was assumed for the mild steel used in the construction of the structure. The safety factors of the material against yielding are shown in Figure C 7. A minimum safety factor of 0.72 was determined and localized at the application of the boundary conditions. The areas where the boundary conditions were applied are known to have discontinuities and therefore act as stress raisers. The rest of the structure had a safety factor greater than one. The exceedance of a safety factor of one was localized to the boundary condition areas, thus a static failure of the structure was not expected.

The size of the weld between the side frame and the structure was calculated based on the bending stress and the shear stress at the junction with a safety factor of 1.5. The bottom leg of the fillet weld was calculated to be a minimum of 0.3 in. All welds on the structural member complied with this minimum dimension.

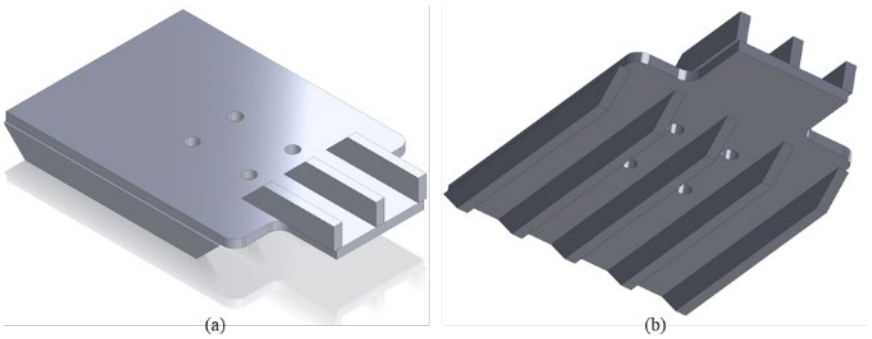


**Figure C 5. Half Section of the Structural Member Connecting the Railway Wheelsets to the Leaf Spring Suspension with (a) Top and (b) Bottom Angled Views**

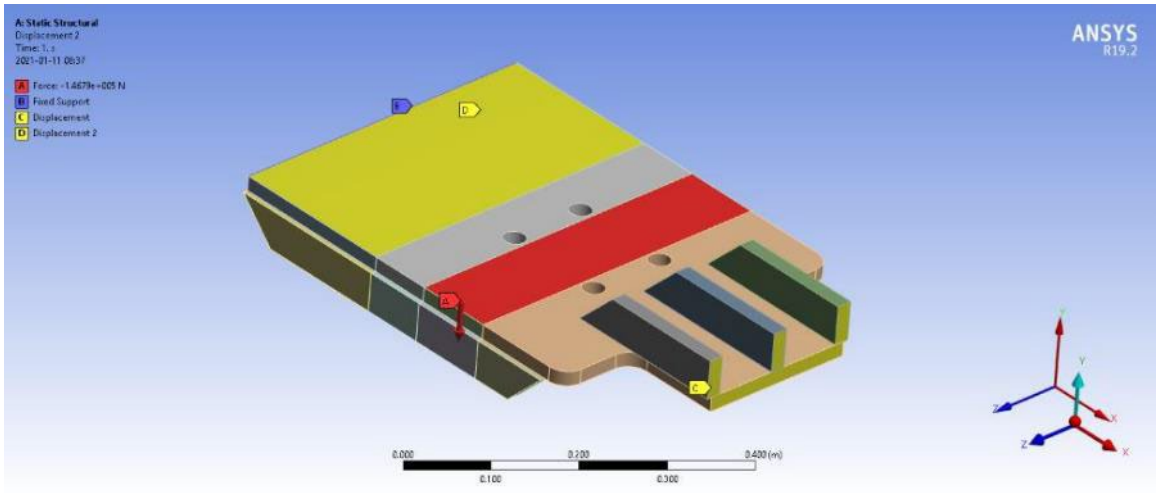


**Figure C 6. ANSYS Model of the Structural Member Connecting the Railway Wheelsets to the Leaf Spring Suspension**

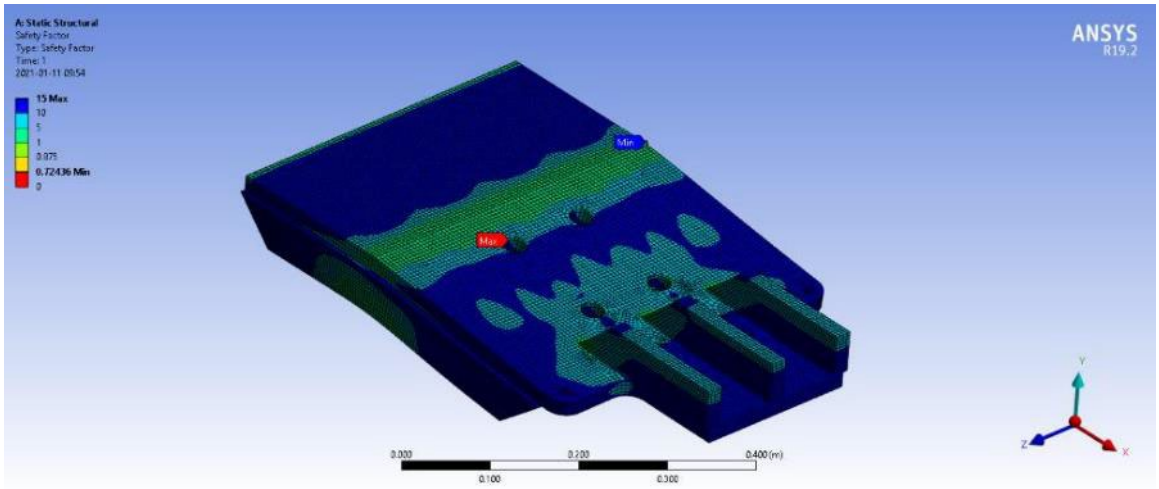


**Figure C 7. Factors of Safety Against Material Yielding**

# Appendix D.
# Tender Carbody Modeling

Tied constraints were included on the tender carbody to define connections between the outer tank and the bolsters, center plate, draft gear cover plate, and cabinet frame (Figure D 1). In addition to the tied constraints shown in Figure D 1, the tender carbody included tied constraints attaching the inner and outer tanks and a tied constraint between the inner tank and the membrane enclosing the hydraulic and pneumatic cavities.

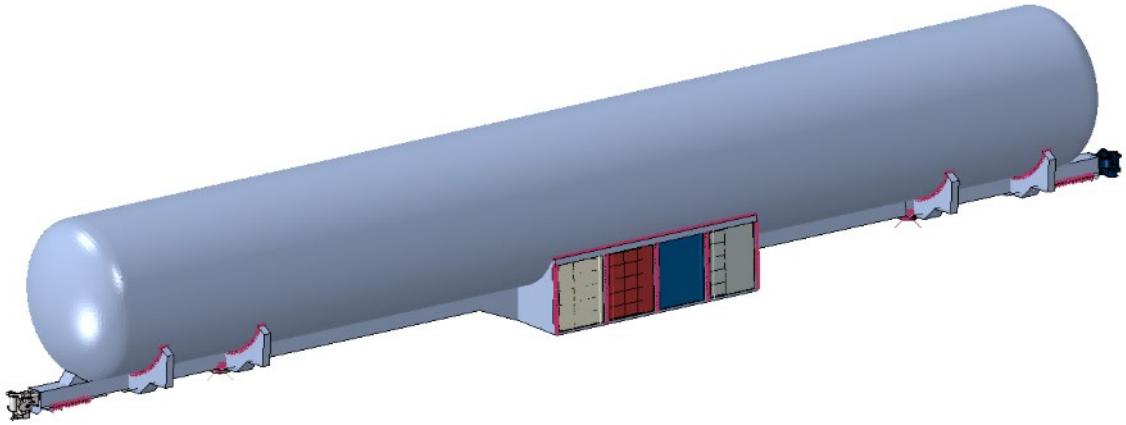

**Figure D 1. Tied Constraints on Tender Carbody Exterior**

A series of multi-point constraints (MPCs) were used to simulate the hinges and latches on the tender cabinet doors, as shown in Figure D 2.

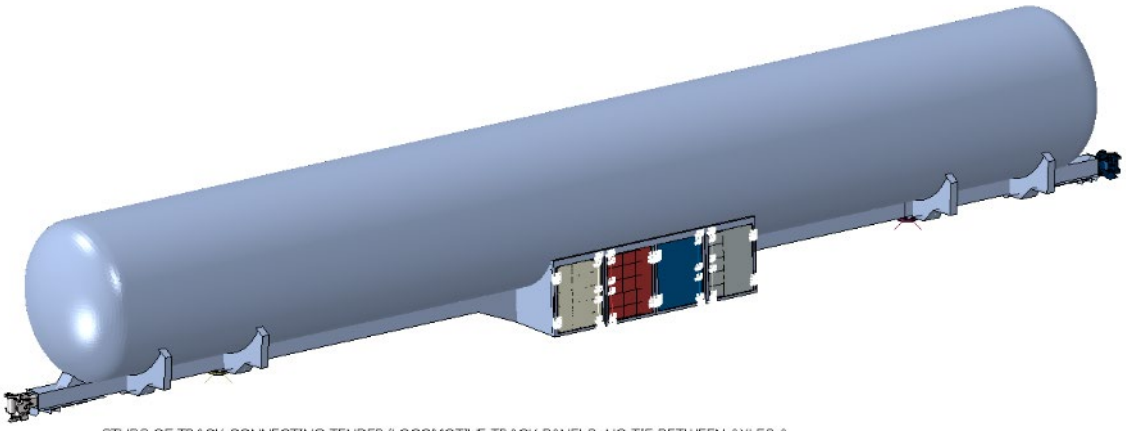

**Figure D 2. MPCs on Tender Cabinet Doors**

The inner tank of the tender was made of ASTM A240 Type 304 (T304) stainless steel. The outer tank of the tender was made of AAR TC128-B carbon steel. Various other steel alloys were used throughout the tender. Elastic-plastic material behaviors were defined for each alloy in the material. For A516-70, T304, and TC128-B piecewise linear properties were developed based on material properties measured in previous research programs. For the remaining alloys a simplified linear stress-strain response based on the minimum yield strength, ultimate tensile strength, and elongation at break was developed based on published minimum values for the alloys. The material properties used in the tender model are summarized in Table D1.

**Table D1. Summary of Material Properties Defined in Tender FE Model**

| Alloy | Plastic Stress-strain Response | Reference Source |
|---|---|---|
| A500GR-B | Linear, minimum properties | [2] |
| A516-70 | Piecewise linear | [3] |
| SA36 | Linear, minimum properties | [4] |
| AISI1045 | Linear, minimum properties | [5] |
| SA517-E | Linear, minimum properties | [6] |
| T304 | Piecewise linear | [7] |
| TC128-B | Piecewise linear | [8] |

## Appendix E.
## Three-piece Freight Truck Modeling

The three-piece freight trucks supporting the tender were modeled using a combination of deformable elements, rigid elements, and connectors with prescribed behaviors to attach discrete parts to one another. Developing a detailed model of a three-piece freight truck suitable for vehicle-track interaction or trackworthiness simulations requires a great deal of effort and input data from the particular components (e.g., springs, friction wedges, wheel profiles, etc.) that comprise the truck. The three-piece freight trucks in the FE model and the test were used to support the tender and constrain its dynamic response in a reasonable approximation of service conditions.

Each freight truck assembly included two wheelsets, two sideframes, one bolster, and two side bearings. The wheelsets were modeled using solid hexahedral brick elements with an elastic steel material property. All other parts were modeled as rigid bodies with assigned inertial properties. Connector element properties were defined to allow the constant contact side bearings (CCSBs) and the secondary suspension to deflect. Contact was enabled between the sideframes and axles, and between the bolster and sideframes. The bolster had two tabs on each corner to represent the bolster gibs. These tabs initially provided clearance of ±0.25 inches (6.35 mm) from the sideframe. If the truck bolster attempted to move in the lateral direction relative to the sideframe, the initial motion would be resisted by the lateral stiffness secondary suspension connector. Once the bolster displaced by ±0.25 inches (6.35 mm), the gibs would make contact with the sideframe and lateral force could be transmitted directly between truck bolster and sideframe. An annotated three-piece freight truck model from the FE model showing the parts and connector elements is shown in Figure E 1.

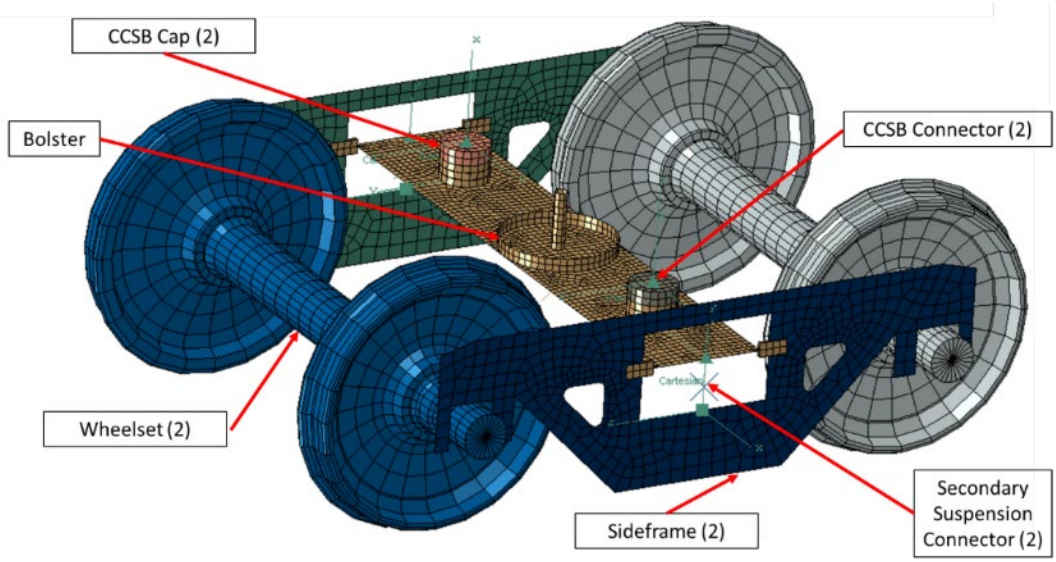


**Figure E 1. Annotated Three-piece Freight Truck FE Model**

The parameters used for dimensions, inertias, stiffnesses, and damping of truck components were based on a variety of published sources of three-piece freight truck data for North America. The resulting three-piece freight truck model was highly simplified, and does not represent any specific freight truck design. Rather, it is an amalgamation of data from various trucks and

components that were thought to be typical of the properties encountered in the North American fleet. Creating a detailed model of a specific truck design was outside of the scope of this modeling task.

The deformable wheelset consisted of two 36-inch diameter wheels and an axle. The wheel profile was based on an AAR 1-B wide-flange contour [9]. The axle geometry was adapted from geometry contained in [10]. Four instances of the wheelset were created in the FE model. The wheelset was modeled using solid deformable elements with an elastic steel material assignment. The wheelset is shown in Figure E 2. The coordinate system in this figure is the same as the global coordinate system in the assembled FE model of the tender, locomotives, dump truck, and track structure.

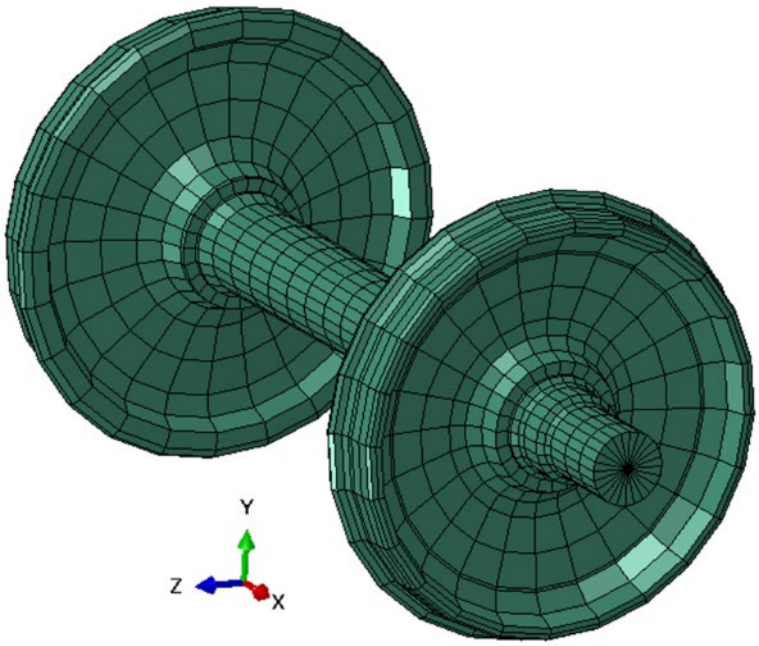


**Figure E 2. Wheelset Mesh**

The properties of the wheelset mesh are summarized in Table E 1. The wheelset was modeled using deformable elements and a steel material. Therefore, the inertial properties of this part was calculated based on the geometric arrangement of the wheelset.

**Table E 1. Summary of Deformable Wheelset Mesh**

| Part | Deformable Wheelset |
|---|---|
| Element Type | C3D8R |
| Material Assignment | Elastic steel |
| Number of Elements | 2,353 |
| Part Mass (lbf-s$^2$/in) | 7.70292 |
| Part Weight (lbf) | 2,976 |
| $I_{xx}$ (lbf-s$^2$-in) (about center of mass) | 886.449 |
| $I_{yy}$ (lbf-s$^2$-in) (about center of mass) | 5948.88 |
| $I_{zz}$ (lbf-s$^2$-in) (about center of mass) | 5948.88 |
| Boundary Conditions | None |
| Constraints | None |
| Connectors | None |

Each sideframe (two per three-piece freight truck) was modeled as a 2-D rigid body (see Figure E 3). The "x" in this image denotes the rigid body reference point for the sideframe, at which the inertial properties are applied. This reference point is intended to approximate the C.G. of the sideframe. The rigid sideframe geometry is a rough approximation of the geometry of an actual three-piece freight truck's sideframe. The critical aspects of the sideframe model were its inertial properties and geometry that accommodated the bolster and axles at appropriate locations. The axles had a 70-inch spacing that informed the spacing of the pockets that would have held the bearing adapters in an actual sideframe. The opening through which the bolster passed allowed the bolster to travel up and down, subject to the constraint provided by a connector element representing the secondary suspension's spring group at each end of the bolster.

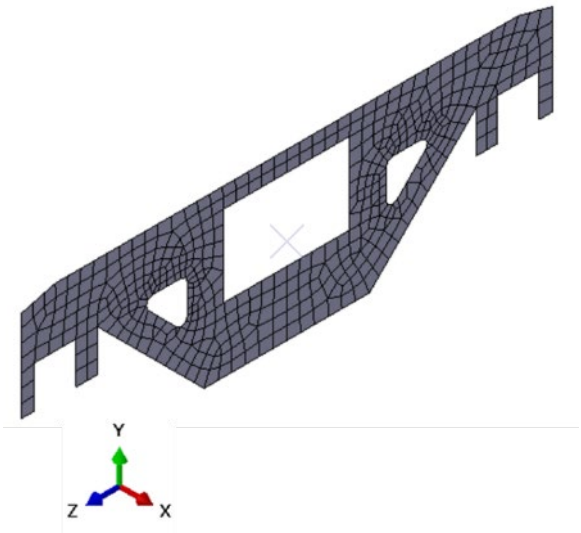


**Figure E 3. Rigid Sideframe Part Mesh**

The rigid sideframe's mesh is summarized in Table E 2. As a rigid part, the inertial properties of the sideframe were user-defined and not calculated based on the geometry of the mesh. The inertial properties of the sideframe were approximated based on numerous sideframe properties assembled from published sources [11][12][13][14][15].

**Table E 2. Summary of Rigid Sideframe Mesh**

| Part | Rigid Sideframe |
|---|---|
| Element Type | MASS: 1<br>RNODE3D: 4<br>ROTARYI: 1<br>R3D3: 18<br>R3D4: 447 |
| Number of Elements | 471 |
| Part Mass (lbf-s$^2$/in) | 2.97761 |
| Part Weight (lbf) | 1150.5 |
| $I_{xx}$ (lbf-s$^2$-in) (about center of mass) | 1,370 |
| $I_{yy}$ (lbf-s$^2$-in) (about center of mass) | 1,370 |
| $I_{zz}$ (lbf-s$^2$-in) (about center of mass) | 900 |
| Boundary Conditions | None |
| Constraints | None |
| Connectors | Cartesian Connector to Bolster |

The rigid bolster (one per three-piece freight truck) was modeled as a 3-D rigid body, shown in Figure E 4. The rigid bolster geometry is a rough approximation of the geometry of an actual three-piece freight truck's sideframe. The critical aspects of the bolster model were its inertial properties and geometry that allowed the bolster to contact the sideframes and tender carbody. The bolster geometry also included two "cups" that constrained the motion of the CCSB caps, similar to the cage of a real CCSB. Each bolster was attached to two CCSB caps via two Translator Connector elements that represented the CCSB's responses and attached to each sideframe via two Cartesian Connector elements that represented the spring groups' responses.

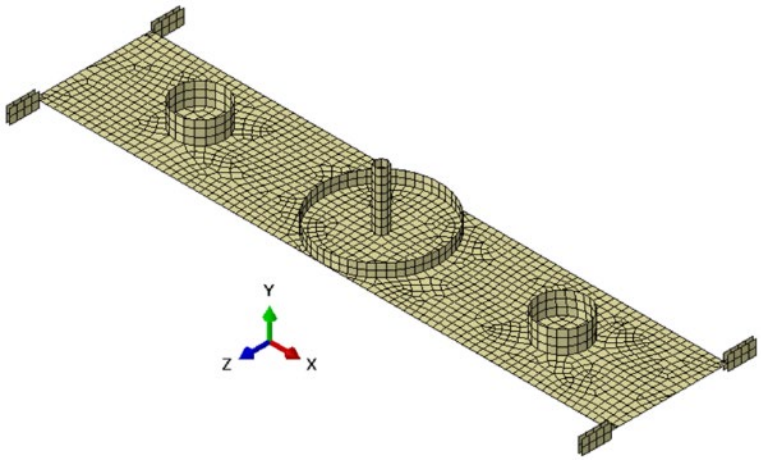


**Figure E 4. Rigid Truck Bolster Mesh used in all FE Models**

The rigid bolster part's mesh is summarized in Table E 3. As a rigid part, the inertial properties of the bolster were user-defined and not calculated based on the geometry of the mesh. The inertial properties of the bolster were approximated based on numerous bolster properties assembled from published sources [11][12][13][14][15][16].

**Table E 3. Summary of Rigid Bolster Mesh**

| Part | Rigid Bolster |
|---|---|
| Part Mass (lbf-s$^2$/in) | 3.77697 |
| Part Weight (lbf) | 1,459 |
| $I_{xx}$ (lbf-s$^2$-in) (about center of mass) | 204 |
| $I_{yy}$ (lbf-s$^2$-in) (about center of mass) | 2,760 |
| $I_{zz}$ (lbf-s$^2$-in) (about center of mass) | 2,760 |
| Boundary Conditions | None |
| Constraints | None |
| Connectors | Cartesian Connector to Each Sideframe (2x)<br>Translator Connector to Each CCSB Cap (2x) |

The rigid CCSB cap's mesh is shown in Figure E 5. This part was highly simplified and intended to serve as a contact surface that could interact with the underside of the tender's body bolster. The rigid CCSB cap part's mesh is summarized in Table E 4. Each rigid cap (two per three-piece freight truck) was attached to the truck bolster via a Translator Connector that limited its motion to the vertical direction. As the CCSB cap was only allowed to translate in the vertical direction, rotation inertial properties did not need to be defined. Contact between the CCSB cap and the truck bolster and the bolster on the tender further served to limit the CCSB cap's motion.

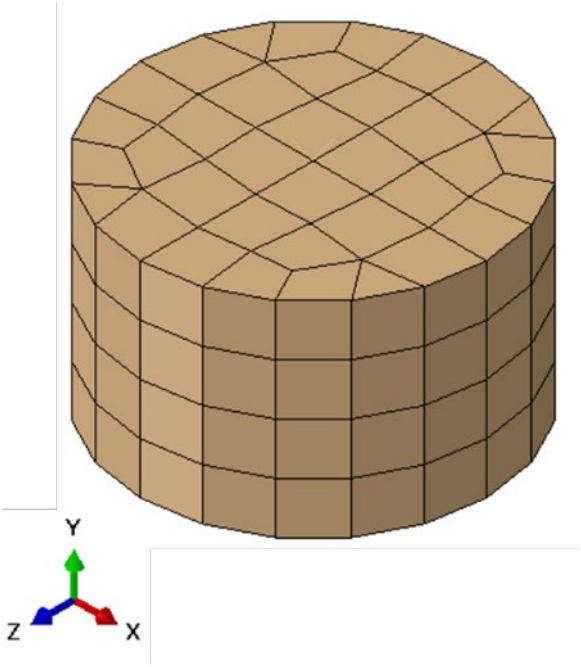


**Figure E 5. CCSB Cap Mesh**

**Table E 4. Summary of Rigid CCSB Cap Mesh**

| | |
|---|---|
| Part | Rigid CCSB Cap |
| Part Mass (lbf-s$^2$/in) | 0.0258 |
| Part Weight (lbf) | 10 |
| $I_{xx}$ (lbf-s$^2$-in) (about center of mass) | N/A |
| $I_{yy}$ (lbf-s$^2$-in) (about center of mass) | N/A |
| $I_{zz}$ (lbf-s$^2$-in) (about center of mass) | N/A |
| Boundary Conditions | None |
| Constraints | None |
| Connectors | Cartesian Connector to Bolster |

A Cartesian connector element was defined between each sideframe and each end of the bolster (two Cartesian connector elements per three-piece freight truck). This connector element represented the spring stiffness and damping of the secondary suspension. The connector definition included a nonlinear elastic response in the vertical direction, linear elastic responses in the two shear directions of the springs, and vertical damping. The properties of the connector are shown in Table E 5.

**Table E 5. Properties of Secondary Suspension Cartesian Connector**

| | |
|---|---|
| Part | Spring Group |
| Element Type | CONN3D2 |
| Number of Elements | 1 (per bolster end) |
| Boundary Conditions | None |
| Constraints | None |
| Connector Type | Cartesian |
| Connector Behaviors | Nonlinear elastic behavior<br>Linear elastic behavior<br>Damping |

A linear elastic response was defined for the shear (i.e., longitudinal and lateral) stiffness of the connector element representing the spring group at each end of the bolster. A value of 8,000 lbf/in was used for each connector in each lateral direction (i.e., forward-backward and side-to-side spring shear). This value is based on the unloaded shear stiffness of typical spring groups obtained from published literature [11], [12], [13]. Several of these publications also include published values for the lateral stiffness of loaded spring groups that are significantly stiffer than the unloaded stiffness. For simplicity, the modelers in the fuel tender impact test chose the softer lateral stiffness associated with the unloaded state. This simplification was expected to be conservative from the perspective of tender rollover, meaning that a softer shear stiffness was expected to provide less resistance to the simulated tender rolling over.

A nonlinear elastic behavior was defined for the vertical stiffness to allow the spring group to reach its travel limits and behave appropriately. To facilitate the initial model reaching static equilibrium, the connector elements were defined with a preload based on the estimated weight of the loaded tender. Each three-piece freight truck in the FE model featured one connector element at each end of the truck bolster, for a total of four connector elements in the full tender model. Each connector element represented the combined stiffness of the arrangement of the numerous springs making up the spring nest in an actual three-piece freight truck. The properties for free spring height, solid spring height, load at solid height, stiffness, and allowable spring travel will all vary based on the particular three-piece freight truck being modeled and the specific arrangement of springs. Values for the parameters of free height, solid height, and vertical stiffness were chosen for the three-piece freight truck in the FE model based on values obtained from publicly-available sources [14], [15]. These values were judged to be reasonable representations of typical freight spring properties, but do not represent the behavior of any specific truck design. The preload on each spring group was based on the assumed weight of the loaded tender in the FE models. Finally, the preloaded height of the spring group is a function of its free height, vertical stiffness, and amount of preload. The assumed properties of each secondary suspension spring group in the model are shown in Table E 6.

**Table E 6. Summary of Assumed Properties for Secondary Suspension Spring Group**

| Parameter | Value |
|---|---|
| Free Height | 10.25 in |
| Solid Height | 6.5625in |
| Vertical Stiffness | ~24,000 lbf/in |
| Preload (based on loaded tender weight) | 65,250 lbf |
| Preloaded Height (based on loaded tender weight, vertical stiffness, and free height) | 7.5 in |

The preloaded height of the spring group was used to define the length of the connector element in the FE model. The nonlinear vertical force versus change in height for the connector element at each end of each truck bolster is shown in Figure E 6. At its preloaded height, each connector element is preloaded based on the weight of the tender. If the truck bolster lifts vertically relative to the sideframe the spring will unload, extending for approximately 2.75 inches (i.e., the difference between the free height and the preloaded height) before the truck bolster is assumed to lift off of the spring. Any additional vertical lift by the truck bolster will take place without the springs engaged (i.e., a spring force of 0 kips). Similarly, if the truck bolster moves downward relative to its initial position the springs will carry more load, compressing for approximately 0.9375 inches (i.e., the difference between the preloaded height and the solid height) before

reaching their solid height. The connector element definition features a significant increase in stiffness for any further downward motion of the truck bolster once the solid length has been reached. In addition to the nonlinear elastic vertical spring stiffness damping was also defined for the connector element representing each spring group.

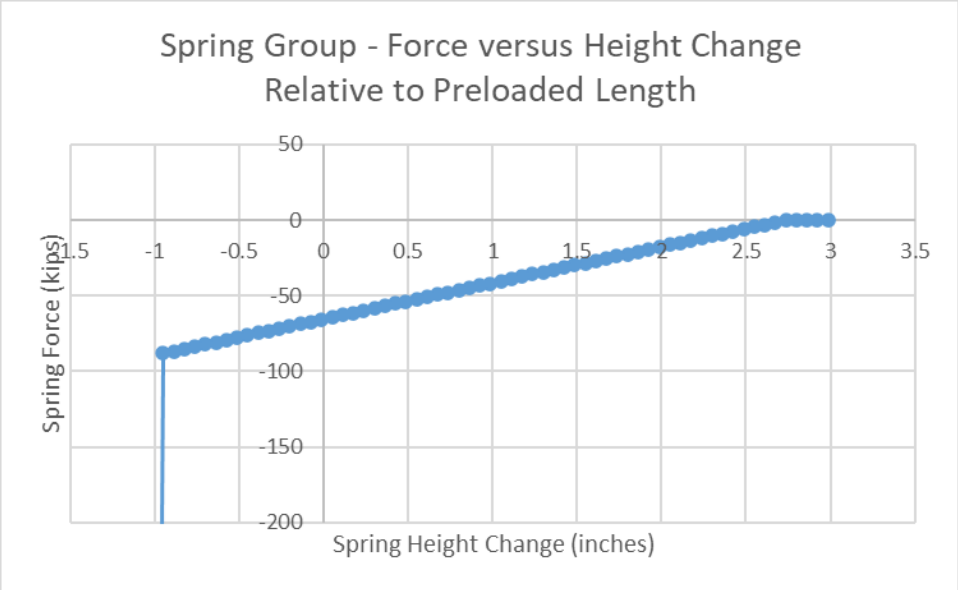


**Figure E 6. Force versus Change in Height Relative to Preloaded Length, Bolster-to-sideframe Connector Representing Spring Group**

A Translator connector element was defined between each CCSB cap and the truck bolster. This connector element definition represented the vertical stiffness of the CCSB. Contact between the sides of the CCSB cap and sides of the CCSB cage (incorporated into the bolster part in the model) would inhibit lateral and longitudinal motion of the CCSB cap. Figure E 7 shows a section cut through one truck bolster and its two CCSB caps with the connector elements visible. Each CCSB connector element had properties as shown in Table E 7.

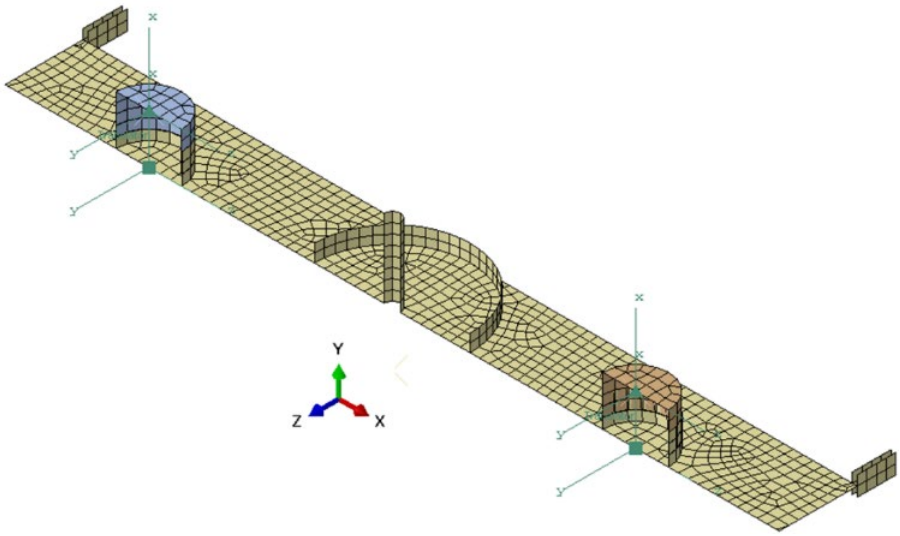


**Figure E 7. Full Section through Truck Bolster Showing CCSB Caps and Connector Elements**

**Table E 7. Properties of CCSB Connector**

| | |
|---|---|
| Part | CCSB Connector |
| Element Type | CONN3D2 |
| Number of Elements | 1 (per CCSB) |
| Boundary Conditions | None |
| Constraints | None |
| Connector Type | Translator |
| Connector Behaviors | Nonlinear elastic behavior (see Figure E 8)<br>Damping |

Each CCSB was modeled in its initial pre-loaded state. At its initial length the CCSB was assumed to be compressed by 6,000 lbf. This value is typical of commercially-available types of CCSB [17][18]. If the distance between the truck bolster and body bolster decreased, the CCSB connector would compress and carry additional load. The modeled CCSB was assumed to be compressed solidly after approximately 5/8 inches (15.875 mm) of compression relative to its preloaded length of 5-1/16 inches (0.129 m) [16][18]. Additional compression beyond this value would produce a sharp increase in the stiffness of the resistance of the CCSB. If the distance between the truck bolster and body bolster increased, the CCSB connector would increase its length and partially unload. The modeled CCSB was assumed to be fully-unloaded after approximately 0.8 inches (20.32 mm) of length increase compared to its initial, preloaded height (based on an assumed free height of slightly less than 6 inches (152.4 mm)). Any additional increase in the distance between the truck bolster and body bolster would take place without the CCSB's involvement. The force versus change in height (relative to the preloaded height) defined for the CCSB is shown in Figure E 8. In addition to the nonlinear elastic spring stiffness damping was defined for the connector element representing the CCSB.

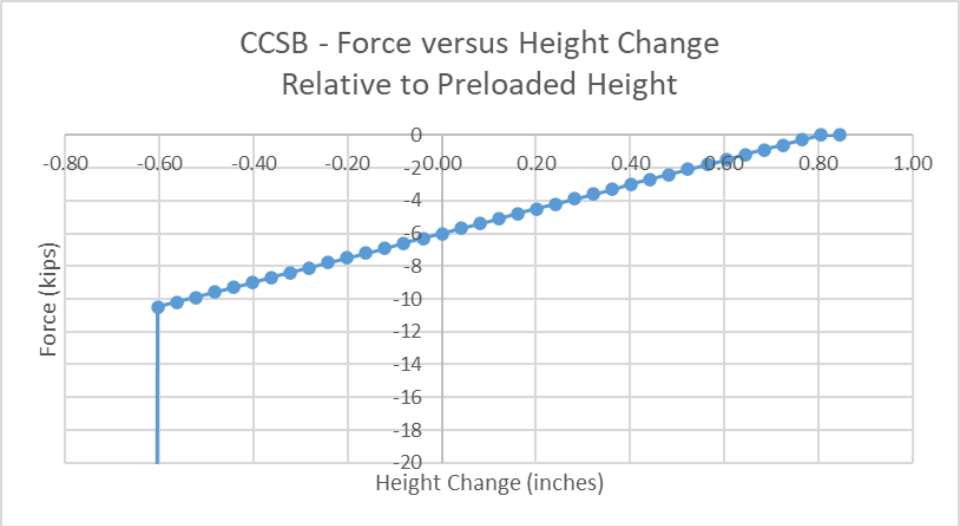


**Figure E 8. Force versus Change in Height Relative to Preloaded Length, CCSB Cap to Bolster Connector Representing Spring Group**

When fully assembled, each three-piece freight truck had the inertial parameters summarized in Table E 8.

## Table E 8. Summary of Three-piece Freight Truck Properties

| Parameter | Value |
|---|---|
| Total Mass | 25.19 lbf-$s^2$/in |
| Total Weight | 9,733 lbf |
| X-location of C.G. | Mid-length of axles |
| Y-location of C.G. | 0.21 inches below centerline of axles |
| Z-location of C.G. | Centered between axles |
| $I_{xx}$ (pitch) About C.G. | 23,600.84 lbf-$s^2$-in |
| $I_{yy}$ (yaw) About C.G. | 45,593.91 lbf-$s^2$-in |
| $I_{zz}$ (roll) About C.G. | 25,793.36 lbf-$s^2$-in |
| X-location of Center Bowl | Mid-length of axles |
| Y-location of Center Bowl | 4.25 inches (0.108 m) above C.G. |
| Z-location of Center Bowl | Centered between axles |
| $I_{xx}$ (pitch) About Center Bowl | 24,055.43 lbf-$s^2$-in |
| $I_{yy}$ (yaw) About Center Bowl | 45,593.91 lbf-$s^2$-in |
| $I_{zz}$ (roll) About Center Bowl | 26,247.96 lbf-$s^2$-in |

# Appendix F.
# Rail and Track Structure Modeling

## Dump Truck Guide Track (Existing Track)

The guide track that the dump truck coasted along was modeled as two rigid, 1,300-inch long RE136 [19] rails. Each rail was constrained in all six degrees-of-freedom (DOF), meaning that the tracks were neither able to deform nor displace. The mesh on each rail is summarized in Table F 1.

**Table F 1. Summary of Rigid Rail Part Mesh**

| | |
|---|---|
| Part | Rigid Rail |
| Element Type | Rigid Shell (R3D4) |
| Number of Elements | 9,724 |
| Boundary Conditions | Ux = Uy = Uz = URx = Ury = Urz = 0 |

## Test Consist Stub Track (Newly-constructed)

The test consist stub track was modeled using techniques that would allow the rails and the ties to deform during the impact forces. The deformable track model was made up of 4 deformable rails (long), 126 rigid concrete ties, 126 rigid ground planes, and various constraints, connectors, and boundary conditions. Additionally, several models were run using a deformable rail (short) to bridge the gap between deformable rails (long), forming a continuous rail.

Figure F 1 shows two views of the deformable track model near its center. The top image is a side view showing the rigid concrete ties, rigid ground, deformable rails, and the connectors between ties and ground. The bottom image is an angled view showing several constraints that were used to attach the deformable rails to one another, and to attach the deformable rails to the concrete ties.

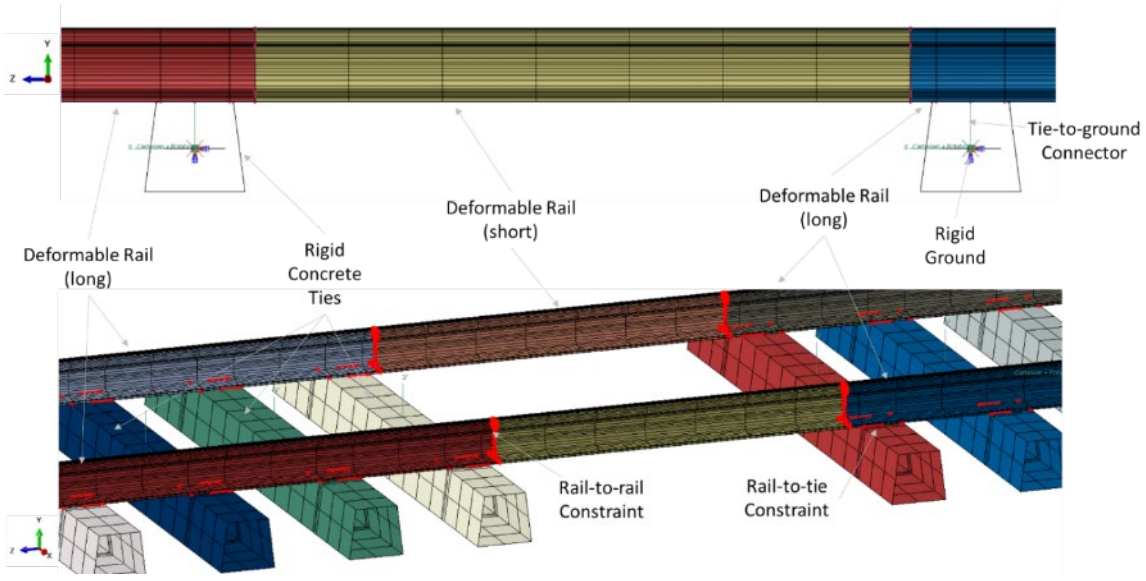


**Figure F 1. Annotated Deformable Track Model, Side View (top) and Angled View (bottom)**

The wheels of the tender and locomotives sat upon two long deformable rails. Each rail was modeled using an RE136 rail profile [19]. Each deformable rail (long) measured 1,500 inches in length. A total of 4 deformable rails (long) were used in the model. The mesh for each deformable rail (long) part is summarized in Table F 2.

**Table F 2. Summary of Deformable Rail (long) Part Mesh**

| Part | Deformable Rail |
|---|---|
| Element Type | 8-node continuum, reduced integration (C3D8R) |
| Number of Elements | 45,760 |
| Material Behaviors | Elastic-plastic |
| Boundary Conditions | None |
| Constraints | TIE constraint between base of rail and top of concrete tie, and;<br>TIE constraint between end of rail and end of short rail spanning dump truck guide track |
| Part Mass (lbf-s$^2$/in) | 1.47344 |
| Part Weight (lbf) | 5,693.4 |

The deformable rails were assigned an elastic-plastic material response. Tensile tests of various rail steels were previously conducted under a separate research program [20]. A typical engineering stress-strain response for rail steel was developed based on the engineering stress-strain responses measured in that program. The typical engineering stress-strain response was then converted into a true stress, true plastic strain response in the format required by the Abaqus FE software. The resulting true stress-strain response is plotted in Figure F 2.

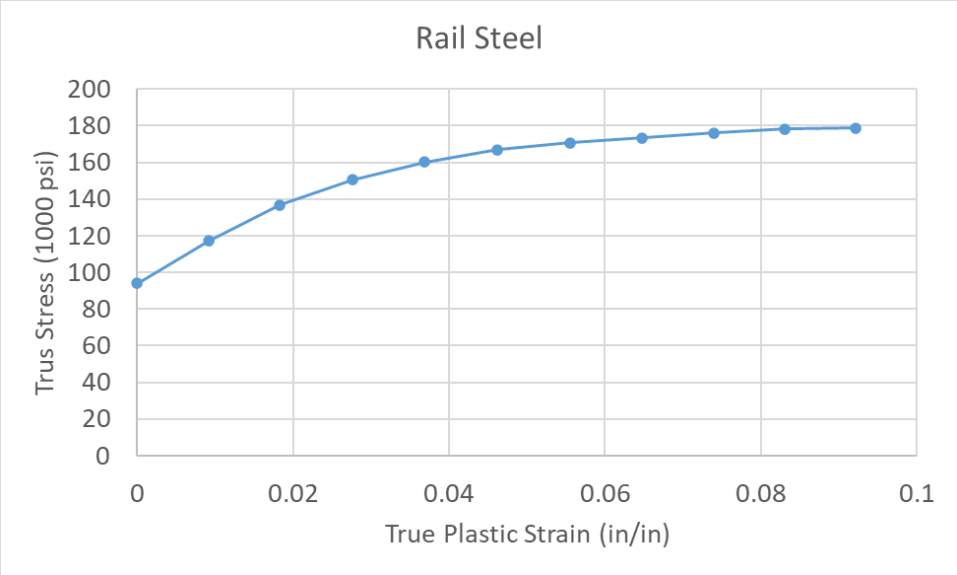


**Figure F 2. True Plastic Stress-strain Response for Rail Steel**

A short length of deformable rail was used in several models to eliminate the gap between long deformable rails to either side of the rigid guide track for the dump truck. The deformable rail (short) used the same profile and material properties as the deformable rail (long) but was only 65.4 inches (1.66 m) long. A total of 2 deformable rails (short) were used in the model. The mesh for each deformable rail (short) part is summarized in Table F 3.

**Table F 3. Summary of Deformable Rail (short) Part Mesh**

| | |
|---|---|
| Part | Deformable Rail |
| Element Type | 8-node continuum, reduced integration (C3D8R) |
| Number of Elements | 882 |
| Material Behaviors | Elastic-plastic |
| Boundary Conditions | None |
| Constraints | TIE constraint between ends of rail and end of long rails |
| Part Mass (lbf-s$^2$/in) | 0.642372 |
| Part Weight (lbf) | 248.2 |

The deformable rails were supported by 126 rigid concrete ties. The rails were attached to the ties through a TIE constraint between the base of each rail and top of each concrete tie. Ties had a 24-inch center-to-center spacing. Each concrete tie measured 102 inches in length. Each tie was attached to the ground using a connector element with prescribed properties (discussed below). The cross-section of the concrete tie is shown in Figure F 3. The "X" in the center of the cross-section denotes the reference point to which the boundary conditions, inertial properties, and connector elements are attached. Tie geometry and inertial properties were highly simplified but based on published data for existing concrete ties [21]. The mass moments of inertia for the tie were calculated using the Abaqus FE software assuming the total mass of the tie was uniformly distributed throughout the geometry of the tie. The concrete tie mesh is summarized in Table F 4.

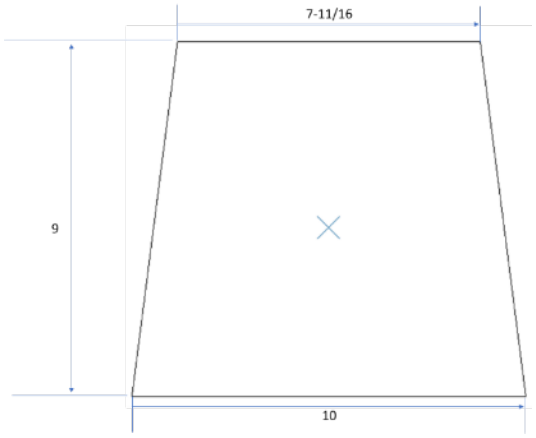


**Figure F 3. Concrete Tie Cross-section (dimensions in inches)**

**Table F 4. Summary of Rigid Concrete Tie Part Mesh**

| | |
|---|---|
| Part | Concrete Tie |
| Element Type | R3D4 |
| Number of Elements | 160 |
| Material Behaviors | Rigid |
| Boundary Conditions | UZ = URY = 0 |
| Constraints | TIE constraint between base of rail and top of concrete tie |
| Connectors | CARTESIAN + ROTATION type connector with prescribed UX, UY, and URZ behaviors (see below) |
| $I_{xx}$ (lbf-s$^2$-in) | 24.18 |
| $I_{yy}$ (lbf-s$^2$-in) | 1583.78 |
| $I_{zz}$ (lbf-s$^2$-in) | 1583.93 |
| Part Mass (lbf-s$^2$/in) | 1.811 |
| Part Weight (lbf) | 699.8 |

Each concrete tie was paired with a rigid ground plane. The rigid ground planes were fixed in all 6 DOF. Each rigid ground plane was initially located at a point in space collocated with its companion tie's reference point. Each concrete tie was attached to its ground plane using a CARTESIAN + ROTATION-type connector element. The tie-to-ground connector had different distinct behaviors for translations in the X and Y directions and for rotations about the Z-axis. These behaviors were simplified representations of the resistance to tie motion provided by ballast and substructure.

In the vertical (UY) direction, track modeling was based on a beam on elastic foundation (BEF) approach. In a BEF approach, each rail is assumed to be supported by a continuous elastic foundation with a uniform stiffness per unit area [22]. This approach is a reasonable simplification for the discrete support provided by railroad ties provided the gap between adjacent ties is not overly large. Equation F 1 describes the relationship between the continuous foundation stiffness, the tie-to-tie spacing, and the equivalent stiffness per tie. The foundation modulus ($k_{foundation}$) for the deformable track was assumed to be 3,000 psi [23]. With the 24-inch center-to-center spacing used between concrete crossties in the model, each tie-to-ground connector element was assigned a vertical stiffness ($k_{equivalent}$) of 72,000 lbf/in/tie. Additionally, a vertical damping constant of 10 lbf/(in/s) was assigned to each tie.

**Equation F 1. Equivalent Spring Stiffness Per Tie**

$$k_{equivalent} = k_{foundation} \cdot d_{centers}$$

$$\frac{72{,}000\,\frac{lbf}{in}}{tie} = 3{,}000psi \cdot 24in/tie$$

Each tie was allowed to rotate about the Z direction. The resistance offered by the track structure below the tie was approximated by defining a moment-angle relationship, which was then assigned to the CARTESIAN + ROTATION-type connector. The moment-angle relationship was derived based on the vertical foundation stiffness *($k_{equivalent}$)* assigned to each tie's connector. To determine the moment-angle relationship, it was first assumed that the single vertical spring represented by the connector element is equivalent to numerous *($n_{springs}$)* springs distributed across the length *(L)* of the rigid tie. This situation is illustrated schematically in Figure F 4.

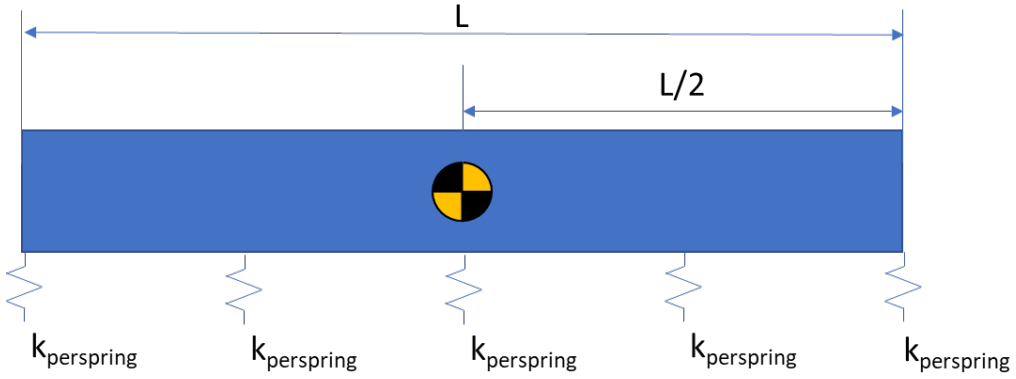


**Figure F 4. Schematic Showing Multiple Springs Distributed Across Length of Rigid Concrete Tie**

If the concrete tie that was supported by multiple springs along its length was loaded vertically through its center of rotation, then these springs would behave in parallel. Thus, the per-spring stiffness ($k_{perspring}$) would be calculated using Equation F 2.

**Equation F 2. Vertical Stiffness Per Spring, Multiple Springs Across Tie**

$$k_{perspring} = \frac{k_{equivalent}}{n_{springs}}$$

The stiffness of a linear spring is proportional to the force required to deform that spring by a given change in length [24]. For a rigid tie with multiple springs along its length, the force developed in each spring ($F_{perspring}$) is calculated according to Equation F 3, where the deflection of a given spring is represented by $\Delta_{perspring}$.

**Equation F 3. Force Per Spring, Multiple Springs Across Tie**

$$F_{perspring} = k_{perspring} \cdot \Delta_{perspring}$$

For a concrete tie that was supported by multiple springs along its length subjected to a moment *(M)*, the tie will rotate by an angle *(θ)* about its center of rotation. Individual springs on one side of the center of rotation will lengthen and apply a tensile restoring force, while springs on the other side of the center of rotation will shorten and apply a compressive restoring force, as illustrated schematically in Figure F 5.

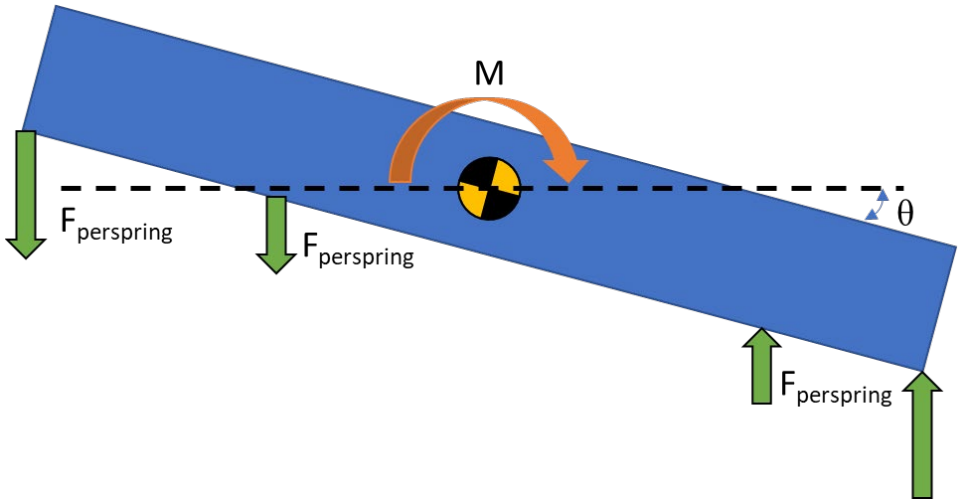


**Figure F 5. Schematic Showing Restoring Force from Multiple Springs Distributed Across Length of Tie Subjected to a Moment**

The vertical deflection of a single spring *($\Delta_{perspring}$)* caused by moment *(M)* will vary based on the spring's distance from the center of rotation, with the springs at the end of the tie undergoing a larger deflection than the springs near the center of the tie. The deflection of the $n_{th}$ spring from the center of rotation can be calculated according to Equation F 4.

**Equation F 4. Deflection of a Single Spring**

$$\Delta_{perspring} = \frac{n \cdot L}{n_{springs}} \cdot \sin(\theta)$$

Combining equations Equation F 3 and Equation F 4, the force per spring resisting moment *M* is shown to vary with both the number of springs assumed along the length of the tie and the angle of rotation as shown in Equation F 5.

**Equation F 5. Force Per Spring as a Function of Angle**

$$F_{perspring} = k_{perspring} \cdot \frac{n \cdot L}{n_{springs}} \cdot \sin(\theta)$$

The value of $F_{perspring}$ developed by each spring produces a corresponding moment about the center of rotation of the tie. The moment produced by each individual spring is based on its force and its horizontal distance ($D_{horizontal}$) from the center of rotation, as shown in Equation F 6.

**Equation F 6. Moment Per Spring**

$$M_{perspring} = F_{perspring} \cdot D_{horizontal}$$

The horizontal distance of a single spring ($D_{horizontal}$) from the center of rotation will vary with the angle of rotation and number of springs assumed along the length of the tie. The horizontal distance between the $n_{th}$ spring and the center of rotation can be calculated using Equation F 7.

**Equation F 7. Horizontal Distance Between Single Spring and Center of Rotation**

$$D_{horizontal} = \frac{n \cdot L}{n_{springs}} \cdot \cos(\theta)$$

Combining Equation F 5 through Equation F 7, the moment developed by each individual spring around the center of rotation of the concrete tie is shown in Equation F 8.

**Equation F 8. Moment versus Angle Relationship for Individual Springs**

$$M_{perspring} = F_{perspring} \cdot D_{horizontal} = k_{perspring} \cdot \frac{n \cdot L}{n_{springs}} \cdot \sin(\theta) \cdot \frac{n \cdot L}{n_{springs}} \cdot \cos(\theta)$$

Finally, the moment versus angle relationship for the rigid concrete tie can be obtained by adding the contributions of each assumed spring along the length of the rigid concrete tie. Because the center of rotation is at the centroid of the rigid tie in the model, symmetry can be used to simplify this calculation. The *nth* spring on the end of the tie that has rotated downward will have a companion spring at the same location on the opposite end of the tie that has rotated upward by the same distance, forming a couple. Thus, the total moment developed by the couple is twice the moment developed by the *nth* spring. Consequently, only the total moment generated by the springs over the distance L/2 need to be calculated and then multiplied by 2 to account for the contributions from the other end of the tie. The moment versus angle relationship for the whole tie ($M_{total}$)is calculated according to Equation F 9.

**Equation F 9. Moment versus Angle Relationship for Entire Tie**

$$M_{total}(\theta) = \sum_{n=1}^{\frac{n_{springs}}{2}} 2\left(k_{perspring} \cdot \frac{n \cdot L}{n_{springs}} \cdot \sin(\theta) \cdot \frac{n \cdot L}{n_{springs}} \cdot \cos(\theta)\right)$$

The CARTESIAN + ROTATION connector type is intended to represent the continuous support provided to the tie by the ballast and subgrade. To approximate this continuous support using a discrete number of assumed linear springs, the value of $n_{springs}$ was increased several times until the moment-versus-angle relationship converged. The resulting moment-versus-angle relationships from this convergence study are shown in Figure F 6.

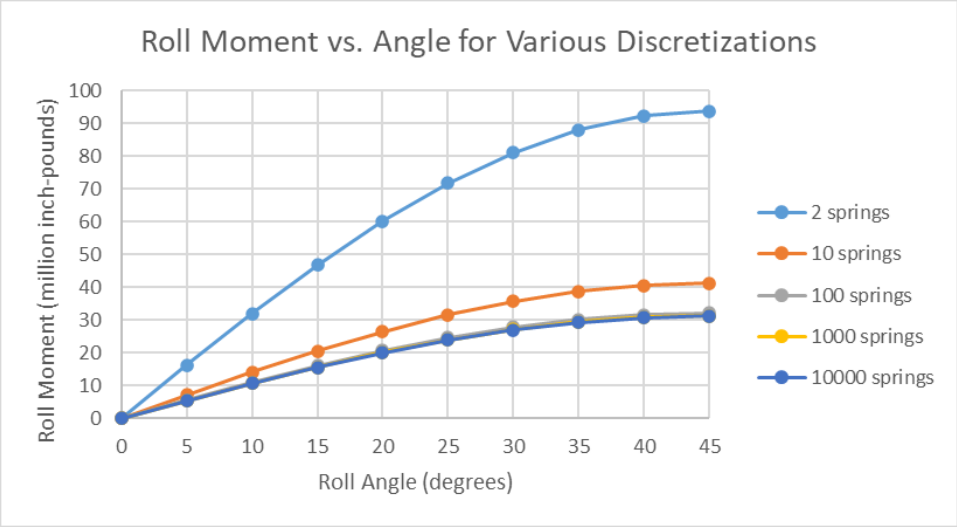


**Figure F 6. Roll Moment versus Angle for Various Numbers of Springs Assumed Along Length of Tie**

If $n_{springs}$ is assumed to be 100 or greater, the moment versus angle relationship remains virtually unchanged. The moment versus angle data that defined the URZ behavior of the CARTESIAN + ROTATION connector between each concrete tie and its ground plane are provided in Table F 5.

**Table F 5. Moment versus Angle Response for URZ**

| Roll Moment inch-pounds | Angle Radians |
|---|---|
| -3.12E+07 | -7.85E-01 |
| -3.08E+07 | -6.98E-01 |
| -2.93E+07 | -6.11E-01 |
| -2.70E+07 | -5.24E-01 |
| -2.39E+07 | -4.36E-01 |
| -2.01E+07 | -3.49E-01 |
| -1.56E+07 | -2.62E-01 |
| -1.07E+07 | -1.75E-01 |
| -5.42E+06 | -8.73E-02 |
| 0 | 0 |
| 5.42E+06 | 8.73E-02 |
| 1.07E+07 | 1.75E-01 |
| 1.56E+07 | 2.62E-01 |
| 2.01E+07 | 3.49E-01 |
| 2.39E+07 | 4.36E-01 |
| 2.70E+07 | 5.24E-01 |
| 2.93E+07 | 6.11E-01 |
| 3.08E+07 | 6.98E-01 |
| 3.12E+07 | 7.85E-01 |

In the lateral (UX) direction, each tie's force-versus-displacement response was developed based on a single tie push test (STPT) approach. In an STPT, the tie is disconnected from the rail and then pushed or pulled and the resulting resistance to displacement is measured [25].

Railroad tie lateral resistance is a complicated behavior to simulate for several reasons. Resistance to lateral motion is largely provided by contact between a tie and the ballast surrounding it [26]. The bottom of the tie will slide along the top of the ballast beneath it, resisted by friction between the two materials. The force that develops between the bottom surface of the tie and the ballast below it depends not only on the coefficient(s) of friction between the two materials, but also on the normal force pressing the tie down into the ballast. Further, the coefficient of friction can vary based on the normal load acting on the tie [26]. This normal load depends not only on the weight of the tie and rail, but also on the live load transmitted through the rail and into the tie. On the sides of the tie, the lateral resistance is also provided by contact between the tie and the ballast, but this resistance may not vary as greatly with the vertical load supported by the tie. Finally, at the end of the tie, a lateral motion on the tie will "plow" ballast away from it which will create some resistance regardless of the live load carried by that tie. Since the FE model was being principally developed to simulate the impact response of a fuel tender and not detailed track response, significant simplifications had to be made in the way the lateral resistance of the track structure was modeled.

The goal in developing a lateral response behavior in the connector between each tie and its ground plane was to provide a credible amount of resistance to lateral shift of the ties caused by an impact. Assuming that the ties were fixed in space (i.e., infinite resistance) was neither practical nor conservative, as track panel shift could affect tender dynamics and rollover tendency. Similarly, assuming that the ties were unconstrained (i.e., zero resistance) was also neither practical nor conservative, since allowing the ties to shift freely could also affect the conclusions on tender rollover likelihood. A reasonable estimate of lateral resistance was developed subject to numerous simplifications and assumptions, as well as the limitations of the behaviors that could be defined within the available connector behaviors in the Abaqus software.

Equation F 10 defines the total lateral resistance of a tie ($F_d$) in terms of the lateral resistance of an unloaded tie ($F_s$) plus the contribution of friction ($\mu$) when the tie is supporting a vertical load ($R_v$). Note that for an unloaded tie (i.e., when $R_v = 0$) the total tie lateral resistance is equal to $F_s$.

**Equation F 10. Total Tie Lateral Resistance (from [26], [27])**

$$F_d = F_s + \mu R_v$$

Three connector behaviors were used to describe the lateral resistance to motion: elastic behavior, plastic behavior, and friction. Initially, only plastic behavior and friction behaviors were defined. However, elastic connector behavior must be defined in Abaqus if plastic behavior is also defined. Using a tabular implementation of connector plastic behavior in Abaqus, the lateral resistance ($F_s$) was defined at regularly-spaced values of tie displacement (w). The force-versus-displacement response for plastic behavior of an unloaded tie [$F_s(w)$] was developed based on the "full nonlinear lateral resistance characteristic" described in [27]. Equation F 11 shows the equation used to develop the plastic force-displacement response for lateral tie motion.

**Equation F 11. Full Nonlinear Characteristic for Lateral Resistance from [27]**

$$F_s(w) = (1 - e^{-\mu_1 w}) \cdot [F_L + (F_P - F_L) \cdot e^{-4(w - w_1)/w_L}]$$

The parameters used in Equation F 11 are summarized in Table F 6. Note that except for parameter $w_1$, the values in this table were obtained directly from the cited reference (a value for parameter $w_1$ was not given in the reference). Parameter $w_1$ was instead calculated using an equation from the cited reference.

**Table F 6. Parameters Used to Develop Single-tie Lateral Plastic Force-displacement Characteristic**

| Parameter | Value | Source |
|---|---|---|
| $F_p$ | 3,600 lbf | [27] |
| $F_L$ | 2,200 lbf | [27] |
| $w_p$ | 0.18 in | [27] |
| $w_L$ | 5.0 in | [27] |
| $w_1$ | 0.22158 in | Calculated according to Equation 9 in [27] |
| $\mu_1$ | 24.134 $in^{-1}$ | [27] |

Lateral displacements (w) were defined from 0 to 2.5 inches in 0.05 inch increments. The resulting lateral force-displacement response is shown in Figure F 7.

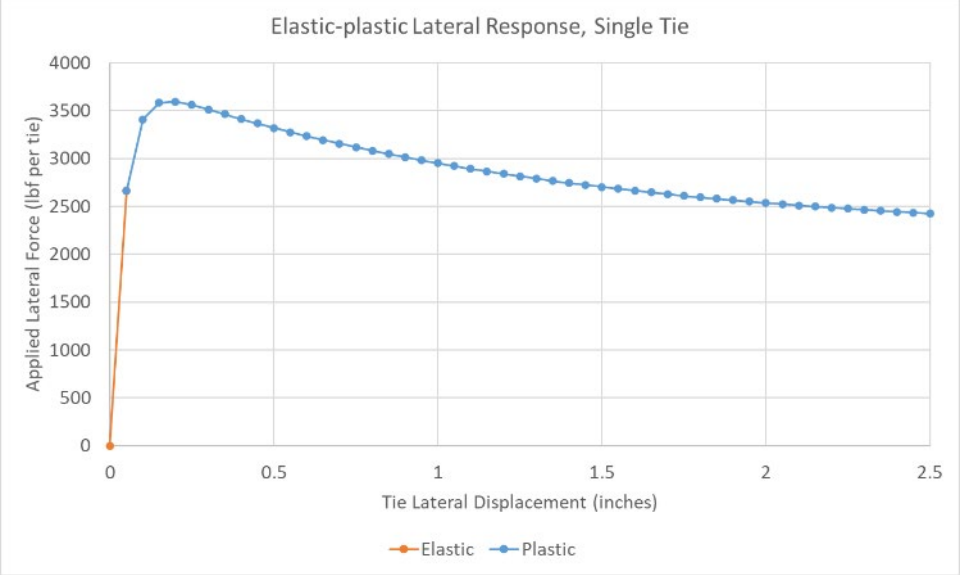


**Figure F 7. Elastic-plastic Lateral Tie Response [$F_s(w)$]**

The Abaqus software requires the definition of an elastic behavior in a connector section if a plastic behavior is also defined. The portion of the lateral response from the origin to the first defined displacement (i.e., 0.05 in) was assumed to behave elastically. Using Equation F 11 with w=0.05 in produces a force of 2667.298 lbf. Dividing this force by the displacement of 0.05 inch produces an elastic stiffness of 53,345.97 lbf/in, which was the value defined in the FE model for elastic stiffness.

After a displacement of 0.05 inch of lateral displacement was reached, the remaining lateral force-displacement behavior would be plastic. The tabular data input to the connector definition describing the plastic behavior must be input as a function of plastic displacement, not total displacement. Plastic displacement is simply the total displacement with the elastic displacement

(i.e., 0.05 in) subtracted. The corresponding plastic force $F^p_s(w)$ at each plastic lateral displacement ($w^p$) calculated using Equation F 11 is shown in Table F 7.

**Table F 7. Lateral Tie Loading Plastic Force-displacement Response**

| Lateral Plastic Force $F^p_s(w)$ | Lateral Plastic Displacement $w^p$ | Lateral Plastic Force $F^p_s(w)$ | Lateral Plastic Displacement $w^p$ | Lateral Plastic Force $F^p_s(w)$ | Lateral Plastic Displacement $w^p$ |
|---|---|---|---|---|---|
| lbf | inches | lbf | inches | 2551.25 | 1.9 |
| 2667.3 | 0 | 2951.06 | 0.95 | 2537.48 | 1.95 |
| 3407.97 | 0.05 | 2921.62 | 1 | 2524.24 | 2 |
| 3583.89 | 0.1 | 2893.32 | 1.05 | 2511.53 | 2.05 |
| 3595.34 | 0.15 | 2866.13 | 1.1 | 2499.31 | 2.1 |
| 3559.98 | 0.2 | 2840.02 | 1.15 | 2487.58 | 2.15 |
| 3512.35 | 0.25 | 2814.92 | 1.2 | 2476.3 | 2.2 |
| 3462.57 | 0.3 | 2790.81 | 1.25 | 2465.47 | 2.25 |
| 3413.56 | 0.35 | 2767.64 | 1.3 | 2455.06 | 2.3 |
| 3366.12 | 0.4 | 2745.38 | 1.35 | 2445.06 | 2.35 |
| 3320.44 | 0.45 | 2724 | 1.4 | 2435.45 | 2.4 |
| 3276.52 | 0.5 | 2703.45 | 1.45 | 2426.22 | 2.45 |
| 3234.31 | 0.55 | 2683.71 | 1.5 | | |
| 3193.76 | 0.6 | 2664.75 | 1.55 | | |
| 3154.79 | 0.65 | 2646.52 | 1.6 | | |
| 3117.35 | 0.7 | 2629.01 | 1.65 | | |
| 3081.38 | 0.75 | 2612.19 | 1.7 | | |
| 3046.82 | 0.8 | 2596.03 | 1.75 | | |
| 3013.62 | 0.85 | 2580.5 | 1.8 | | |
| 2981.72 | 0.9 | 2565.58 | 1.85 | | |

The coefficient of friction (μ) between a concrete tie and ballast is dependent on the normal force acting on the tie ($R_v$) [26]. The ballast-tie coefficient of friction (μ) can be calculated according to Equation F 12. The parameters used in this equation are shown in Table F 8. Note that the symbol $\mu_1$ in the friction calculations represents a different quantity than when this symbol was used in the lateral force equation shown in Equation F 11.

**Equation F 12. Tie-ballast Coefficient of Friction [26]**

$$\mu = \mu_2 + (\mu_1 - \mu_2) \cdot e^{-\beta \cdot R_v}$$

**Table F 8. Parameters Used to Develop Single-tie Lateral Friction Characteristic**

| Parameter | Value | Units | Source |
|---|---|---|---|
| $\mu_1$ | 0.9 | - | [26] |
| $\mu_2$ | 0.75 | - | [26] |
| β | 0.16 | $kip^{-1}$ | [26] |

Figure F 8 contains a plot of the tie-ballast coefficient of friction versus vertical load per tie for loads between 5 (22.241) and 50 (222.41) kips (kN). As the vertical load increases, the coefficient of friction asymptotically approaches the value of $\mu_2$. While the connector friction behavior in the Abaqus FE software can make the lateral friction *force* dependent on the normal (i.e., vertical) load carried by the connector element, the lateral friction *coefficient of friction* cannot be made dependent on the vertical load. For simplicity, a constant value of 0.77 was used in the FE model for μ regardless of the vertical load carried by the tie.

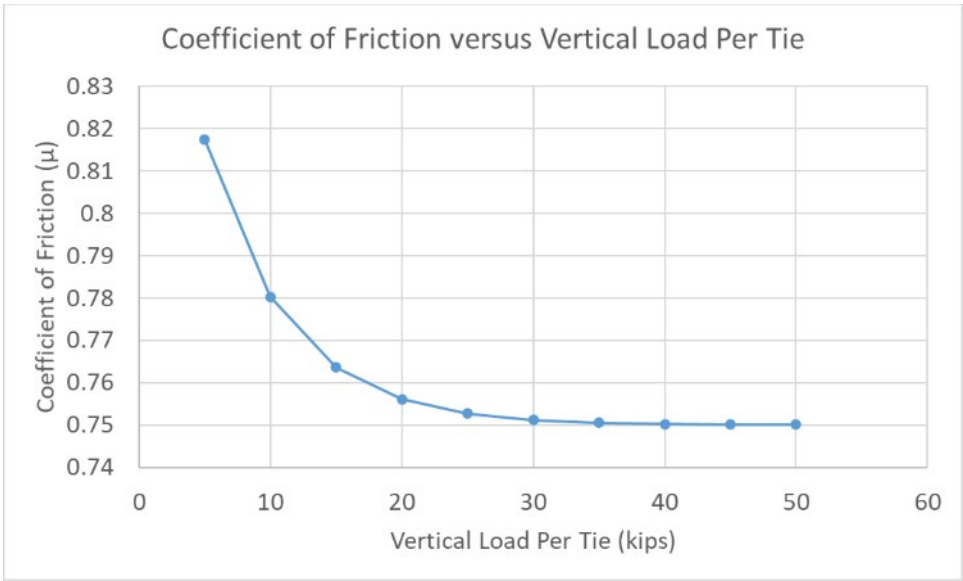


**Figure F 8. Connector Coefficient of Friction versus Vertical Load Per Tie**

As a check that the assembled (i.e., the elastic, plastic, and friction) lateral characteristic was behaving as expected, a series of STPTs were simulated. Two different approaches were taken. In the first, the coefficient of friction (μ) was held constant at 0.77 and the vertical load on the tie was varied between 0 and 50,000 lbf. A 50,000 lbf lateral force was applied to the tie, and the resulting force and displacement behavior in the connector element was extracted. The results of this first approach are plotted in Figure F 9. The desired outcome of this study was verification that as the vertical load increased so too did the resistance to the tie's lateral motion while the overall shape of the response remained similar.

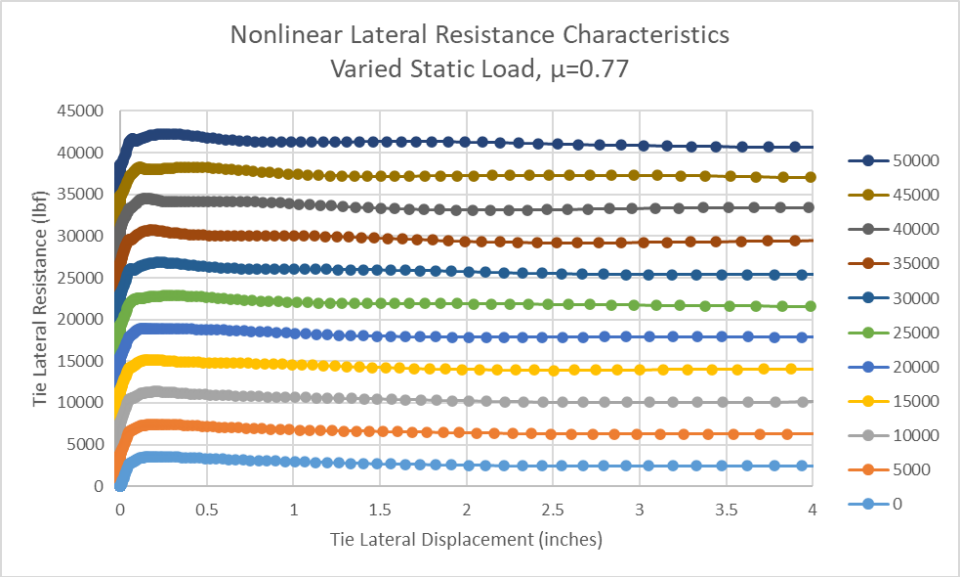


**Figure F 9. Tie Lateral Resistance Characteristics with Varied Static Loads and μ=0.77**

In the second approach, a constant vertical load of 50 kips was applied and the coefficient of friction was varied. For each simulation, a constant value of coefficient of friction was used, but this coefficient was varied from simulation to simulation (i.e., the coefficient of friction did not

vary based on the load or displacement of the tie). The results of this second approach are plotted in Figure F 10. For each coefficient of friction, the lateral load was applied for 1.0 seconds. As the coefficient of friction increased the maximum lateral displacement in 1.0 seconds decreased. The desired outcome of this study was verification that as the coefficient of friction increased so too did the resistance to the tie's lateral motion while the overall shape of the response remained similar.

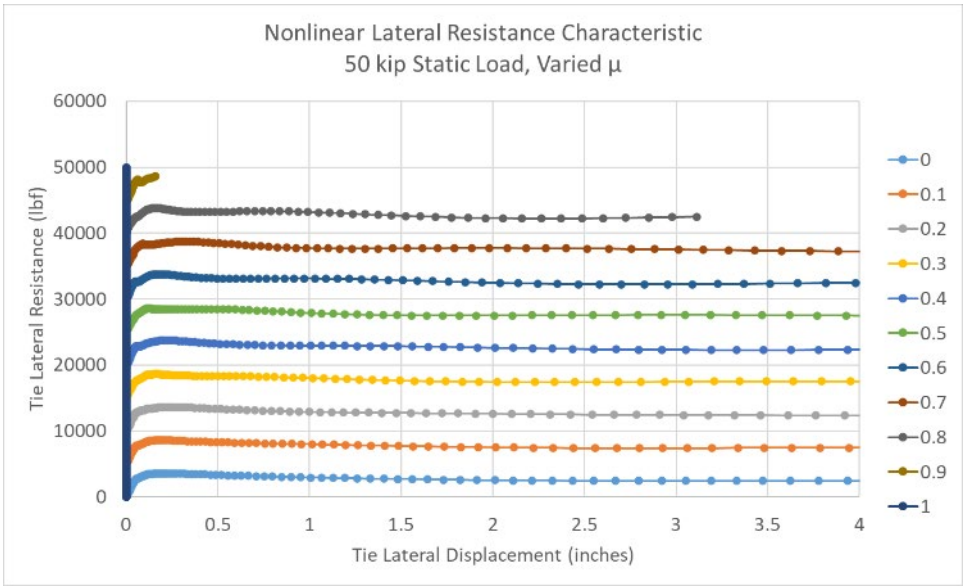


**Figure F 10. Tie Lateral Resistance Characteristics with 50 kip Static Load and Varied μ**

# Appendix G.
# Outage Volume and Pressure Calculations

Several different outage volume and pressure conditions were considered for this test. Additionally, several different outage volume calculations were made by different organizations involved with the test preparations and execution. While the results are similar, different assumptions or data sources (e.g., density, saturation pressure) used in the different calculations resulted in slight differences in the calculated outage volume.

## G1. Using Original Conditions Given in M-1004

At the time test planning commenced, AAR M-1004 defined the test conditions to be a pressure of 150 psig (i.e., 162.3 psia at Pueblo, CO's altitude [28], [29]), a temperature of -260 ºF and a filling level of no greater than 85 percent by volume (i.e., a minimum outage of 15 percent by volume). Since the fuel tender was intended to carry LNG, properties of liquid methane were used to perform the initial calculations of the filling conditions per M-1004 [30]. The inner tank of the fuel tender had a volume of 29,926 gallons of water[1], based on information provided by the tender's manufacturer. Neglecting thermal contraction, the total volume of liquid needed to reach 85 percent full ($V_{85}$) was calculated according to Equation G 1.

**Equation G 1. Target Volume of Liquid for 85% Filling Volume**

$$V_{85} = 0.85 \times V_{tank} = 0.85 \times 29{,}926 \text{ gal} = 25{,}437.1 \text{ gal}$$

At a pressure of 162.3 psia (1.119 MPa) and temperature of 111 K (-260 ºF), liquid methane has a density of 3.542 lbf/gal (424.38 kg/m$^3$) [31]. The weight of LNG at the conditions originally given in M-1004 ($W_{LNG0}$) was calculated according to Equation G 2. Note that the units for $W_{LNG0}$ were converted into the unit system used in the FE model during this calculation.

**Equation G 2. Weight of LNG at Original M-1004 Conditions**

$$W_{LNG0} = V_{85} \times \rho_{LNG0} \times g$$

$$W_{LNG0} = 25{,}437.1 \text{ gal} \times 231 \text{ in}^3/\text{gal} \times [424.38 \text{ kg/m}^3 \times 9.357E^{-8} \text{ (lbf-s}^2\text{/in/in}^3\text{)/(kg/m}^3\text{)}] \times g$$

$$W_{LNG0} = 90{,}158.8 \text{ lbf (401.02 kN)}$$

The tender was filled with LN2 rather than LNG for the test. LN2 has a different saturation pressure versus temperature relationship than LNG. Therefore, the initial conditions for a test using LN2 would not be identical to the initial conditions if LNG were to be used. The test conditions could be selected to either match the initial pressure (150 psig / 1.034 MPa) or the initial temperature (-260 ºF / 111K) given in M-1004, but not both simultaneously. If an initial pressure of 150 psig (1.034 MPa) were chosen for the LN2-filled tank, then the inner tank's temperature could be no higher than -269.7 ºF (105.5 K), compared to the specified value of -260 ºF (111 K) given in M-1004. If an initial temperature of -260 ºF (111 K) were chosen for the LN2 in the test, then the initial pressure could be no lower than 212 psig (1.462 MPa) for nitrogen to remain in the liquid state. The researchers chose to match the test pressure of LN2 to the initial pressure given in M-1004.

[1]Due to thermal contraction, the capacity of the inner tank will be lower when filled with a cryogenic liquid. The temperature of the cryogenic liquid will affect the amount of thermal contraction.

The amount of LN2 to be placed within the tank also varied from the conditions given in M-1004. At 105.5 K (-269.7 °F) and 162.3 psia (1.119 MPa), LN2 has a density of 654.02 kg/m$^3$ (5.458 lbf/gal) [31], substantially higher than LNG's density of 424.38 kg/m$^3$ (3.542 lbf/gal) at 111K (-260 °F) and 162.3 psia (1.119 MPa) [31]. If the researchers chose to fill the tender to 85 percent by volume with LN2 the weight of LN2 would be approximately 1.5 times the weight of LNG filled to the same level. The researchers thought that this excess weight of liquid could potentially influence the test results in an unrealistic way, leading to a greater likelihood of tender rollover and placing unrealistically high stresses on the structure of the tender, its trucks, and the track structure. The team chose to fill the tender with enough LN2 to have the same weight as a tender filled to 85 percent by volume with LNG ($W_{LNG0}$). The volume of LN2 ($V_{LN20}$) weighing the same as $W_{LNG0}$ was calculated according to Equation G 3.

**Equation G 3. Volume of LN2 Having the Same Weight as LNG at Original M-1004 Conditions**

$$V_{LN20} = W_{LNG0} / g / \rho_{LN20}$$
$$V_{LN20} = 90{,}158.8 \text{ lbf} / g / [654.02 \text{ kg/m}^3 \times 9.357E^{-8} \text{ (lbf-s}^2\text{/in/in}^3\text{)/(kg/m}^3\text{)}] / 231 \text{ in}^3\text{/gal}$$
$$V_{LN20} = 16{,}505.6 \text{ gal } (62.48 \text{ m}^3)$$

The volume of LN2 ($V_{LN20}$) that weighed the same as the amount of LNG needed to fill the tender to 85 percent by volume with LNG ($W_{LNG0}$) was substantially lower than the volume of LNG ($V_{85}$) due to the difference in densities. The percent outage remaining in the tank after filling the tank with $V_{LN20}$ was calculated according to Equation G 4.

**Equation G 4. Percent Outage with Equivalent Weight of LN2 in Tank at Original M-1004 Conditions**

$$\text{Outage}_{LN20} = 100 - (V_{LN20}/V_{tank})$$
$$\text{Outage}_{LN20} = 100 - [(16{,}505.6 \text{ gal} / 29{,}926 \text{ gal}) \times 100]$$
$$\text{Outage}_{LN20} = 44.8\%$$

### G2. Using Revised Conditions given in M-1004

After the initial filling level was chosen but before the test, AAR proposed changing the initial conditions for the scenario specified in M-1004. One of the proposed changes was reducing the initial pressure of the lading from 150 psig (1.034 MPa) to 25 psig (0.172 MPa). Since the researchers had already decided that the test pressure should target the pressure given in M-1004, this change to M-1004 required a change to the planned test conditions. The density of both LNG and LN2 vary with pressure and temperature so the calculations above were performed a second time using an updated initial pressure of 25 psig (0.172 MPa). Density values for both LNG and LN2 at the new pressure were obtained from the same source as the original calculations [31]. The weight of LNG at the revised M-1004 condition is calculated in Equation G 5. The volume of LN2 having an equivalent weight to the LNG at the revised M-1004 condition is calculated in Equation G 6. The volume percent of outage in the LN2-filled tank is calculated according to Equation G 7.

**Equation G 5. Weight of LNG at Revised M-1004 Conditions**

$$W_{LNG1} = V_{85} \times \rho_{LNG1} \times g$$
$$W_{LNG1} = 25{,}437.1 \text{ gal} \times 231 \text{ in}^3\text{/gal} \times [423.58 \text{ kg/m}^3 \times 9.357E^{-8} \text{ (lbf-s}^2\text{/in/in}^3\text{)/(kg/m}^3\text{)}] \times g$$
$$W_{LNG1} = 89{,}988.9 \text{ lbf } (400.291 \text{ kN})$$

**Equation G 6. Volume of LN2 Having the Same Weight as LNG at Revised M-1004 Conditions**

$$V_{LN21} = W_{LNG1} / g / \rho_{LN21}$$

$$V_{LN21} = 89{,}988.9 \text{ lbf} / g / [764.1 \text{ kg/m}^3 \times 9.357E^{-8} \text{ (lbf-s}^2\text{/in/in}^3\text{)/(kg/m}^3\text{)}] / 231 \text{ in}^3\text{/gal}$$

$$V_{LN21} = 14{,}101.1 \text{ gal } (53.378 \text{ m}^3)$$

**Equation G 7. Percent Outage with Equivalent Weight of LN2 in Tank at Revised M-1004 Conditions**

$$Outage_{LN21} = 100 - (V_{LN21}/V_{tank})$$

$$Outage_{LN21} = 100 - [(14{,}101.1 \text{ gal} / 29{,}926 \text{ gal}) \times 100]$$

$$Outage_{LN21} = 52.9\%$$

# Appendix H.
# Pre-test FE Model Results

Due to the large number of unknown and/or difficult-to-characterize behaviors in the assembled FE model, it was not possible to run a single pre-test FE model that represented all of the potential variable conditions with certainty. Rather, the pre-test FE models were used to examine several "what-if" scenarios where one or more parameters were varied in the simulation. The effect of each variation could then be examined, with appropriate changes to the test setup if the simulation result indicated an undesirable situation. Additionally, due to the tender cabinet being offset from the tender center in the FE model in an opposite way to how it was offset in the test, some model results are presented in both their original orientation and with the model reflected laterally (i.e., east-west) relative to the point of impact. In plots showing the displacement of each tie over time, the axis of time is offset such that impact occurs at 0.5 seconds (i.e., a time of 0 seconds corresponds to 0.5 seconds prior to impact). In other plots included in this Appendix, the time has been offset so a time of 0 seconds corresponds to the initial contact between the dump truck and the tender in the model.

The results of each case were compared to the test data where applicable. For several channels measured in the test, damage to data acquisition equipment during impact rendered the data from those channels unusable past the time of damage. The specific cutoff time for each channel is indicated in Table H 1. Additionally, the behavior of data channels VLFX and VRFX suggest an increase in dump truck velocity after the point of impact at these locations, the cause of which was not determined. Comparison between the test and model data for these channels may not yield meaningful results.

**Table H 1. Cutoff Times for Specific Data Channels**

| Channel Name | Does Signal Cut Off? | Cutoff Time [s] |
|---|---|---|
| VCTFX | Yes | 0.091172 |
| VLFX | Yes | 0.033203 |
| VRFX | Yes | 0.108203 |
| VCMX | No | N/A |
| VLMX | Yes | 0.186953 |
| VRMX | No | N/A |
| VCBX | Yes | 0.191875 |
| VCGX | No | N/A |
| THLX | Yes | 0.562656 |
| THRX | No | N/A |
| TCLY | No | N/A |
| TCRY | No | N/A |

### Case A

Case A was the baseline case for the pre-test model. All behaviors were at the assumed values summarized in Table H 2. The tender derailed but remained upright. The deformed FE model is shown in Figure H 1.

Note: The arrangement of figures and plots is the same in each sub-section of this appendix. The figures and plots for Case A will be discussed in depth. For subsequent sub-sections, only those plots and figures with notable results will be discussed.

**Table H 2. Pre-test Case A Model Conditions**

| Case | Tender-to-locomotive Couplers | Bolster Pin and Center Bowl | Rail Base to Concrete Tie | Track Vertical Stiffness | Track Lateral Stiffness | Stub Track Connection | Impact Speed | Initial Pressure | Notes | Outcome |
|---|---|---|---|---|---|---|---|---|---|---|
| A | Yes | Yes | Tied | Default | Default | Discontinuous | 40 mph | 150 psig | Baseline Model | Tender derails, remains upright |

Figure H 1 shows the deformed FE simulation for Case A. The tender derailed but remained upright.

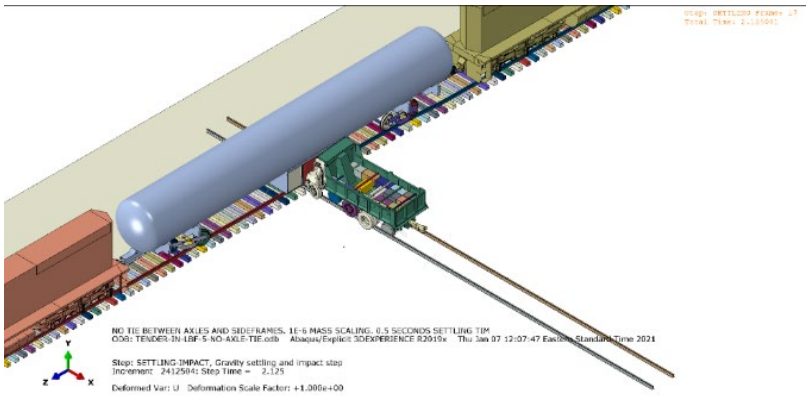

**Figure H 1. Deformed Model, (Case A) Simulation**

Figure H 2 contains a plot of the total vertical force on the connector elements beneath the ties under the deformable rails supporting the tender and locomotive consist as a function of time. The estimated static weight of the locomotives, tender, lading, rails, and the ties themselves is shown as a horizontal line. The period of time from -0.5 seconds to 0 seconds of simulation time in this figure represents the model settling under gravity. Impact occurred at 0 seconds. By 2 seconds post-impact, the total vertical force approached the estimated static weight again. This indicates that while the tender derailed, its weight was still being supported by the ties.

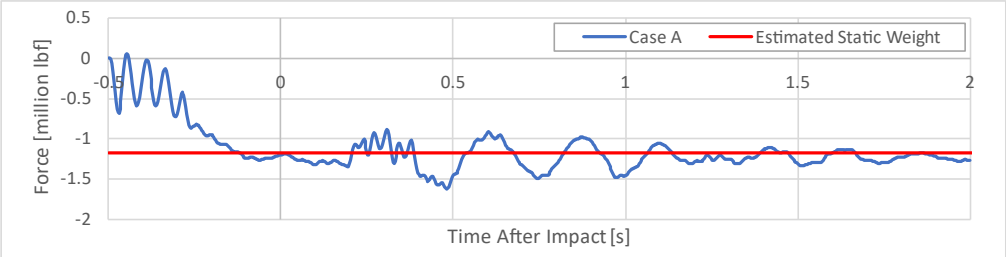


**Figure H 2. Time Response of Total Vertical Force on Ties for Case A**

Figure H 3 contains a plot of the vertical force on the rigid rails forming the dump truck's guide track versus time. A horizontal line indicating the approximate static weight of the dump truck is

also shown on this plot. By 2 seconds post impact the vertical load was approaching the static weight, indicating that although the dump truck had derailed its weight was still being carried by the rigid guide rails.

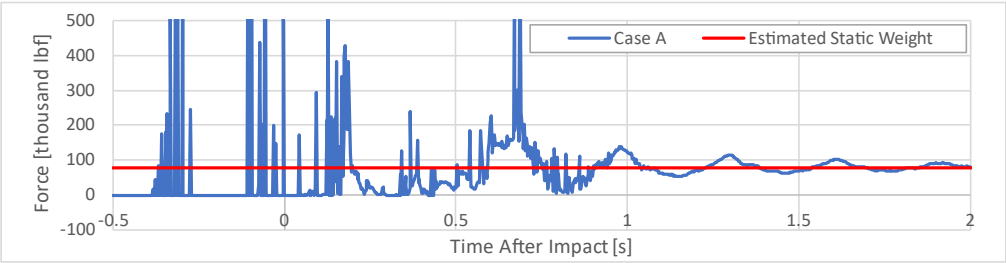


**Figure H 3. Time Response of Total Vertical Force on Dump Truck Guide Rails for Case A**

Figure H 4 contains a plot of the vertical load carried by each tie in the deformable track beneath the tender-locomotive consist at the time of impact. The largest vertical downward forces occurred in proximity to the wheels on the locomotives and the tenders. Between trucks there is an area of uplift where the tie load approaches zero. At the free ends of the rail there are areas of positive tie force, indicating that the uplift forces exceeded the static weight of the rail and the tie connector element must pull the rail downward.

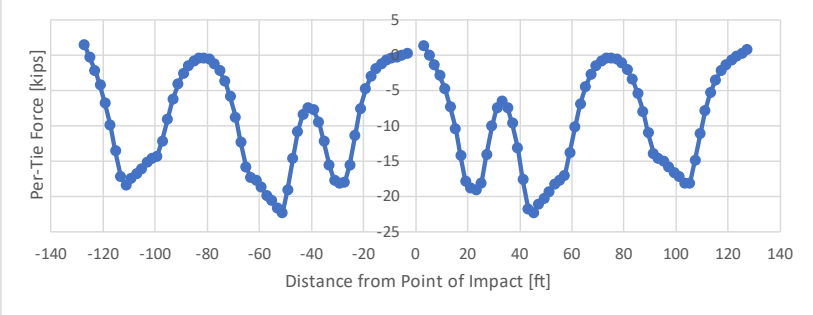


**Figure H 4. Vertical Load Distribution on Ties for Case A**

Figure H 5 contains the same data as the previous figure, but the horizontal axis has been flipped. This plot was produced to account for the discrepancy between the test and the model in which the long- and short-ends of the tender were reversed in the test setup compared to the model arrangement.

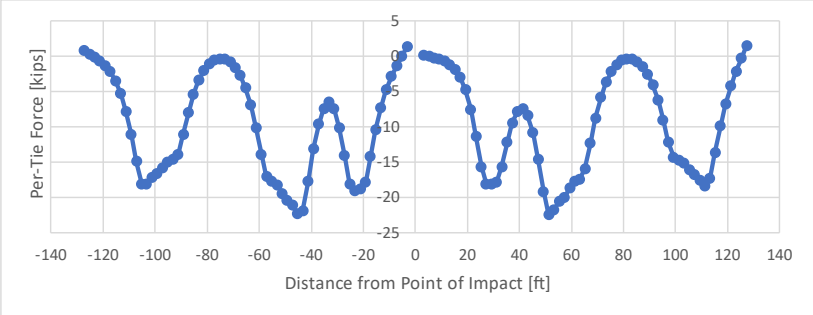


**Figure H 5. Vertical Load Distribution on Ties for Case A: Reflected at Point of Impact**

Figure H 6 contains a plot of the lateral displacement versus time for each tie beneath the deformable rails supporting the tender-locomotive consist. In this figure the impact occurs at a time of 0.5 seconds. Typically, the tie reaches a maximum displacement after impact before rebounding slightly due to elastic recovery.

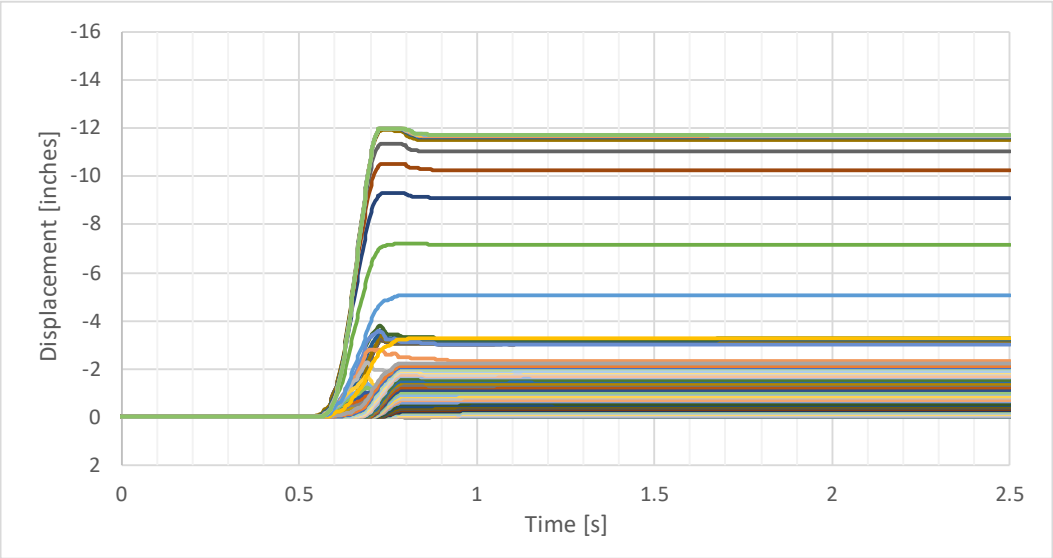


**Figure H 6. Lateral Displacement of Each Tie Over Time for Case A**

Figure H 7 contains a plot of the final displacement of each tie in the Case A model, the final displacement of each tie from the processed drone scan measurements, and the displacement obtained from ground measurements made before and after the test. Figure H 8 contains the same data but with the model data flipped east-west to account for the discrepancy between the tender's orientation in the test and in the pre-test FE models.

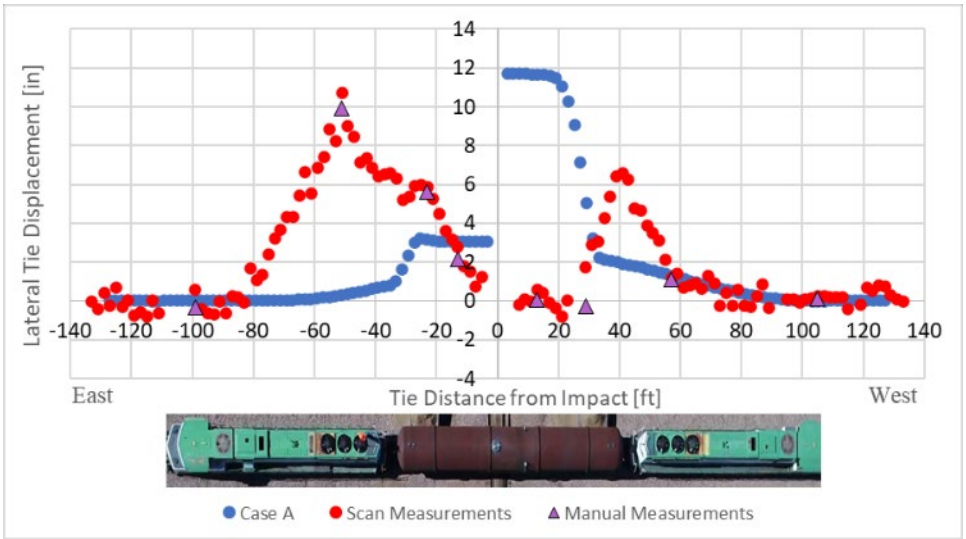


**Figure H 7. Final Lateral Displacement of Each Tie for Case A**

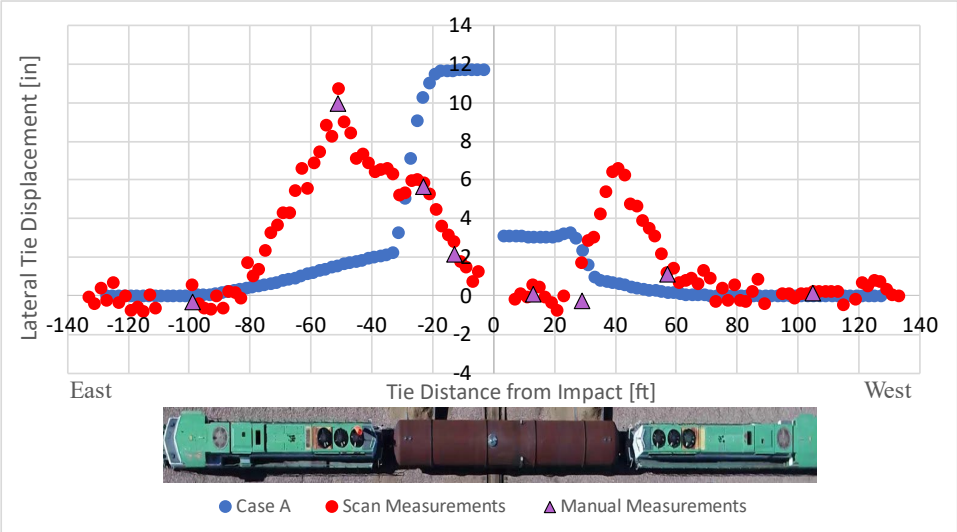


**Figure H 8. Final Lateral Displacement of Each Tie for Case A: Model Data Reflected at Point of Impact**

The distribution of the tie displacements in the test and in the model differed. In the test, the largest displacement measured manually was 10 inches, which was in reasonable agreement with the approximate 11-inch displacement measured from the scans. Regardless of the data source, the peak displacement occurred in the vicinity of the B-end truck on the eastern locomotive. In the FE model, the peak displacement of approximately 12 inches occurred in the ties between the tender's trucks.

Three modeling simplifications may have contributed to the differences between tie displacements measurements and Case A results. The deformable track supporting the locomotive-tender consist was made of two discontinuous "stubs" of track in the Case A model, while the track was continuous in the test. Second, the rails were attached to the ties in the Case A model such that the rail base could not separate from the ties, preventing rail rollover and/or lift. Third, the test setup included two rollover inhibitors to limit the motion of the tender, while the model did not include these features.

Figure H 9 contains four plots of acceleration-time histories from accelerometers on the dump truck from both the test and model Case A. The accelerometer channels VCTFX, VCMX, VCBX, and VCGX are plotted in this figure. These accelerometers were all located along the centerline of the dump truck. The names and locations of the dump truck accelerometers are summarized in Table 4 of the Main Report. All accelerometer data presented in this appendix has been filtered using an SAE60 filter in accordance with SAE J211 [1].

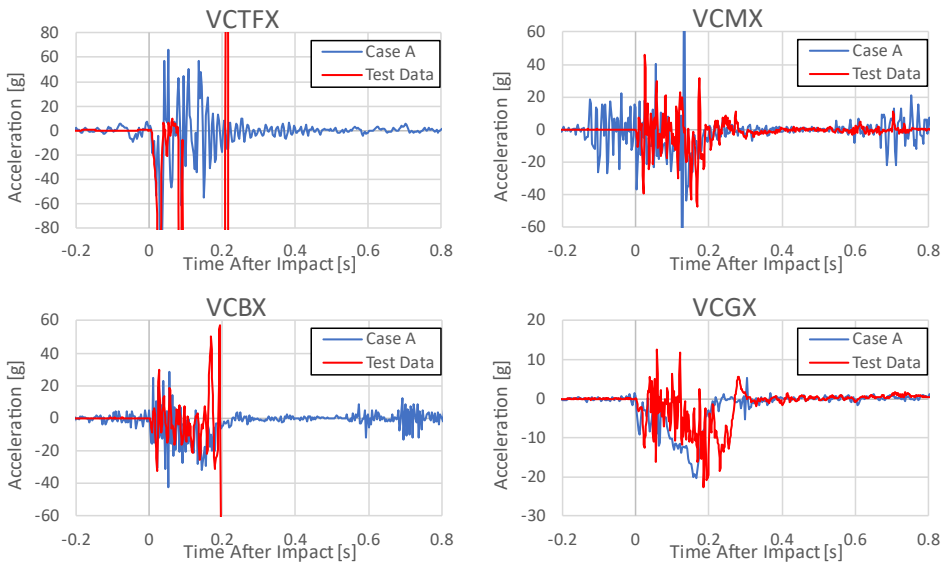


**Figure H 9. Accelerations from Measured and Case A Channels VCTFX, VCMX, VCBX, and VCGX**

Figure H 10 contains four plots of acceleration-time histories from two accelerometer channels on the dump truck from the test and model. The data from VLMX and VLFX are presented alongside the model's accelerations for Case A. Because of the east-west discrepancy between the tender in the model and test, two plots of acceleration-time history are also included where the acceleration of a corresponding location on the opposite side of the dump truck are compared with the test data. That is, the top row compares results from the same side of the modeled and tested dump truck, while the bottom row compares results from the left side of the tested dump truck with the right side of the model.

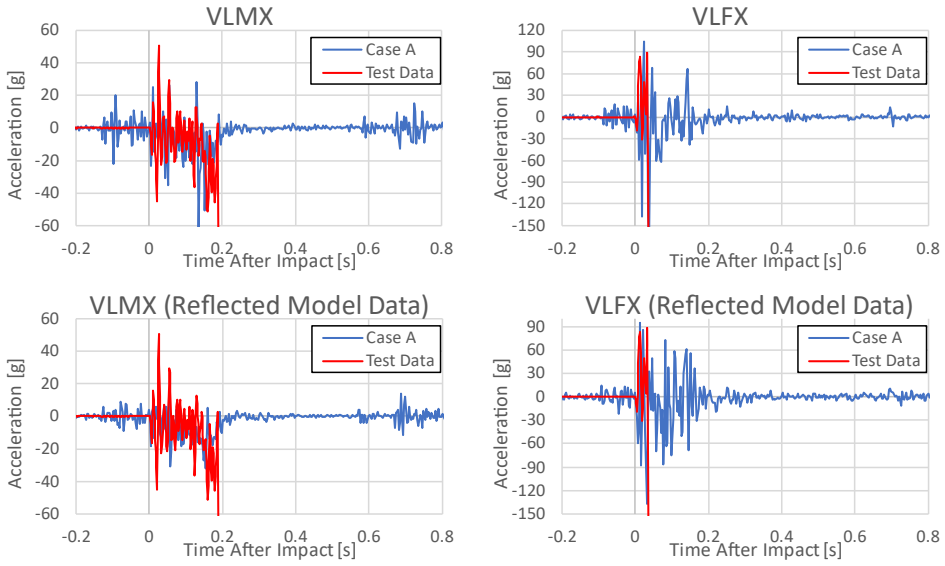


**Figure H 10. Accelerations from Measured and Case A Channels VLMX and VLFX, with Original and Reflected Model Data Presented for Each Channel**

Figure H 11 contains four plots of acceleration-time histories from two accelerometer channels on the dump truck from the test and model. The data from VRMX and VRFX are presented alongside the model's accelerations for Case A. As in the previous figure, the data are presented in the top row as a right-right comparison between test and model, and in the lower row as a right-left comparison.

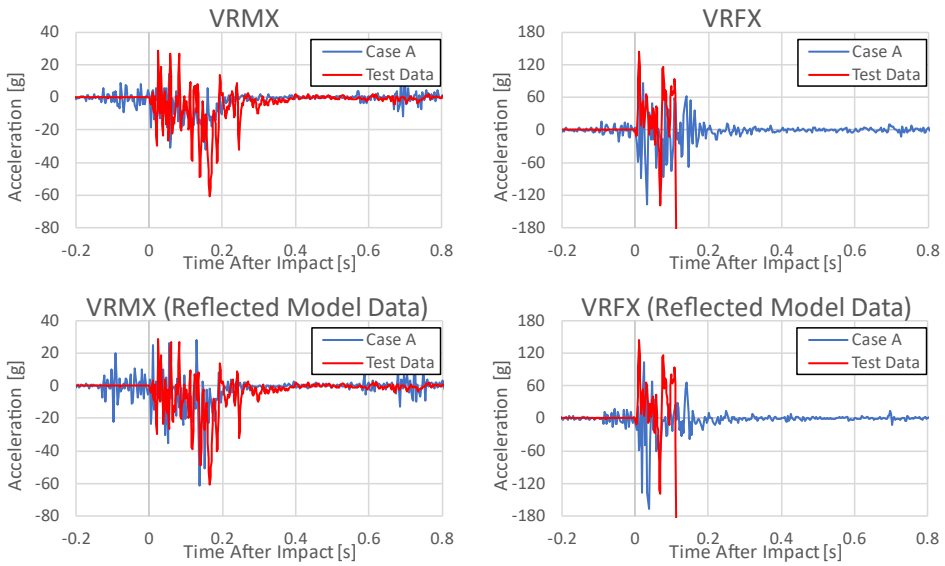


**Figure H 11. Accelerations from Measured and Case A Channels VRMX and VRFX, with Original and Reflected Model Data Presented for Each Channel**

Figure H 12 contains the velocity-time histories of the four accelerometers previously presented in Figure H 9.

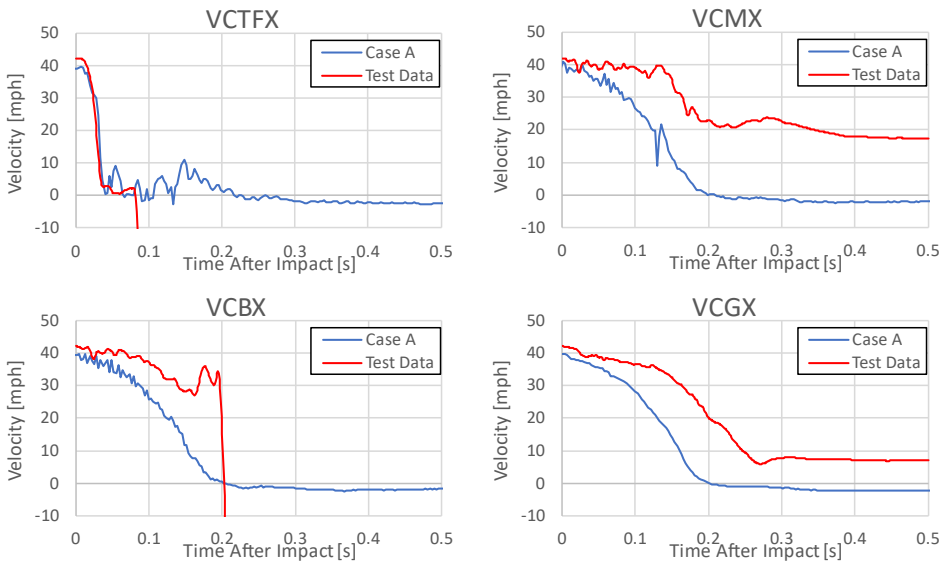


**Figure H 12. Velocities from Measured and Case A Channels VCTFX, VCMX, VCBX, and VCGX**

The velocity-time history provides a clearer view of the results compared to the acceleration-time history due to the noise that remained in the acceleration-time history even after filtering.

The level of agreement between the test data and the model for a given accelerometer location varied significantly. Additionally, it is apparent from the velocity-time histories obtained at different locations throughout the dump truck that the deformation of the dump truck resulted in very different responses throughout the vehicle. Several velocity-time histories (e.g., VCTFX and VCBX) exhibited a sudden drop in velocity indicative of instrumentation channel dropout. Other channels (e.g., VCMX and VCGX) indicated that the dump truck was still traveling forward in the direction of impact after 0.5 seconds post-impact, which is questionable based on review of high-speed video.

Figure H 13 contains velocity-time histories from the accelerometers previously plotted in Figure H 10.

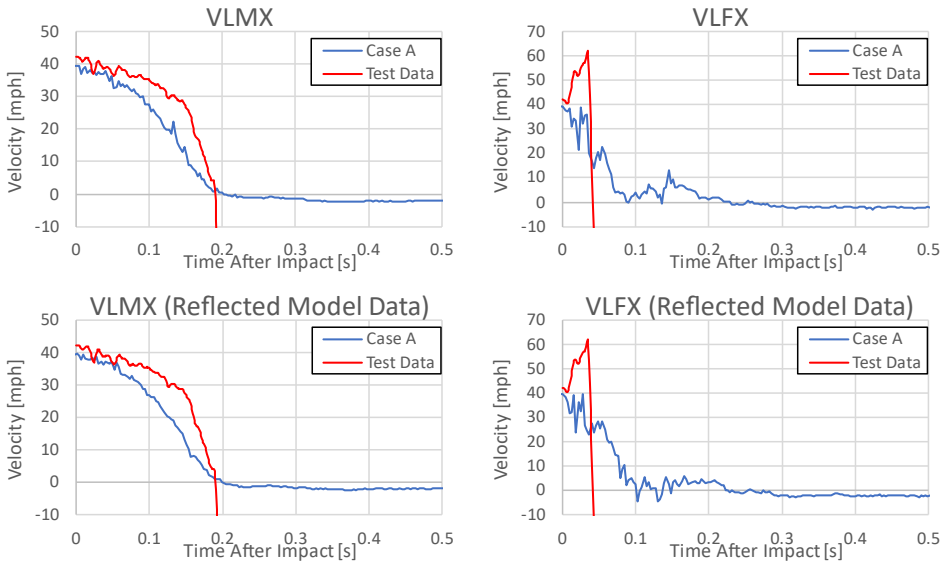


**Figure H 13. Velocities from Measured and Case A Channels VLMX and VLFX, with Original and Reflected Model Data Presented for Each Channel**

As in the accelerometer-time histories, the model results from both the left and right side locations are compared with the test data to account for the tender having its east and west ends reversed between the test and the model. Both channels VLMX and VLFX exhibit sudden near-instant decreases in velocity indicating that the accelerometer dropped out during the test. Additionally, channel VLFX actually indicated an increase in velocity following impact. This result is highly suspicious but no certain explanation for this behavior could be confirmed post-test.

Figure H 14 contains velocity-time histories from the accelerometers previously plotted in Figure H 11. As in the accelerometer-time histories, the model results from both the left and right side locations are compared with the test data to account for the tender having its east and west ends reversed between the test and the model. Channel VRFX exhibited a sudden near-instant decreases in velocity indicating that the accelerometer dropped out during the test. Additionally, channel VRFX actually indicated an increase in velocity following impact. This result is highly suspicious but no certain explanation for this behavior could be confirmed post-test. Channel VRMX did not exhibit a dropout and measured data over the course of the impact event, but indicated that 0.5 seconds after impact the accelerometer was traveling at nearly 30 mph opposite

the direction of impact. This result is not realistic as the dump truck was brought to a stop following the impact without a significant rebound observed on high-speed videos.

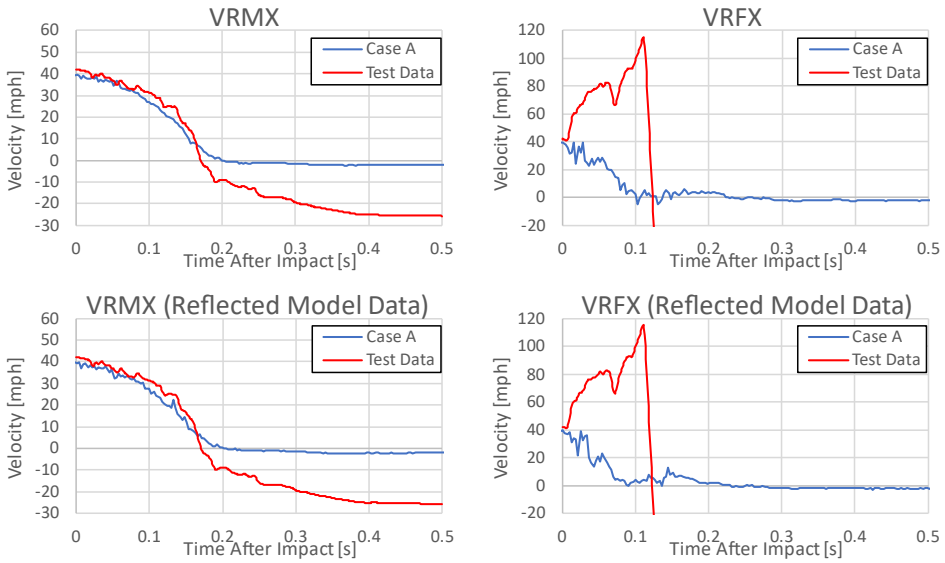


**Figure H 14. Velocities from Measured and Case A Channels VRMX and VRFX, with Original and Reflected Model Data Presented for Each Channel**

Figure H 15 contains a plot of the east (left) head travel measured by string potentiometer THLX on the top and the west (right) head travel measured by string potentiometer THRX on the bottom. Data from the Case A pre-test FE model are also plotted in this figure.

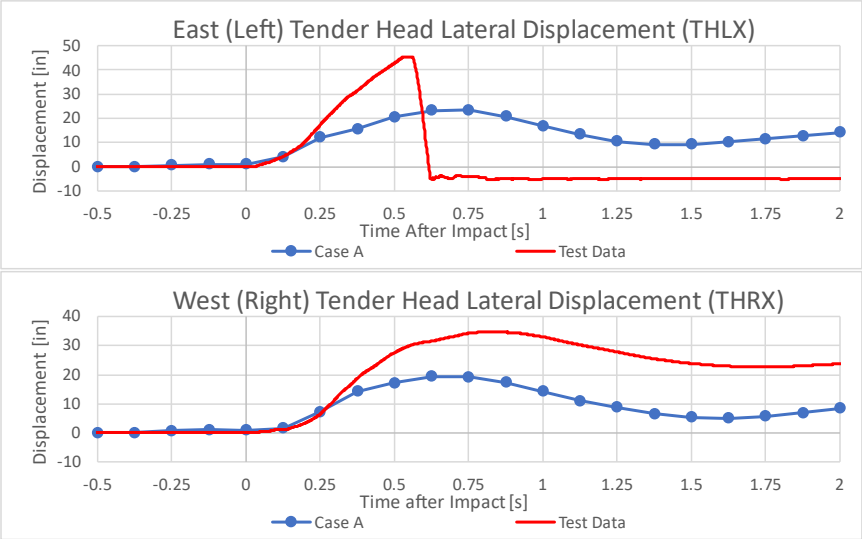


**Figure H 15. Lateral Displacement of the East and West Tender Heads for Case A**

The FE data are from the opposite head than the test data in each plot. That is, the top plot compares the displacement of the left head in the test with the right head in the model and the bottom plot compares the right head in the test with the left head in the model to account for the east-west flip between the tender in the test and in the FE models. During the test, THLX reached its 45-inch travel limit and snapped, causing this channel to register a displacement of -5 inches for the duration of the test. THRX did not reach its travel limit and appears to have

captured valid data throughout the impact event. The Case A model estimated a larger displacement at both ends of the tender than measured during the test. Qualitatively the model data from both ends of the tender resembled the response measured by THRX, with the tender heads moving away in the direction of impact, reaching a maximum, and then returning partway.

Figure H 16 contains a plot of the east (left) locomotive-to-tender coupler travel measured by string potentiometer TCLY on the top and the west (right) locomotive-to-tender coupler travel measured by string potentiometer TCRY on the bottom.

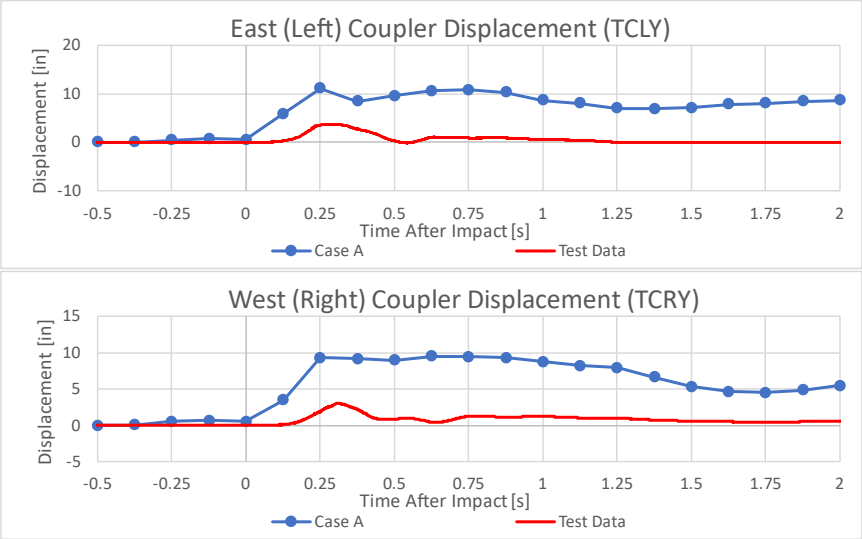


**Figure H 16. Locomotive-to-Tender Coupler Displacements for Case A**

Data from the Case A pre-test FE model are also plotted in this figure. The FE data are again from the opposite coupled interface than the test data in each plot. That is, the top plot compares the displacement of the left coupled interface in the test with the right coupled interface in the model and the bottom plot compares the right coupled interface in the test with the left coupled interface in the model to account for the east-west flip between the tender in the test and in the FE models. At both ends of the tender the model estimated a larger coupler displacement than was measured in the test. The string potentiometer was oriented parallel to the tender and locomotive coupler shanks (i.e., transverse to the direction of the impact). String potentiometers can only measure whether the string is extending or retracting, not whether that change in length was caused by a vertical, lateral, or longitudinal displacement (or combination of displacements) between the two ends of the string.

Figure H 19 contains a plot comparing the test measurements from the string potentiometers installed between the front and back walls of two compartments of the piping cabinet. As shown in Figure H 17 and Figure H 18, in the test the eastern compartment had its string potentiometer installed above a piping passthrough (high location) and the western compartment had its string potentiometer installed below that piping passthrough (low location). For thoroughness, the Case A model results are presented first comparing proximate locations in the FE model with the test measurements.

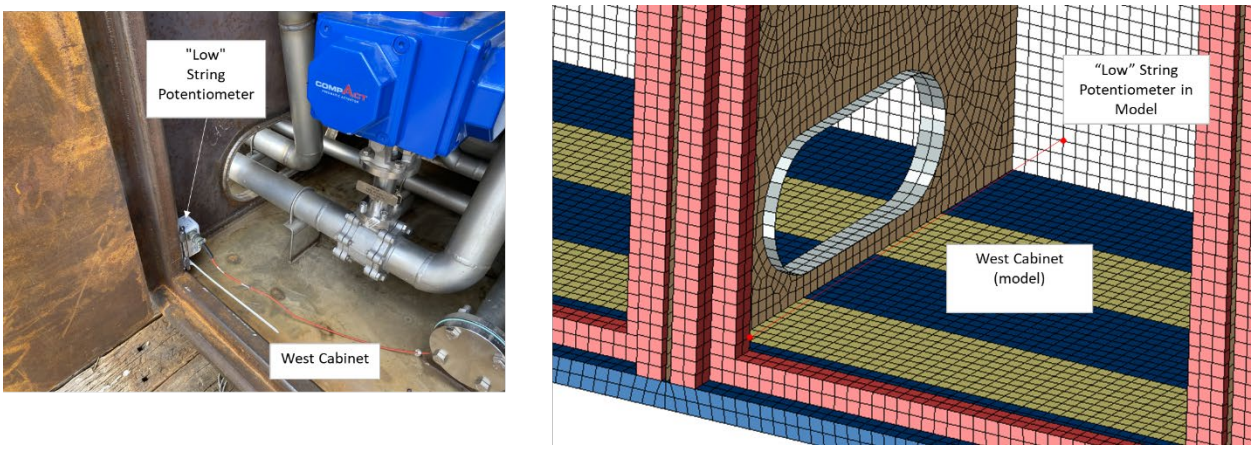


**Figure H 17. West Housing String Potentiometer Location in Test (left) and FE Model (right)**

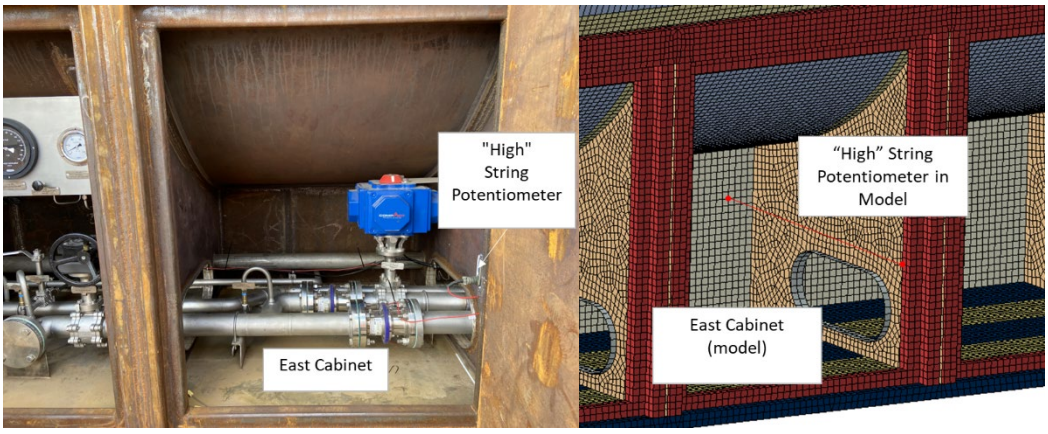


**Figure H 18. East Housing String Potentiometer Location in Test (left) and FE Model (right)**

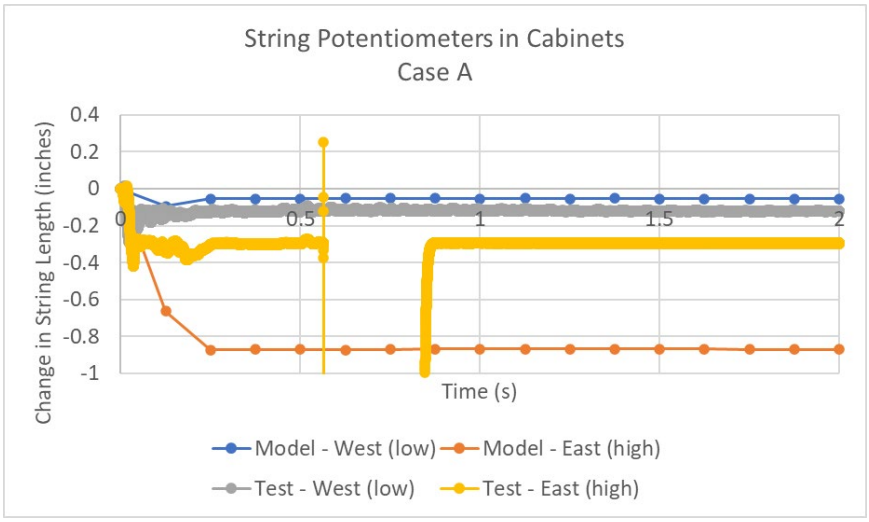


**Figure H 19. String Potentiometers in Piping Cabinet, Case A**

To account for the east-west flip between the tender in the test and in the FE models, Figure H 20 contains the same test data compared against model results from a low location on the east side and a high location on the west side.

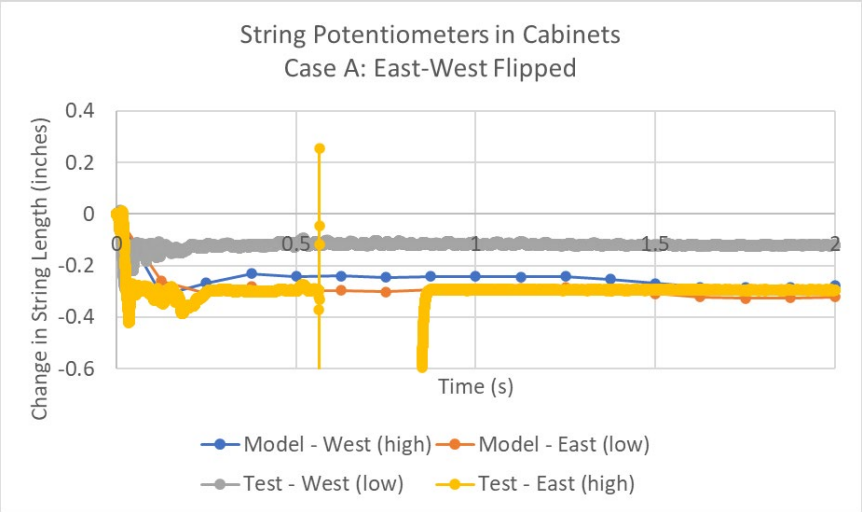


**Figure H 20. String Potentiometers in Piping Cabinet, Case A, East-West Flipped**

The model results indicate some sensitivity to whether the data is obtained from the east or west cabinet in the model. The test data measured in the east cabinet exhibited an unexplained dropout in the measurement that is not attributed to any physical behavior during the test.

### Case B

One of the unknown conditions in the test was the capabilities of the couplers on the tender and locomotive to resist the loads resulting from the impact. Characterizing the failure loads and moments in each of the three translational and rotation directions would have required a substantial effort and been susceptible to assumptions about the actual conditions of the couplers installed on the test vehicles. However, it was important to consider whether the test's outcome would be substantially affected by failure of any of the couplers. As a lower-bound estimate, Case B was run with all of the conditions at their nominal values, but without any connections between the tender and locomotive couplers. This represented an absolute minimum condition for the couplers, where they were assumed to fail as soon as the simulation started. This is obviously worse than could be expected during the test and is therefore a conservative assumption. The conditions for Case B are summarized in Table H 3. The deformed FE model is shown in Figure H 21.

**Table H 3. Pre-test Case B Model Conditions**

| Case | Tender-To-Locomotive Couplers | Bolster Pin and Center Bowl | Rail Base to Concrete Tie | Track Vertical Stiffness | Track Lateral Stiffness | Stub Track Connection | Impact Speed | Initial Pressure | Notes | Outcome |
|---|---|---|---|---|---|---|---|---|---|---|
| B | No | Yes | Tied | Default | Default | Discontinuous | 40 mph | 150 psig | Simulate Instant Coupler Failure | Tender derails, remains upright |

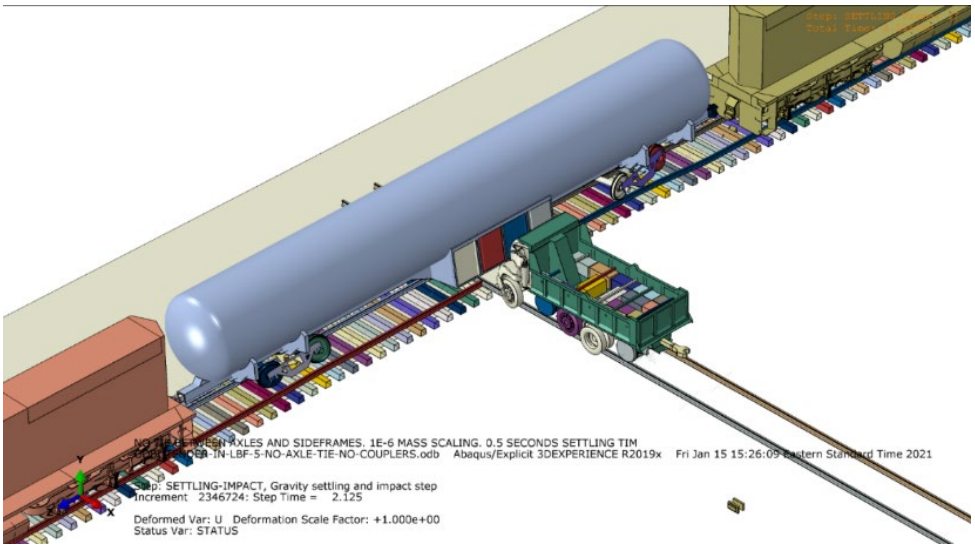


**Figure H 21. Deformed Model, Case B Simulation**

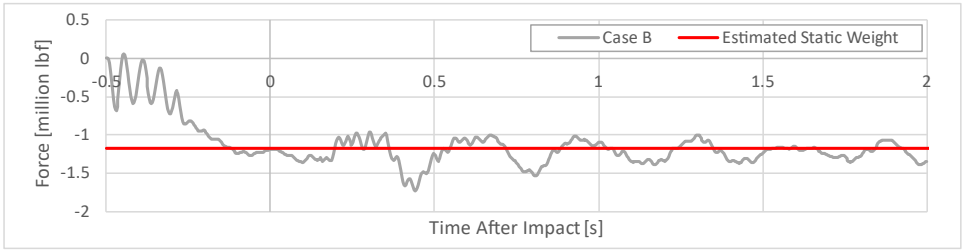


**Figure H 22. Time Response of Total Vertical Force on Ties for Case B**

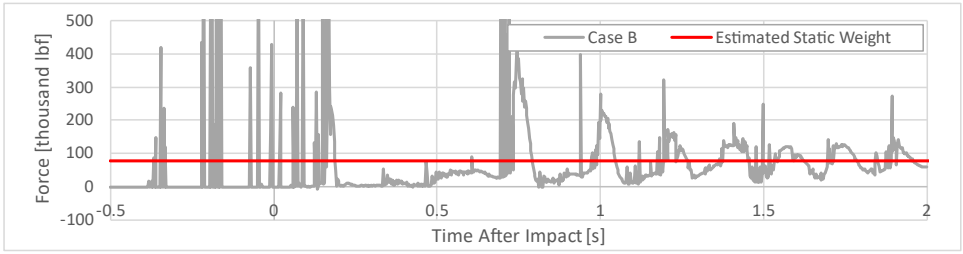


**Figure H 23. Time Response of Total Vertical Force on Dump Truck Guide Rails, Case B**

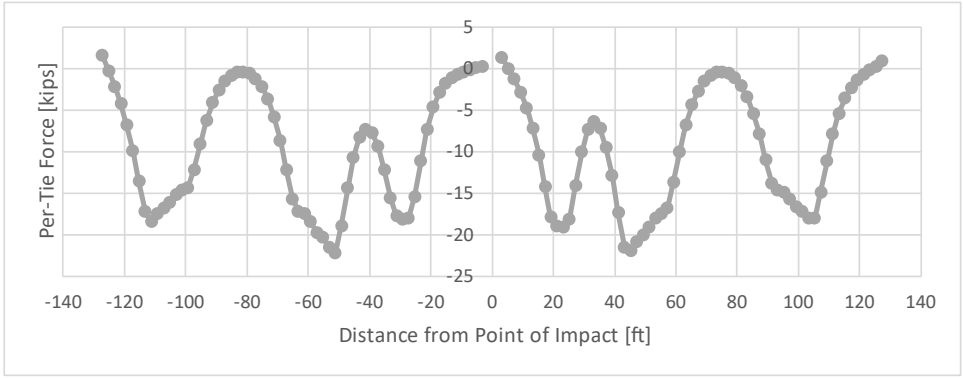


**Figure H 24. Vertical Load Distribution on Ties, Case B**

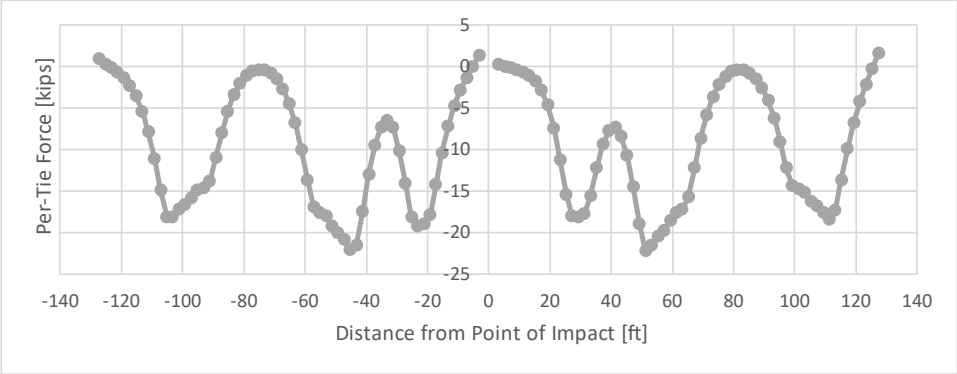


**Figure H 25. Vertical Load Distribution on Ties for Case B: Reflected at Point of Impact**

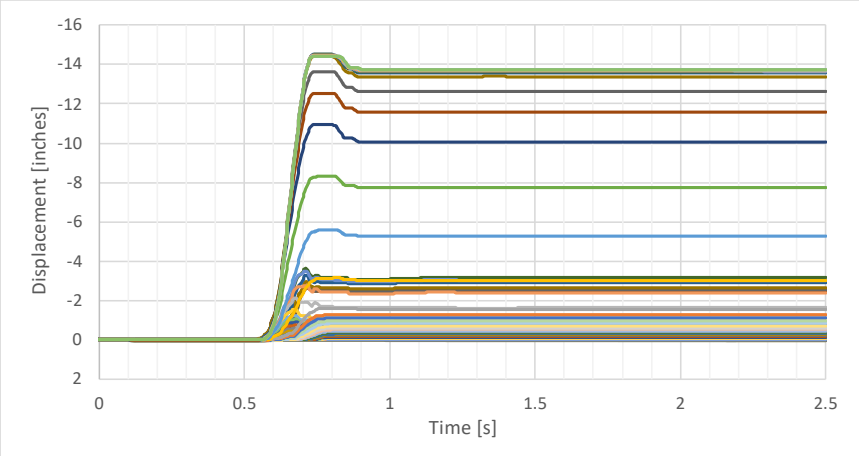


**Figure H 26. Lateral Displacement of Each Tie Over Time for Case B**

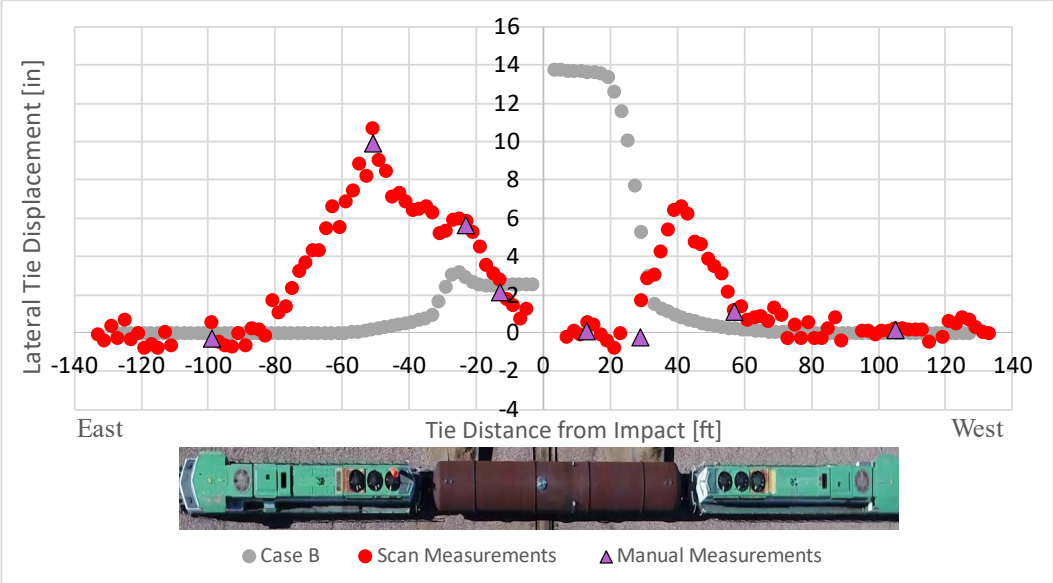


**Figure H 27. Final Lateral Displacement of Each Tie for Case B**

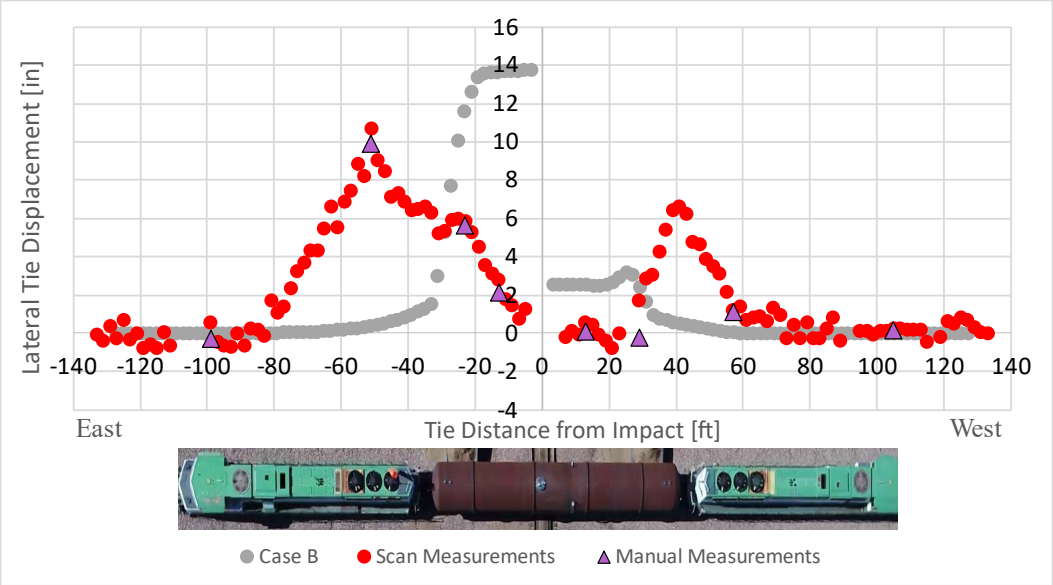


**Figure H 28. Final Lateral Displacement of Each Tie for Case B: Model Data Reflected at Point of Impact**

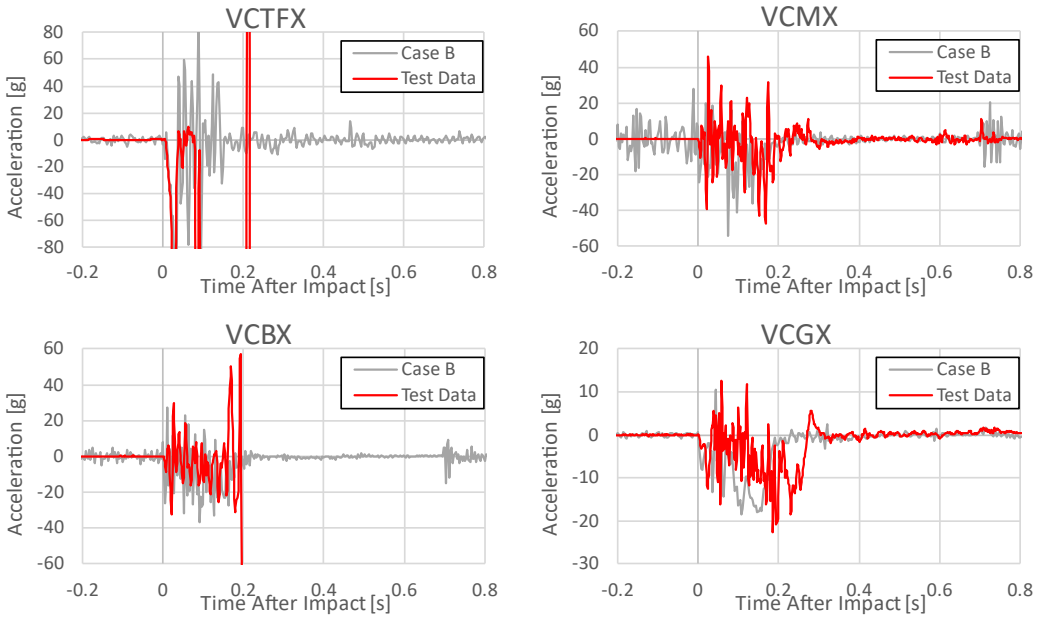


**Figure H 29. Accelerations from Measured and Case B Channels VCTFX, VCMX, VCBX, and VCGX**

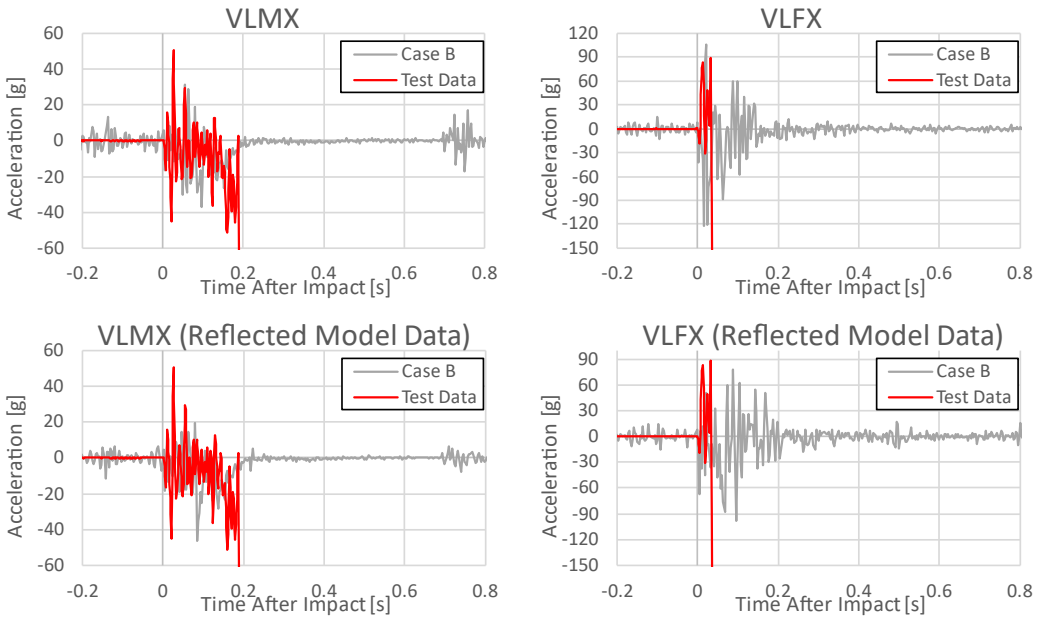


**Figure H 30. Accelerations from Measured and Case B Channels VLMX and VLFX, with Original and Reflected Model Data Presented for Each Channel**

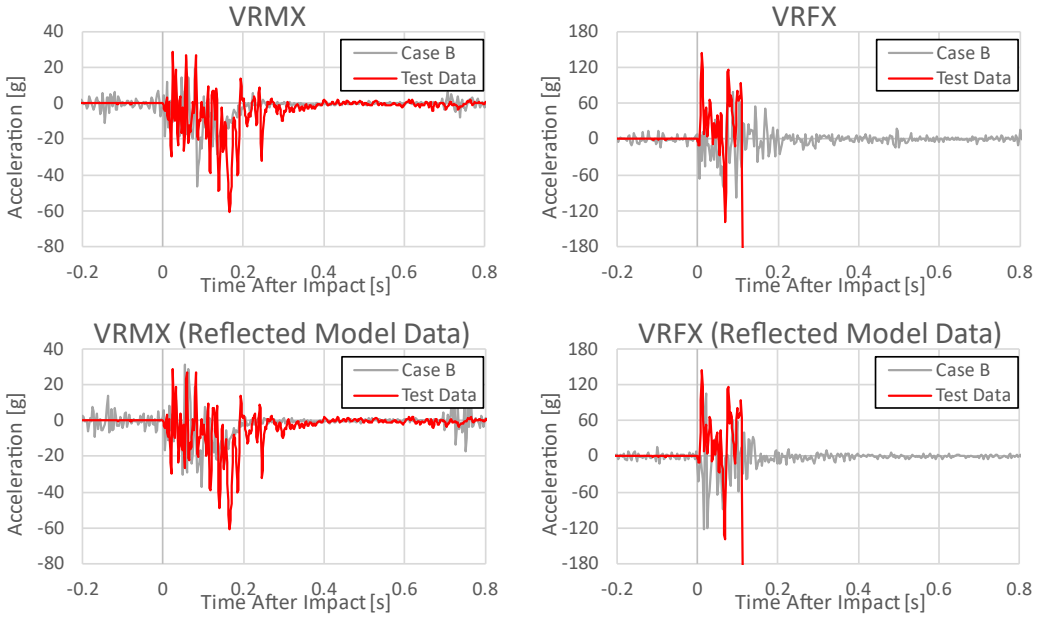


**Figure H 31. Accelerations from Measured and Case B Channels VRMX and VRFX, with Original and Reflected Model Data Presented for Each Channel**

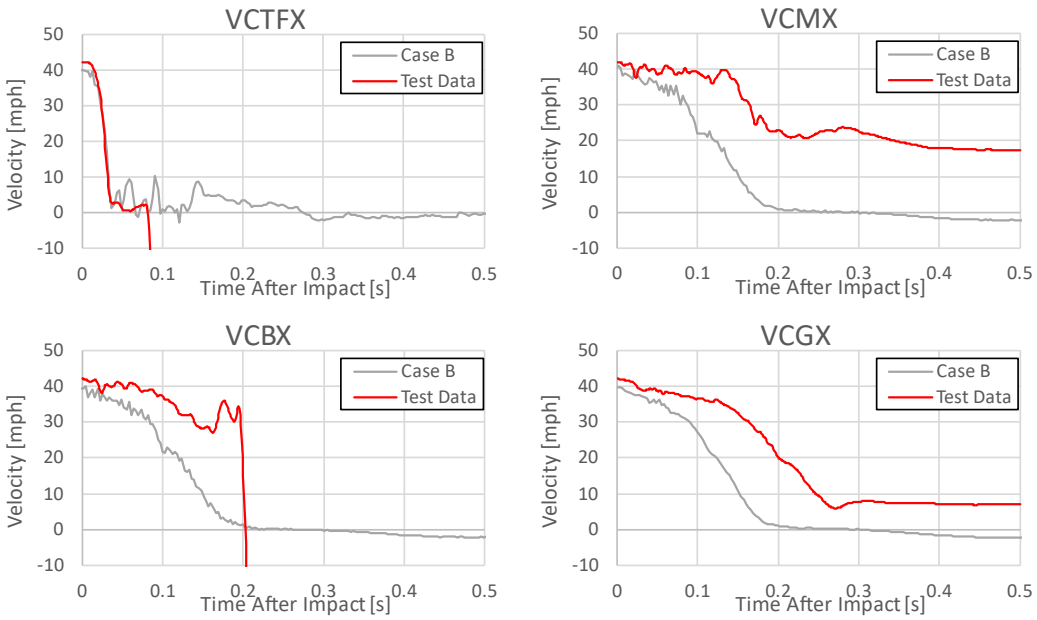


**Figure H 32. Velocities from Measured and Case B Channels VCTFX, VCMX, VCBX, and VCGX**

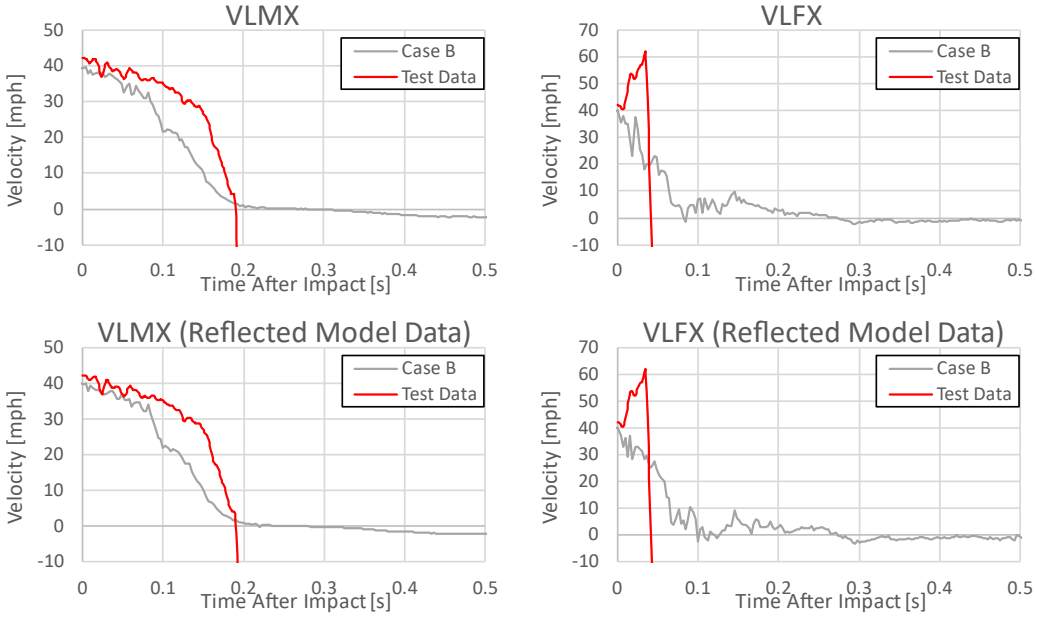


**Figure H 33. Velocities from Measured and Case B Channels VLMX and VLFX, with Original and Reflected Model Data Presented for Each Channel**

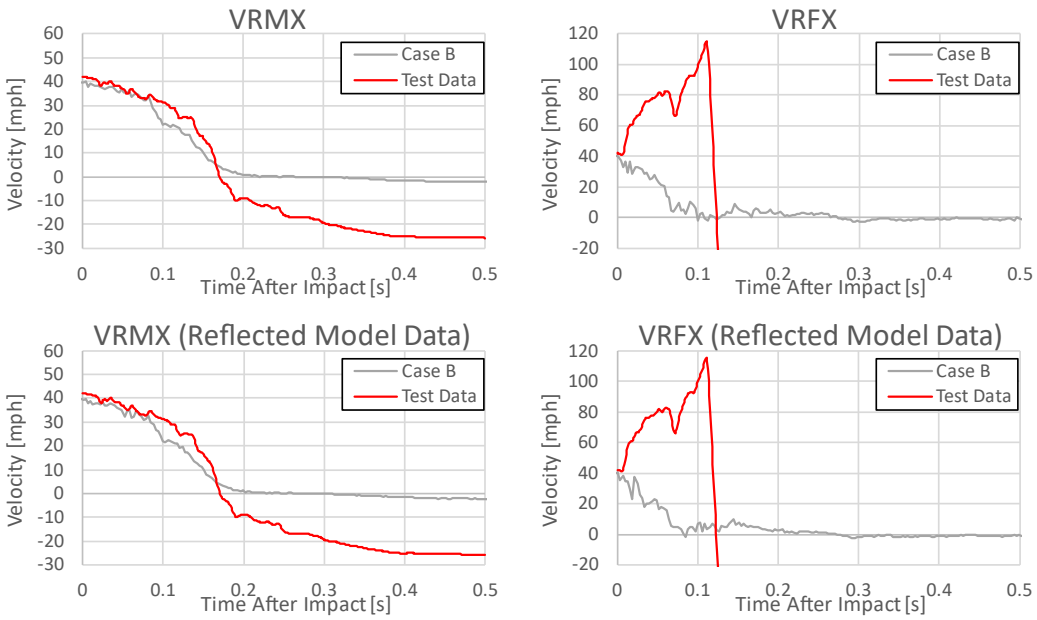


**Figure H 34. Velocities from Measured and Case B Channels VRMX and VRFX, with Original and Reflected Model Data Presented for Each Channel**

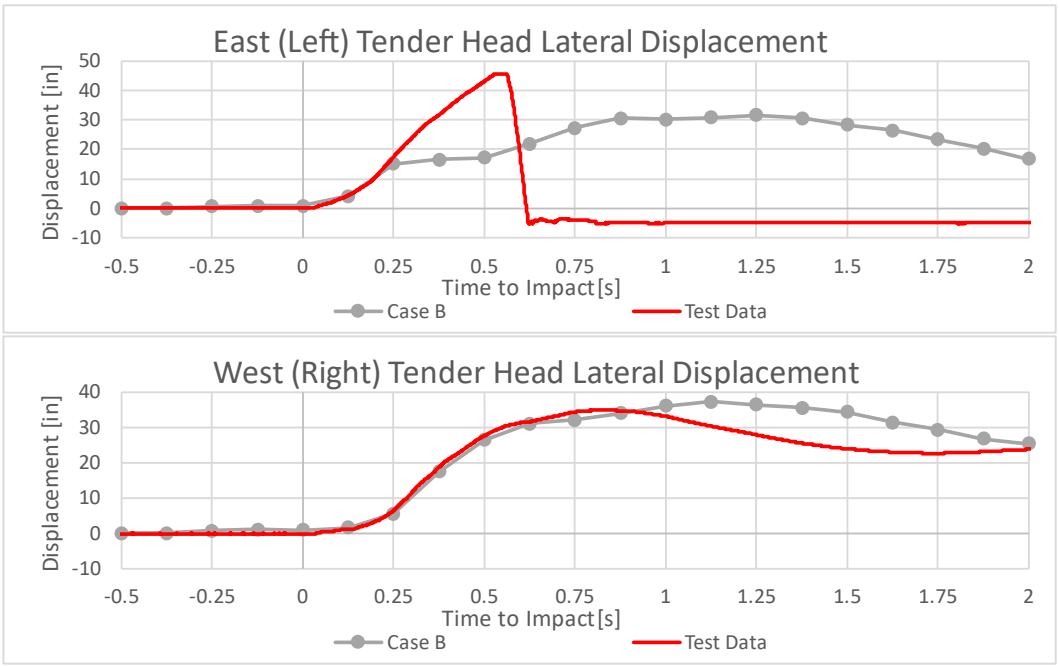


**Figure H 35. Lateral Displacement of the East and West Tender Heads for Case B**

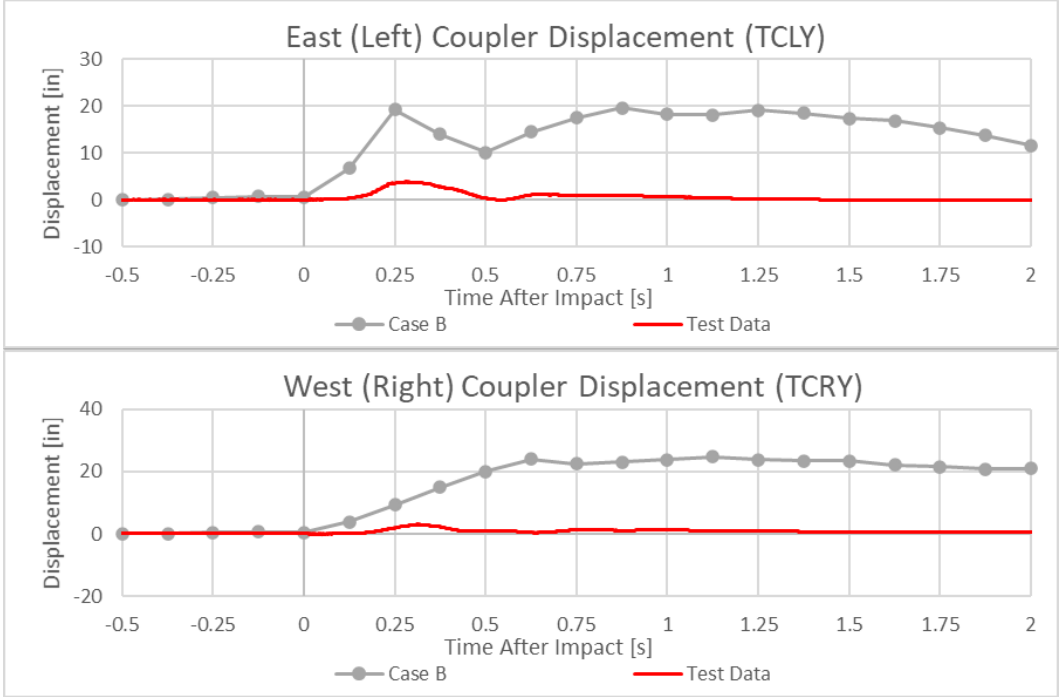


**Figure H 36. Locomotive-to-Tender Coupler Displacements for Case B**

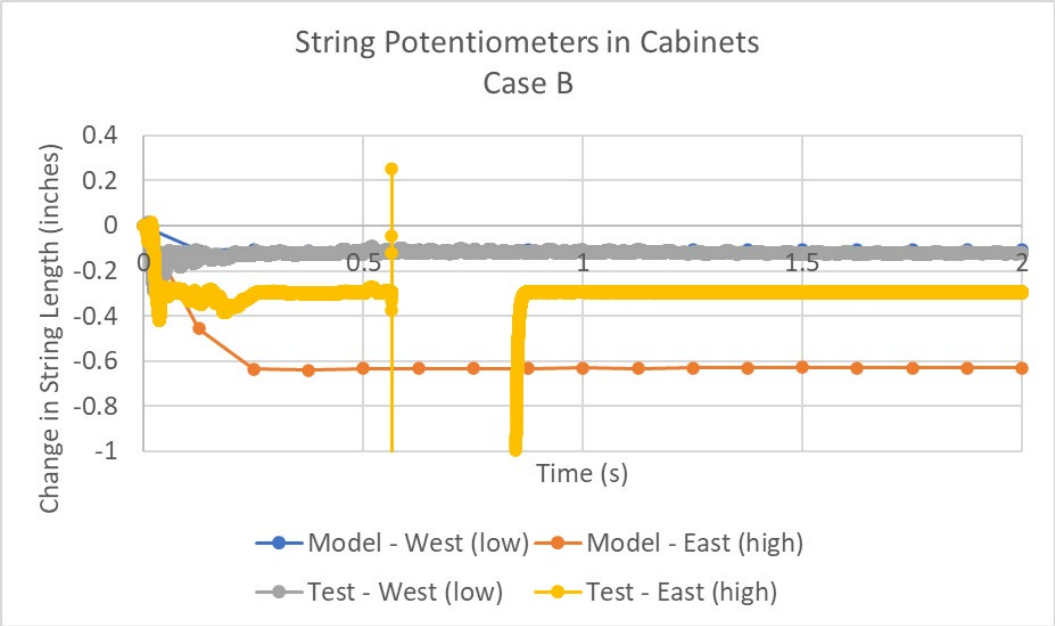


**Figure H 37. String Potentiometers in Piping Cabinet, Case B**

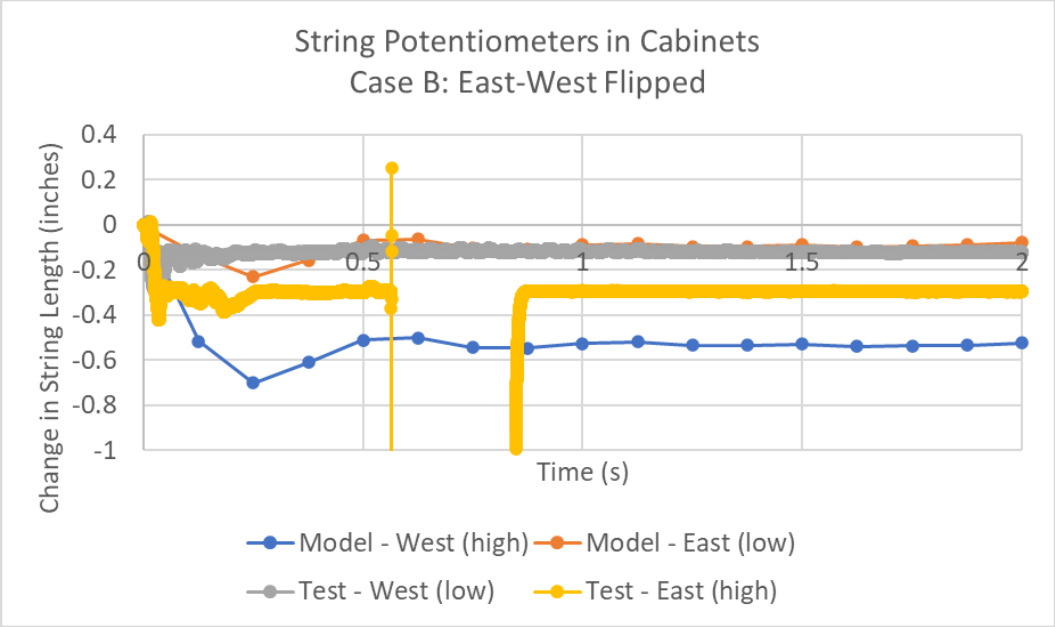


**Figure H 38. String Potentiometers in Piping Cabinet, Case B, East-West Flipped**

### Case C

Like Case B, Case C was also run without tender-to-locomotive couplers connected. Additionally, Case C had contact deactivated between the bolster pins and center bowls on the three-piece freight trucks and the center plates on the tender's body bolsters. This model simulated two failures occurring in the same test, a broken coupler and a separation of the carbody from the bolsters. Once again, rather than characterizing the potential modes of failure of the center pin and bowl and the forces and moments necessary to cause them, a simplified "worst case" scenario was examined in which the body bolsters were essentially sitting on flat planes atop the truck bolsters. The conditions for Case C are summarized in Table H 4. The deformed FE model is shown in Figure H 37.

**Table H 4. Pre-test Case C Model Conditions**

| Case | Tender-to-locomotive Couplers | Bolster Pin and Center Bowl | Rail Base to Concrete Tie | Track Vertical Stiffness | Track Lateral Stiffness | Stub Track Connection | Impact Speed | Initial Pressure | Notes | Outcome |
|---|---|---|---|---|---|---|---|---|---|---|
| C | No | No | Tied | Default | Default | Discontinuous | 40 mph | 150 psig | Simulate instant coupler and center pin/bowl failure | Tender rollover |

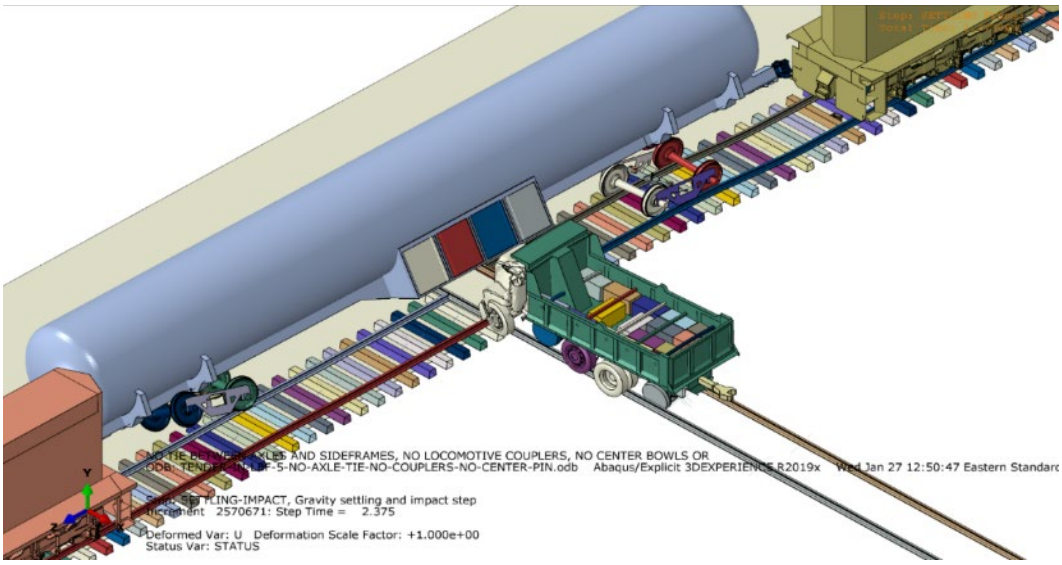


**Figure H 39. Deformed Model, Case C Finite Element Analysis (FEA)**

The results for the total vertical force on the ties (Figure H 38) and the total vertical force carried by the rigid dump truck rails (Figure H 39) differ in Case C from the previously presented cases. The total load carried by the ties decreased after the impact, while the total load carried by the rigid dump truck guide rails increased. This change is attributed to the tender rolling over in this simulation. The far (i.e., non-impact) side of the cabinet contacted the dump truck guide rails on the far side of the model. Some portion of the tender's weight was carried by the rigid dump truck's guide rails following rollover, in addition to the weight of the dump truck.

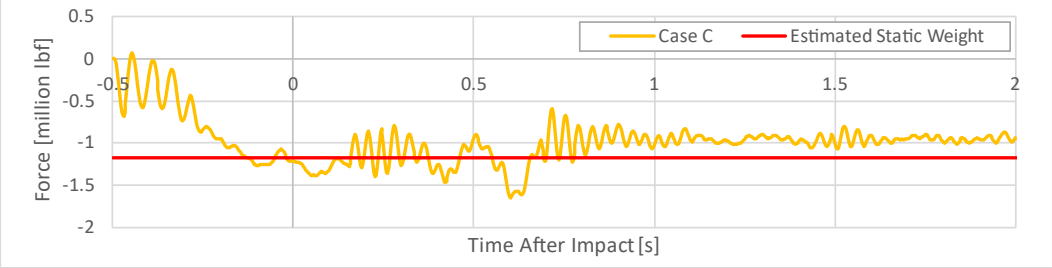


**Figure H 40. Time Response of Total Vertical Force on Ties for Case C**

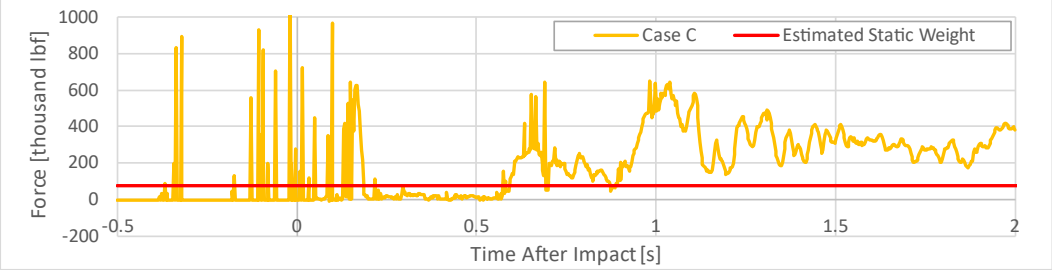


**Figure H 41. Time Response of Total Vertical Force on Dump Truck Guide Rails, Case C**

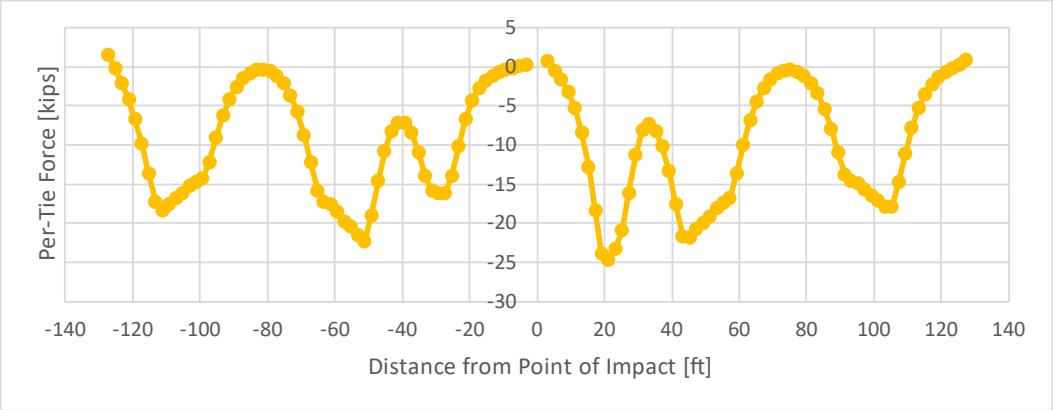


**Figure H 42. Vertical Load Distribution on Ties, Case C**

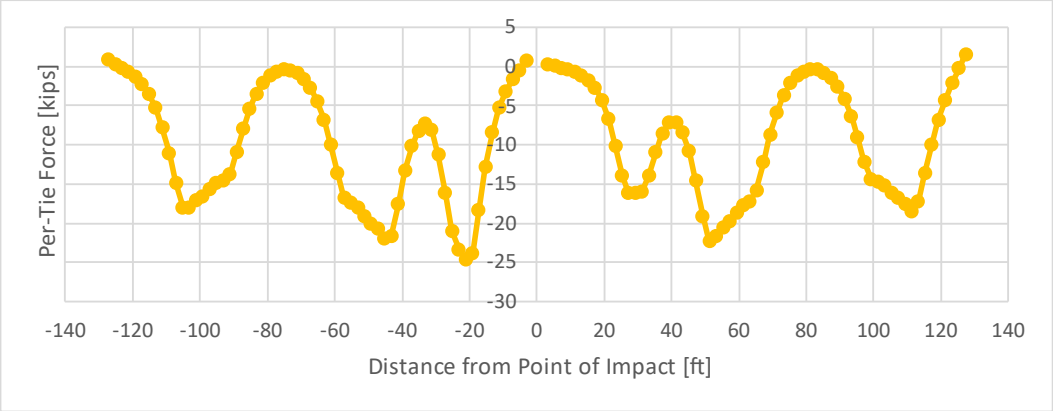


**Figure H 43. Vertical Load Distribution on Ties for Case C: Reflected at Point of Impact**

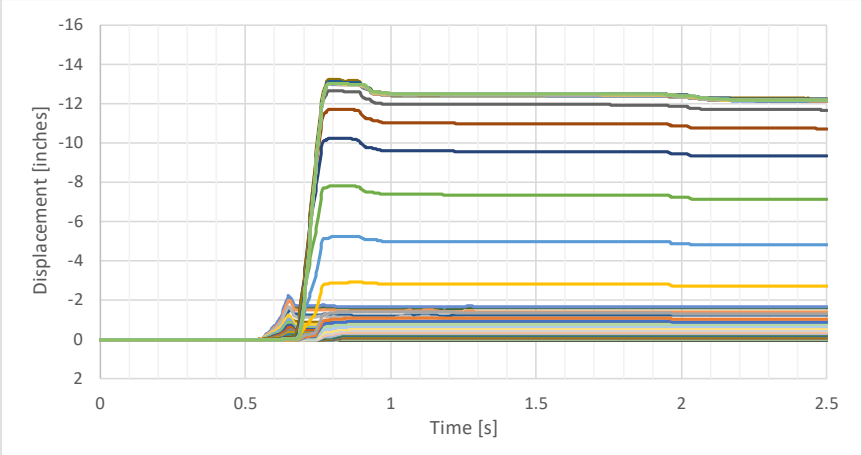


**Figure H 44. Lateral Displacement of Each Tie Over Time for Case C**

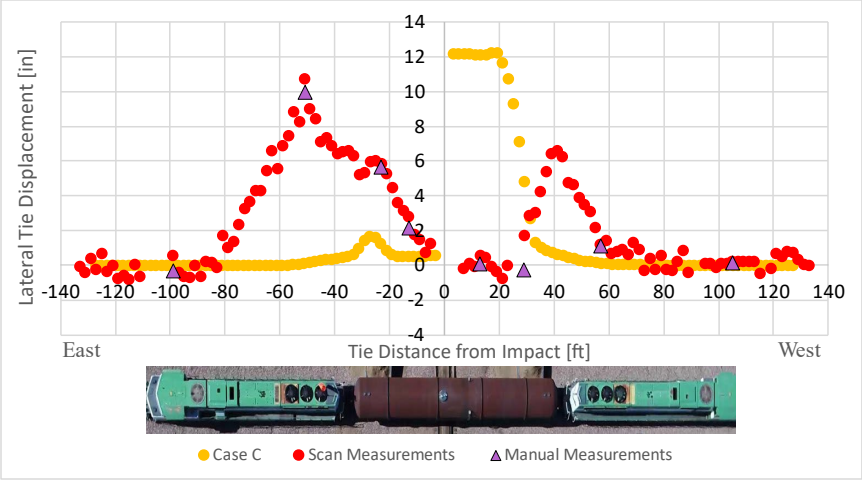


**Figure H 45. Final Lateral Displacement of Each Tie for Case C**

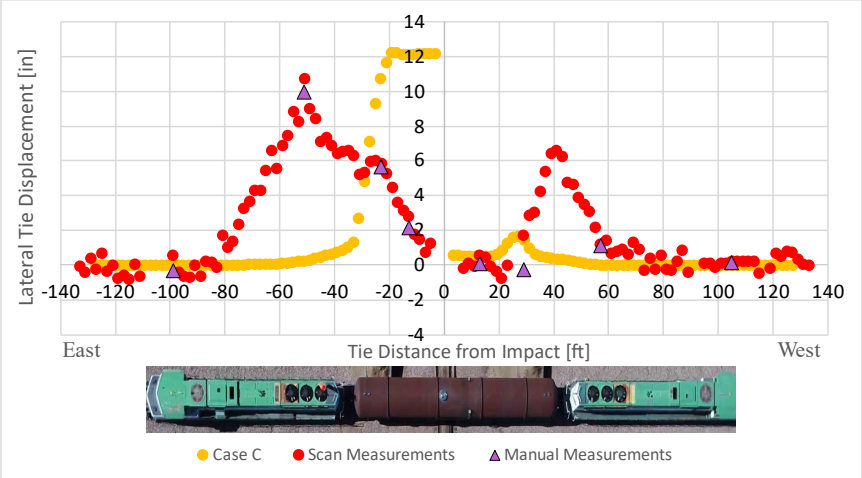


**Figure H 46. Final Lateral Displacement of Each Tie for Case C: Model Data Reflected at Point of Impact**

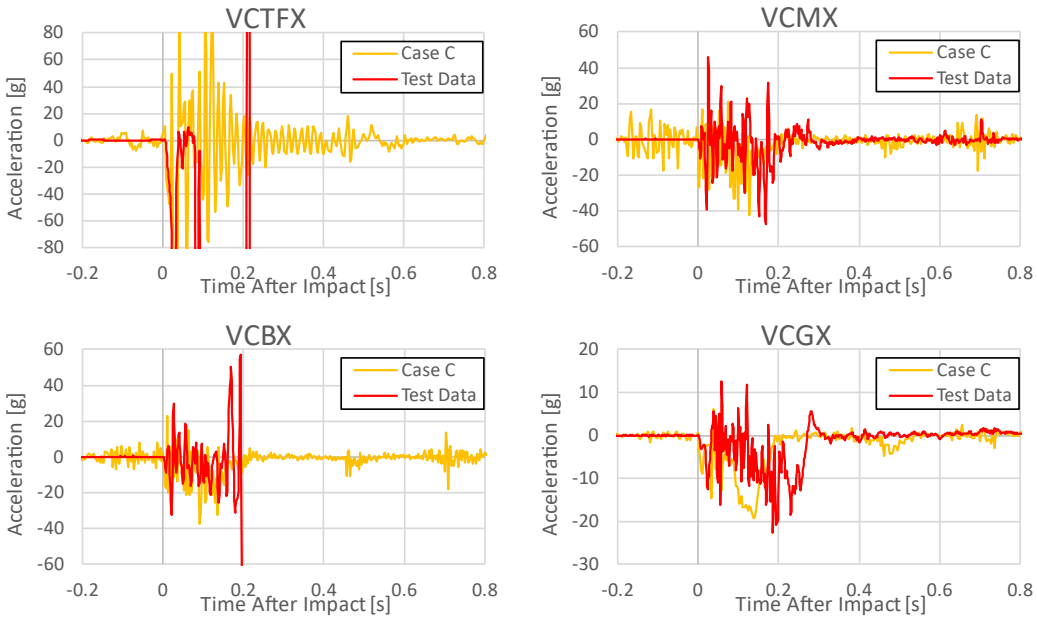


**Figure H 47. Accelerations from Measured and Case C Channels VCTFX, VCMX, VCBX, and VCGX**

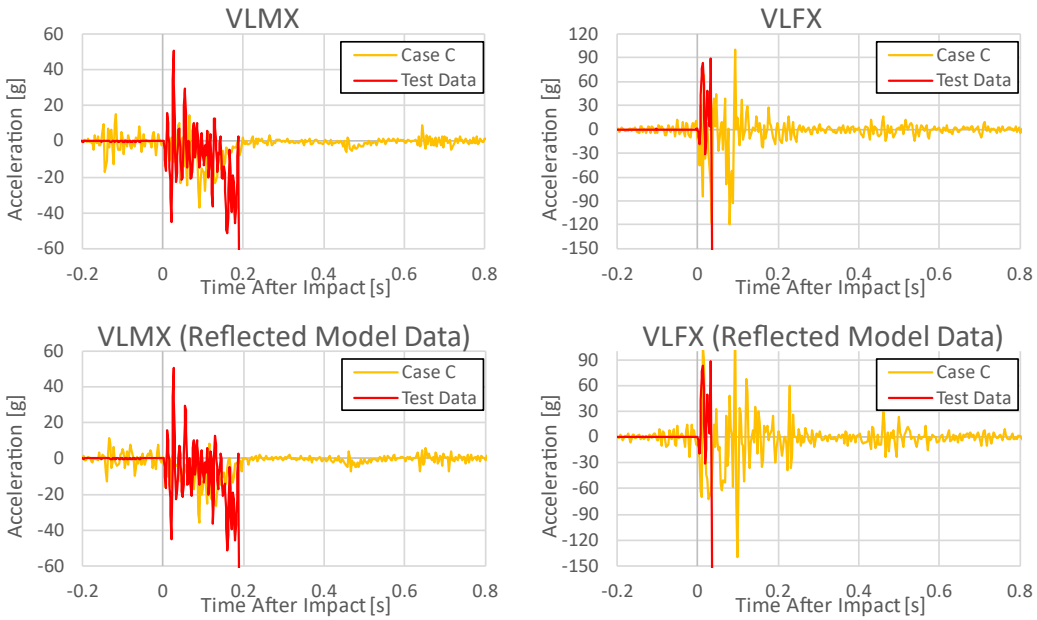


**Figure H 48. Accelerations from Measured and Case C Channels VLMX and VLFX, with Original and Reflected Model Data Presented for Each Channel**

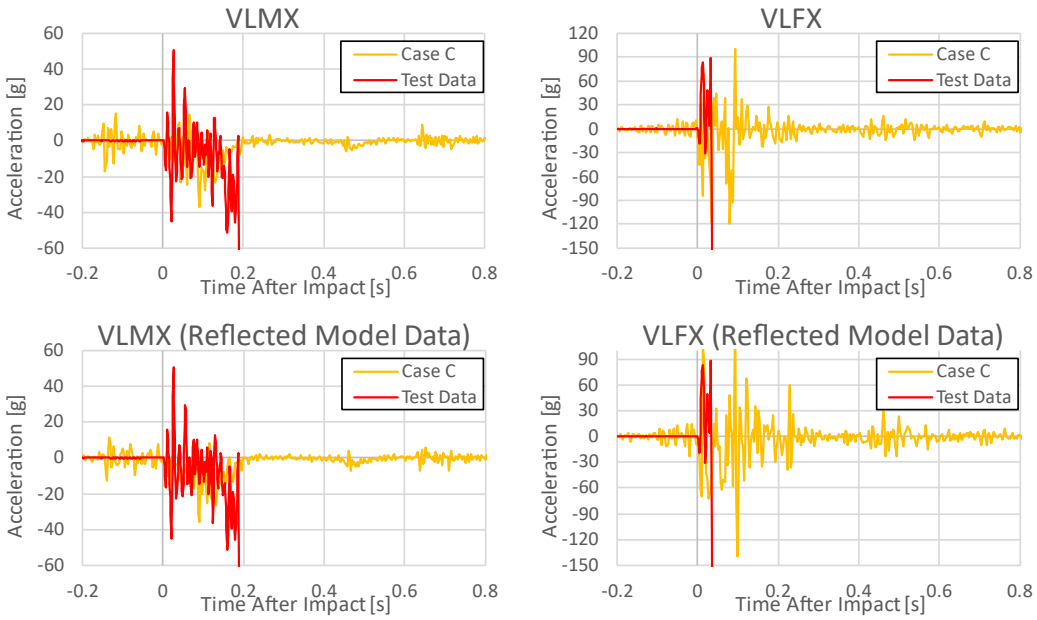


**Figure H 49. Accelerations from Measured and Case C Channels VRMX and VRFX, with Original and Reflected Model Data Presented for Each Channel**

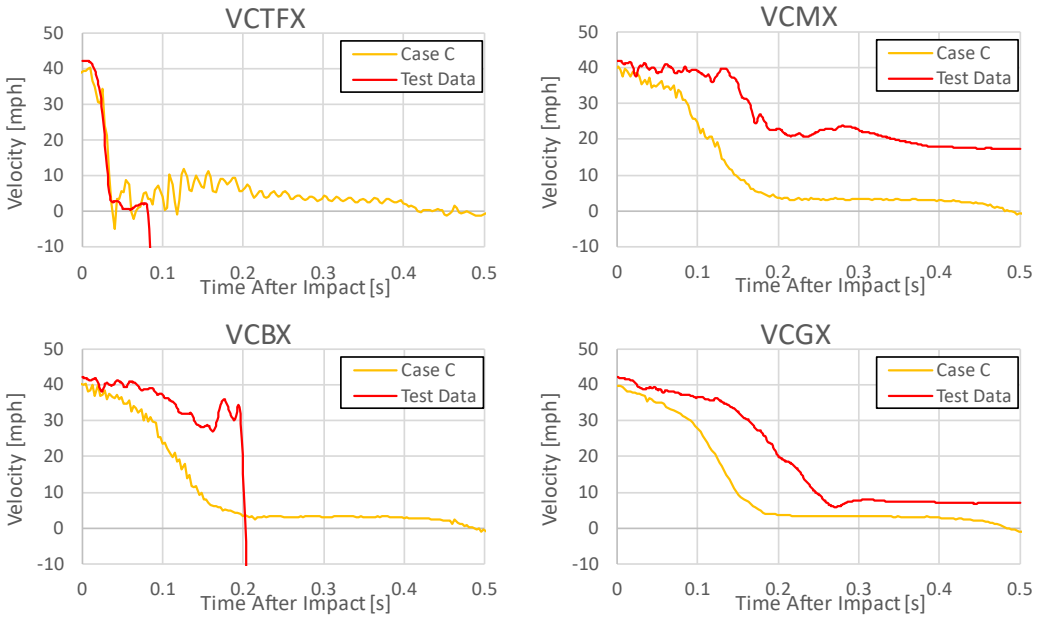


**Figure H 50. Velocities from Measured and Case C Channels VCTFX, VCMX, VCBX, and VCGX**

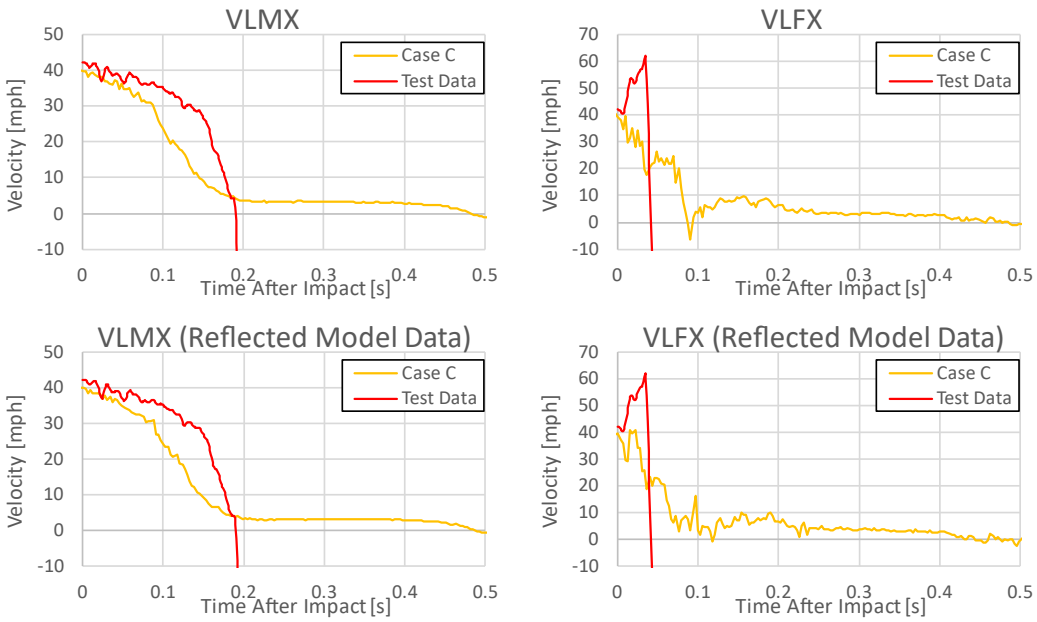


**Figure H 51. Velocities from Measured and Case C Channels VLMX and VLFX, with Original and Reflected Model Data Presented for Each Channel**

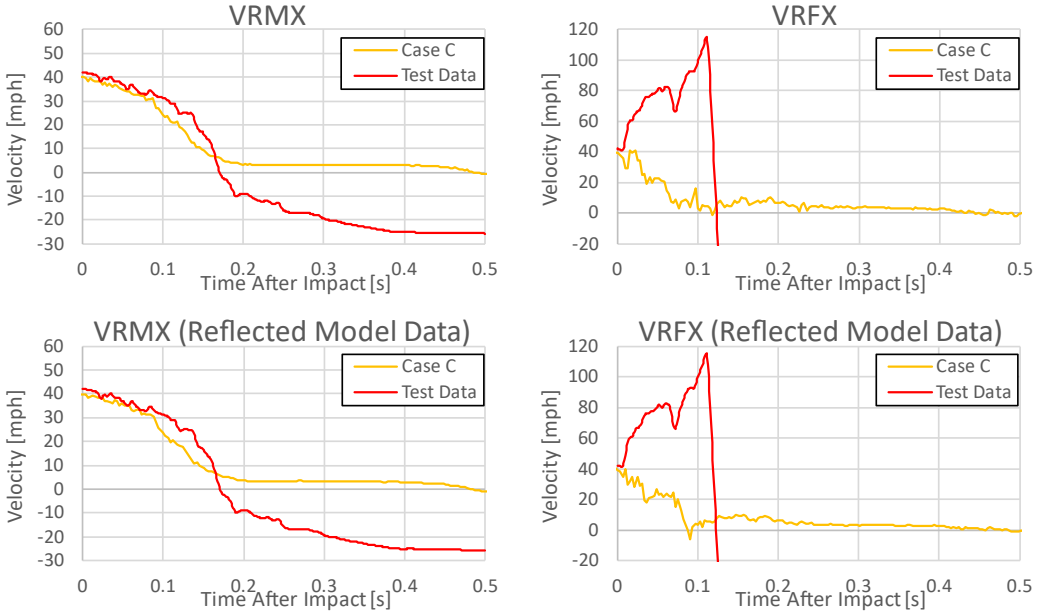


**Figure H 52. Velocities from Measured and Case C Channels VRMX and VRFX, with Original and Reflected Model Data Presented for Each Channel**

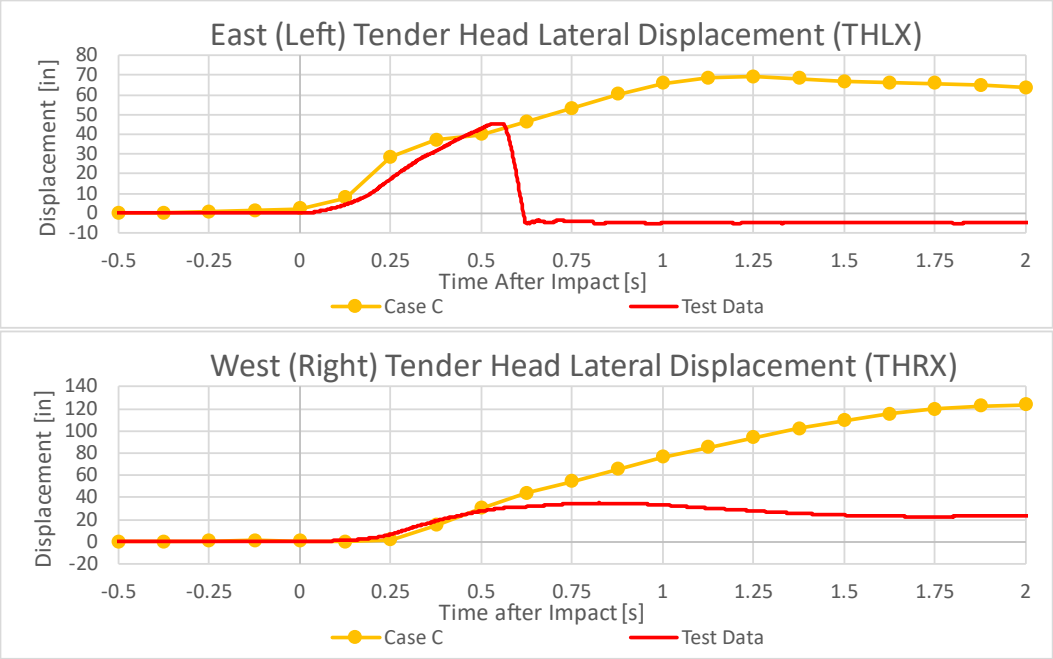


**Figure H 53. Lateral Displacement of the East and West Tender Heads for Case C**

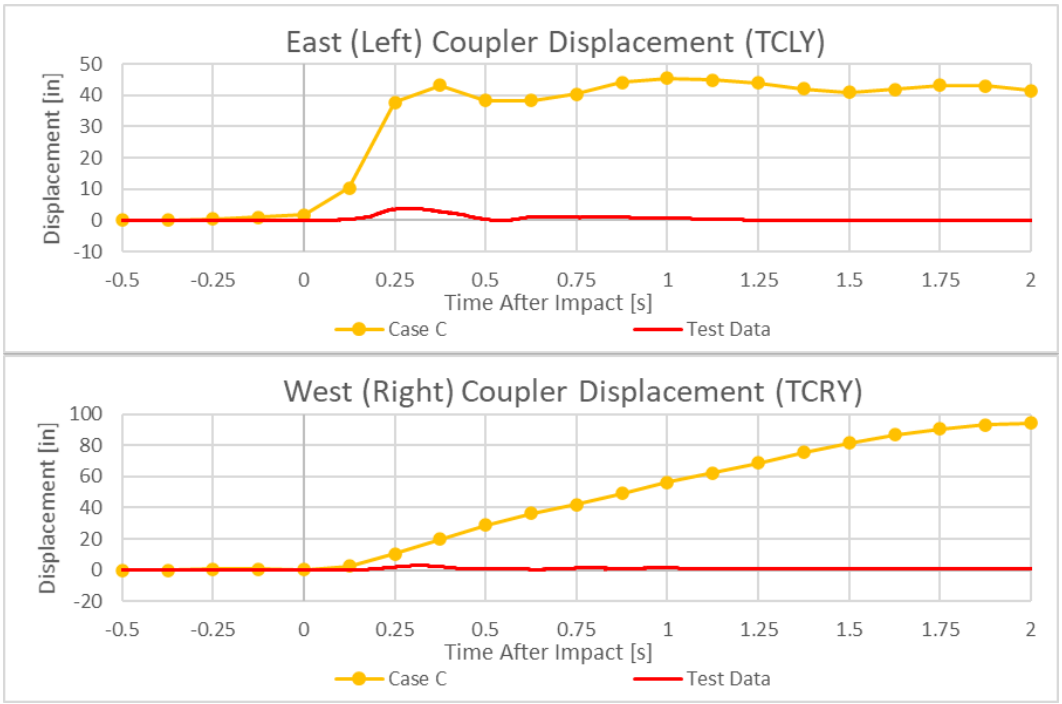


**Figure H 54. Locomotive-to-Tender Coupler Displacements for Case C**

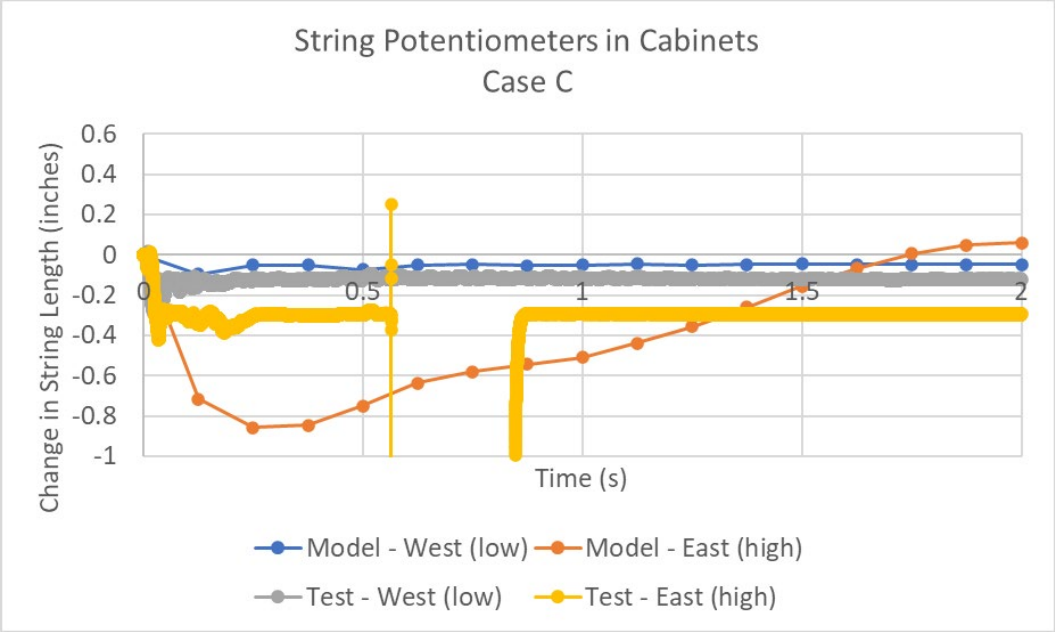


**Figure H 55. String Potentiometers in Piping Cabinet, Case C**

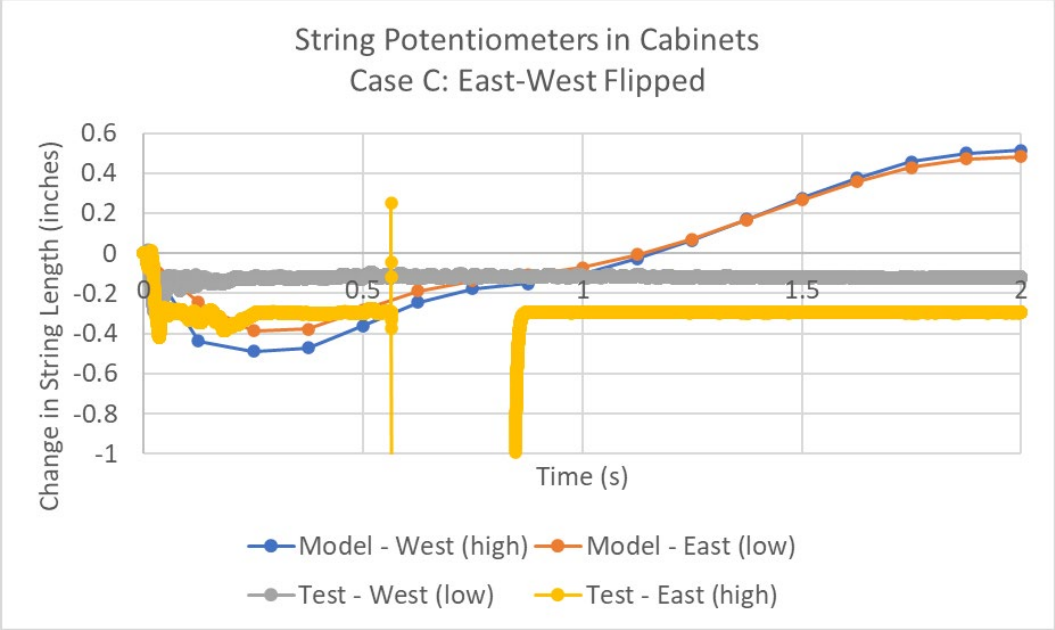


**Figure H 56. String Potentiometers in Piping Cabinet, Case C, East-West Flipped**

### Case D

Due to an input error, the results of Case D are highly unrealistic. The results of this case are included in this report in the interest of completeness only. Case D was intended to simulate a situation in which both the couplers and the rail-to-tie connections failed. Similar to the previous two cases, the couplers were modeled as disconnected from the very beginning of the impact, representing the worst case for coupler performance. Additionally, the tied constraints between the rails and concrete ties on the stub track were deactivated, representing an instantaneous

failure of the rail-to-tie clips. However, due to an input error, the rails were excluded from contact with the concrete ties. As a result, the rails immediately passed through the concrete ties under the effects of gravity. The wheels of the tender and locomotives also descended until encountering the concrete ties. This situation is highly unrealistic, as the locomotives and tender essentially started off the simulation sitting on the tops of the concrete ties. The Case D model conditions are summarized in Table H 5. The deformed FE model is shown in Figure H 55.

**Table H 5. Pre-test Case D Model Conditions**

| Case | Tender-to-locomotive Couplers | Bolster Pin and Center Bowl | Rail Base to Concrete Tie | Track Vertical Stiffness | Track Lateral Stiffness | Stub Track Connection | Impact Speed | Initial Pressure | Notes | Outcome |
|---|---|---|---|---|---|---|---|---|---|---|
| D | No | Yes | Not Tied | Default | Default | Discontinuous | 40 mph | 150 psig | Simulate instant coupler failure, unrestrained rail | Questionable results |

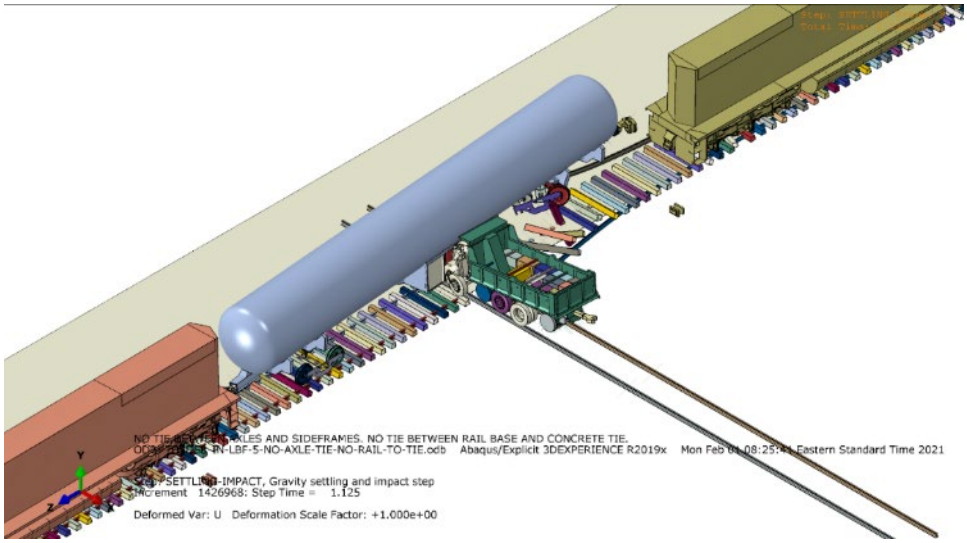


**Figure H 57. Deformed Model, Case D FEA**

### Case E

Case E represented the lower-bound strength of the fasteners used to attach the rails to the concrete ties. In the baseline model, the rails were attached to the ties using tied constraints that did not allow separation, regardless of the forces and moments transmitted across them. That behavior represents the upper-bound strength of the fasteners, but it was unknown whether the fasteners would fail or become loosened during the impact. As a lower-bound estimate, the tied constraints were suppressed so that the rails merely sat atop the concrete ties. This case is conservative, as it would correspond to all of the restraints on the rails simultaneously failing without any load transmitted on them. The tenders and locomotives derailed but remained upright. The tender's cabinet made contact with the rigid dump truck guide rails on the opposite

side of the impact. Table H 6 summarizes the conditions of the Case E model. The deformed shape of the Case E FE model is shown in Figure H 56.

**Table H 6. Pre-test Case E Model Conditions**

| Case | Tender-to-locomotive Couplers | Bolster Pin and Center Bowl | Rail Base to Concrete Tie | Track Vertical Stiffness | Track Lateral Stiffness | Stub Track Connection | Impact Speed | Initial Pressure | Notes | Outcome |
|---|---|---|---|---|---|---|---|---|---|---|
| E | Yes | Yes | Not Tied | Default | Default | Discontinuous | 40 mph | 150 psig | Simulate unrestrained rail | Tender derailed, contact with cabinet on far side, locomotives derailed |

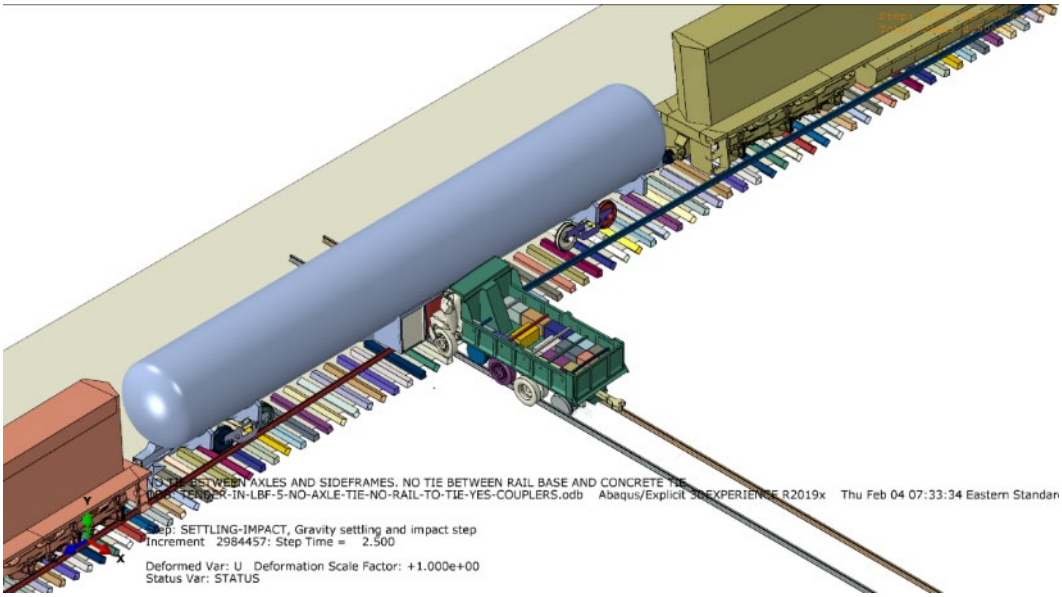


**Figure H 58. Deformed Model, Case E FEA**

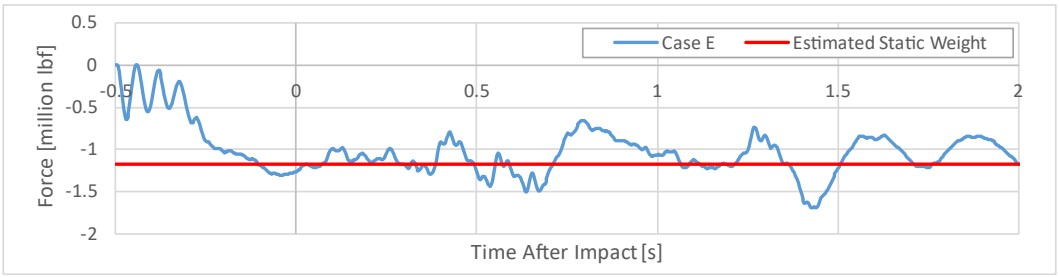


**Figure H 59. Time Response of Total Vertical Force on Ties for Case E**

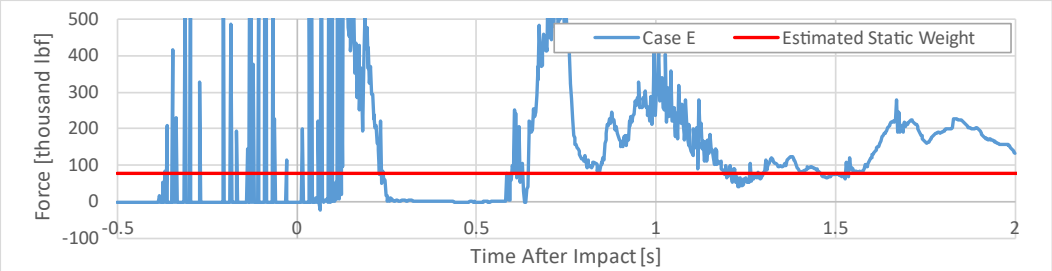


**Figure H 60. Time Response of Total Vertical Force on Rails for Case E**

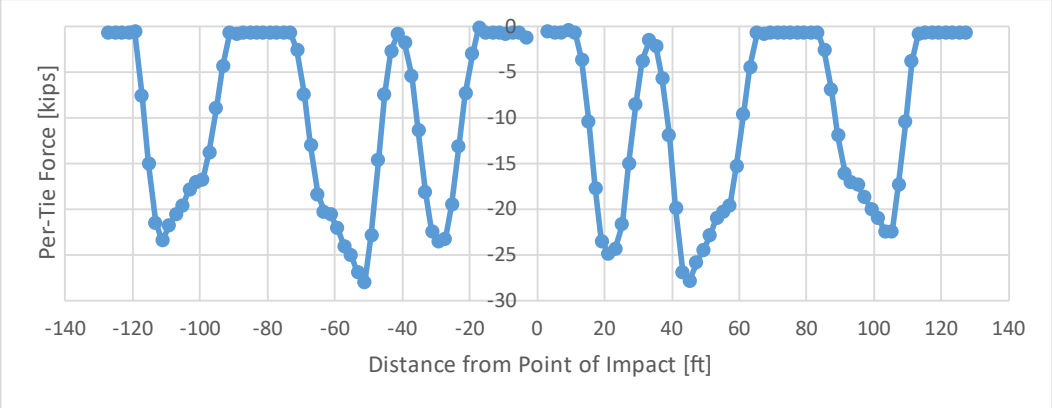


**Figure H 61. Vertical Load Distribution on Ties for Case E**

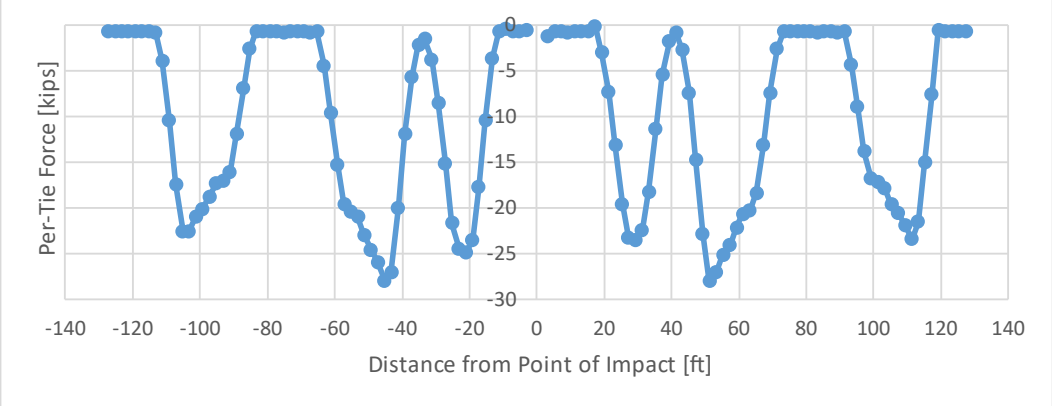


**Figure H 62. Vertical Load Distribution on Ties for Case E: Reflected at Point of Impact**

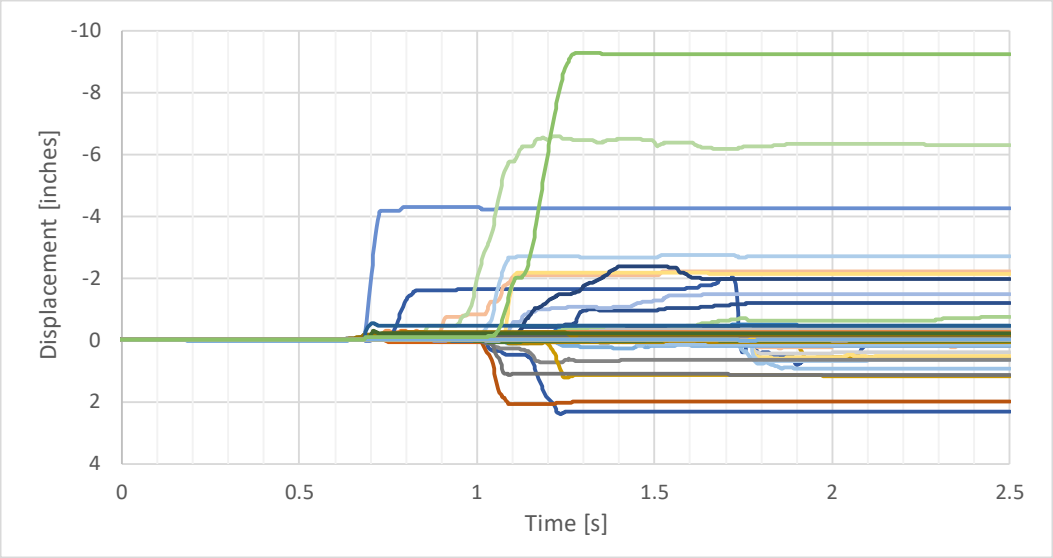


**Figure H 63. Lateral Displacement of Each Tie Over Time for Case E**

The tie displacements shown in the nominal (Figure H 62) and east-west flipped (Figure H 63) configurations are substantially different in Case E compared to the other pre-test models. The tie displacements are much lower in Case E than in the other cases, likely due to the exclusion of a rail-tie constraint in Case E. The rail can only exert force on the ties through contact between the bodies, while in previous cases the rail base was attached to the ties. The tie displacement results from Case E illustrate the significant effect the rail-to-tie connection can have on the overall response of the deformable track.

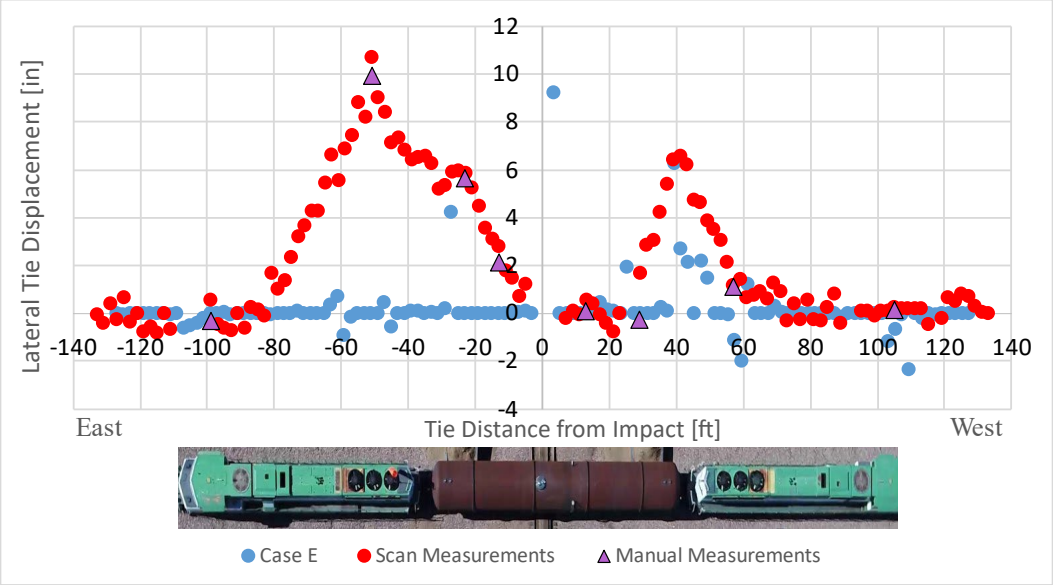


**Figure H 64. Final Lateral Displacement of Each Tie for Case E**

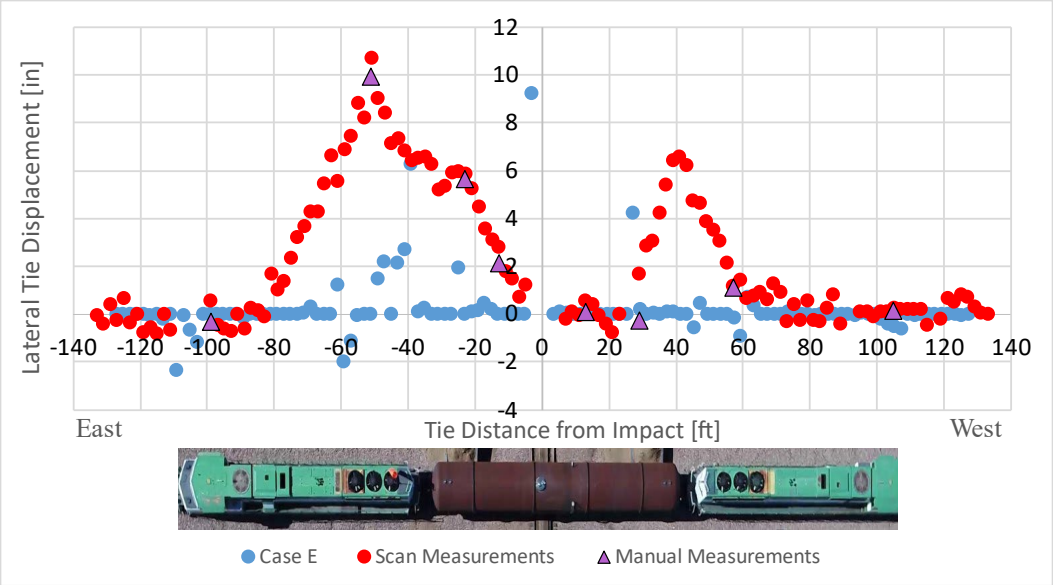


**Figure H 65. Final Lateral Displacement of Each Tie for Case E: Model Data Reflected at Point of Impact**

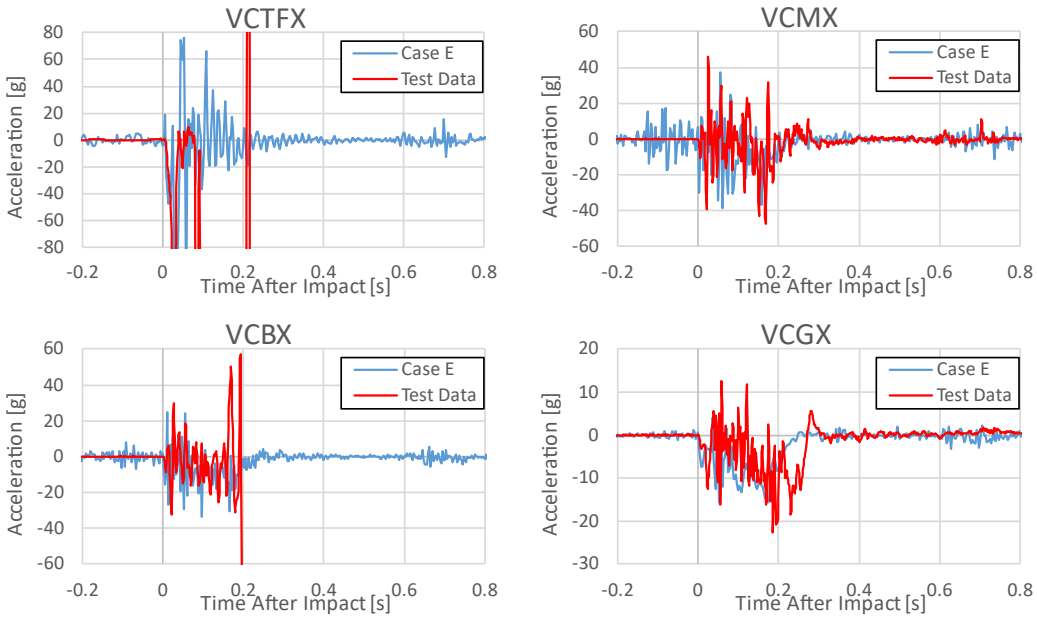


**Figure H 66. Accelerations from Measured and Case E Channels VCTFX, VCMX, VCBX, and VCGX**

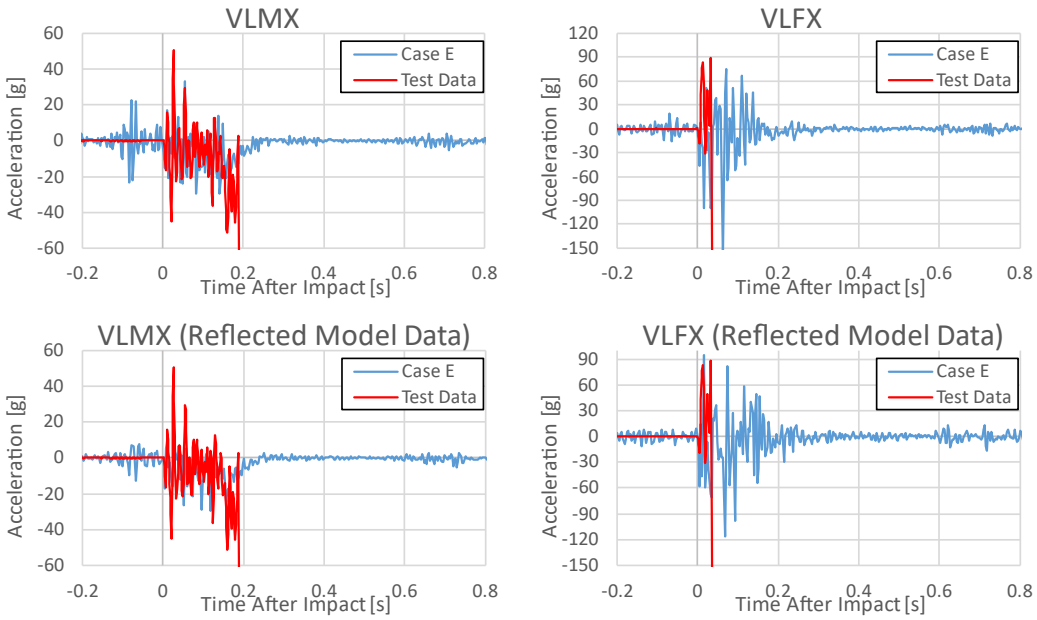


**Figure H 67. Accelerations from Measured and Case E Channels VLMX and VLFX, with Original and Reflected Model Data Presented for Each Channel**

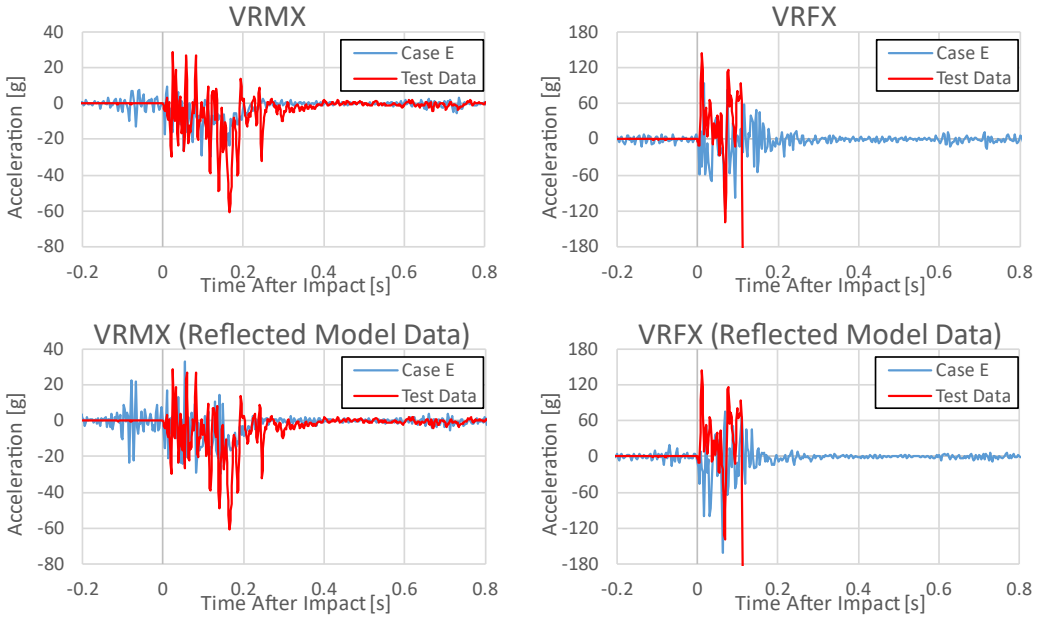


**Figure H 68. Accelerations from Measured and Case E Channels VRMX and VRFX, with Original and Reflected Model Data Presented for Each Channel**

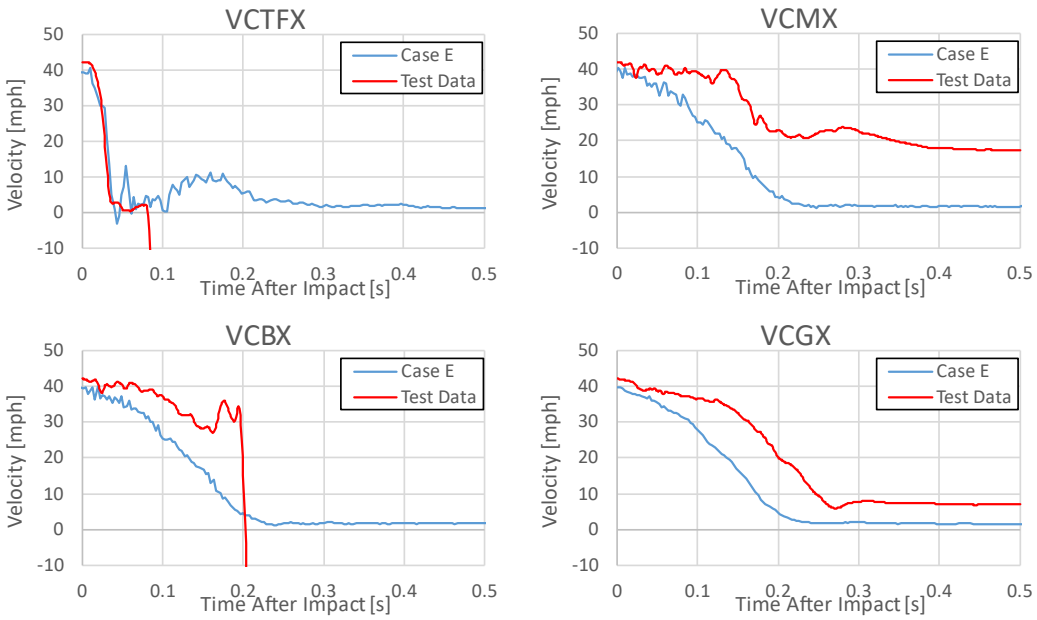


**Figure H 69. Velocities from Measured and Case E Channels VCTFX, VCMX, VCBX, and VCGX**

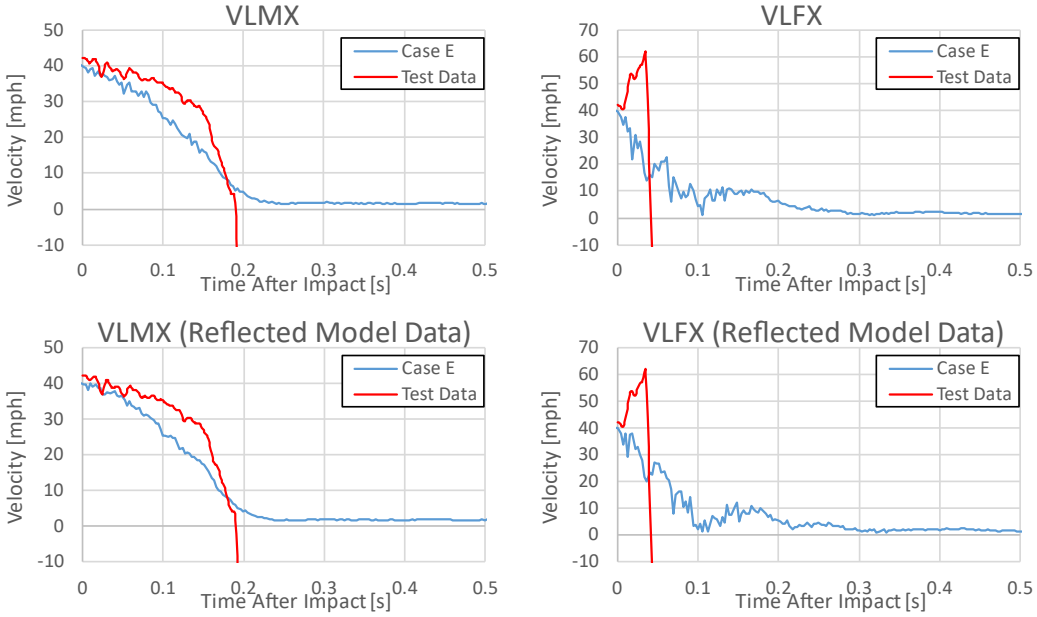


**Figure H 70. Velocities from Measured and Case E Channels VLMX and VLFX, with Original and Reflected Model Data Presented for Each Channel**

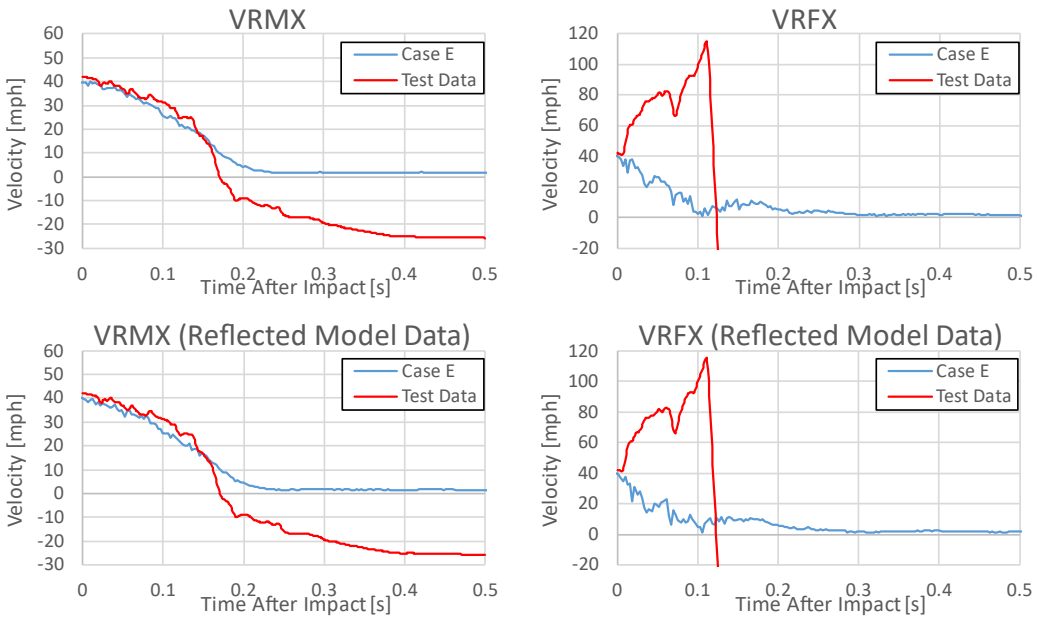


**Figure H 71. Velocities from Measured and Case E Channels VRMX and VRFX, with Original and Reflected Model Data Presented for Each Channel**

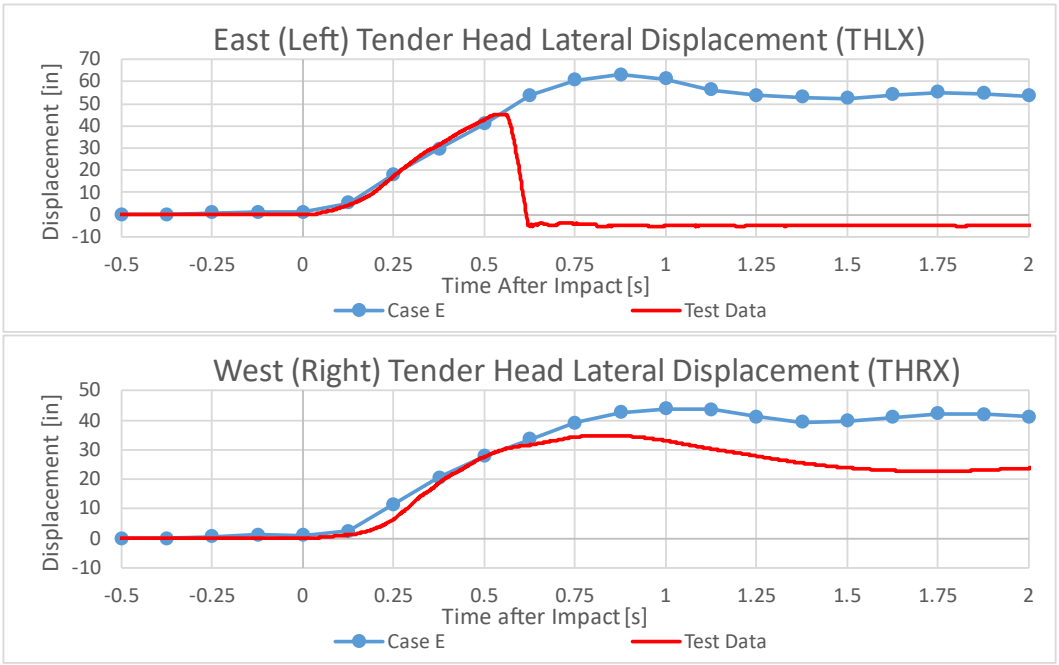


**Figure H 72. Lateral Displacement of the East and West Tender Heads for Case E**

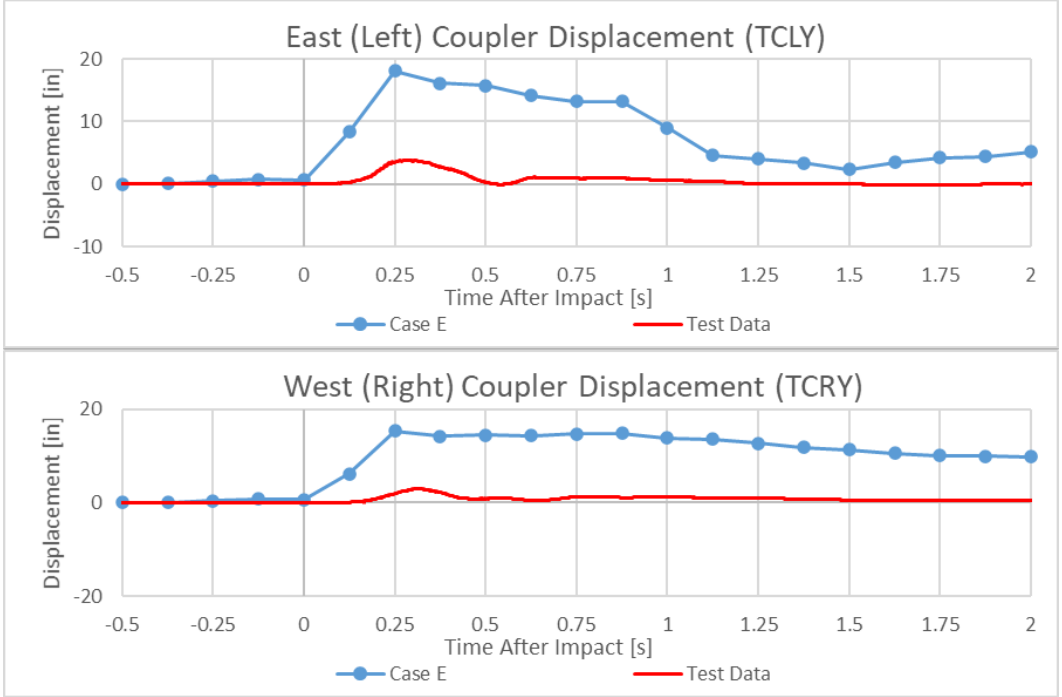


**Figure H 73. Locomotive-to-Tender Coupler Displacements for Case E**

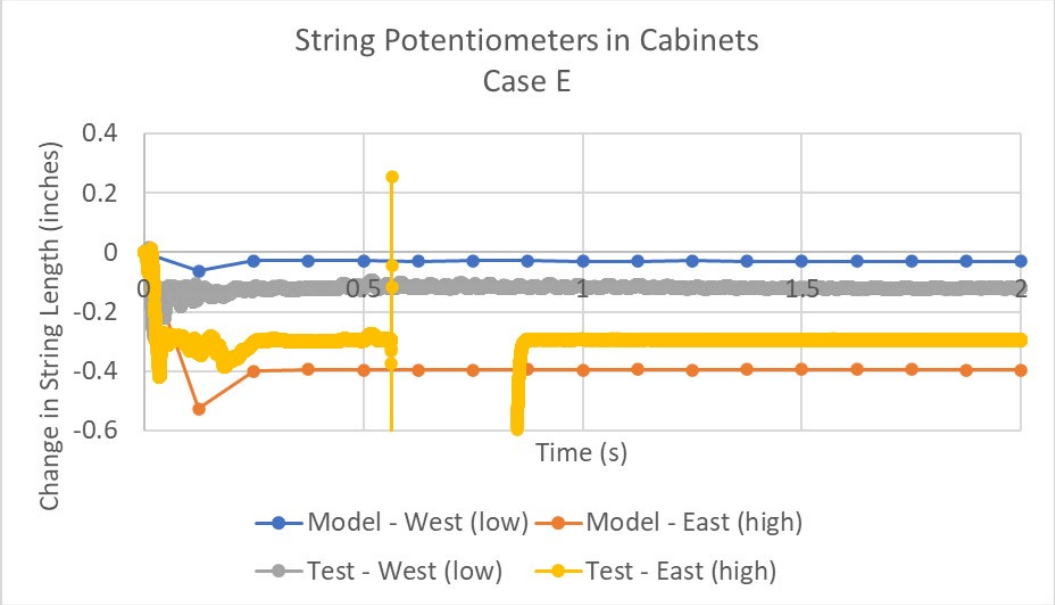


**Figure H 74. String Potentiometers in Piping Cabinet, Case E**

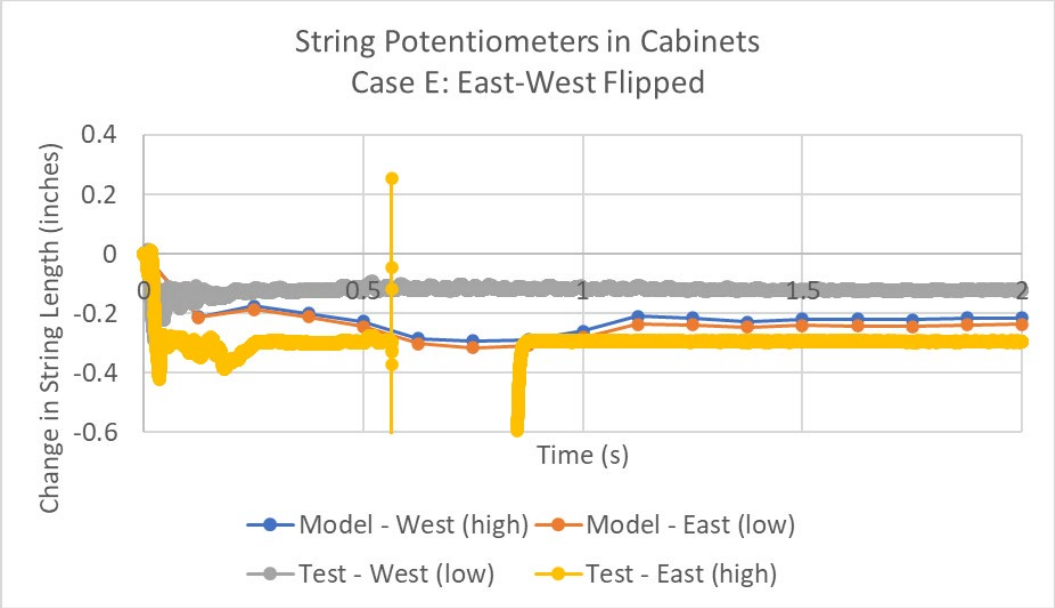


**Figure H 75. String Potentiometers in Piping Cabinet, Case E, East-West Flipped**

### Case F

Case F simulated a failed connection between the center plates of the tender and the center pin and bowl of the truck bolsters. As a lower-bound estimate of strength, contact between the center bowl and pin and the tender bolster was deactivated, representing an instantaneous failure of the connection. Unlike Case C, in Case F the tender-to-locomotive couplers were connected and not allowed to fail. The Case F model conditions are summarized in Table H 7. Figure H 74 shows the deformed shape of the Case F model. As a result of the impact the tender derailed but remained upright.

**Table H 7. Pre-test Case F Model Conditions**

| Case | Tender-to-locomotive Couplers | Bolster Pin and Center Bowl | Rail Base to Concrete Tie | Track Vertical Stiffness | Track Lateral Stiffness | Stub Track Connection | Impact Speed | Initial Pressure | Notes | Outcome |
|---|---|---|---|---|---|---|---|---|---|---|
| F | Yes | No | Tied | Default | Default | Discontinuous | 40 mph | 150 psig | Simulate instant center pin/bowl failure | Tender derailed, remains upright |

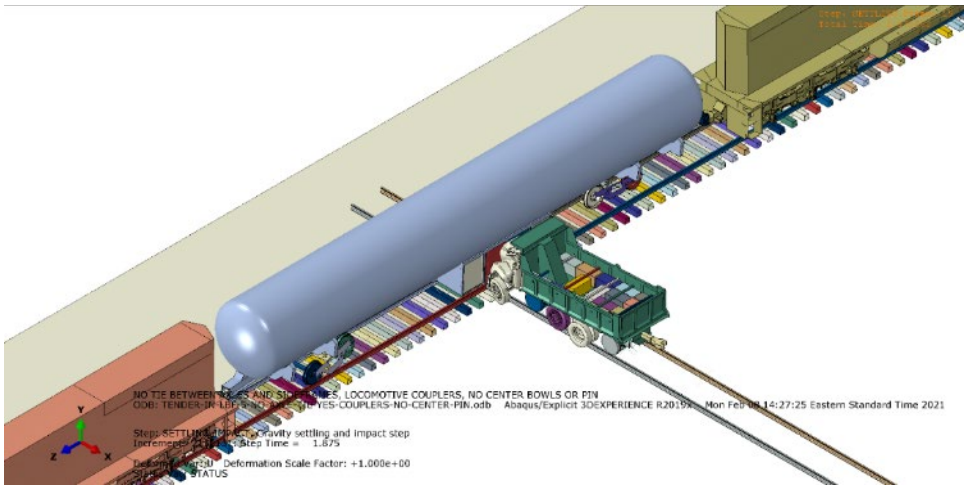


**Figure H 76. Deformed Model, Case F FEA**

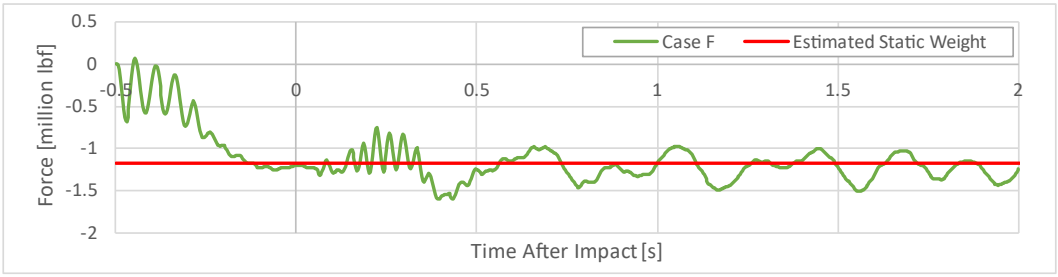


**Figure H 77. Time Response of Total Vertical Force on Ties (Total CTF2) for Case F**

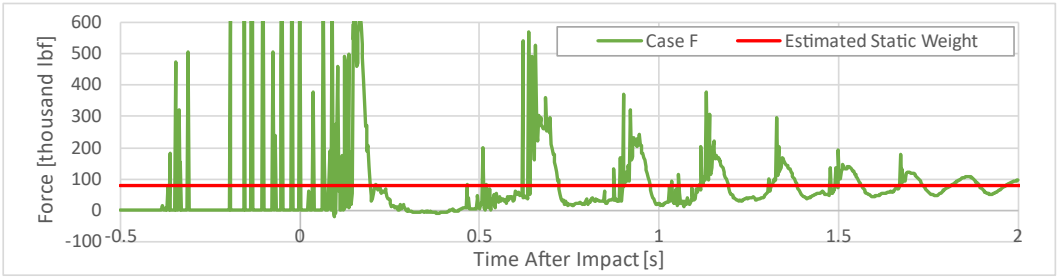


**Figure H 78. Time Response of Total Vertical Force on Rails for Case F**

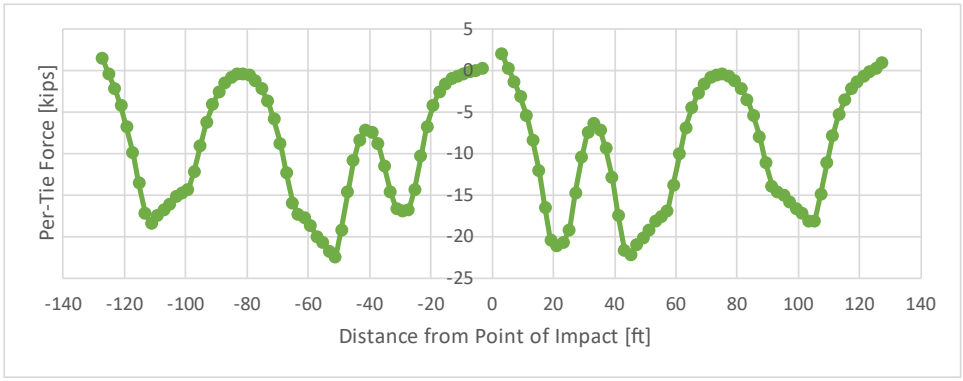


**Figure H 79. Vertical Load Distribution on Ties for Case F**

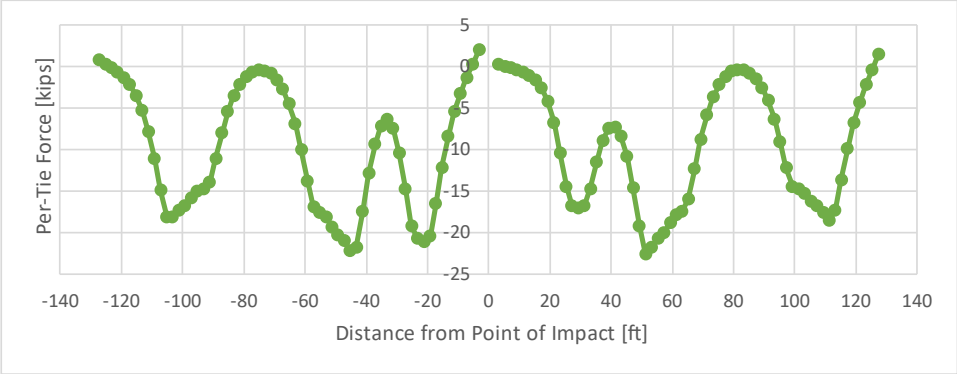


**Figure H 80. Vertical Load Distribution on Ties for Case F: Reflected at Point of Impact**

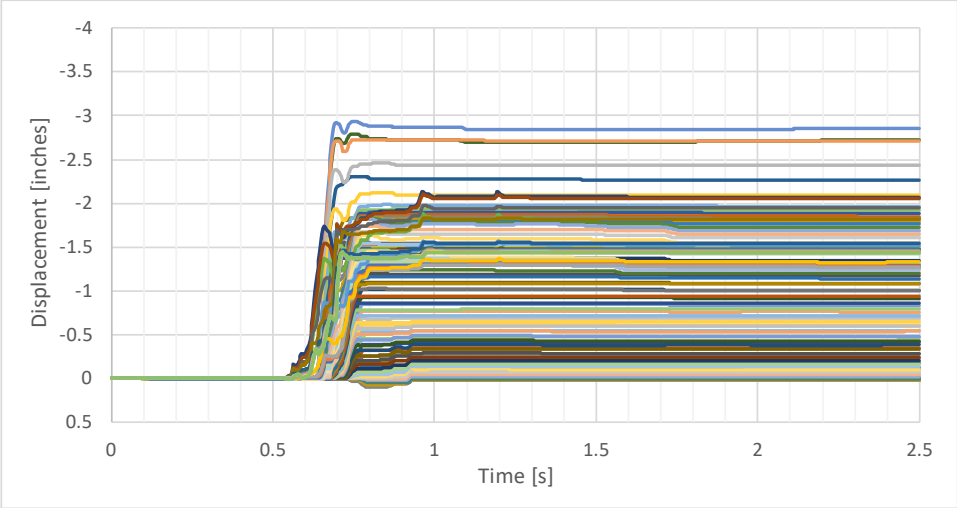


**Figure H 81. Lateral Displacement Relative to Ground of Each Tie for Case F**

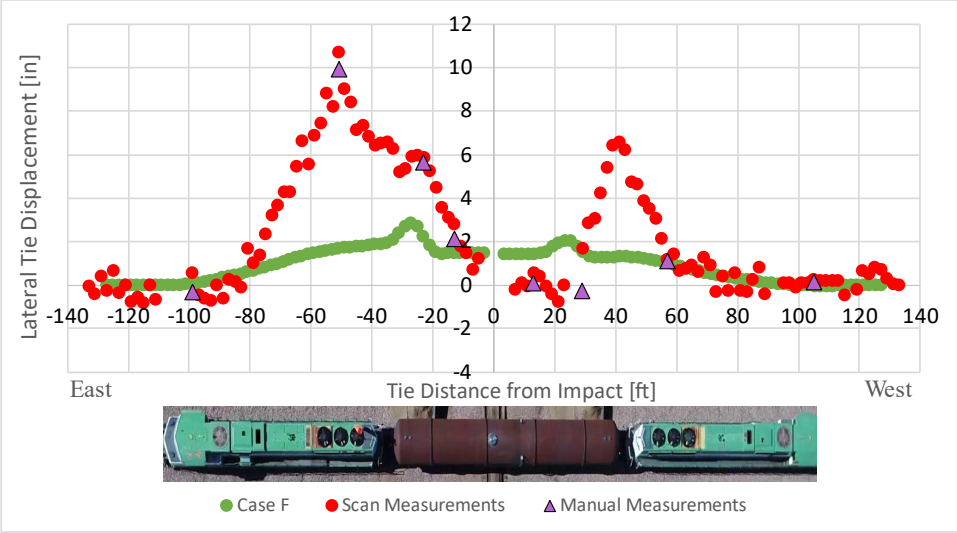


**Figure H 82. Final Lateral Displacement of Each Tie for Case F**

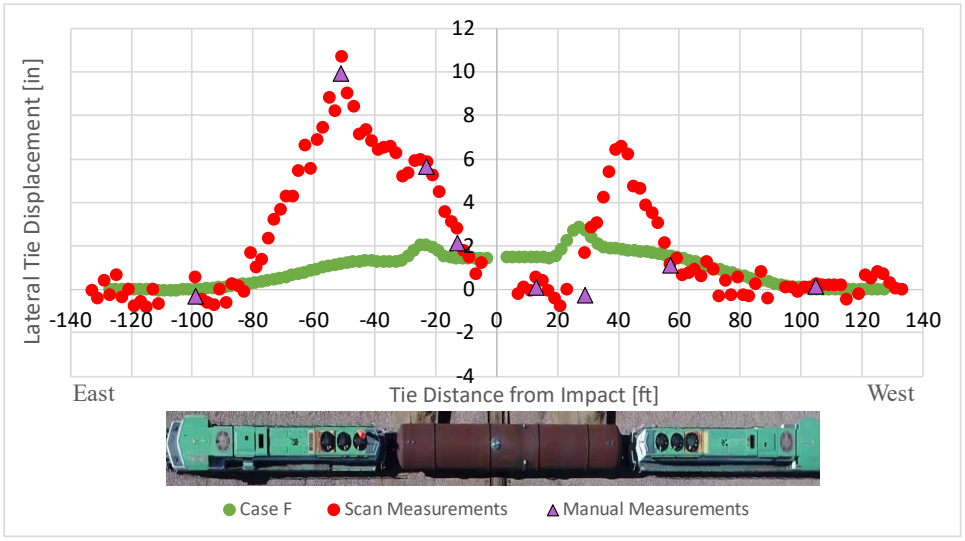


**Figure H 83. Final Lateral Displacement of Each Tie for Case F: Model Data Reflected at Point of Impact**

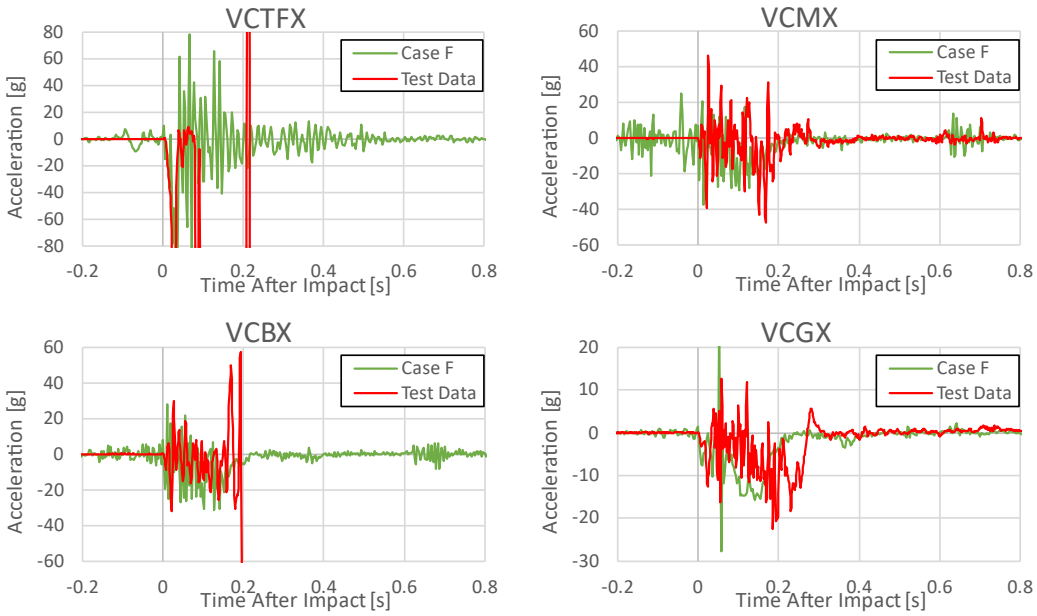


**Figure H 84. Accelerations from Measured and Case F Channels VCTFX, VCMX, VCBX, and VCGX**

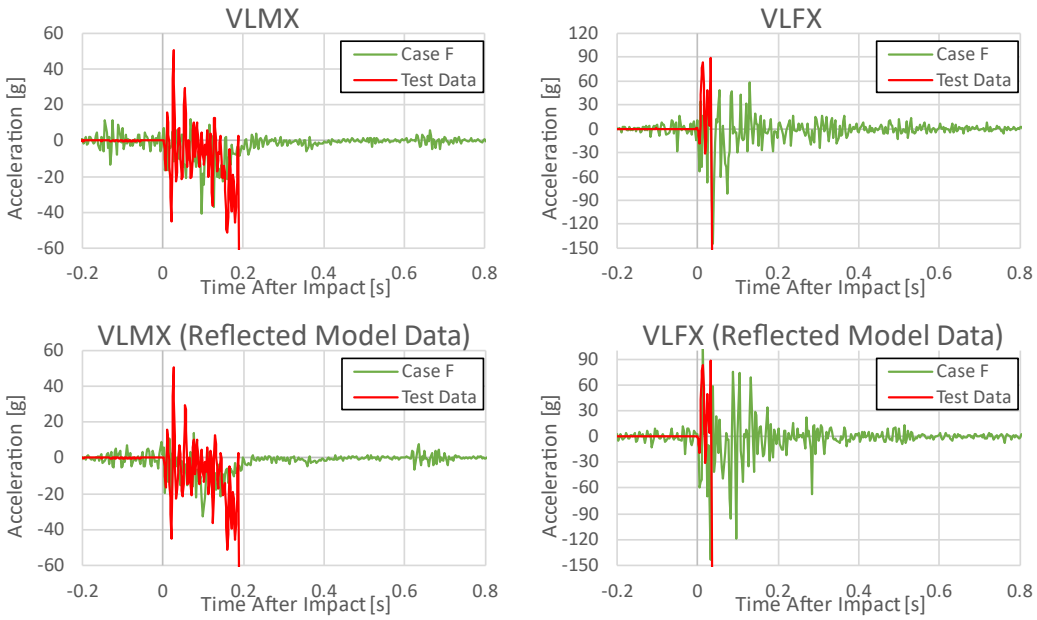


**Figure H 85. Accelerations from Measured and Case F Channels VLMX and VLFX, with Original and Reflected Model Data Presented for Each Channel**

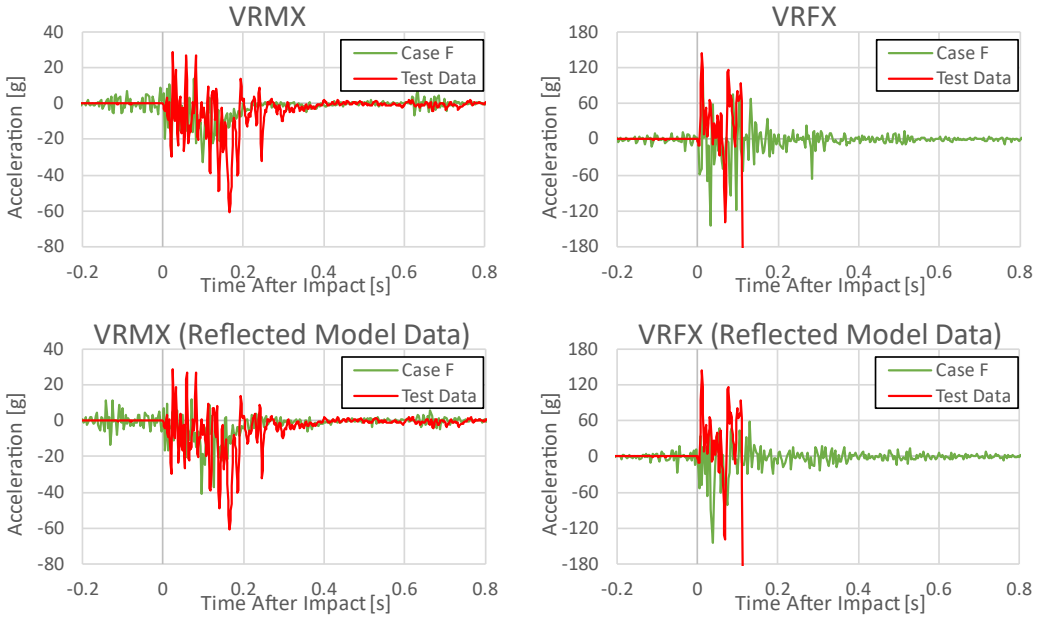


**Figure H 86. Accelerations from Measured and Case F Channels VRMX and VRFX, with Original and Reflected Model Data Presented for Each Channel**

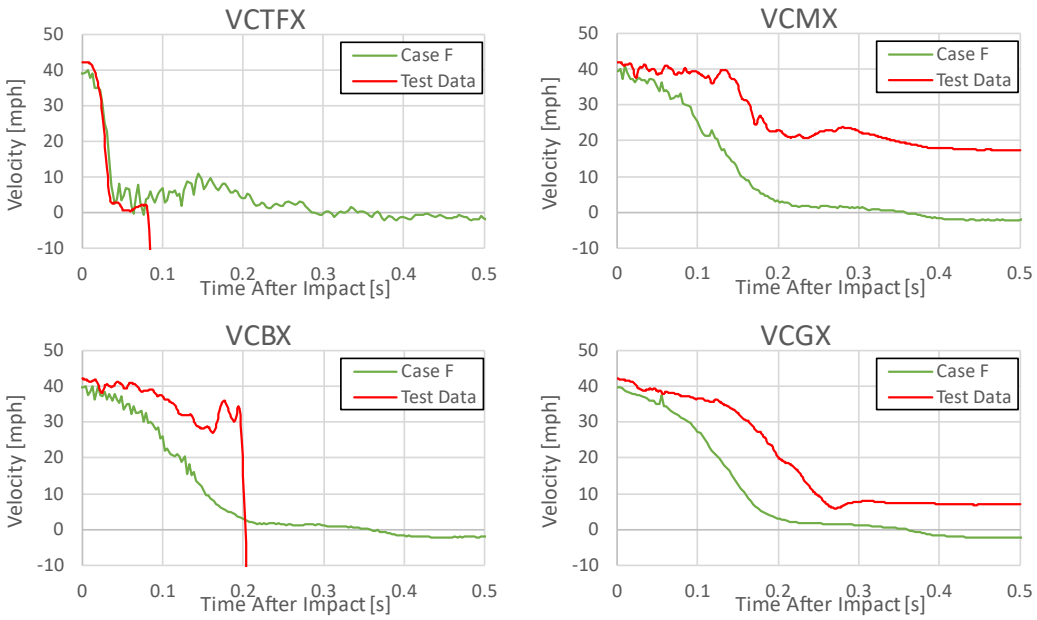


**Figure H 87. Velocities from Measured and Case F Channels VCTFX, VCMX, VCBX, and VCGX**

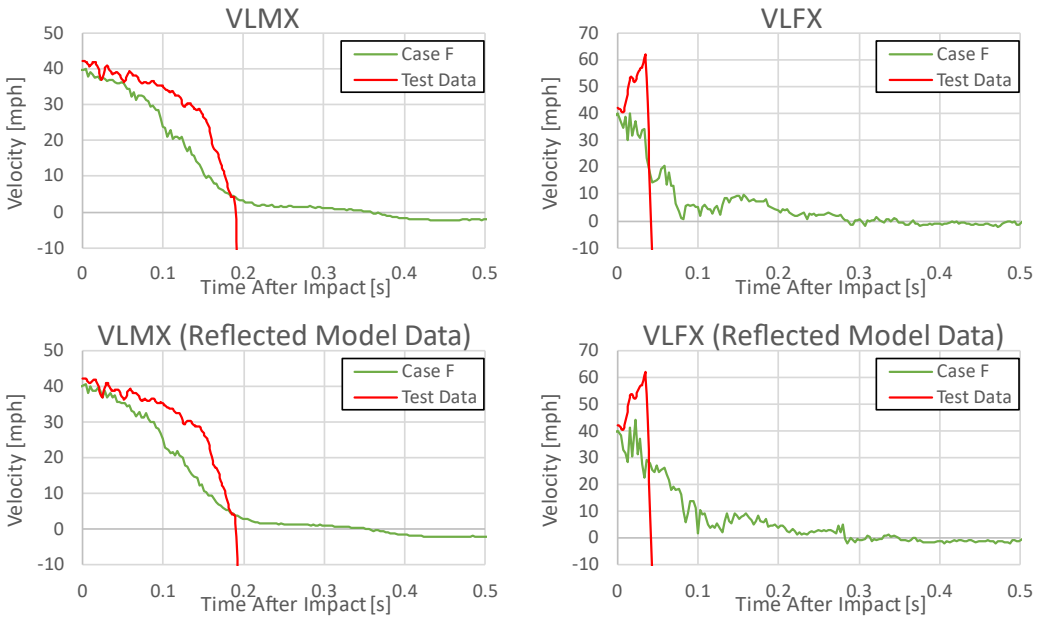


**Figure H 88. Velocities from Measured and Case F Channels VLMX and VLFX, with Original and Reflected Model Data Presented for Each Channel**

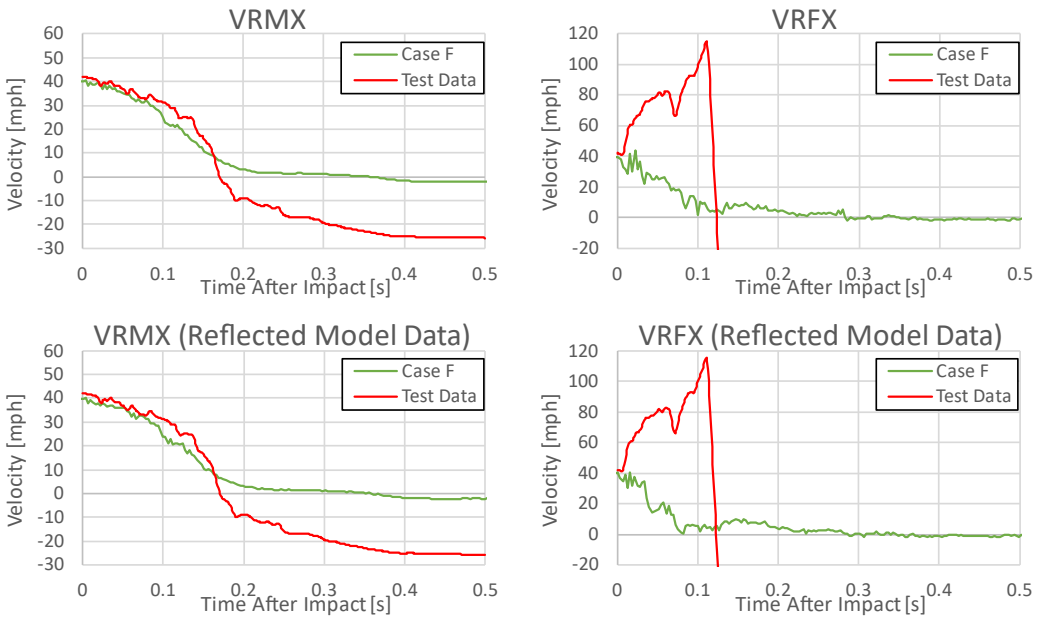


**Figure H 89. Velocities from Measured and Case F Channels VRMX and VRFX, with Original and Reflected Model Data Presented for Each Channel**

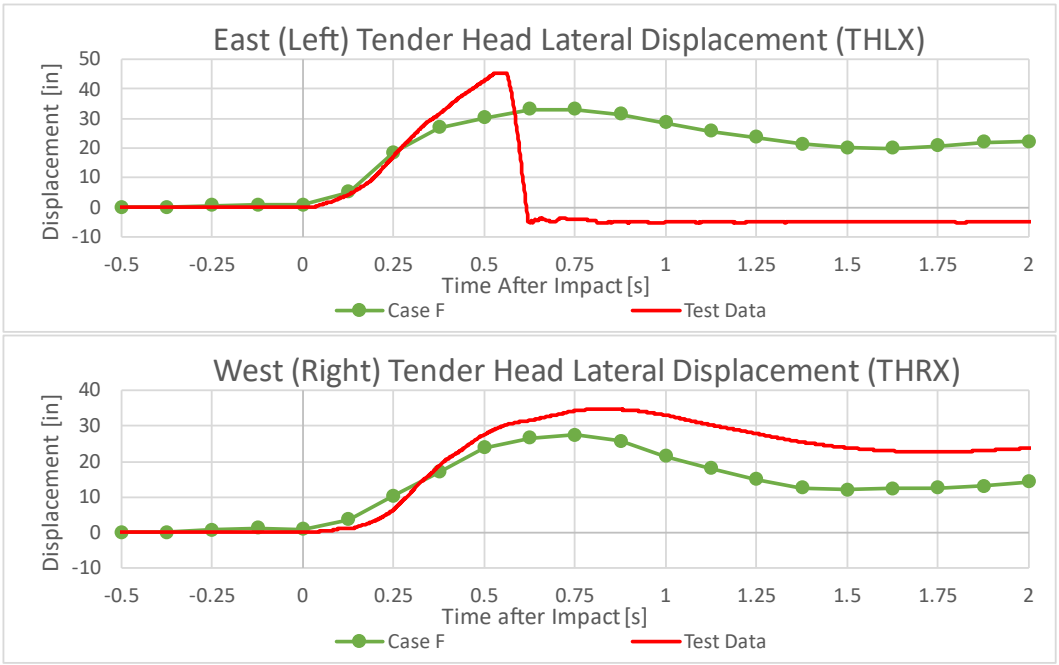


**Figure H 90. Lateral Displacement of the East and West Tender Heads for Case F**

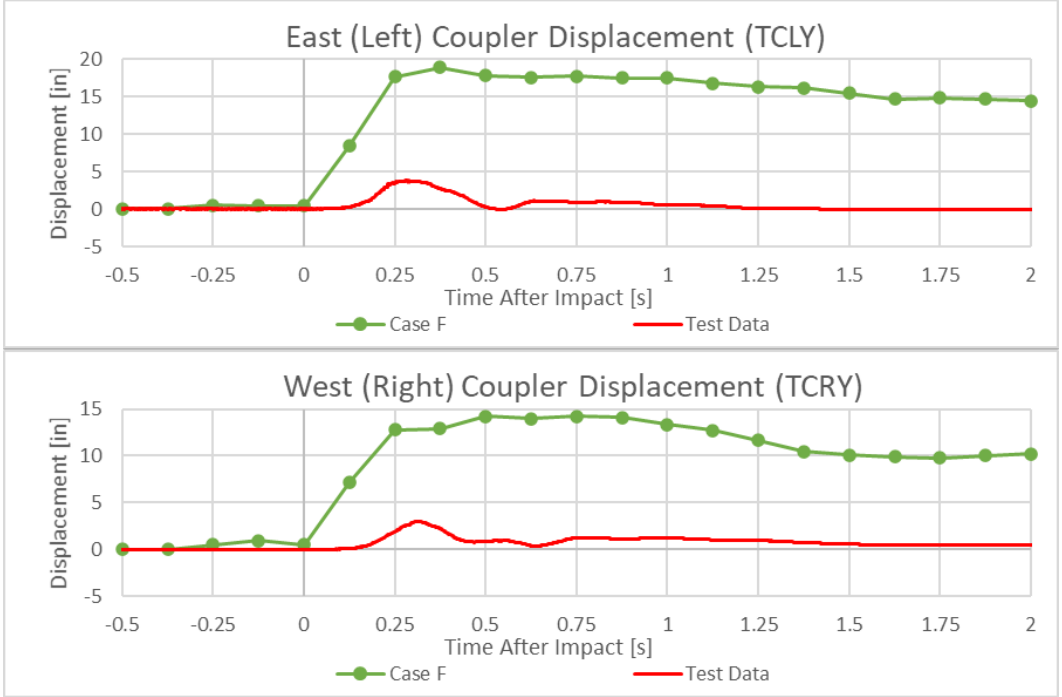


**Figure H 91. Locomotive-to-Tender Coupler Displacements for Case F**

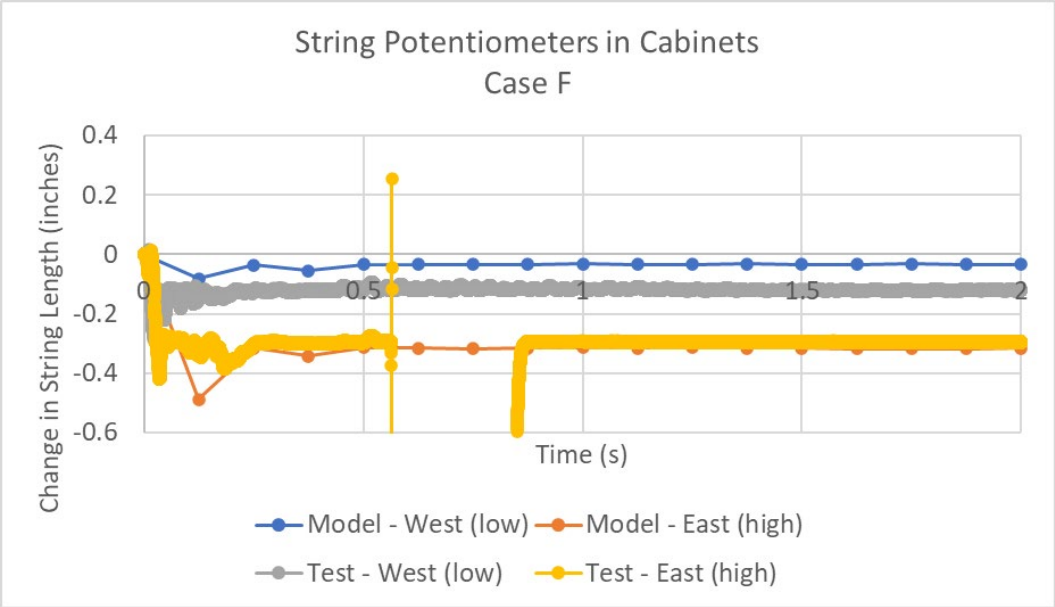


**Figure H 92. String Potentiometers in Piping Cabinet, Case F**

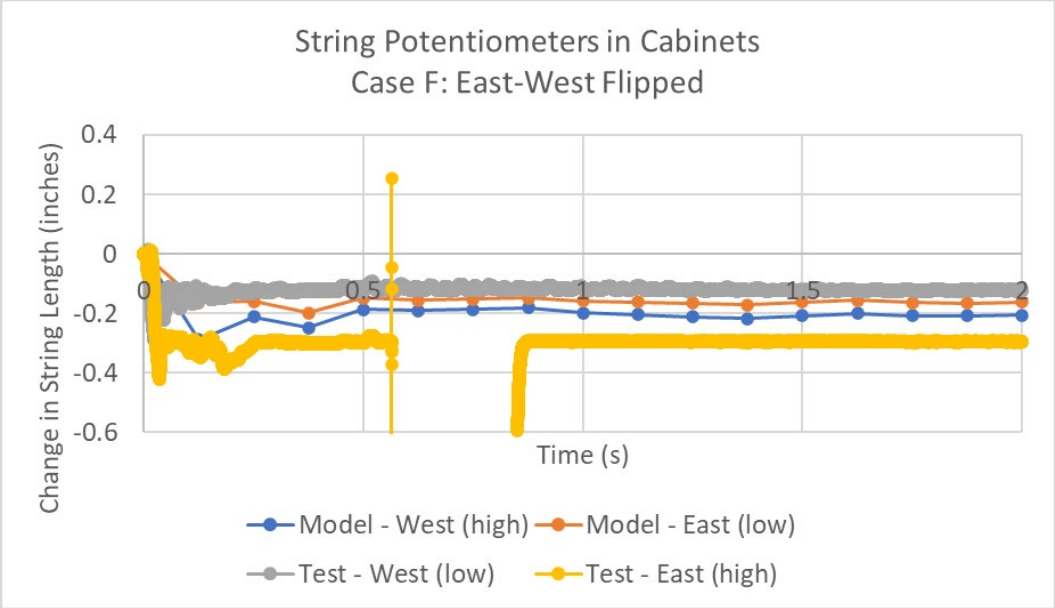


**Figure H 93. String Potentiometers in Piping Cabinet, Case F, East-West Flipped**

### Case G

Case G simulated an overspeed impact. While the test was planned to occur at no less than 40 mph, the test team was interested in verifying that the outcome of the test would not be substantially different at 45 mph than at the planned 40 mph. All of the conditions of the model were the same as the baseline case with the exception of the impact speed. These conditions are summarized in Table H 8. The deformed shape of the model is shown in Figure H 92. As a result of the impact the tender derailed but remained upright. The results were substantially similar to the baseline case.

**Table H 8. Pre-test Case G Model Conditions**

| Case | Tender-to-locomotive Couplers | Bolster Pin and Center Bowl | Rail Base to Concrete Tie | Track Vertical Stiffness | Track Lateral Stiffness | Stub Track Connection | Impact Speed | Initial Pressure | Notes | Outcome |
|---|---|---|---|---|---|---|---|---|---|---|
| G | Yes | Yes | Tied | Default | Default | Discontinuous | 45 mph | 150 psig | Simulate 5 mph overspeed impact | |

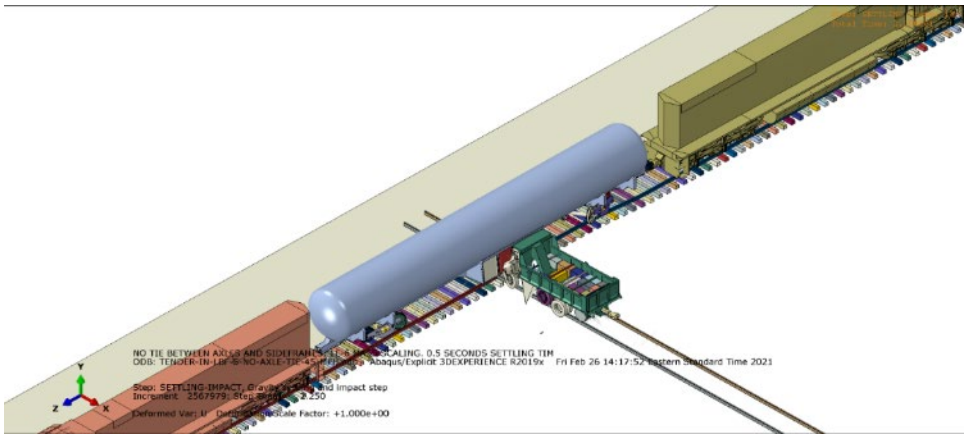

**Figure H 94. Deformed Model, Case G FEA**

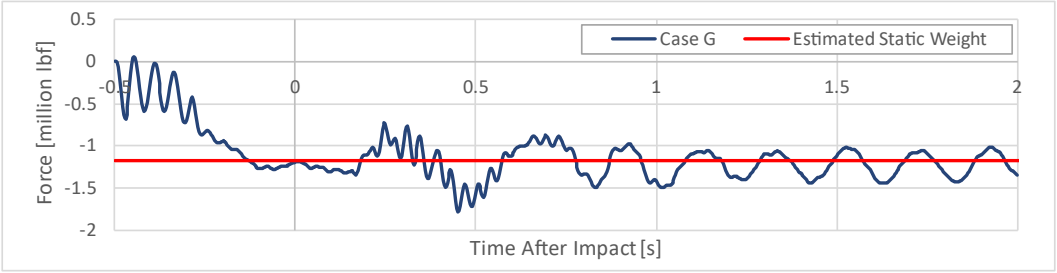


**Figure H 95. Time Response of Total Vertical Force on Ties for Case G**

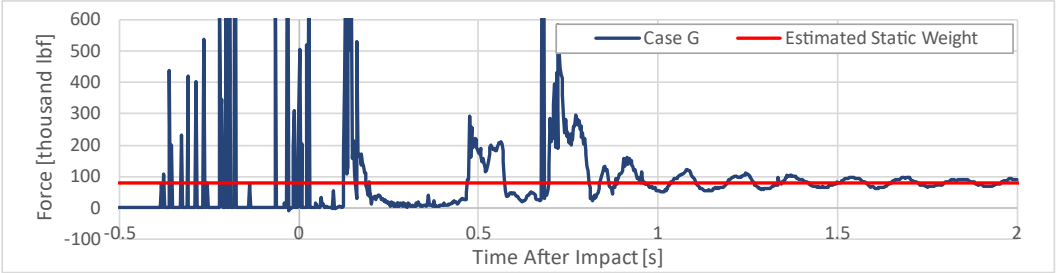


**Figure H 96. Time Response of Total Vertical Force on Rails for Case G**

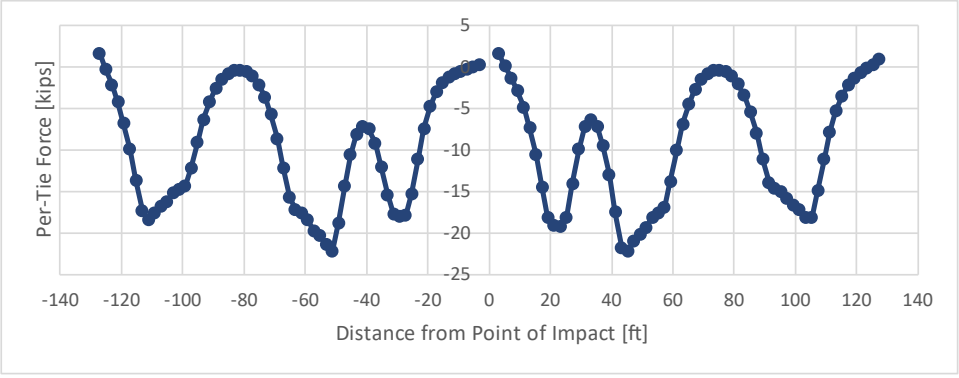


**Figure H 97. Vertical Load Distribution on Ties for Case G**

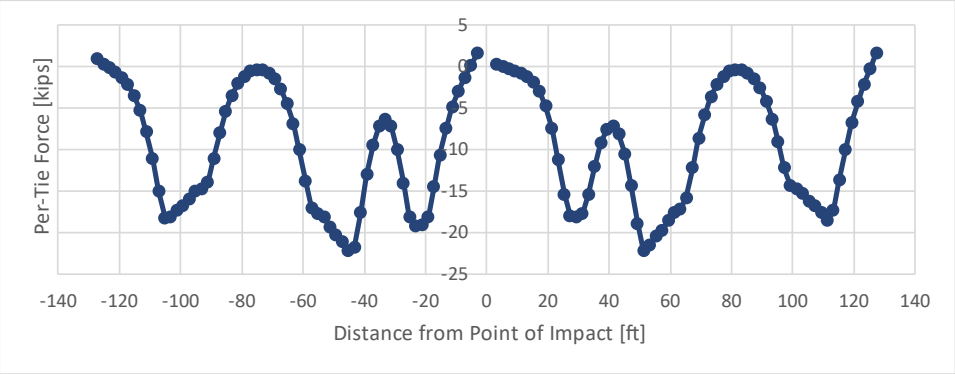


**Figure H 98. Vertical Load Distribution on Ties for Case G: Reflected at Point of Impact**

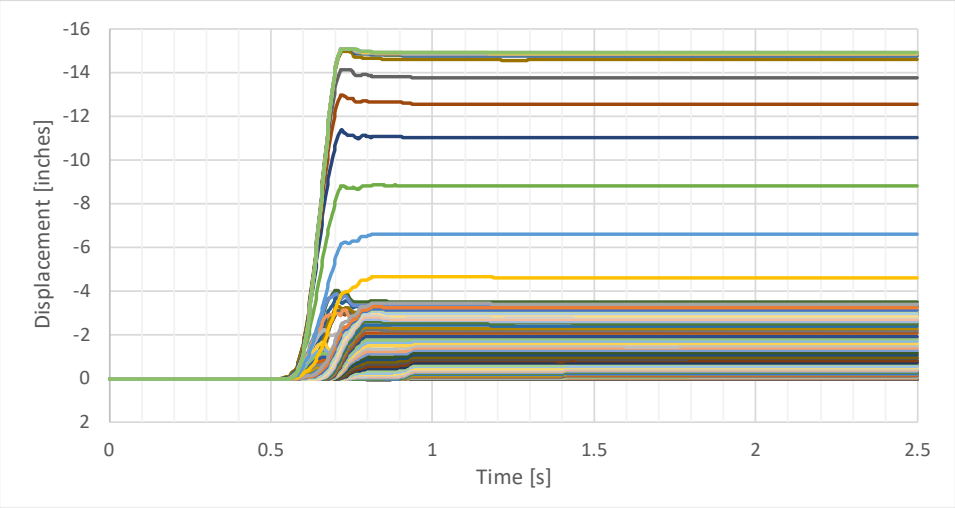


**Figure H 99. Lateral Displacement Over Time of Each Tie for Case G**

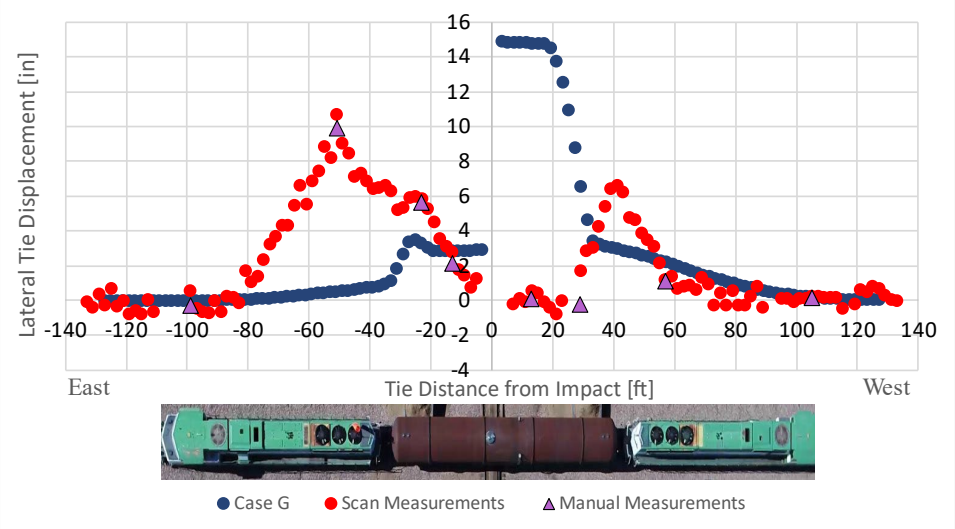


**Figure H 100. Final Lateral Displacement of Each Tie for Case G**

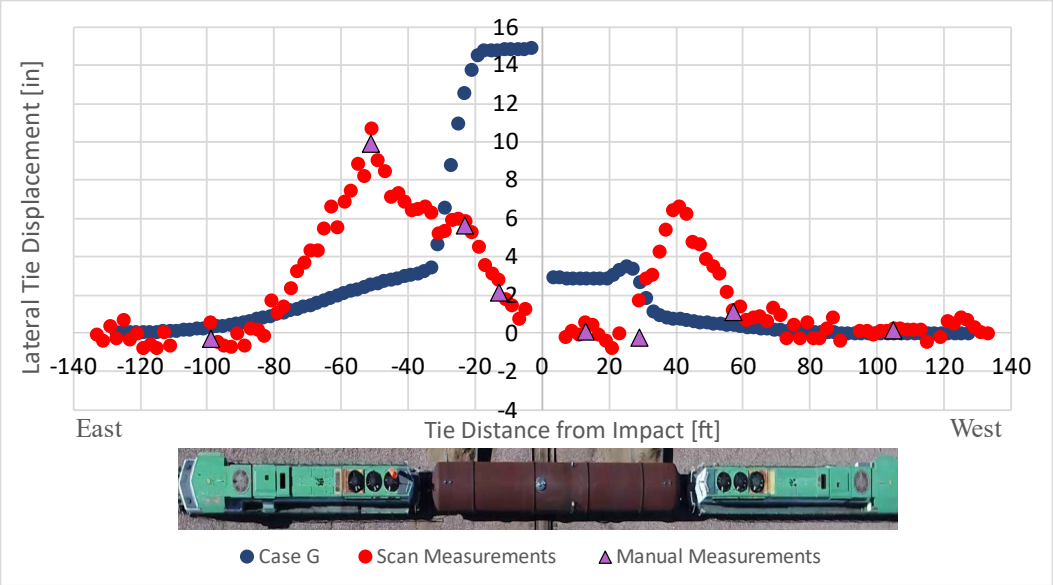


**Figure H 101. Final Lateral Displacement of Each Tie for Case G: Model Data Reflected at Point of Impact**

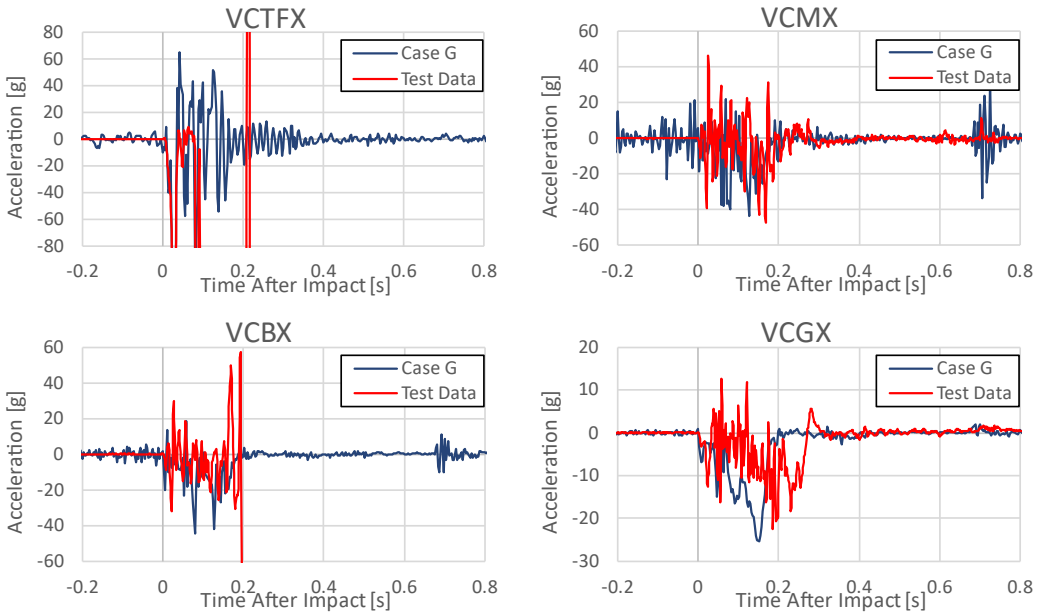


**Figure H 102. Accelerations from Measured and Case G Channels VCTFX, VCMX, VCBX, and VCGX**

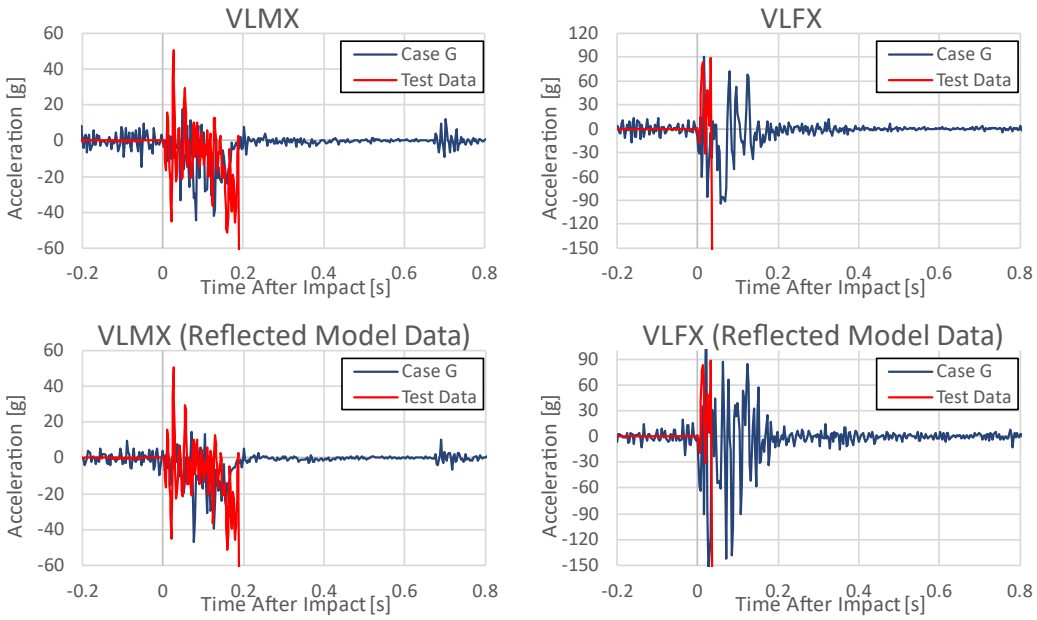


**Figure H 103. Accelerations from Measured and Case G Channels VLMX and VLFX, with Original and Reflected Model Data Presented for Each Channel**

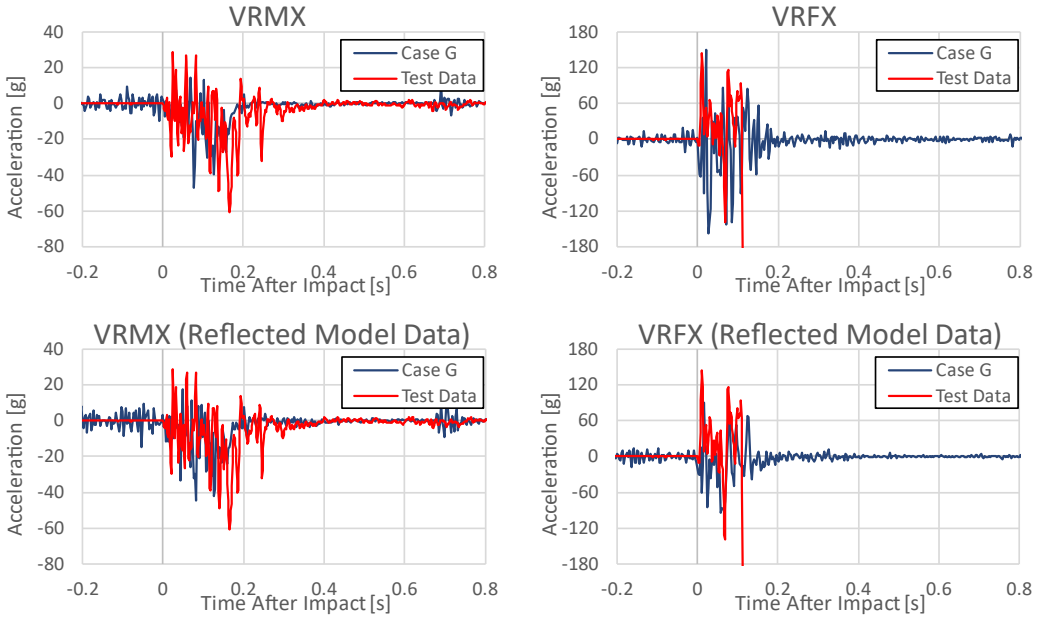


**Figure H 104. Accelerations from Measured and Case G Channels VRMX and VRFX, with Original and Reflected Model Data Presented for Each Channel**

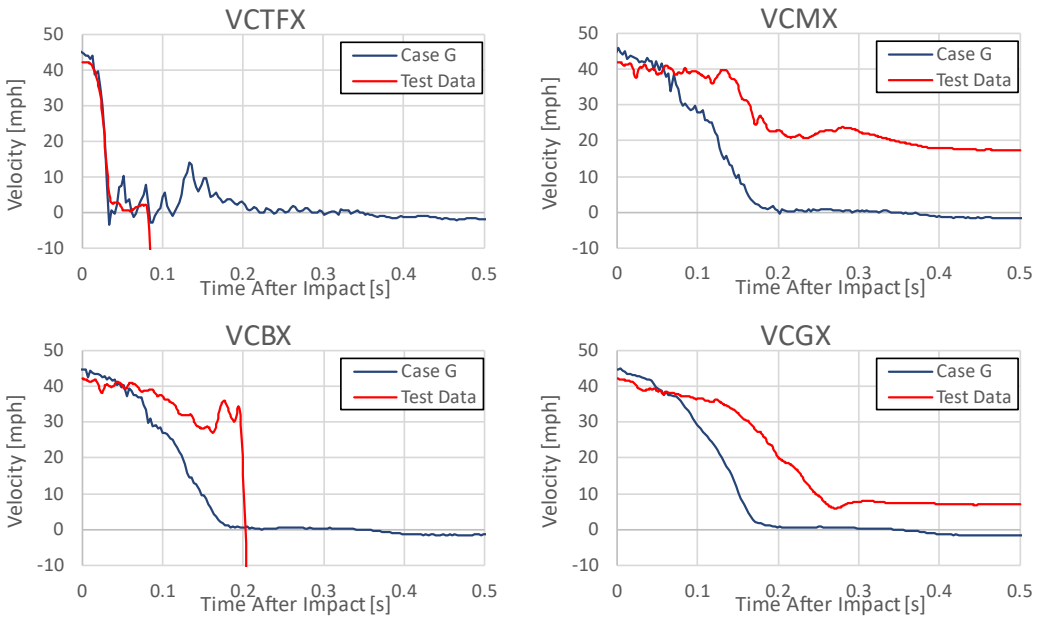


**Figure H 105. Velocities from Measured and Case G Channels VCTFX, VCMX, VCBX, and VCGX**

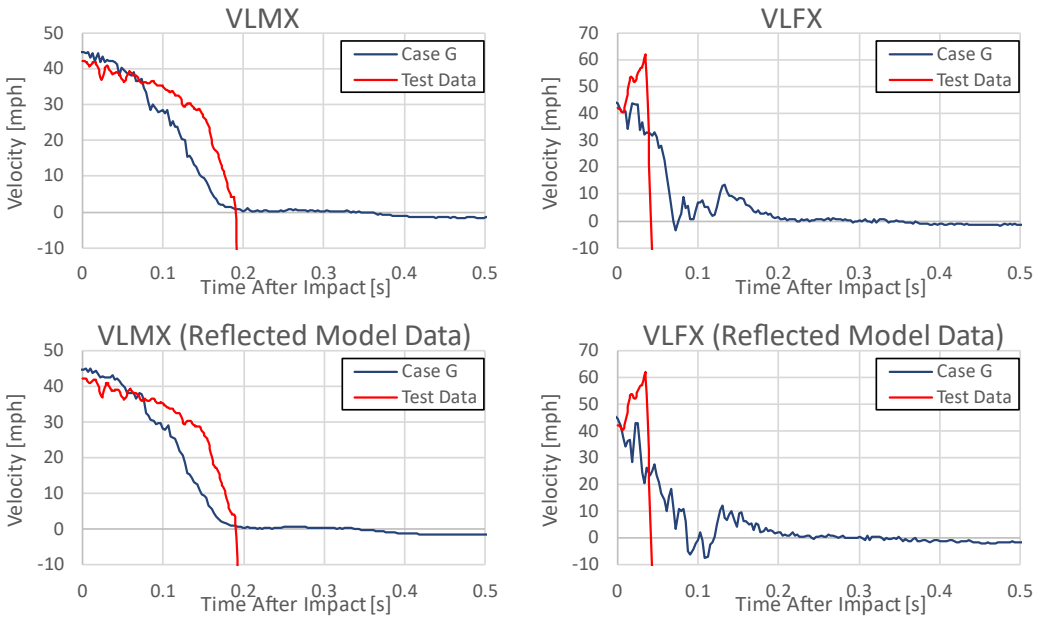


**Figure H 106. Velocities from Measured and Case G Channels VLMX and VLFX, with Original and Reflected Model Data Presented for Each Channel**

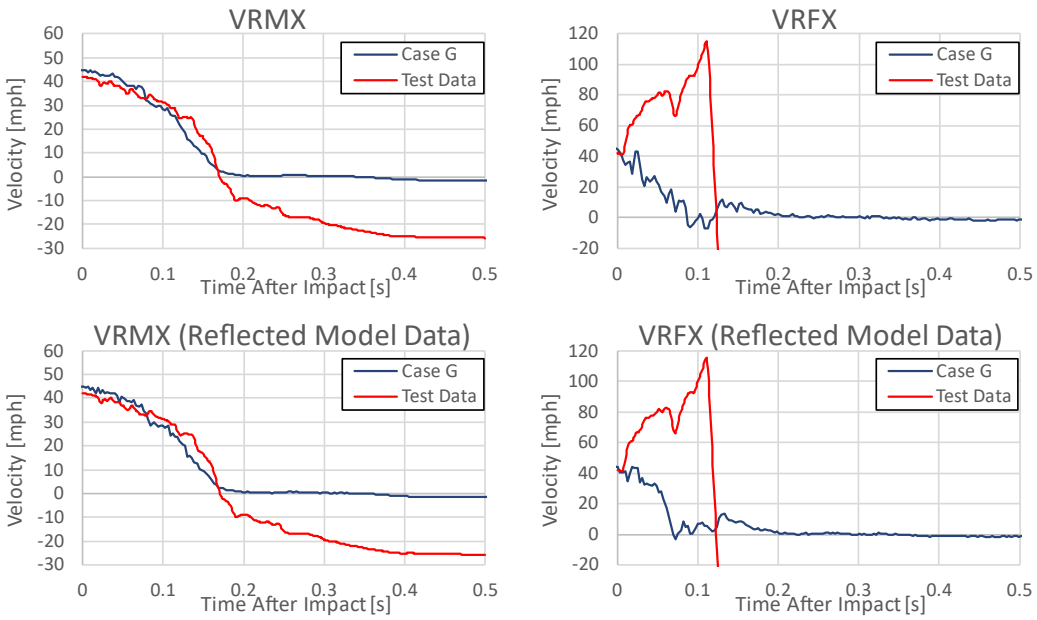


**Figure H 107. Velocities from Measured and Case G Channels VRMX and VRFX, with Original and Reflected Model Data Presented for Each Channel**

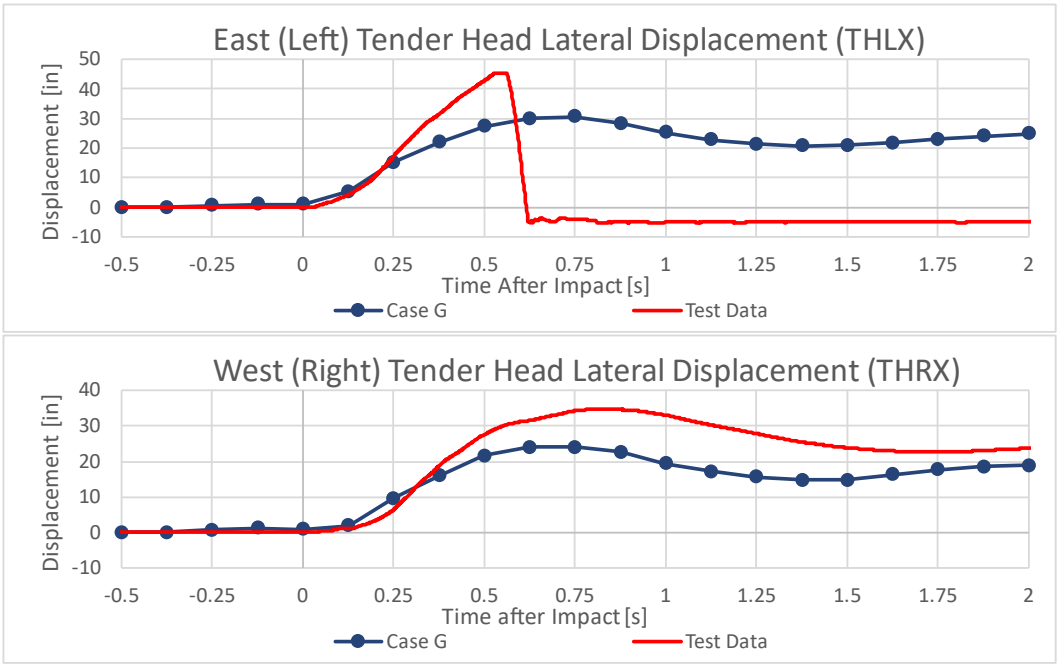


**Figure H 108. Lateral Displacement of the East and West Tender Heads for Case G**

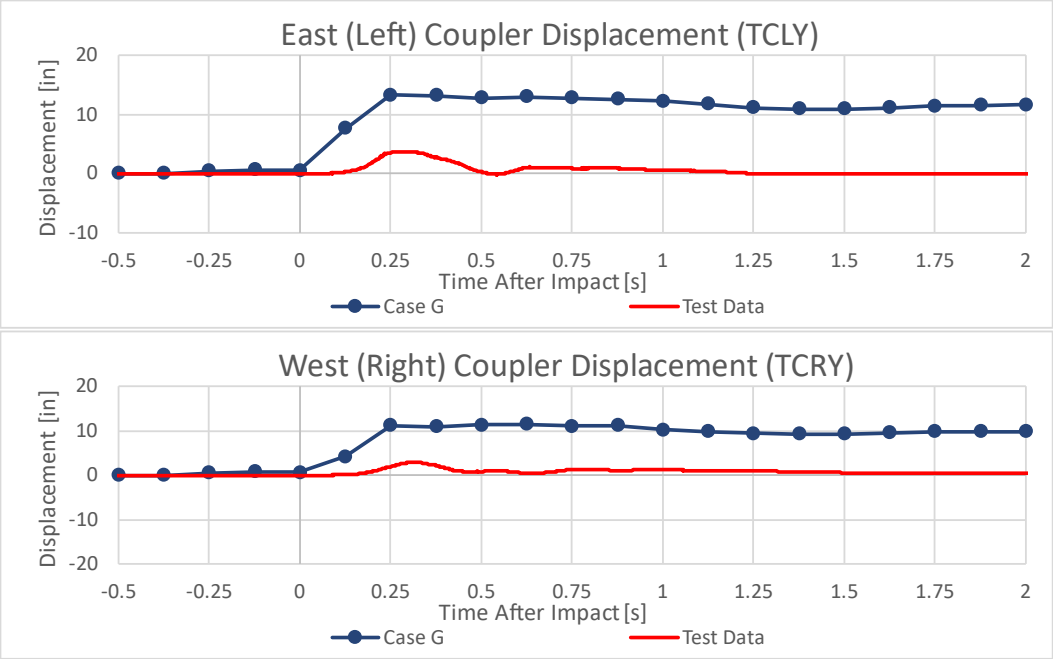


**Figure H 109. Locomotive-to-Tender Coupler Displacements for Case G**

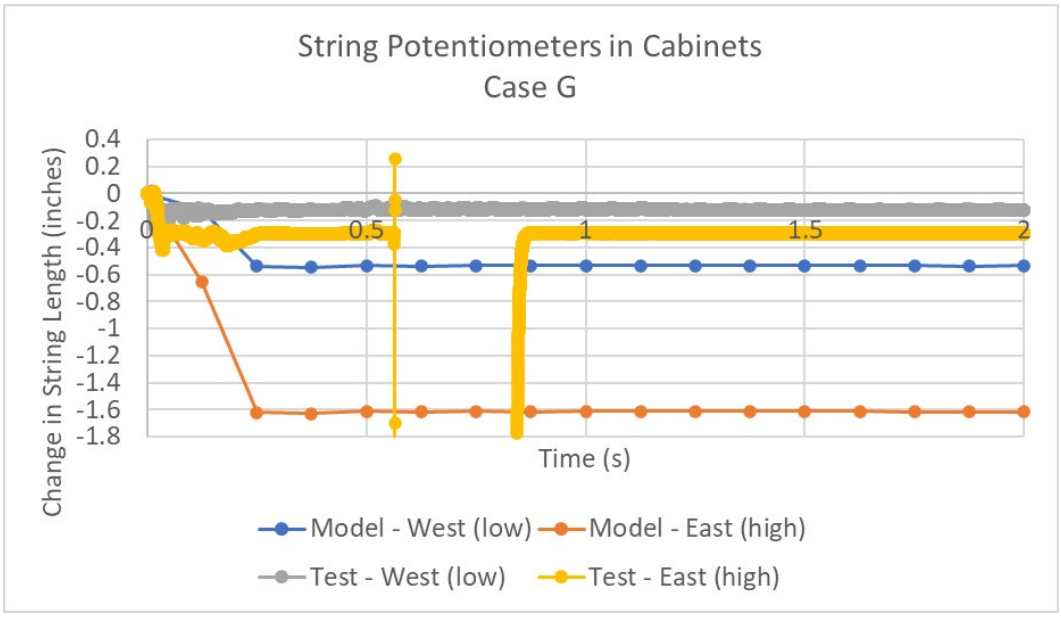


**Figure H 110. String Potentiometers in Piping Cabinet, Case G**

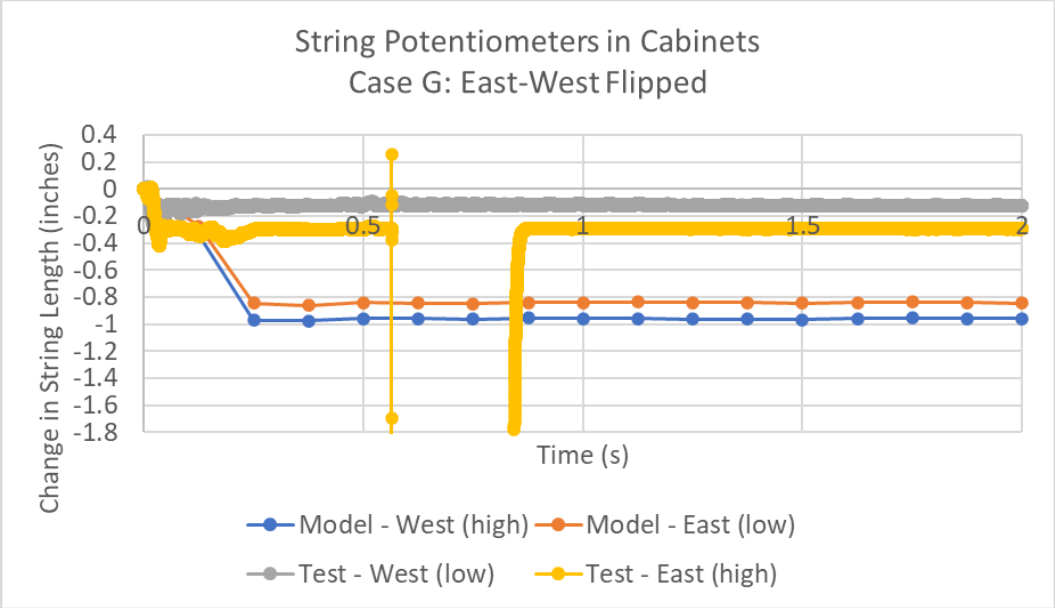


**Figure H 111. String Potentiometers in Piping Cabinet, Case G, East-West Flipped**

### Case H

Originally, the FE models were run with the two stubs of track supporting the tender and locomotives disconnected from one another. As the test setup was developed in greater detail, the team was able to make the stub tracks continuous, with the guide track for the dump truck terminating near the point of impact. Case H was run at the baseline conditions, but with an additional short section of rail tied into the stub track rails to make each rail continuous. Table H 9 contains a summary of the conditions in the Case H model. Figure H 110 shows the deformed shape of the FE model.

**Table H 9. Pre-test Case H Model Conditions**

| Case | Tender-to-locomotive Couplers | Bolster Pin and Center Bowl | Rail Base to Concrete Tie | Track Vertical Stiffness | Track Lateral Stiffness | Stub Track Connection | Impact Speed | Initial Pressure | Notes | Outcome |
|---|---|---|---|---|---|---|---|---|---|---|
| H | Yes | Yes | Tied | Default | Default | Continuous Rail | 40 mph | 150 psig | Simulate continuous rail under tender | Tender derailed, remained upright |

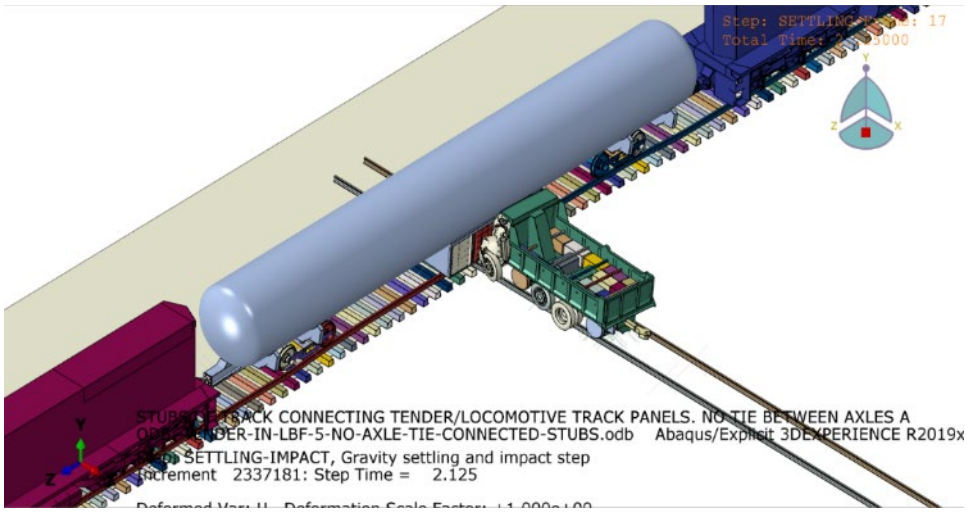


**Figure H 112. Deformed Model, Case H FEA**

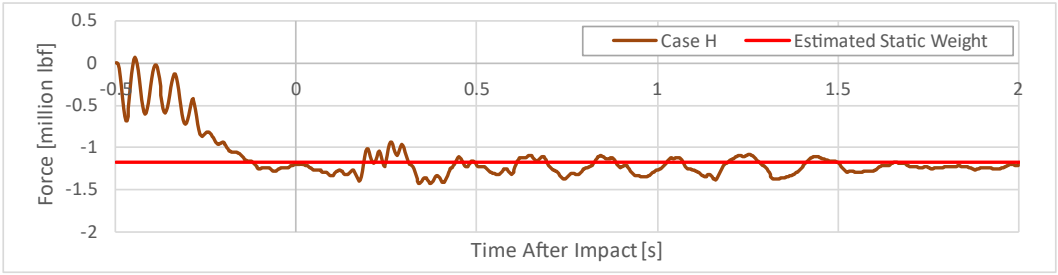


**Figure H 113. Time Response of Total Vertical Force on Ties for Case H**

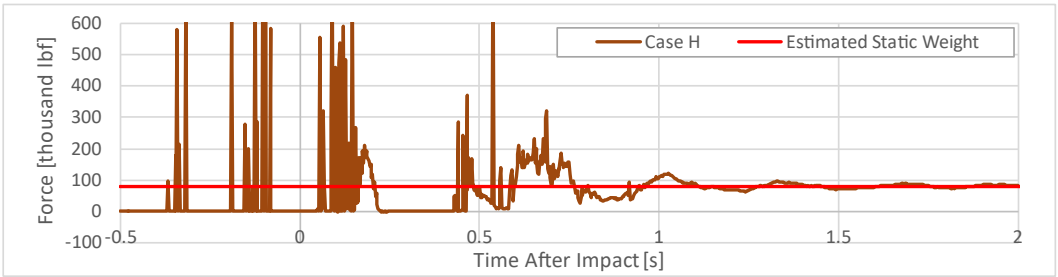


**Figure H 114. Time Response of Total Vertical Force on Rails for Case H**

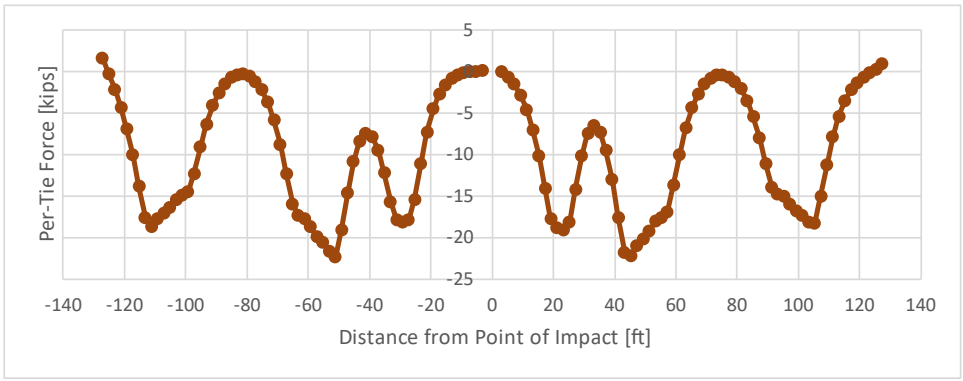


**Figure H 115. Vertical Load Distribution on Ties for Case H**

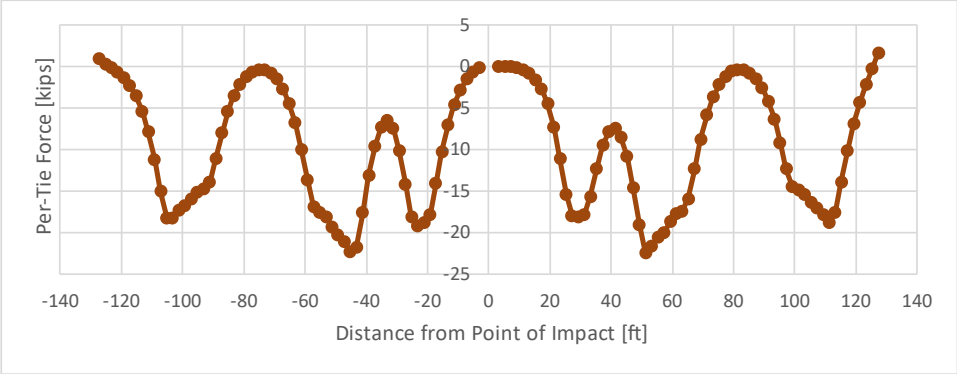


**Figure H 116. Vertical Load Distribution on Ties for Case H: Reflected at Point of Impact**

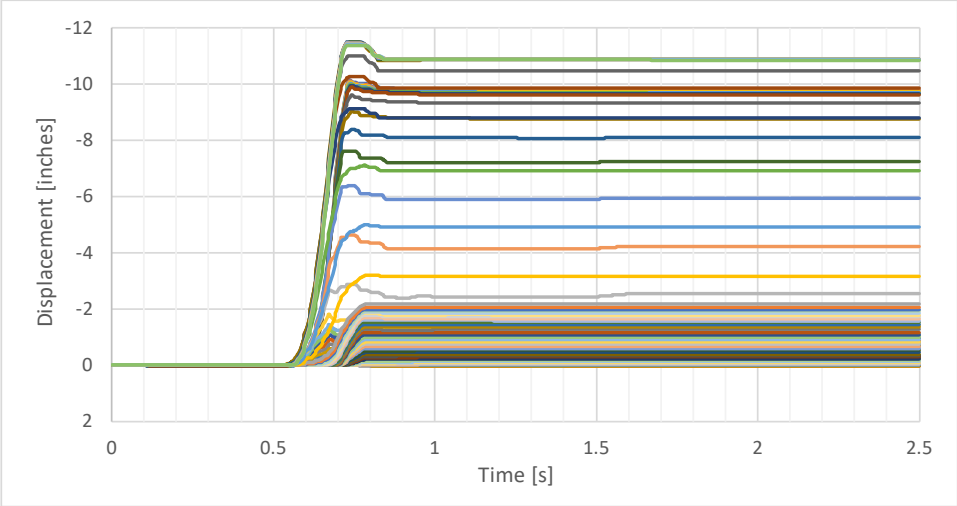


**Figure H 117. Lateral Displacement Over Time of Each Tie for Case H**

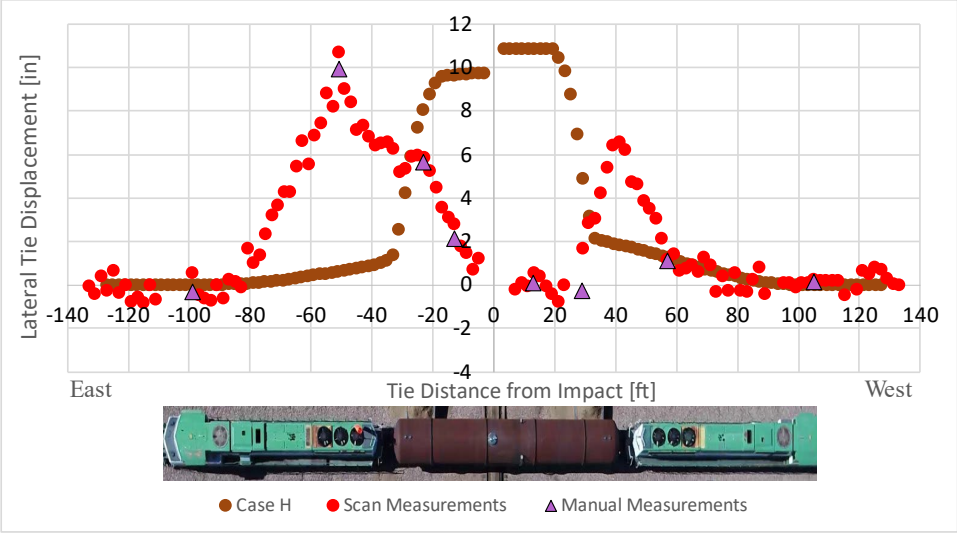


**Figure H 118. Final Lateral Displacement of Each Tie for Case H**

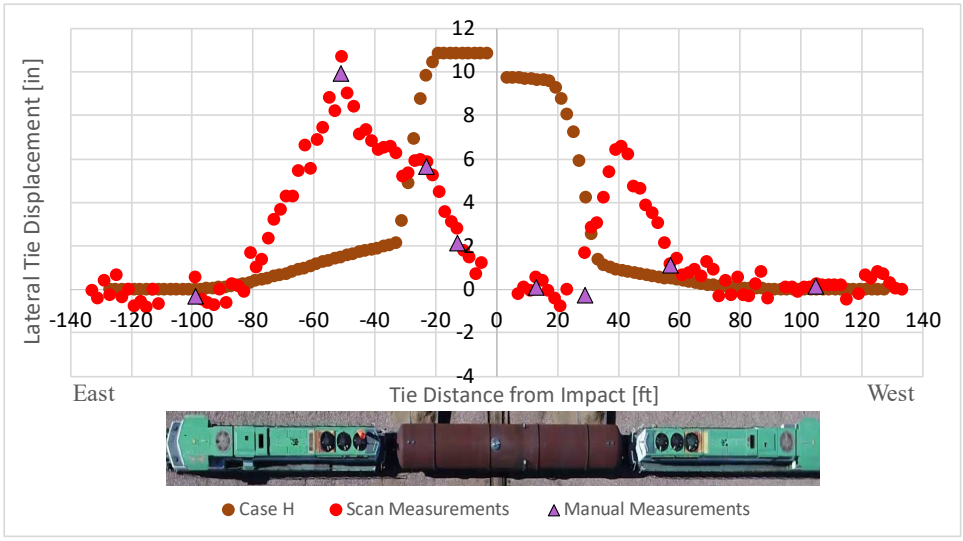


**Figure H 119. Final Lateral Displacement of Each Tie for Case H: Model Data Reflected at Point of Impact**

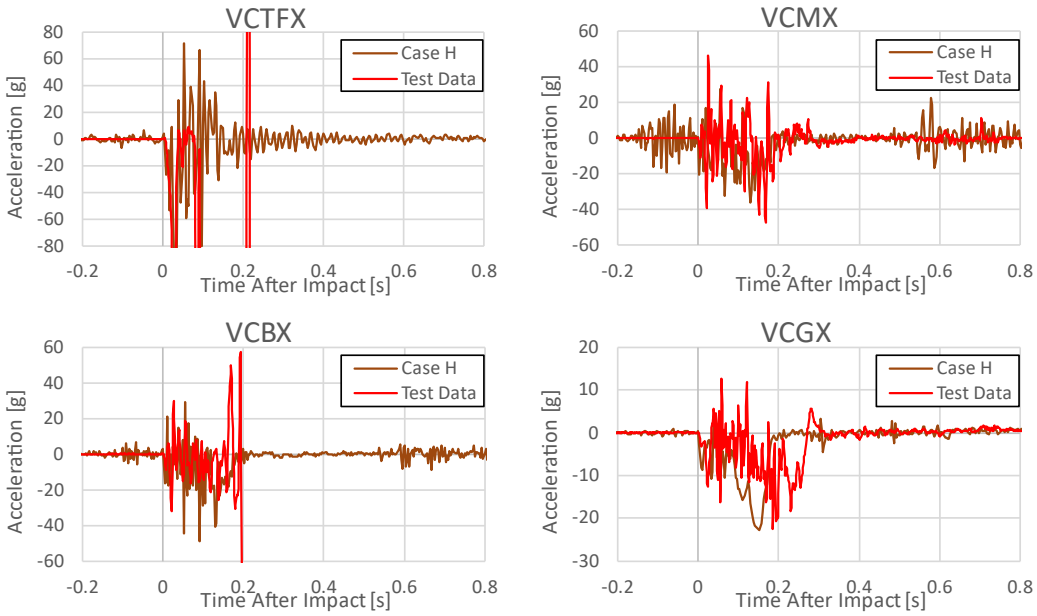


**Figure H 120. Accelerations from Measured and Case H Channels VCTFX, VCMX, VCBX, and VCGX**

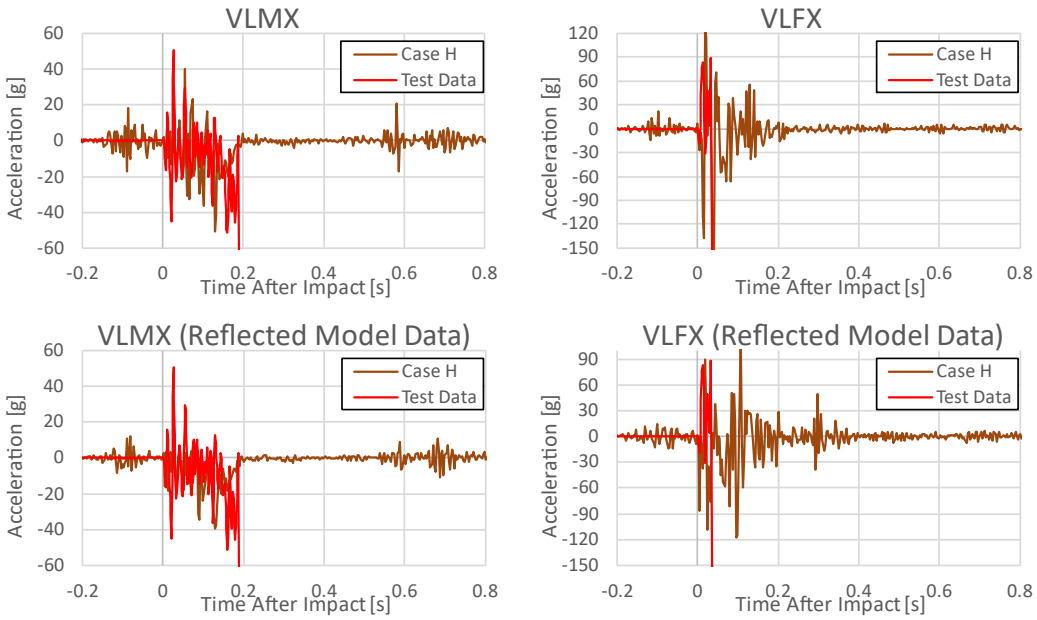


**Figure H 121. Accelerations from Measured and Case H Channels VLMX and VLFX, with Original and Reflected Model Data Presented for Each Channel**

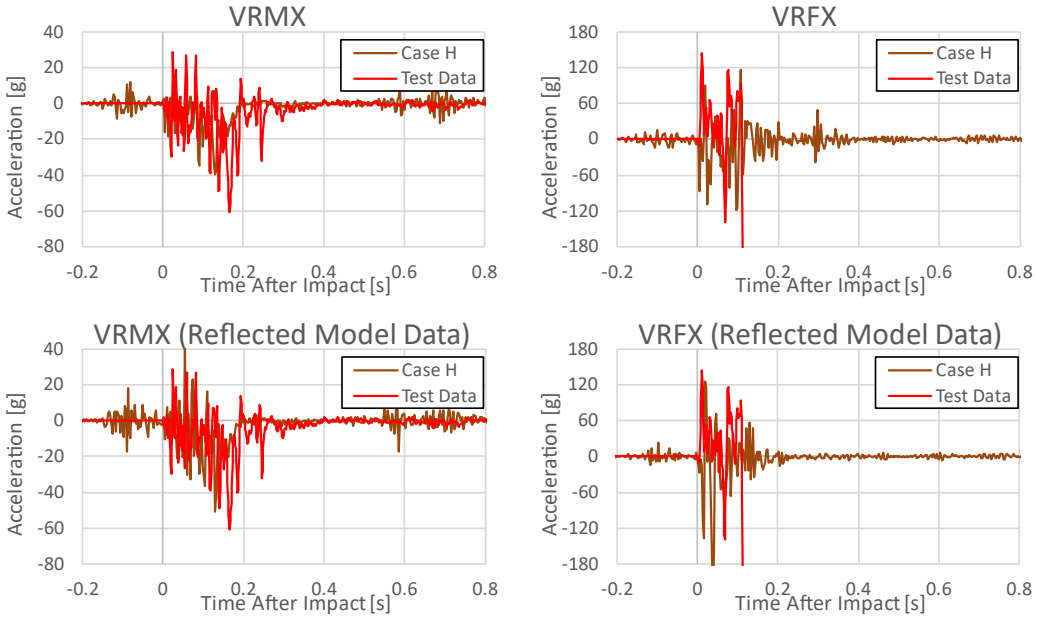


**Figure H 122. Accelerations from Measured and Case H Channels VRMX and VRFX, with Original and Reflected Model Data Presented for Each Channel**

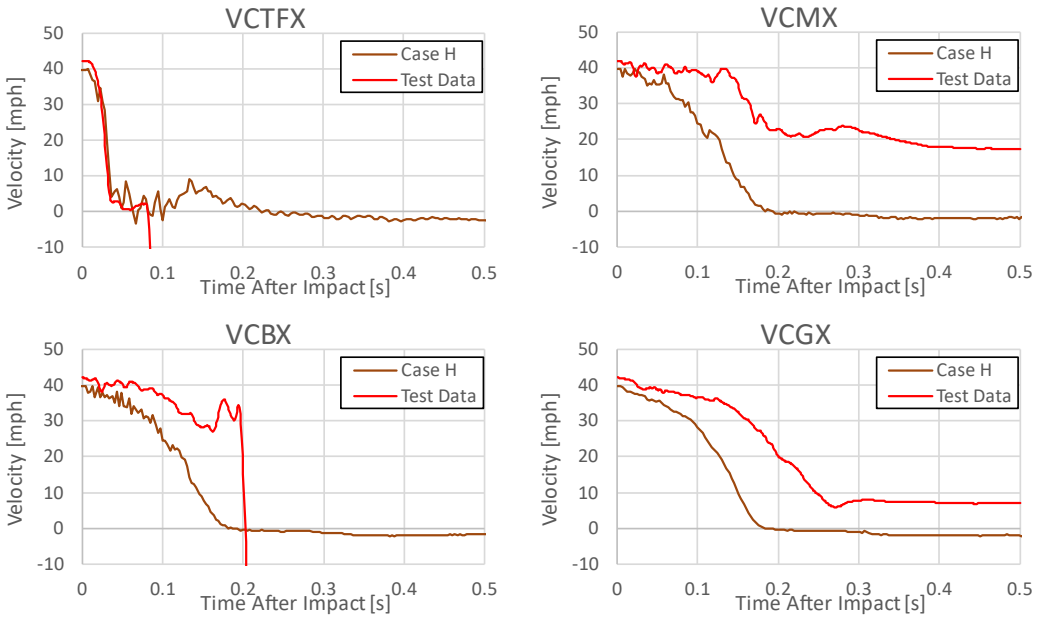


**Figure H 123. Velocities from Measured and Case H Channels VCTFX, VCMX, VCBX, and VCGX**

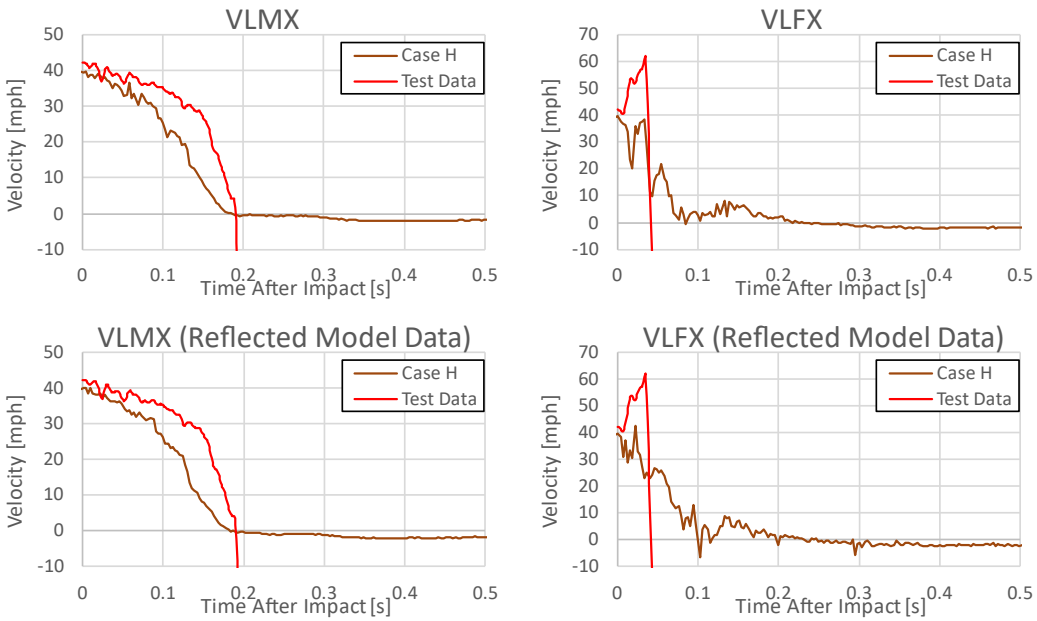


**Figure H 124. Velocities from Measured and Case H Channels VLMX and VLFX, with Original and Reflected Model Data Presented for Each Channel**

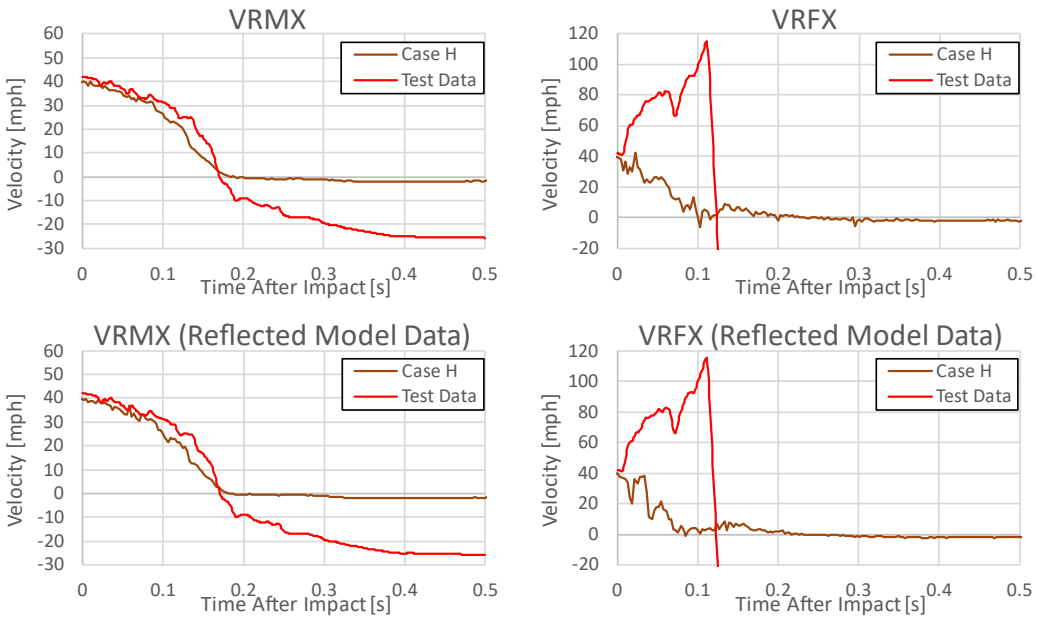


**Figure H 125. Velocities from Measured and Case H Channels VRMX and VRFX, with Original and Reflected Model Data Presented for Each Channel**

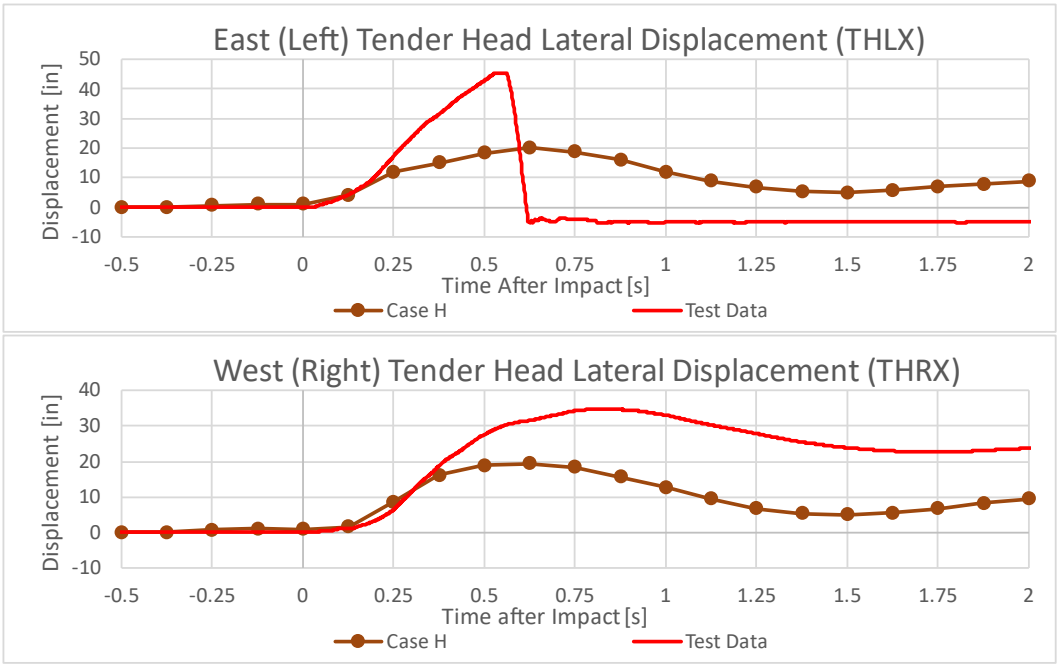


**Figure H 126. Lateral Displacement of the East and West Tender Heads for Case H**

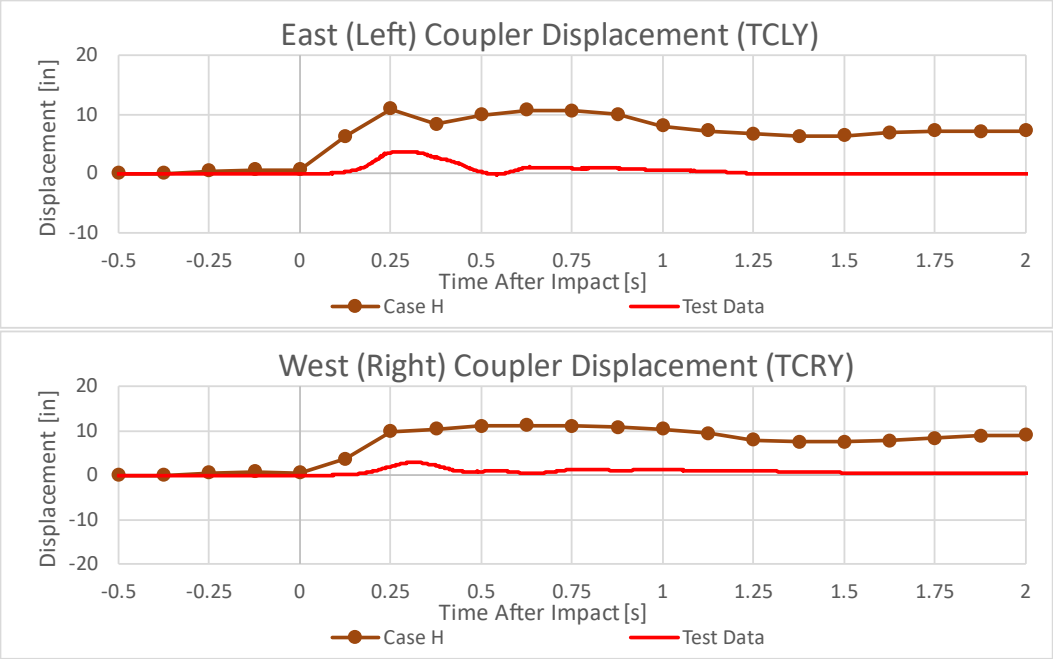


**Figure H 127. Locomotive-to-Tender Coupler Displacements for Case H**

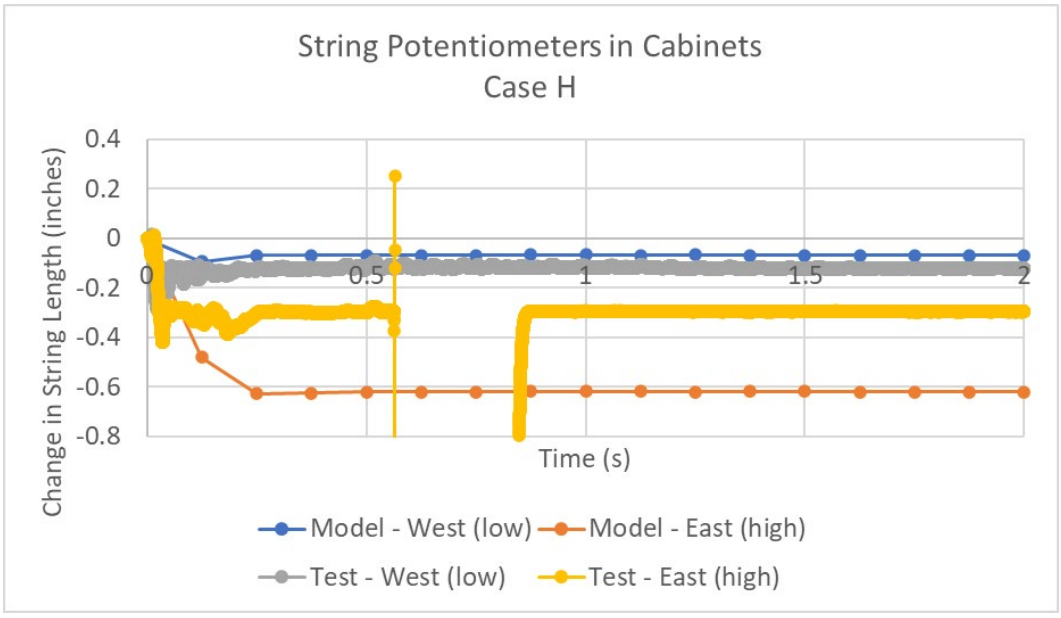


**Figure H 128. String Potentiometers in Piping Cabinet, Case H**

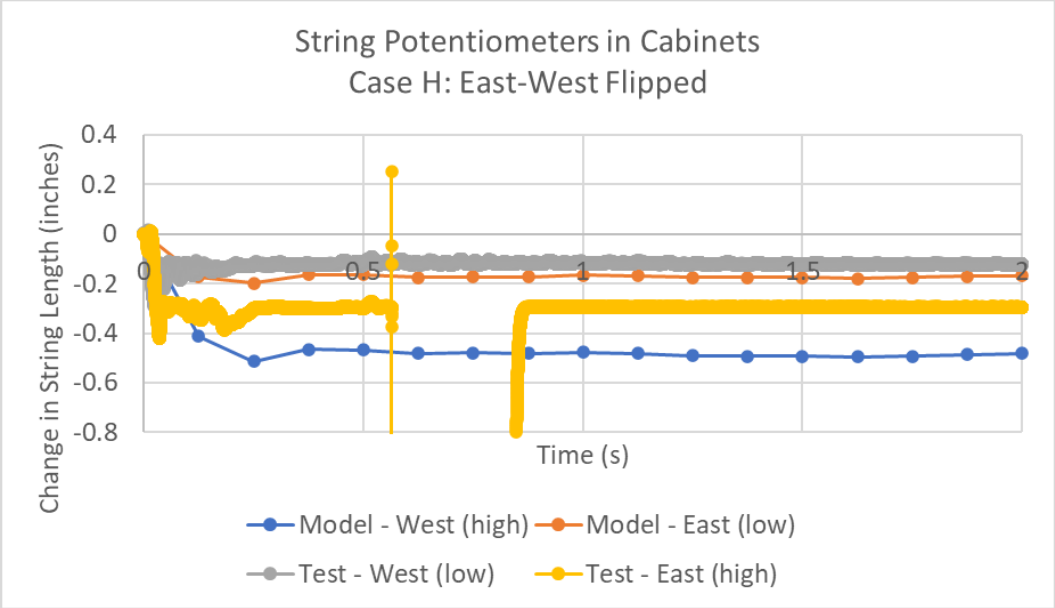


**Figure H 129. String Potentiometers in Piping Cabinet, Case H, East-West Flipped**

### Case I

As the test plans evolved during this project, standard M-1004 continued to evolve, as well. While the standard always stated that the impact between the highway vehicle and the tender was to occur at a highway-rail grade crossing, in 2021 the standard was changed to specify that the highway was to be 48 feet (14.63 m) wide. This change was intended to standardize the increased track stiffness associated with a highway-rail grade crossing. As a means of estimating the upper-bound of lateral track stiffness, the concrete ties spanning 24-feet (7.315 m) to either side of the point of impact were fully constrained using boundary conditions. For the specific fuel tender used in this program, the inboard wheelset of each truck would be on the crossing for an impact aligned with the center of the cabinet. In the baseline model, the ties under the crossing had the same connector behavior as the ties outside this area. The Case I model conditions are summarized in Table H 10. The deformed model is shown in Figure H 128. As a result of this impact, the tender derailed but remained upright. This outcome was similar to the baseline model's outcome.

**Table H 10. Pre-test Case I Model Conditions**

| Case | Tender-to-locomotive Couplers | Bolster Pin and Center Bowl | Rail Base to Concrete Tie | Track Vertical Stiffness | Track Lateral Stiffness | Stub Track Connection | Impact Speed | Initial Pressure | Notes | Outcome |
|---|---|---|---|---|---|---|---|---|---|---|
| I | Yes | Yes | Tied | Default | Default | 48-ft Grade Crossing | 40 mph | 150 psig | Simulate upper limit of grade crossing stiffness | |

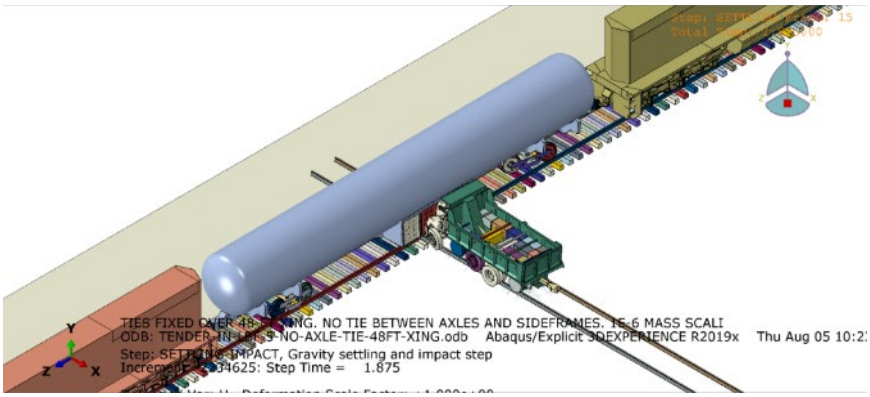


**Figure H 130. Deformed Model, Case I FEA**

Figure H 129 contains a plot of the vertical force on each tie over the course of the simulation. This plot differs slightly from previous plots of vertical tie forces in that the tie forces are shown as two discrete data series. One series shows the total vertical force carried by the ties that are outside of the grade crossing and are therefore modeled using the same techniques as the other simulations in this appendix. A second series has been added to show the vertical load carried by the ties that have had their DOF constrained to represent the grade crossing. At the time of impact (i.e., 0 seconds) the crossing ties are carrying approximately 250,000 pounds (1.1 MN). By the end of the simulated impact the crossing ties are carrying approximately 50,000 pounds (222.4 kN).

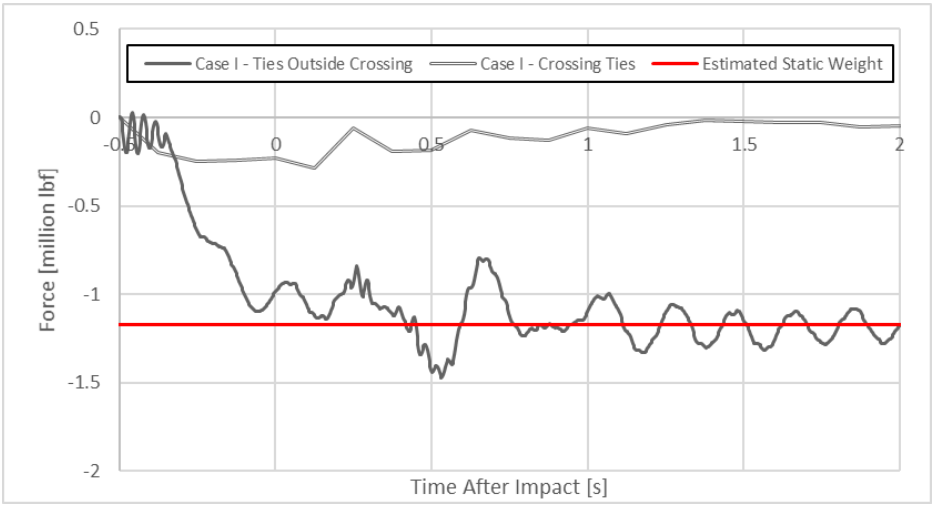


**Figure H 131. Time Response of Total Vertical Force on Ties for Case I**

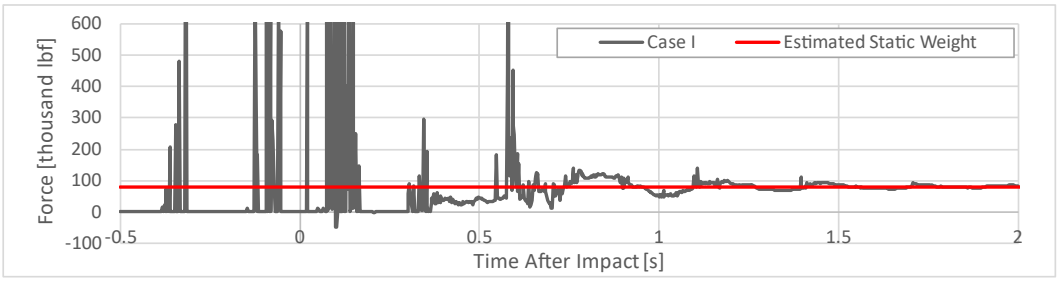


**Figure H 132. Time Response of Total Vertical Force on Rails for Case I**

Figure H 131 presents the vertical load per tie just prior to impact. Figure H 132 contains the same data but flipped east-west. There are abrupt transitions at the limits of the grade crossing on both ends of the tender. The outboard tie of the crossing carries a disproportionate amount of vertical force compared with the other ties. Note that the data in this plot differs slightly from the previous load cases. In general, the tie forces were obtained from the reaction forces in the connector elements between each tie and its grounded end. Since the grade crossing in Case I is represented as a series of ties with boundary conditions on all DOFs, the reaction forces on these ties are requested instead of connector element forces.

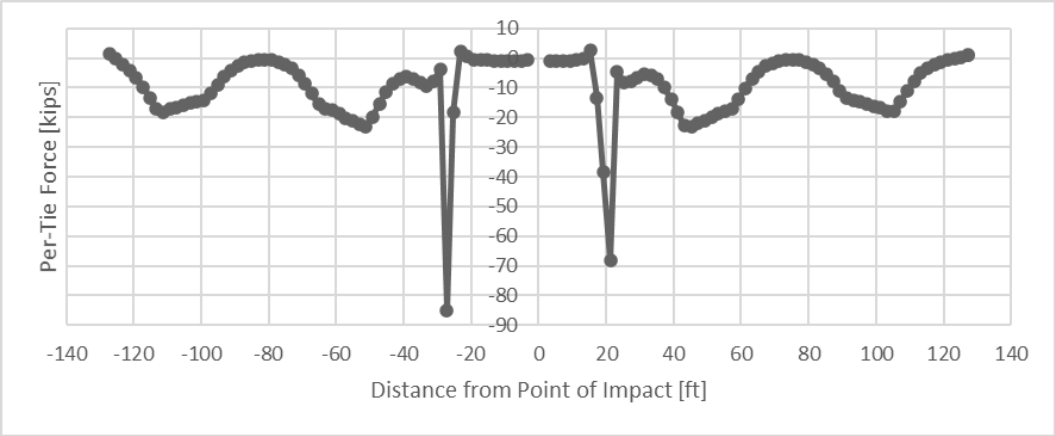


**Figure H 133. Vertical Load Distribution on Ties for Case I**

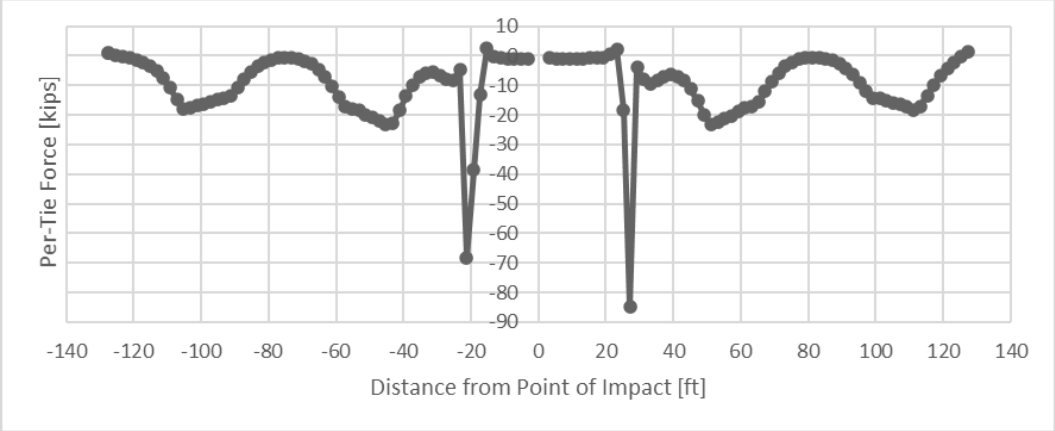


**Figure H 134. Vertical Load Distribution on Ties for Case I: Reflected at Point of Impact**

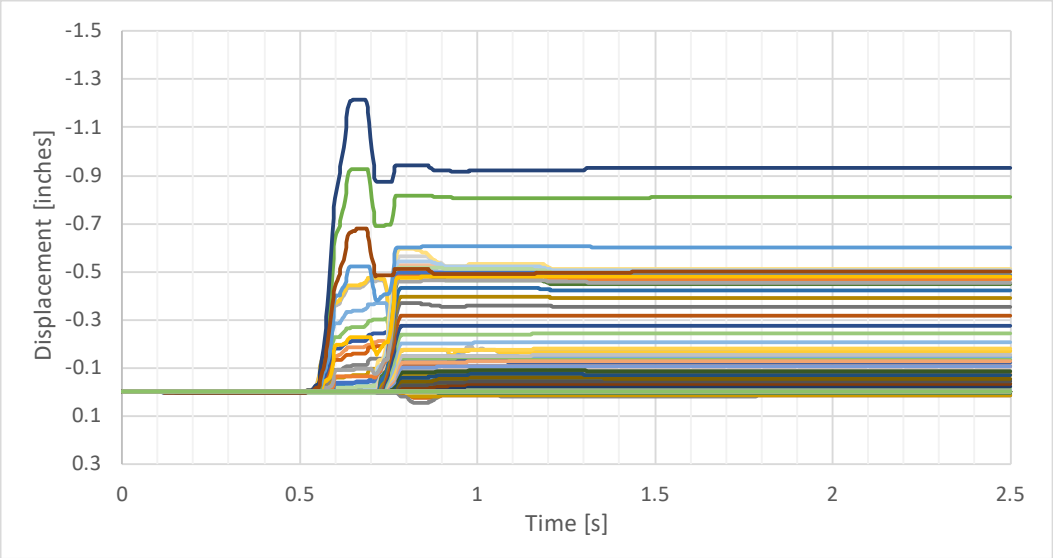


**Figure H 135. Lateral Displacement Over Time of Each Tie for Case I**

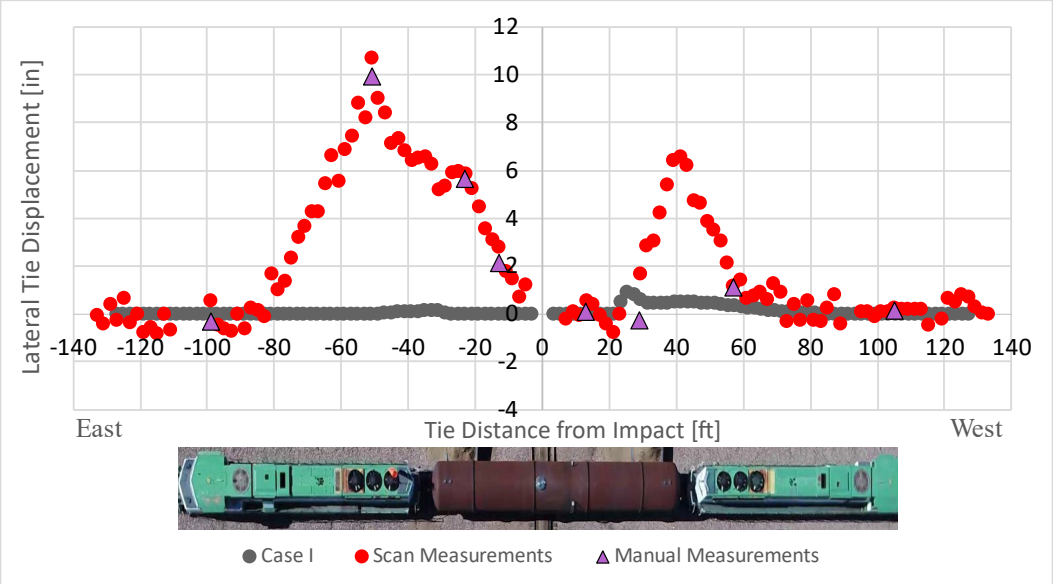


**Figure H 136. Final Lateral Displacement of Each Tie for Case I**

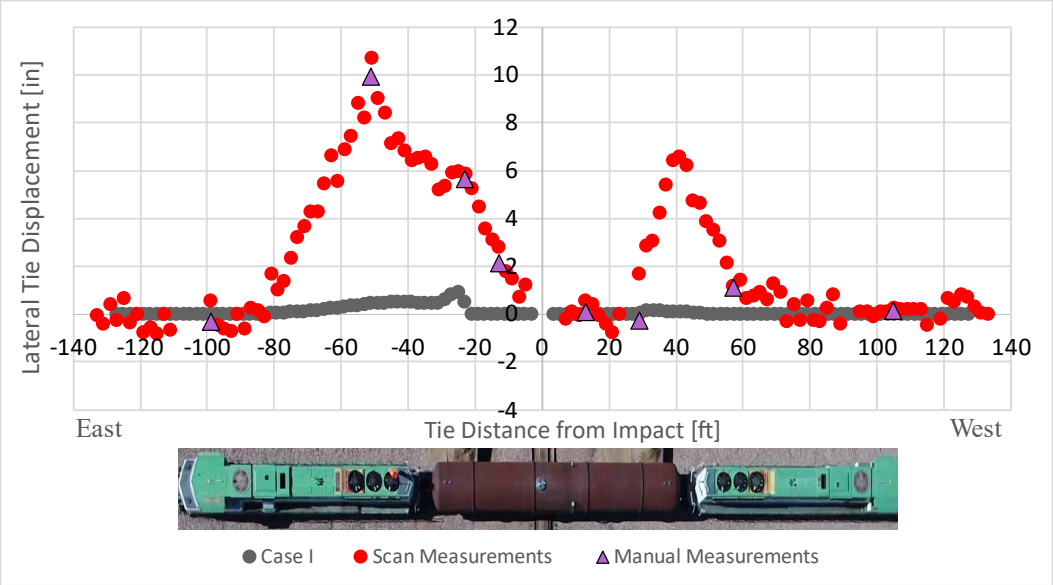


**Figure H 137. Final Lateral Displacement of Each Tie (Final CU1) for Case I: Model Data Reflected at Point of Impact**

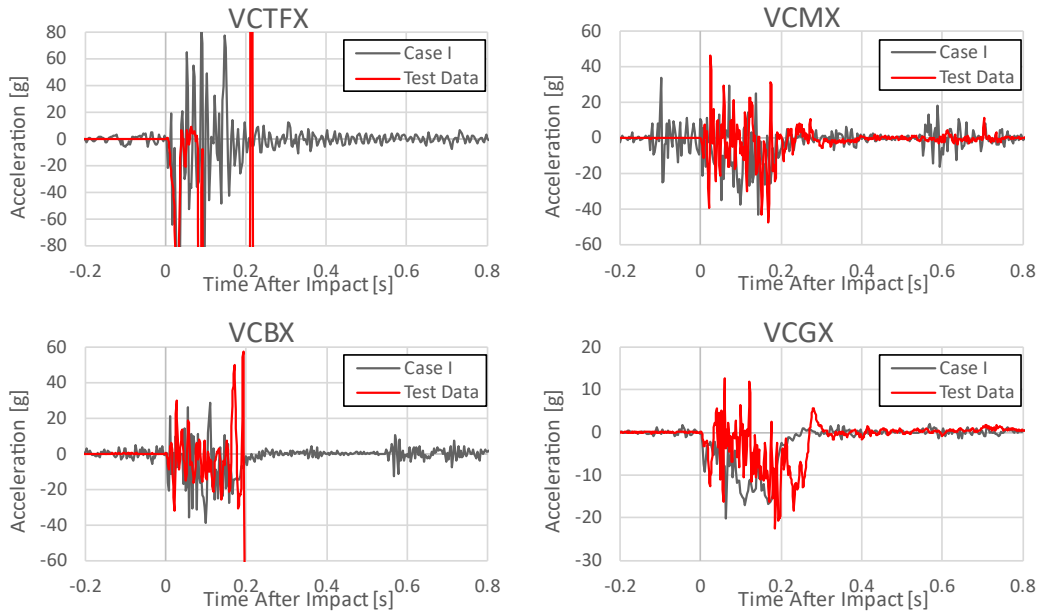


**Figure H 138. Accelerations from Measured and Case I Channels VCTFX, VCMX, VCBX, and VCGX**

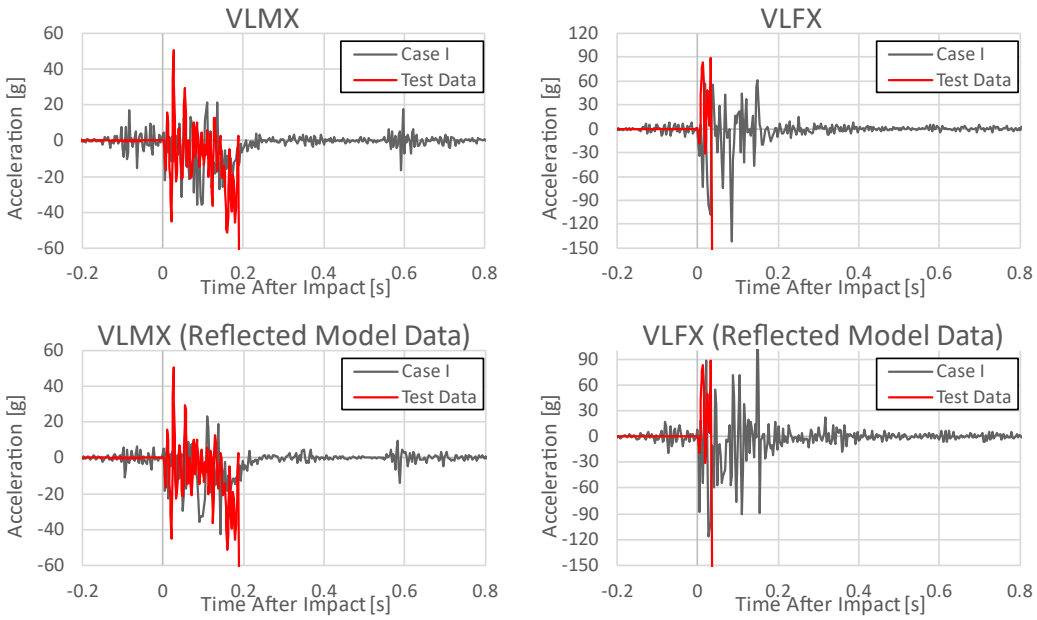


**Figure H 139. Accelerations from Measured and Case I Channels VLMX and VLFX, with Original and Reflected Model Data Presented for Each Channel**

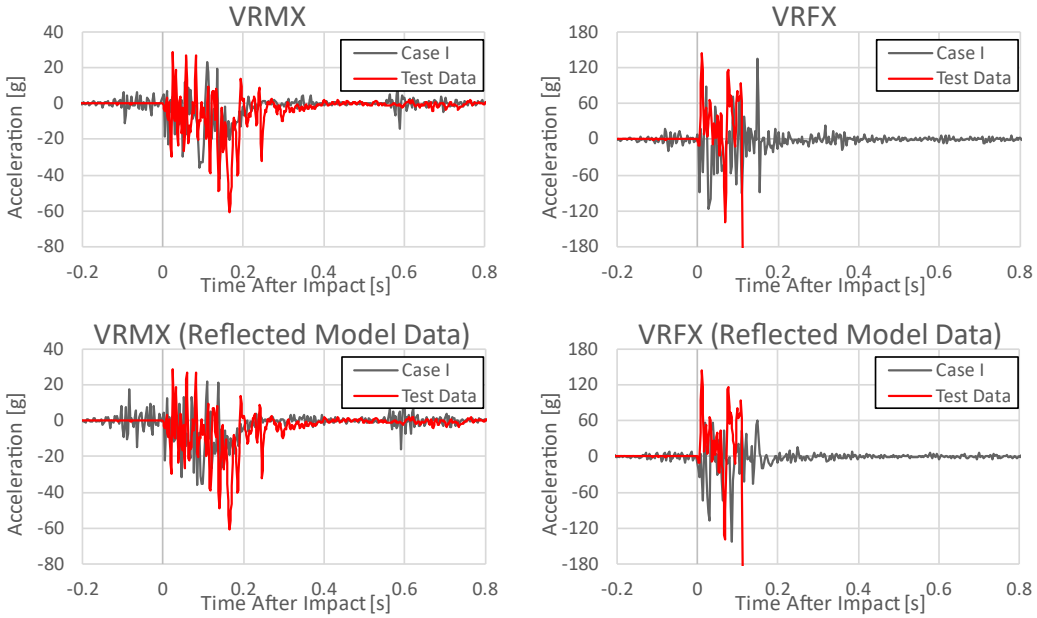


**Figure H 140. Accelerations from Measured and Case I Channels VRMX and VRFX, with Original and Reflected Model Data Presented for Each Channel**

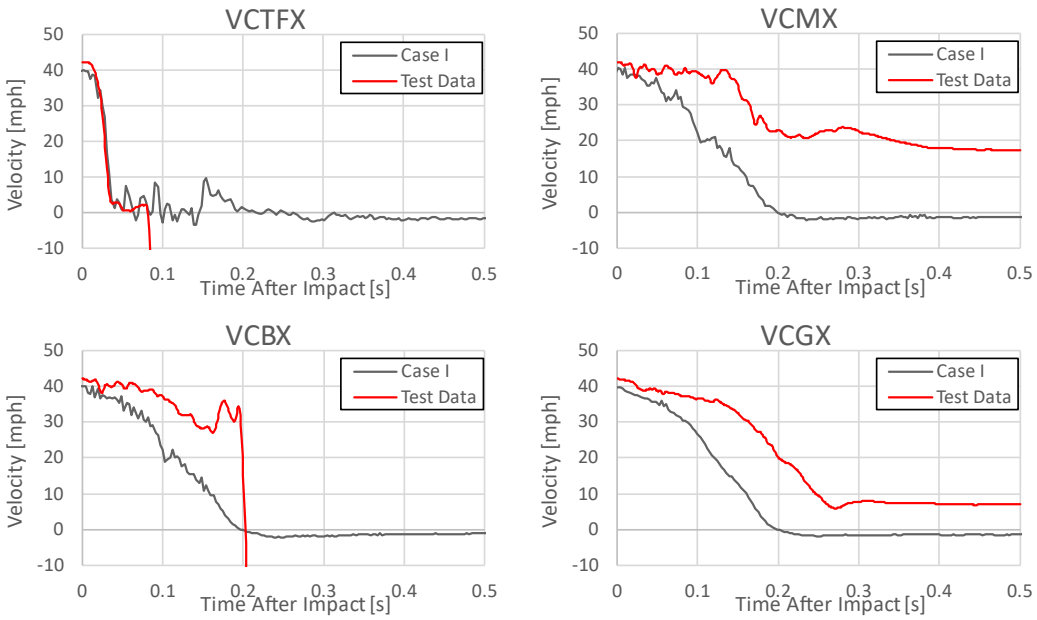


**Figure H 141. Velocities from Measured and Case I Channels VCTFX, VCMX, VCBX, and VCGX**

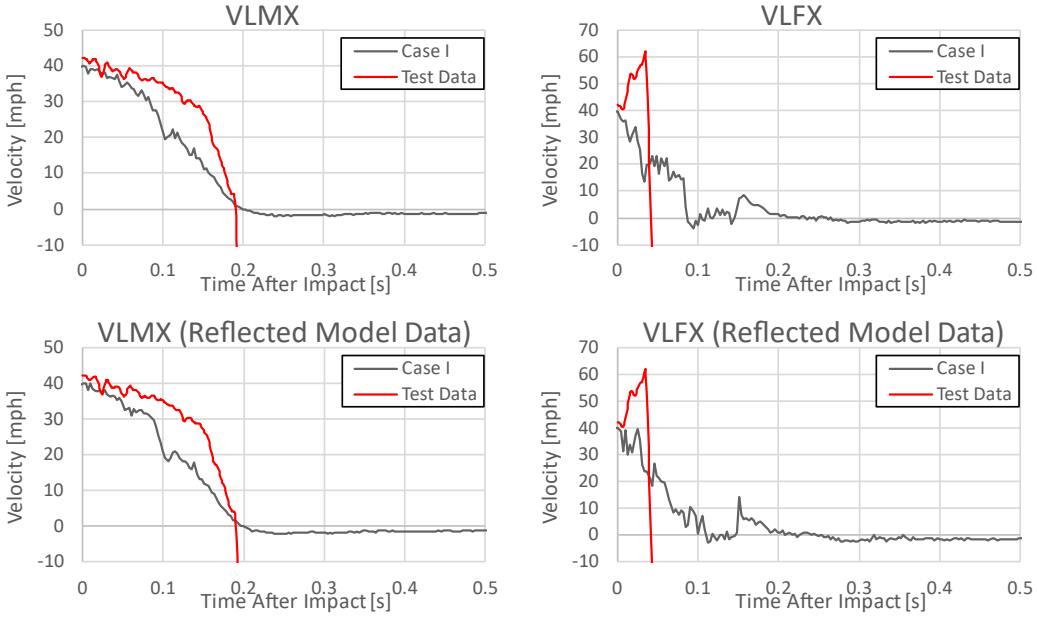


**Figure H 142. Velocities from Measured and Case I Channels VLMX and VLFX, with Original and Reflected Model Data Presented for Each Channel**

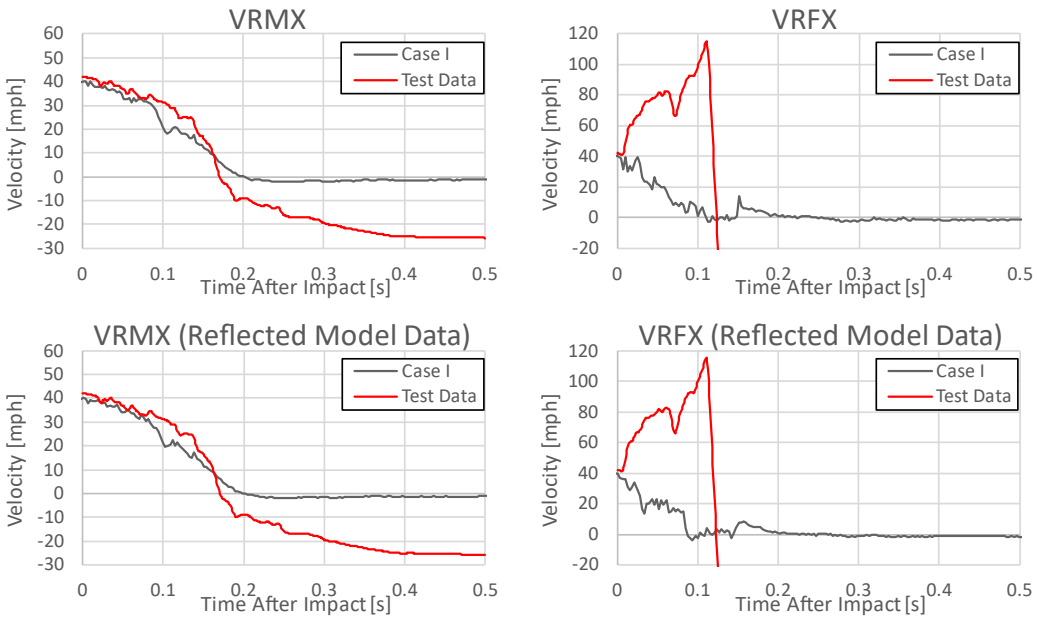


**Figure H 143. Velocities from Measured and Case I Channels VRMX and VRFX, with Original and Reflected Model Data Presented for Each Channel**

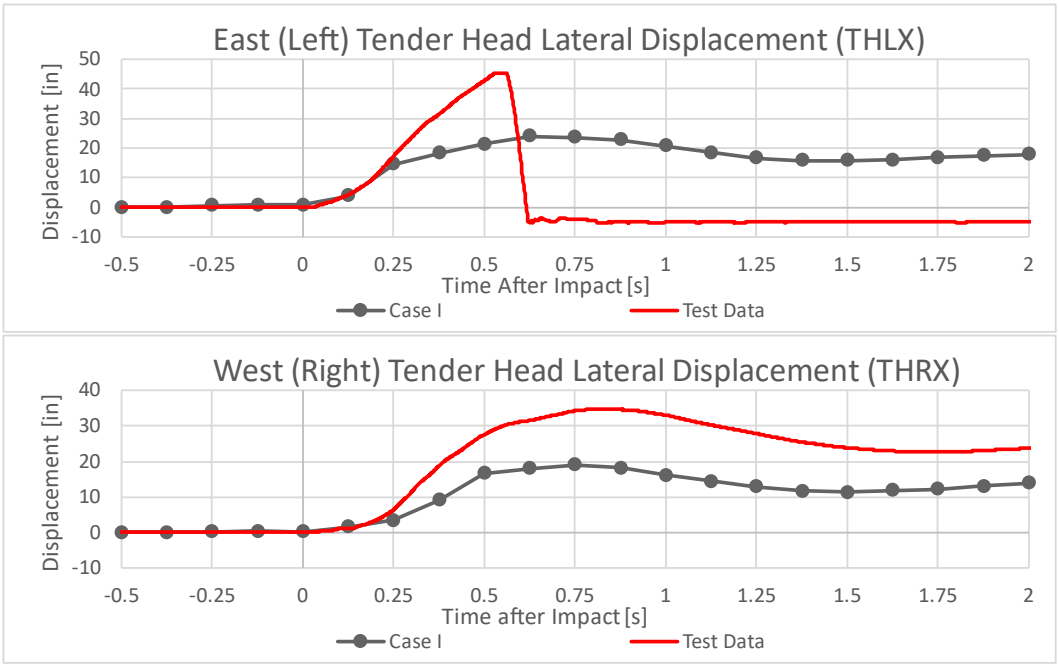


**Figure H 144. Lateral Displacement of the East and West Tender Heads for Case I**

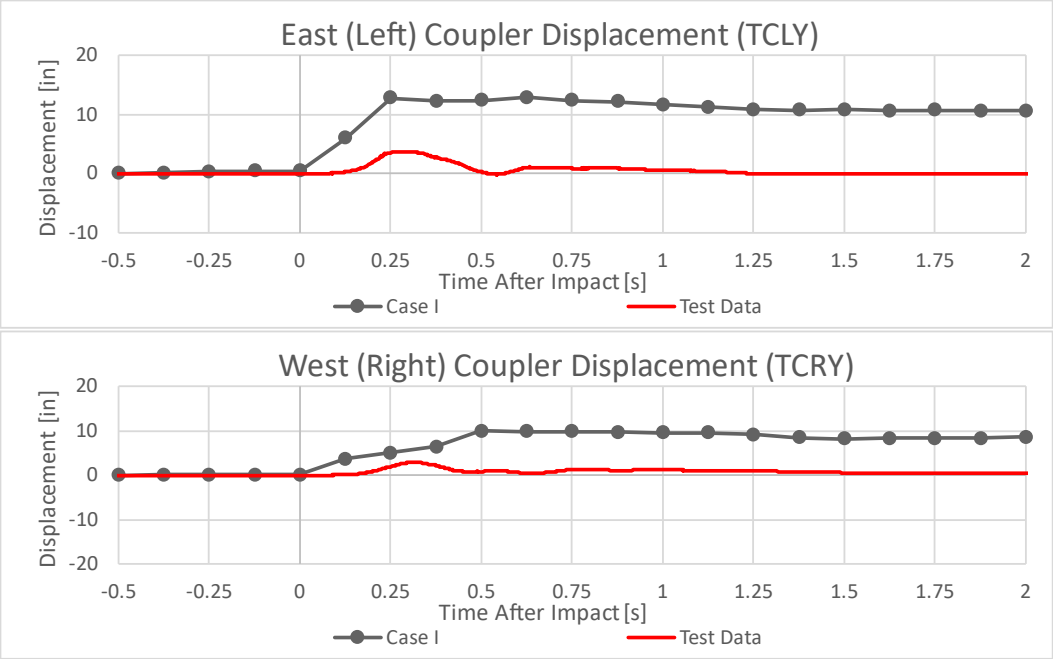


**Figure H 145. Locomotive-to-Tender Coupler Displacements for Case I**

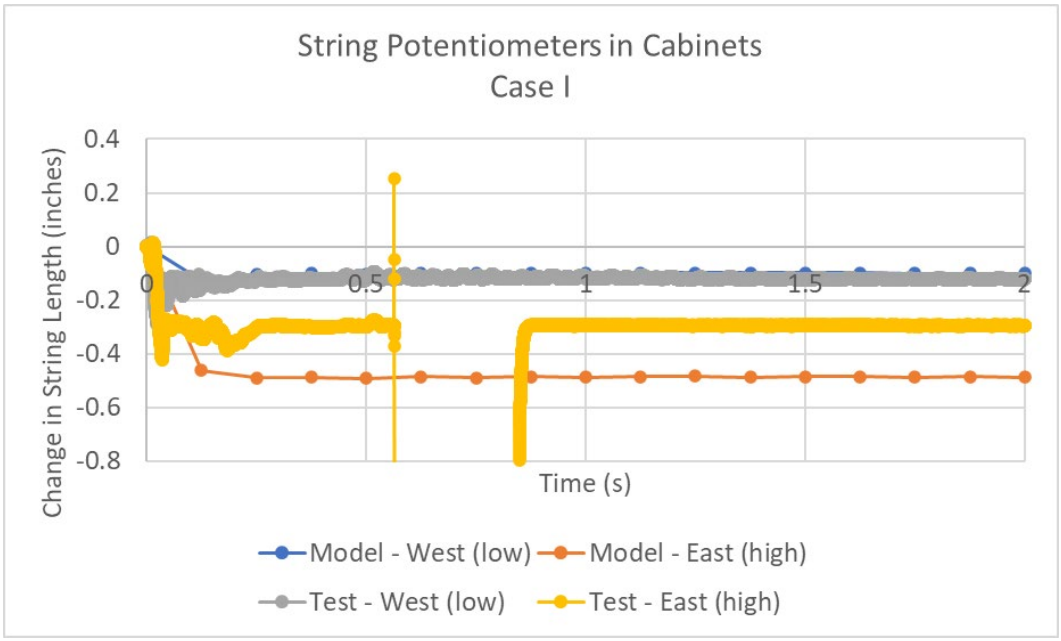


**Figure H 146. String Potentiometers in Piping Cabinet, Case I**

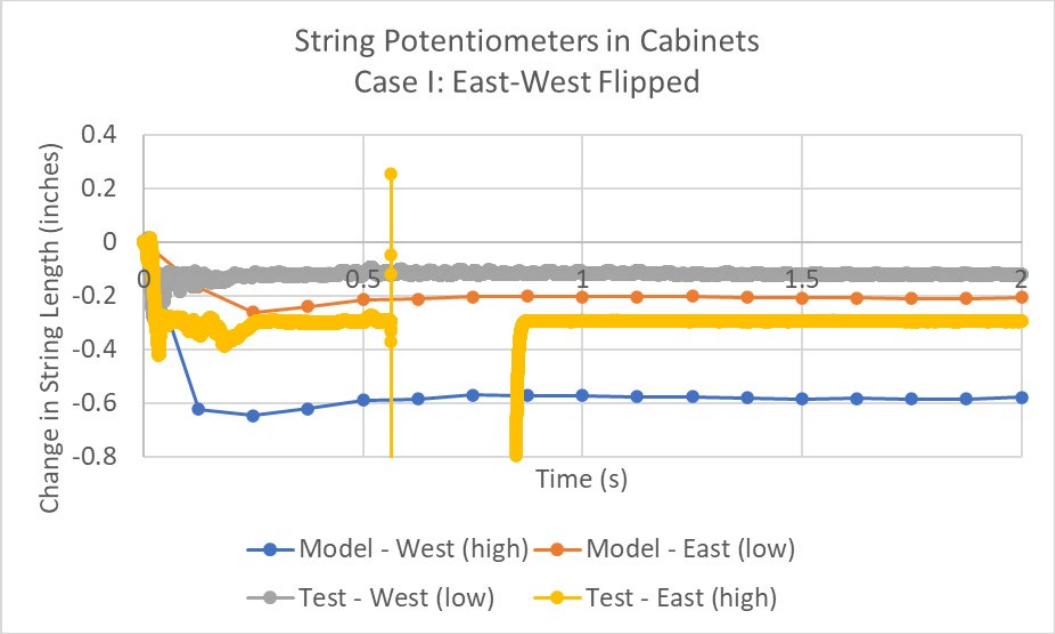


**Figure H 147. String Potentiometers in Piping Cabinet, Case I, East-West Flipped**

### Case J

The M-1004 standard also was revised to update the initial pressure to be used in the simulation. Initially, M-1004 stated that the initial pressure should be 150 psig. In the revision made in 2021, the initial pressure was changed to 25 psig. Case J featured a continuous stub track and an initial pressure of 25 psig. The conditions of the Case J model are summarized in Table H 11. The deformed FE model is shown in Figure H 146. As a result of the impact the tender derailed but remained upright. This outcome is similar to the baseline model.

**Table H 11. Pre-test Case J Model Conditions**

| Case | Tender-to-locomotive Couplers | Bolster Pin and Center Bowl | Rail Base to Concrete Tie | Track Vertical Stiffness | Track Lateral Stiffness | Stub Track Connection | Impact Speed | Initial Pressure | Notes | Outcome |
|---|---|---|---|---|---|---|---|---|---|---|
| J | Yes | Yes | Tied | Default | Default | Continuous Rail | 40 mph | 25 psig | Simulate proposed outage pressure | |

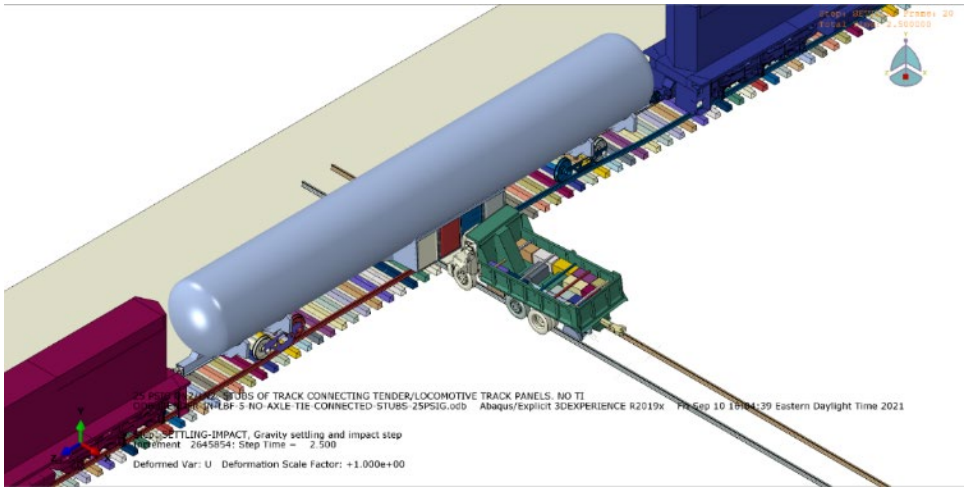


**Figure H 148. Deformed Model, Case J FEA**

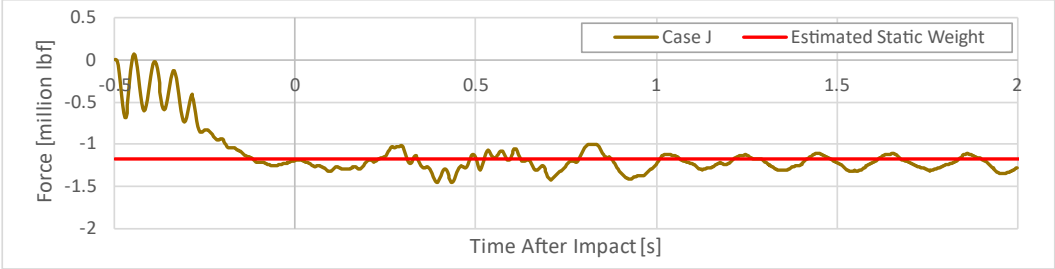


**Figure H 149. Time Response of Total Vertical Force on Ties (Total CTF2) for Case J**

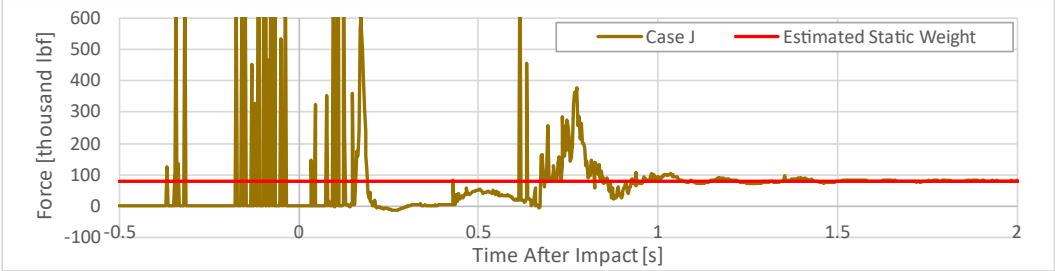


**Figure H 150. Time Response of Total Vertical Force on Rails (Total RF2) for Case J**

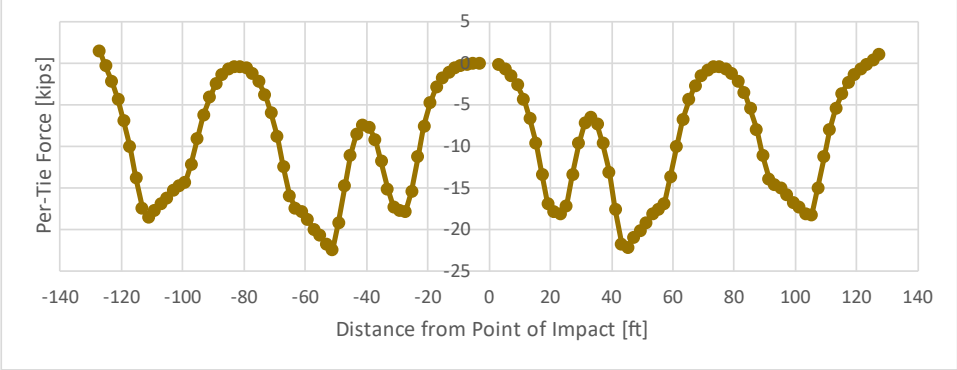


**Figure H 151. Vertical Load Distribution on Ties (CTF2) for Case J**

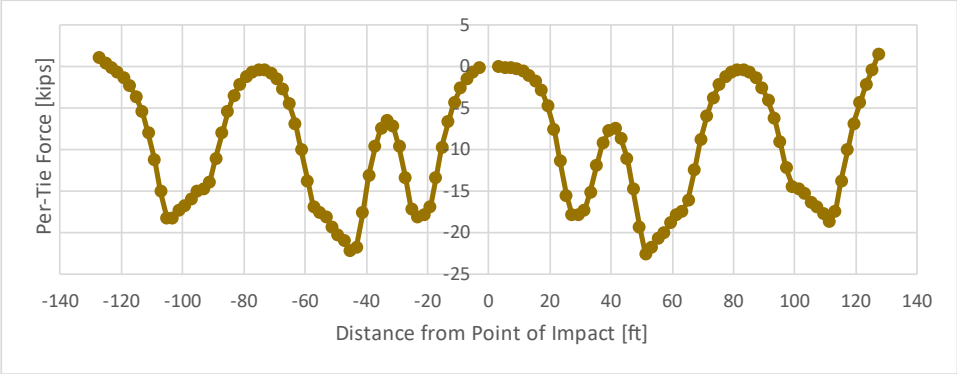


**Figure H 152. Vertical Load Distribution on Ties for Case J: Reflected at Point of Impact**

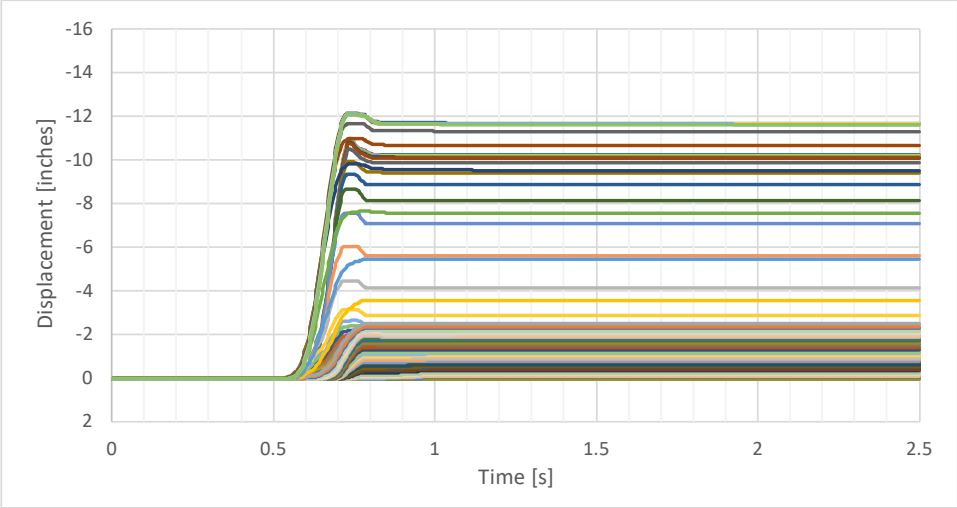


**Figure H 153. Lateral Displacement Over Time of Each Tie for Case J**

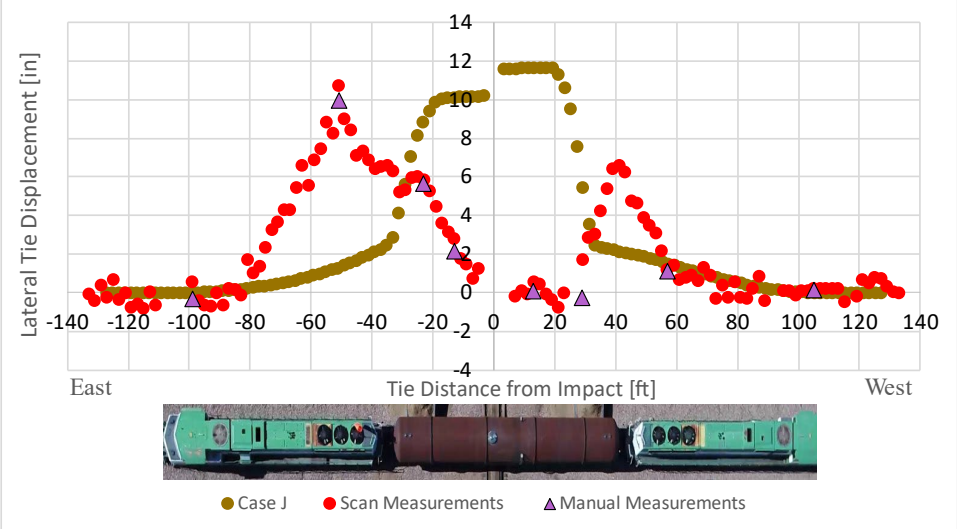


**Figure H 154. Final Lateral Displacement of Each Tie for Case J**

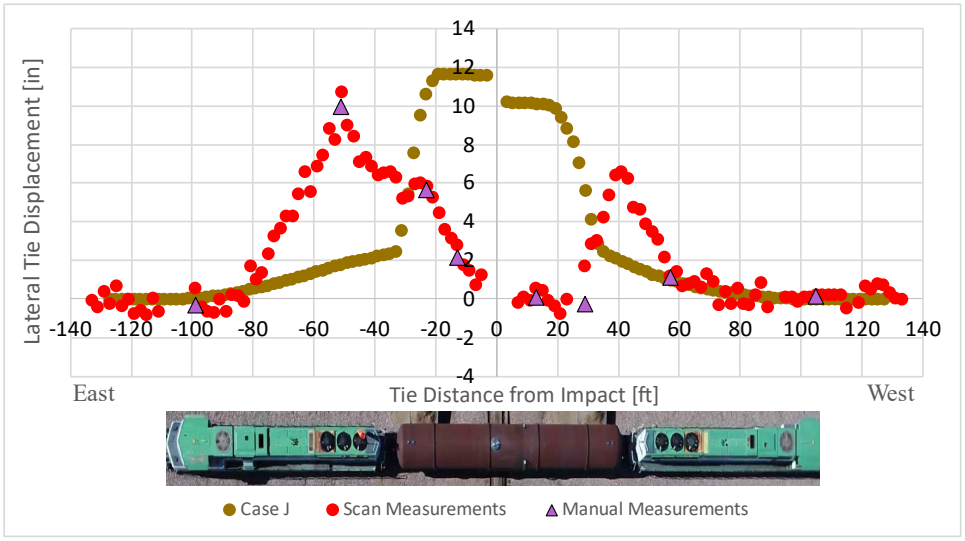


**Figure H 155. Final Lateral Displacement of Each Tie for Case J: Model Data Reflected at Point of Impact**

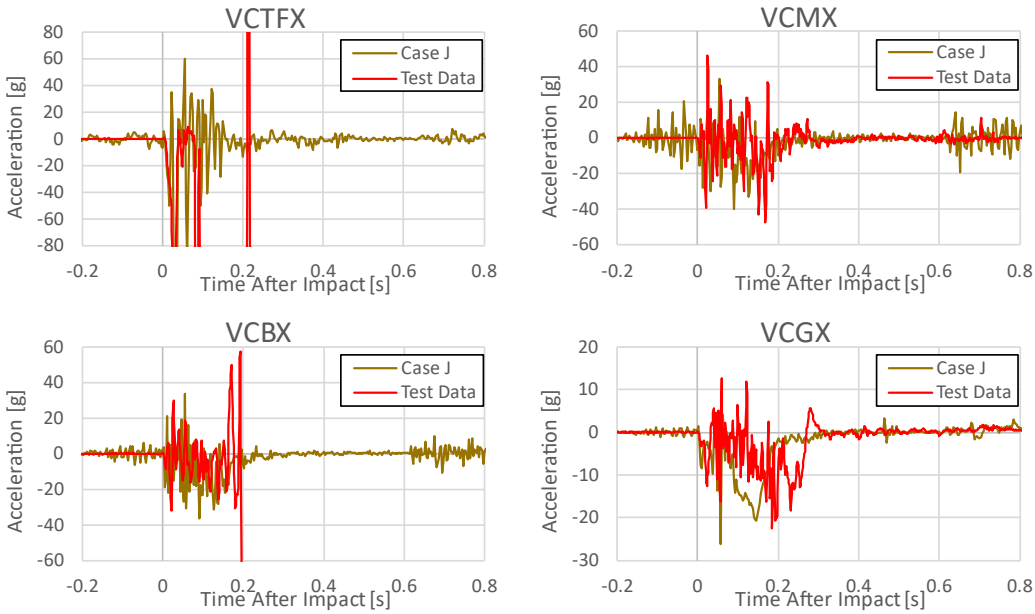


**Figure H 156. Accelerations from Measured and Case J Channels VCTFX, VCMX, VCBX, and VCGX**

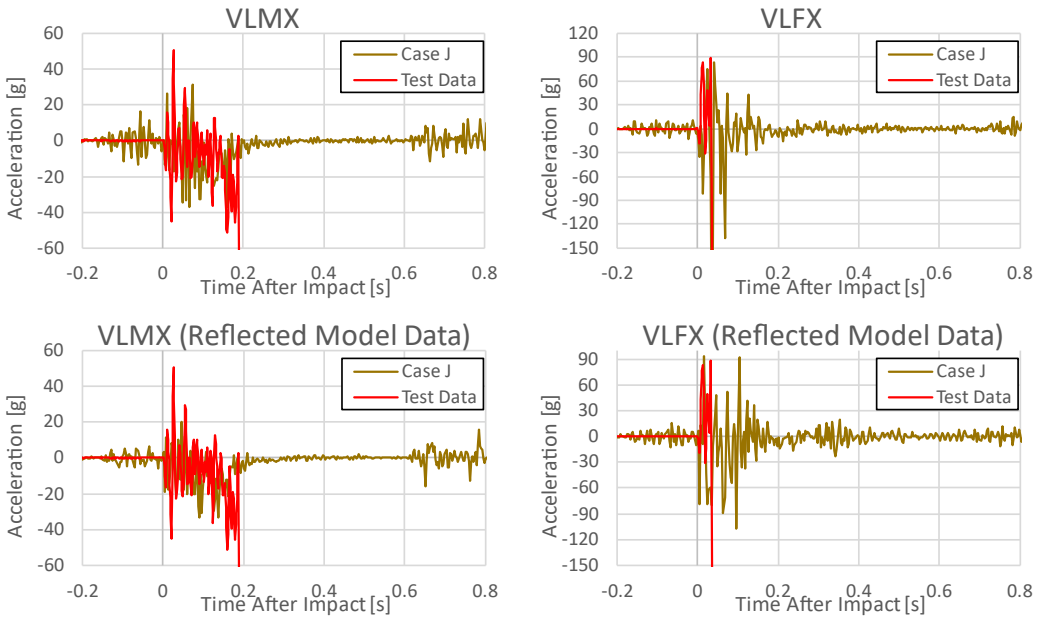


**Figure H 157. Accelerations from Measured and Case J Channels VLMX and VLFX, with Original and Reflected Model Data Presented for Each Channel**

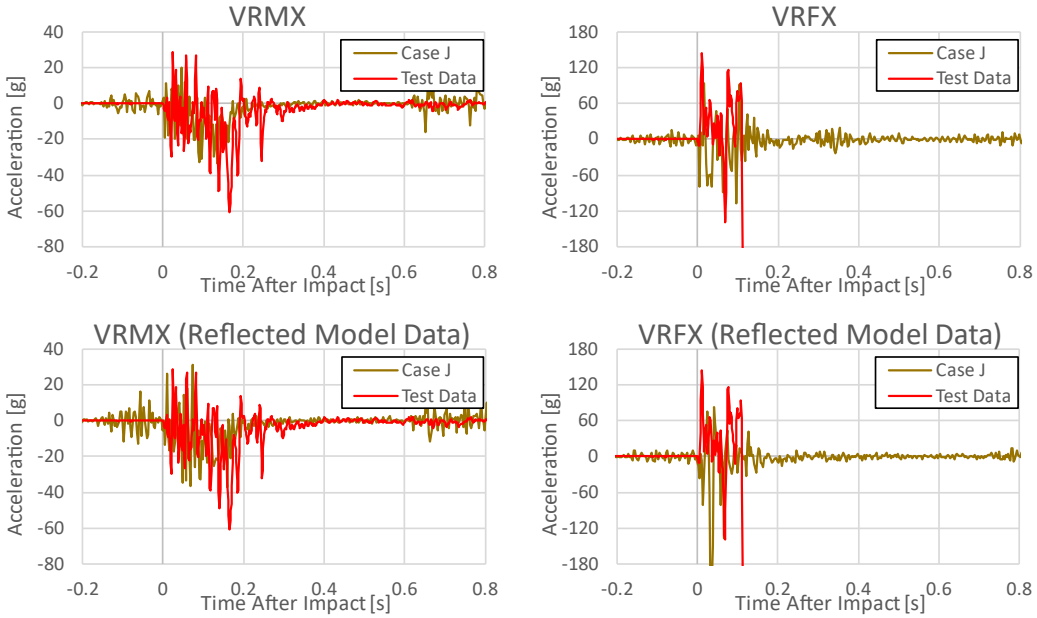


**Figure H 158. Accelerations from Measured and Case J Channels VRMX and VRFX, with Original and Reflected Model Data Presented for Each Channel**

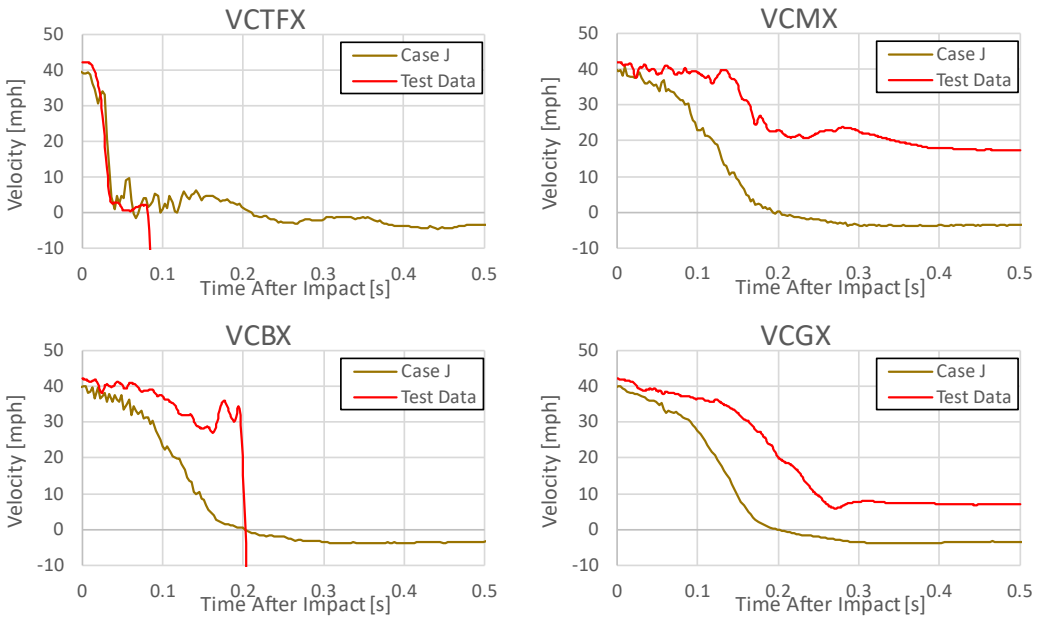


**Figure H 159. Velocities from Measured and Case J Channels VCTFX, VCMX, VCBX, and VCGX**

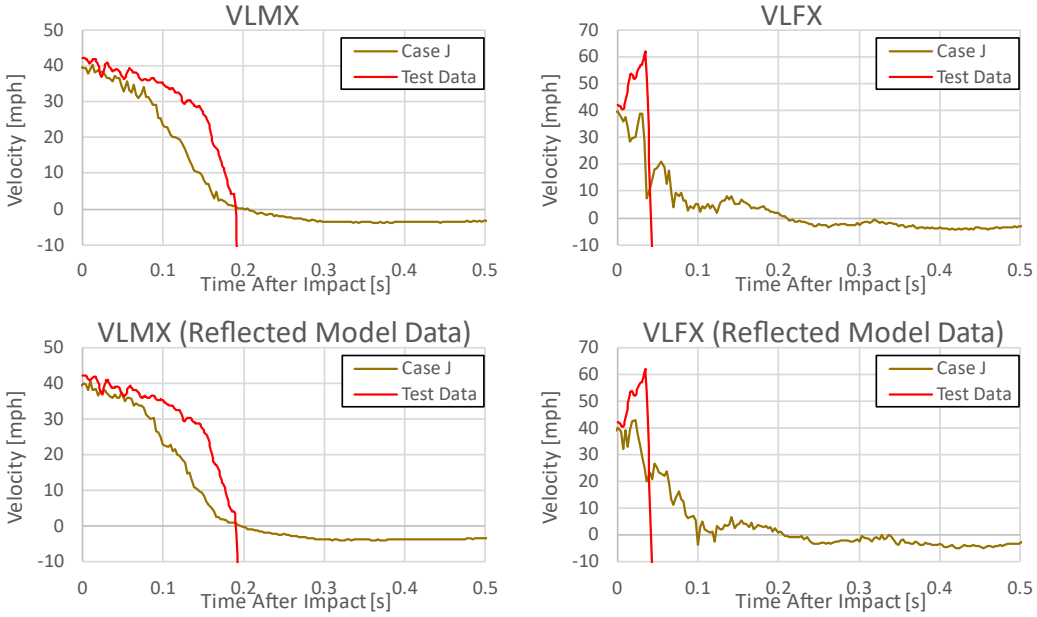


**Figure H 160. Velocities from Measured and Case J Channels VLMX and VLFX, with Original and Reflected Model Data Presented for Each Channel**

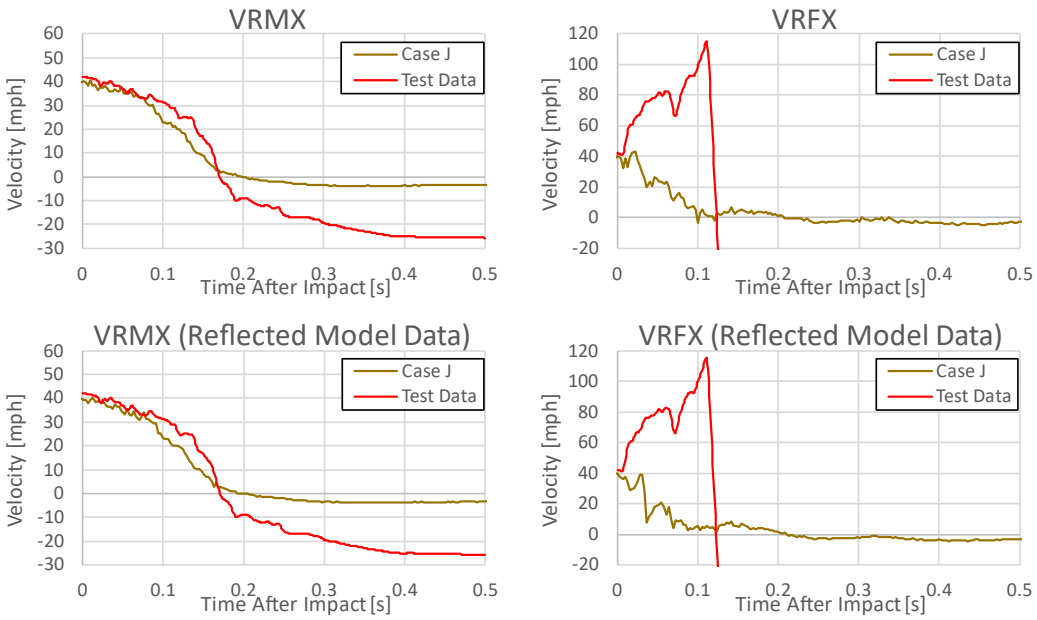


**Figure H 161. Velocities from Measured and Case J Channels VRMX and VRFX, with Original and Reflected Model Data Presented for Each Channel**

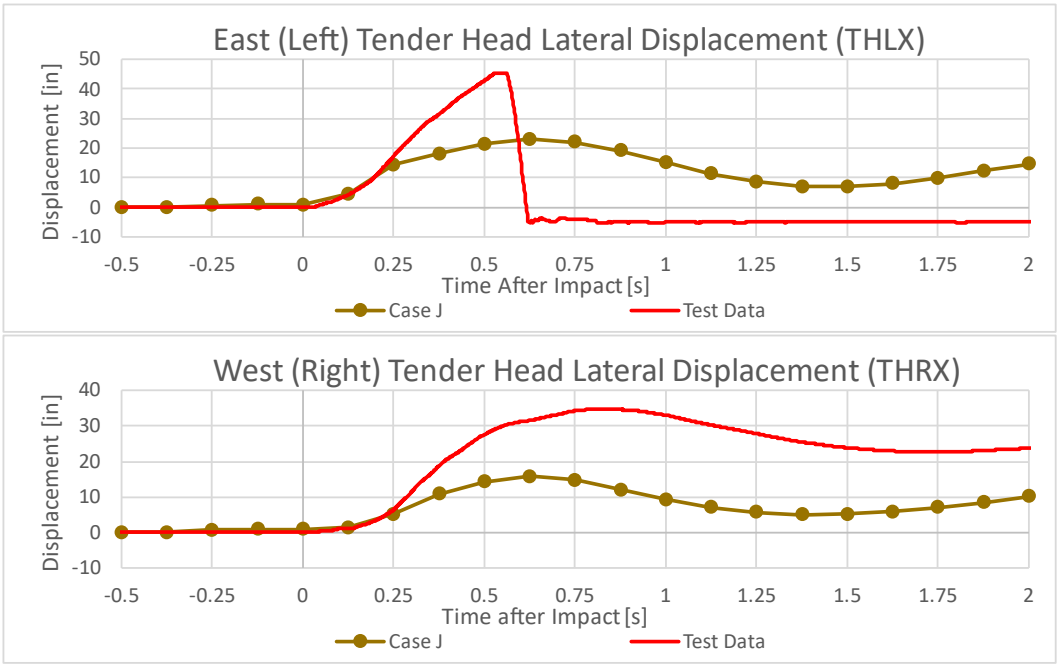


**Figure H 162. Lateral Displacement of the East and West Tender Heads for Case J**

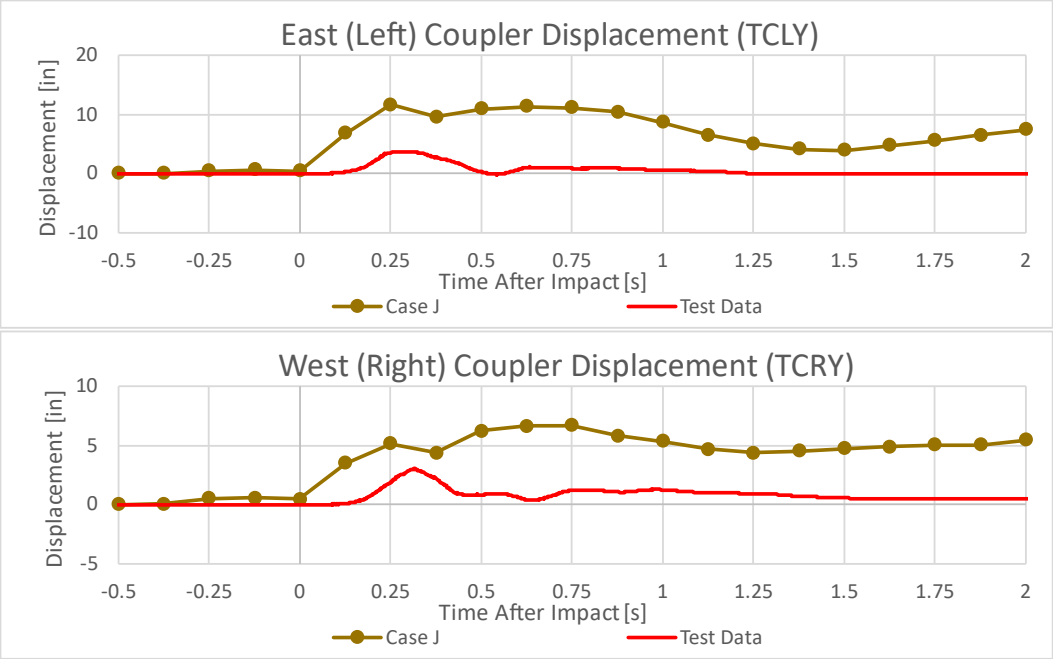


**Figure H 163. Locomotive-to-Tender Coupler Displacements for Case J**

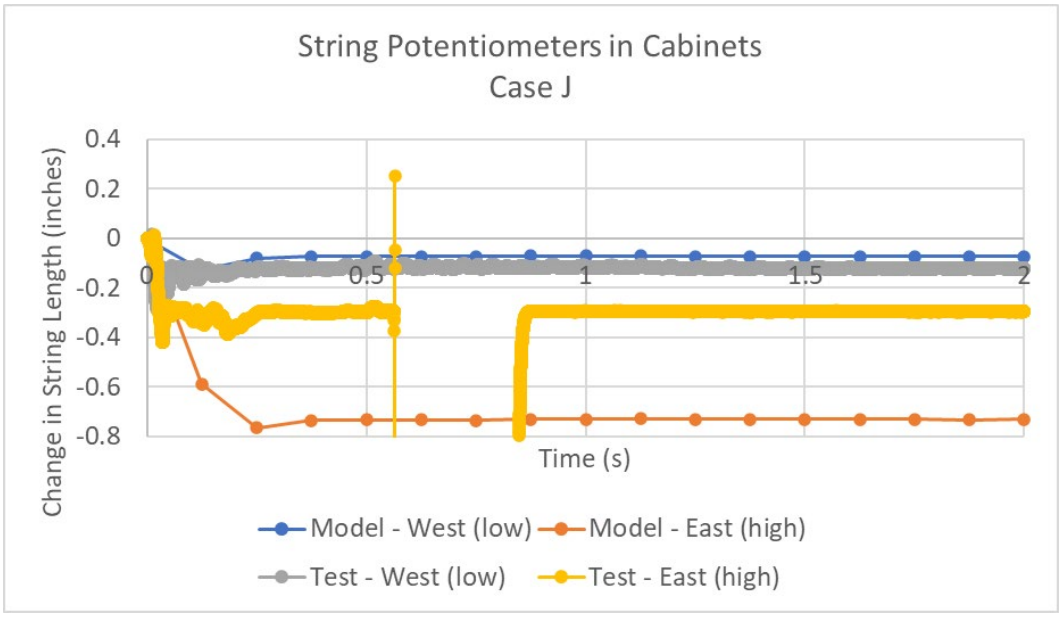


**Figure H 164. String Potentiometers in Piping Cabinet, Case J**

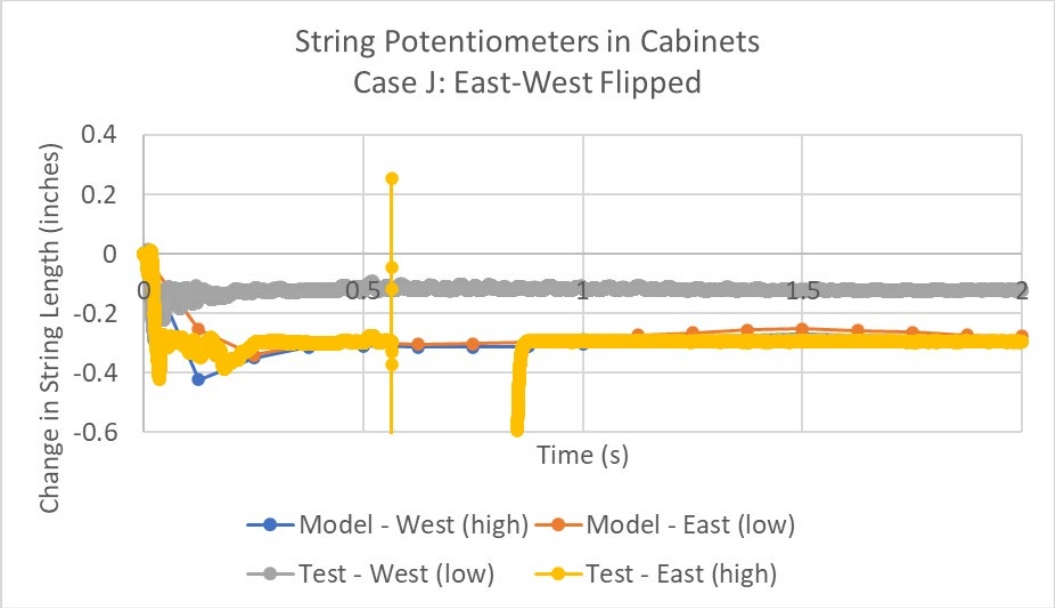


**Figure H 165. String Potentiometers in Piping Cabinet, Case J, East-West Flipped**

## Summary

The team conducted pre-test FE models showing several outcomes that were consistent across all conditions examined. In every case, the tender derailed and the concrete ties shifted. The dump truck experienced substantial damage and was expected to derail. Damage to the tender was focused on the cabinet, without substantial damage to the inner or outer tanks.

In several cases, the models predicted permanent deformation could also occur at the draft sills of the tender or locomotives. These outcomes were associated with cases where the couplers were modeled as intact and not allowed to fail, resulting in large moments and forces being transmitted through the sills. In the cases where the rail was allowed to separate from the ties, the model raised the possibility of the far side cabinet making contact with either the ground or the dump truck guide rails on the far side. Locomotive derailment was also seen in cases where the rail was allowed to separate from the ties.

In general, the model results demonstrated that the test setup was relatively robust, with similar outcomes to the baseline for a 5 mph overspeed, various stub rail connection stiffnesses (e.g., disconnected, continuous rail, 48-foot rigid grade crossing), or completely failed couplers. The models also showed that if two components were assumed to have lower-bound performance, such as the couplers failing and center pin/bowl separating from the center plate in the same simulation, rollover of the tender was a potential outcome. While this outcome is not prohibited by M-1004, it was undesirable in a full-scale test due to the potential for LN2 spillage and more complex post-test cleanup. Based on the pre-test simulations, the test setup included rollover inhibitors designed to allow the tender to begin to roll in response to the impact but prevent it from completely overturning.

# Appendix I.
# Pre-test Lumped Mass Dynamics Model Results

These cases represent the alterations to the lumped mass dynamics model that would be possible during the test. As with the FE model, there are infinite changes that could be made to the model to alter its accuracy relative to the actual test. These cases were developed to include the likely bounds of the test as well as any estimates made for modeling purposes. For example, the target speed of the dump truck for the test was 40 mph (64.4 km/h), but the margin of error was likely ±5 mph (8.05 km/h). The model was therefore run at 35 (56.3) and 45 (72.4) mph (km/h) to assess the results at the speed boundaries. The cases are summarized below in Table I 1.

**Table I 1: Summary of Pre-test Lumped Mass Model Conditions**

| Case | Coupler Cutoff | Coupler Spline | Speed (mph) | Panel Shift (m) | Truck Rollback | Force Location Height | Notes |
|---|---|---|---|---|---|---|---|
| I | 202,500 n-M (149,356 ft-lbs) | Linear stiffness | 40 (64.4 km/h) | 0.3 (11.811 in) | Yes | 1.3462 m (53 in) | Rollover |
| II | none | Linear stiffness | 40 (64.4 km/h) | 0.3 (11.811 in) | Yes | 1.3462 m (53 in) | Rollover |
| III | 1,550,000 n-M (1,143,221 ft-lbs) | Abaqus output | 40 (64.4 km/h) | 0.3 (11.811 in) | Yes | 1.3462 m (53 in) | No rollover |
| IV | 202,500 n-M (149,356 ft-lbs) | Linear stiffness | 45, 35 (72.4, 56.3 km/h) | 0.3 (11.811 in) | Yes | 1.3462 m (53 in) | Rollover |
| V | 202,500 n-M (149,356 ft-lbs) | Linear stiffness | 40 (64.4 km/h) | 0.6 (23.622 in) | Yes | 1.3462 m (53 in) | Rollover |
| VI | 202,500 n-M (149,356 ft-lbs) | Linear stiffness | 40 (64.4 km/h) | 0.3 (11.811 in) | No (friction on) | 1.3462 m (53 in) | Rollover |
| VII | 202,500 n-M (149,356 ft-lbs) | Linear stiffness | 40 (64.4 km/h) | 0.3 (11.811 in) | Yes | 0.8462 m (33.315 in) | No rollover |

The roll angle time history is plotted in Figure I 1. This plot shows the roll angle of Cases III and VII settling back to zero and the angles of all other cases going to an unstable region and the tender car tipping over.

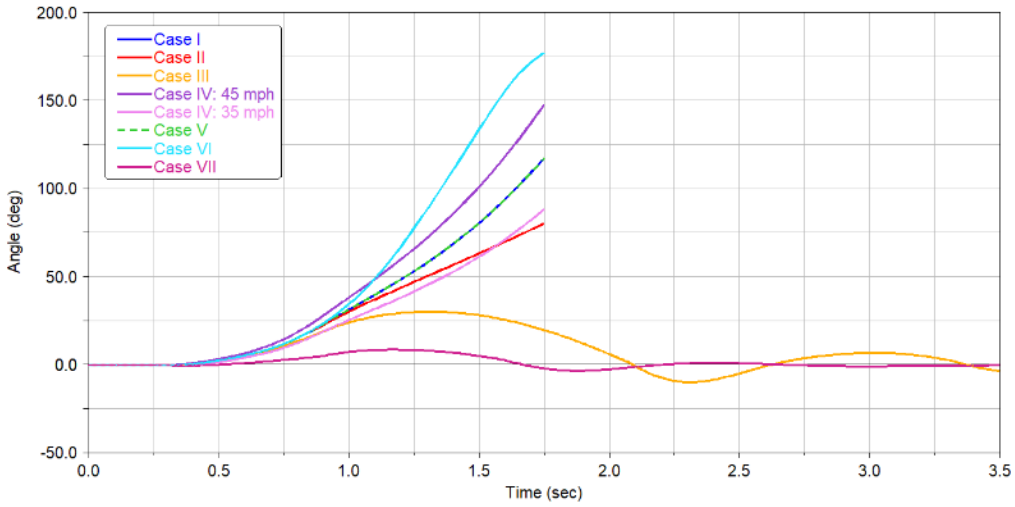


**Figure I 1: Tender roll time history for all cases**

Like the FE model, this model has the dump truck impacting the cabinet on the opposite side compared to the conducted test. Theoretically, this should be inconsequential since the tender car and locomotive bodies are symmetric about the longitudinal axis. This model was also built primarily in SI units, so many if the alterations were made in SI units.

### Case I

This case served as the baseline to assess the impact scenario. The tender car appeared to roll over in this scenario. Variables were altered from this baseline to see how the outcomes were affected.

### Case II

The couplers were a possible failure point during the test, particularly in torsion. The rotational stiffness of the couplers was an estimate, and the cutoff was likely below the actual failure point. This case removed the cutoff altogether and maintained the same rotational stiffness as before. The comparison of the coupler splines is shown in Figure I 2. The couplers in this case could rotate at the same torsional rate as the baseline but would never reach a failure point. Even with the removal of a failure cutoff, the tender car still eventually rolled over as the torsional stiffness was not enough to keep the tender upright.

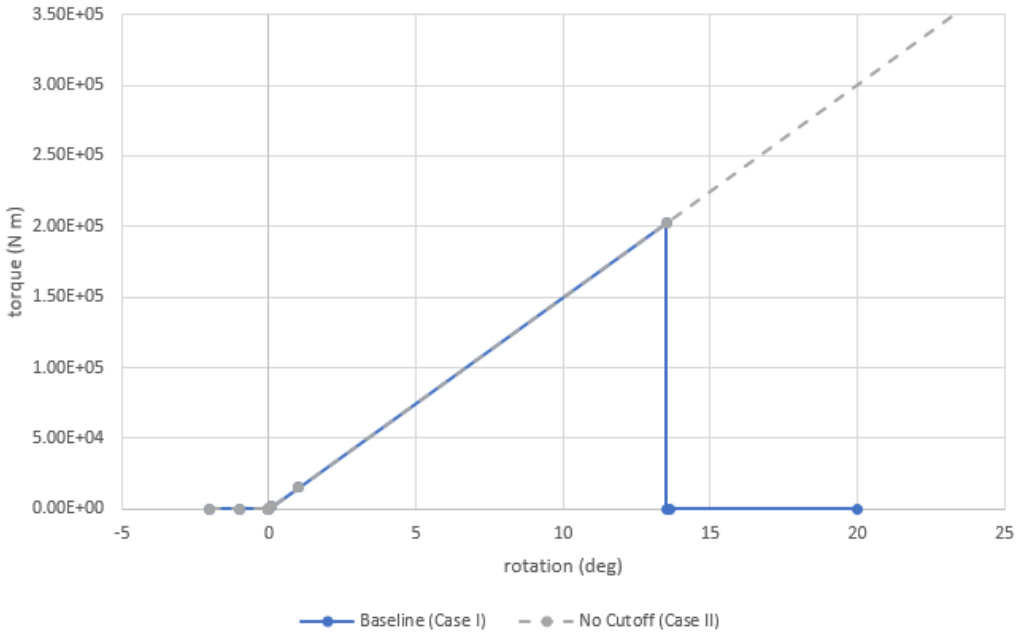


**Figure I 2: Case I and Case II torsional spline comparison**

### Case III

Similar to Case II, this case altered the stiffness of the couplers in torsion. Instead of using a linear stiffness and a cutoff, this case used a spline generated from an intermediate Abaqus simulation of the couplers in the locomotive FE model. The stiffness splines are shown in Figure I 3. The couplers in this case were significantly stiffer and only reached a cutoff at 40 degrees, so the moment created by these couplers was enough to stop the tender from rolling over. Cases II

and III showed that couplers could be a critical component in keeping the tender upright, but without further analysis it was inconclusive whether the couplers would prevent rollover.

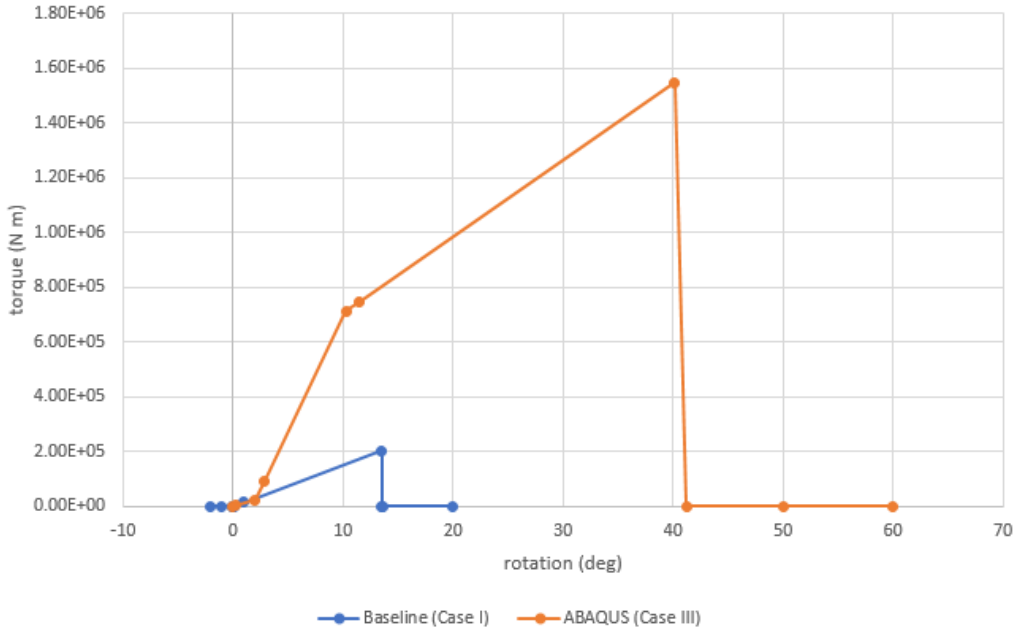


**Figure I 3: Case I and Case III torsional spline comparison**

### Case IV

The target speed in the impact scenario was 40 mph, but that speed was not guaranteed. Test conditions such as wind could influence the actual speed during the test to vary. This case ran the impact scenario at both 35 mph and 45 mph. As expected, the tender rolled over at 45 mph. It also rolled over at 35 mph, but was slower to reach a tipping point. There was likely some speed that would keep the tender model upright, but it would be outside the margin of error for the impact speed on test day.

### Case V

With the high lateral forces applied to the track during the test, some track panel shift was expected. The ADAMS model created to analyze the track and tie behavior showed that the panel shift could vary depending on how the ends of the stubs were constrained and the friction values used. This case extended the allowable range of panel shift from 0.3 m (11.811 in) to 0.6 m (23.622 in), which represented the high end of shift seen in the model. It was possible that more allowable lateral motion could prevent rollover by keeping the carbody's center of gravity between the rail contact points and preventing any "tripping" if the downstream rail stopped too soon. However, the tender car rolled over before it reached the baseline case's hard stop of 0.3 m (11.811 in), so increasing this distance did not prevent rollover.

### Case VI

Post-collision forces could influence outcomes. For the baseline case, the dump truck was allowed to roll back. Case VI applied a "braking" force to the truck, preventing rollback, and continued to apply the force from the force-crush spline where it stopped on the curve. The

reality of the test would likely fall between this and the baseline case. The dump truck would not completely and linearly back off from the tender car as in Case I, but would likely still apply some level of contact force to the tender car once it reached full crush. As expected, the tender car rolled over in this case with the help of the additional force.

**Case VII**

It was unclear where the force between the dump truck would be concentrated. While the force-crush spring was placed in the center of the dump truck's grille and the center of the cabinet, this was a simplification and would not represent all the points of contact between the truck and the cabinet during the test. This case moved the spring vertically downward by 0.5 m (19.685 in), so it was more in line with the truck's front bumper. In this case the moment generated from the dump truck's impact force was not enough to roll the tender car over with this now-shorter lever arm. However, while the front bumper would contact the cabinet first, this would likely not be the resultant force location of all the contact forces during the collision. This case showed that impact location could be an important consideration for rollover, but also would be an unknown quantity. Since the impact would happen over a wide area, there was no guarantee the resultant force would be below the threshold for rollover.

# Appendix J.
# Data Processing Details for Tie Displacement

## Point Cloud Background

As a part of the grade crossing collision test of the LNG fuel tender, point cloud scans were obtained using drones both before and after the test. However, the coordinate systems of the pre-test and post-test scans differ between both each other and the coordinate system of the Abaqus model created for this test. Though the positions and orientation of fixed objects in both tests differ, they have the same scale as each other and the model. In order to compare data between the test and models, a series of transformations was performed on the point cloud data to align the pre-test and post-test point cloud coordinate systems with the test data coordinate system.

Before performing transformations, the coordinates of the markers located on the 1st and 134th ties as well as the southwest corner of a fixed power transformer were obtained from the pre-test and post-test scans, as well as two points from the top of each rail. These points, being remote from the point of impact, were assumed to remain fixed between the pre- and post-test scans and could be used to transform the pre- and post-test point cloud data into a common coordinate system.

## Point Cloud Transformation Steps

**Step 1**. All post-test coordinates for tie markers were translated using the vector from the post-test tie #1 marker to the pre-test tie #1 marker. This aligned the tie #1 marker to a common coordinate in both the pre- and post-test scans. See Figure J 1.

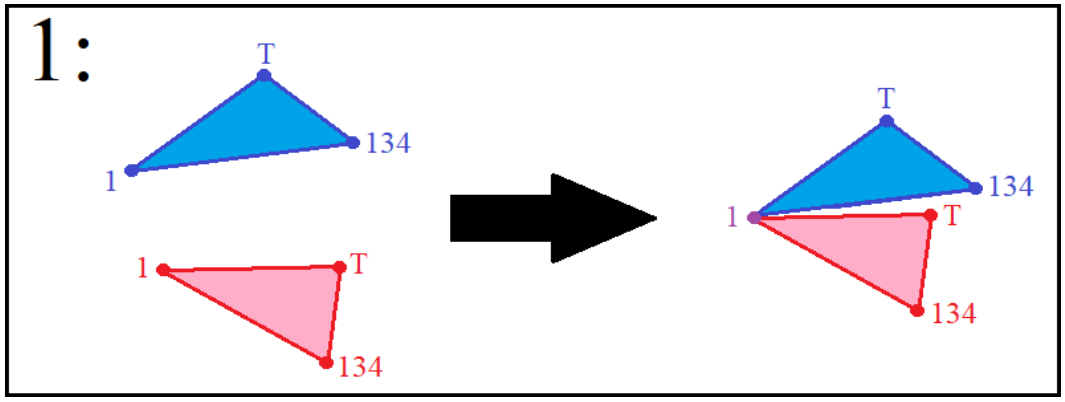


**Figure J 1. Schematic First Translation of Post-test Tie Marker to pre-test**

**Step 2**. A transformation matrix was obtained that rotates the post-test southwest transformer corner and 134th tie marker onto their pre-test analogues. This transformation matrix was applied to the coordinates of each post-test tie marker. After this step, the coordinates for the markers located on the 1st and 134th ties, as well as the southwest corner of the transformer are the same for the pre-test and post-test data. See Figure J 2.

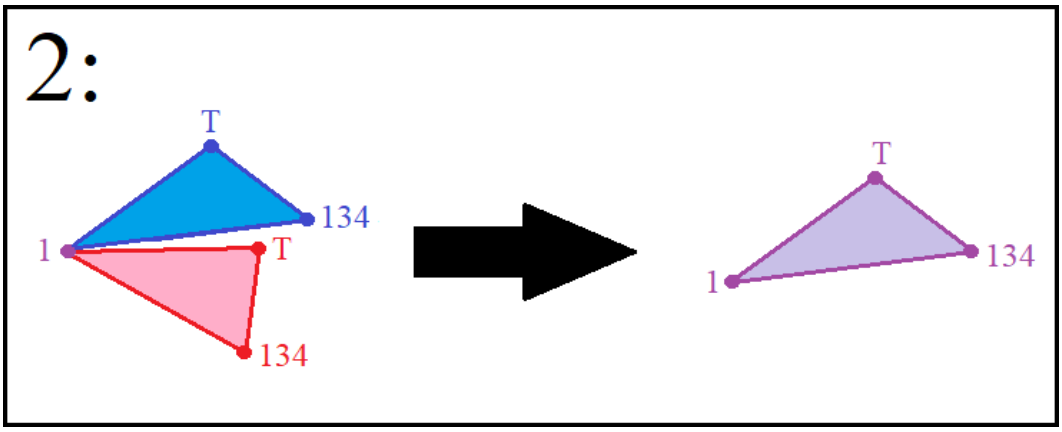


**Figure J 2. Schematic of Translation Matrix from Post-test Position to Pre-test Position**

**Step 3**. The angle from the XY component to the Y component of the vector from ties 1 to 134 was obtained. All data were rotated by this angle about the Z axis such that the XY and Y components of the tie 1 to tie 134 vectors were the same. See Figure J 3.

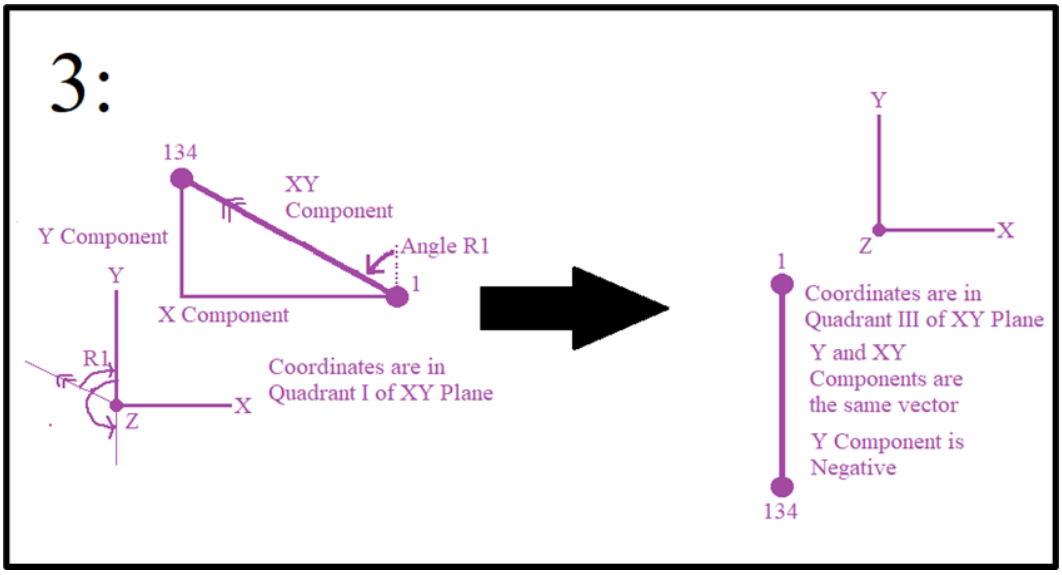


**Figure J 3. Schematic of Rotational Transposition**

**Step 4**. The angle from the YZ component to the Y component of the vector from ties 1 to 134 was obtained. All data was rotated at this angle, plus an additional 90 degrees, about the X axis such that the XY, YZ, and Y components of the tie 1 to tie 134 vectors were the same.

**Step 5**. The angle from the Z component to the X component of the vector between the two top-of-rail markers was obtained. All data was rotated at this angle about the Y axis such that the X and XZ components were the same in the vector between the top of each rail in the pre-test scan.

# Appendix K.
# Detailed Dump Truck Model Development

## Base Truck

The National Transportation Research Center, Inc. (NTRCI) directed the creation of semitrailer truck FE models through a collaboration of Battelle Memorial Institute (BMI), Oak Ridge National Laboratory (ORNL), and the University of Tennessee at Knoxville (UTK). The project was funded under a grant from the U.S. Department of Transportation (DOT) to (1) better understand the crash performance of guardrails and barriers, (2) improve their design, and (3) reduce the likelihood of vehicle-infrastructure crash fatalities and injuries [32].

The research team (NTCRI, CMI, ORNL, and UTK) conducted a three-phase investigation to enhance and refine a FE model of a semitrailer truck (designated as "tractor_V01b") which was originally developed by the National Crash Analysis Center (NCAC) of George Washington University [32].

*Phase A: Conduct an in-depth evaluation of the NCAC tractor only FE model, implement selected modifications, and develop a new trailer model* [33].

*Phase B: Complete preliminary modification of combined tractor-semitrailer FE models, provide them to the FHWA Center of Excellence (COE) community for beta testing, and validate them against suitable full-scale crash tests* [34].

*Phase C: Refine the combined tractor-semitrailer FE models and develop an interactive, online FE model user's website and a User's Manual document to facilitate the use of the model* [35, 36].

Figure K 1 shows the FE model of the publicly available semi-tractor with a sleeper cab and 241-inch wheelbase (designated as "Tractor_Sleeper_v100308") [32] hosted by ORNL in LS-DYNA [37] format. This FE model was modified from NCAC's original tractor FE model (tractor_V01b) to validate it against NCAC's full-scale tractor crash test (No. 03008). This FE model was used as a basis to represent the dump truck from the LNG fuel tender grade crossing test because it had the correct wheelbase (241 inches, 6.121 m) and a similar design to the dump truck. The semi-tractor model with a sleeper cab features approximately 71,000 deformable elements and weighs approximately 17,100 lbs.

**Figure K 1. Semitrailer Truck with Sleeper Cab and 241-inch Wheelbase**

Because the dump truck featured a day cab, another publicly available semi-tractor model with a day cab and 181-inch wheelbase (designated as "Tractor_DayCab_181in") [32] was used to replace the sleeper cab shown above. The day cab from the 181-inch model was chosen over the 194-inch version because it did not feature a smokestack. Figure K 2 shows the semi-tractor model with a day cab and 181-inch wheelbase.

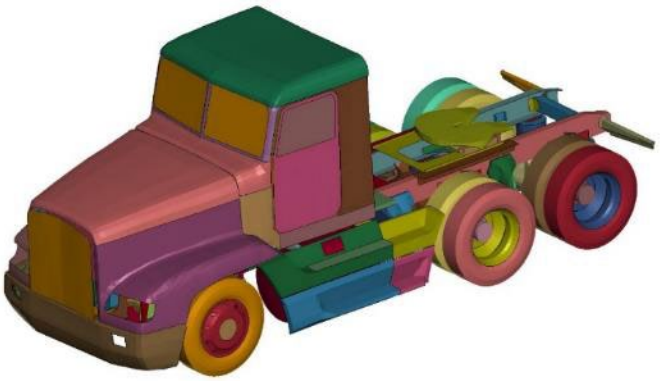

**Figure K 2. Semitrailer Truck with Day Cab and 181-inch Wheelbase**

Figure K 3 shows the modified base truck in LS-DYNA. Various components were removed from the original model which were not present in the test highway vehicle including side sheathing, fuel tanks, fifth wheel, rear axle, etc. After the authors finished modifying the long wheelbase semitrailer truck model, the number of deformable elements and weight were reduced by approximately 30 percent to 50,300 elements and 11,900 lb, respectively. The model shown here was translated from metric to US customary units and rotated in LS-DYNA using the *INCLUDE_TRANSFORM keyword so that it could be included in a simulation with the LNG fuel tender FE model. After the model was transformed, it was converted to Abaqus using a built-in converter in Abaqus CAE. The converted model appears as the grey colored parts in Figure K 4 and Figure K 5.

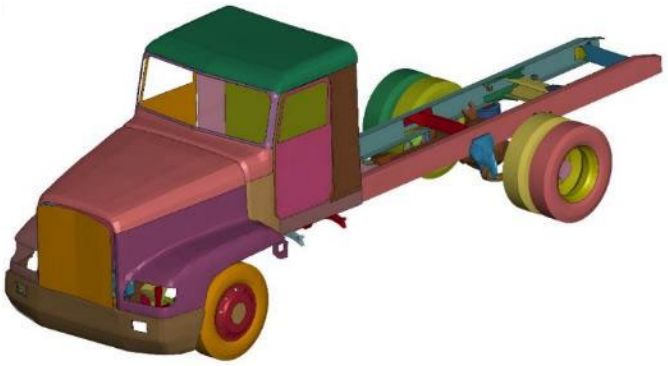

**Figure K 3. Modified Base Truck with Day Cab and 241-inch Wheelbase**

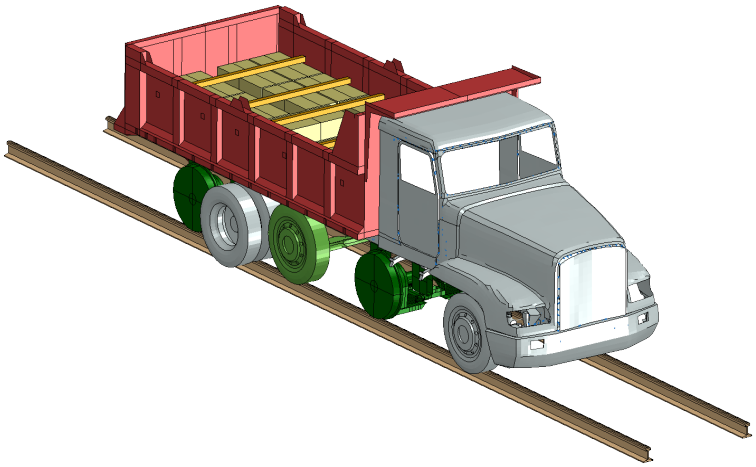

**Figure K 4. Dump Truck Positioned on Rigid Rails Isometric View**

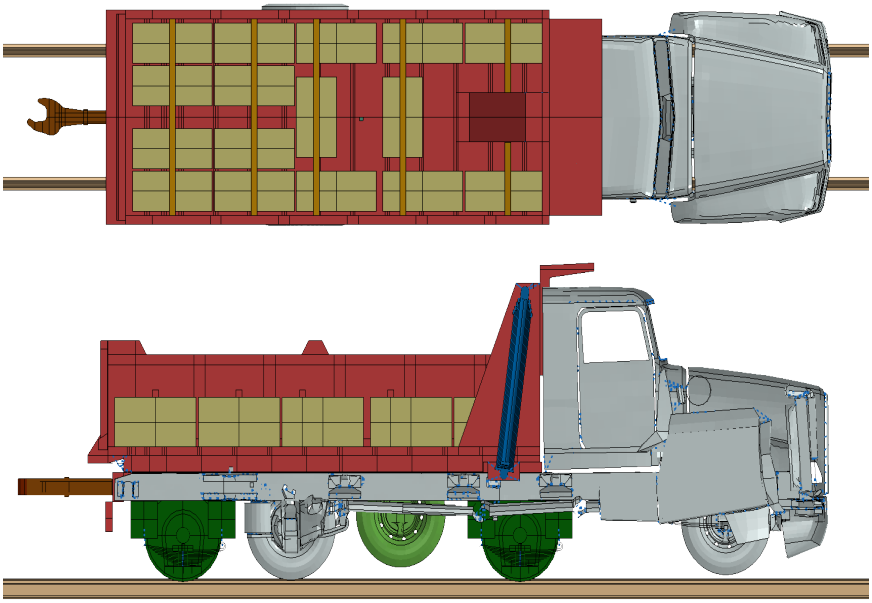

**Figure K 5. Dump Truck Positioned on Rigid Rails Top View (Top) and Section View (Bottom)**

The semitrailer truck model was converted to Abaqus because the highway test vehicle was considered a small part of the overall modeling effort in the LNG fuel tender grade crossing test, and the researchers were more familiar with using Abaqus for modeling the other parts of the grade crossing test. Material properties, constraints, and connector definitions that were not automatically translated in Abaqus/CAE were manually reassigned.

### Modifications

The authors tried to maintain the section and material properties in the base truck model after converting to Abaqus where possible. Damage initiation and progression properties were added to components in the base truck model which experienced unrealistically high levels of plastic strain due to pushback of the engine block and transmission during the impact. Figure K 6 shows the components which were modified in blue. Ductile damage evolution with a plastic equivalent

strain to fracture of 0.25 and linear displacement-based damage progression of 0.01 in/in$^2$ (0.394 m/m$^2$) were added to the native material cards.

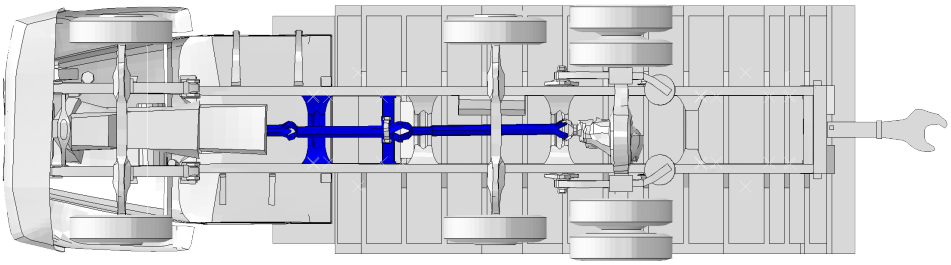

**Figure K 6. Bottom View of Dump Truck FE Model with Fracture-capable Components in Blue (Rail Wheelsets Hidden)**

A drop axle was added to the modified base truck model by copying and translating the front axle. Drop axles are not typically present on semitrailer trucks, but they are common on dump trucks. Figure K 7 shows the MPCs which rigidly attach the drop axle to the truck frame. After the FE model was completed, the team fabricated additional supports for the drop axle which rigidly fixed them to the dump body; however, the FE model was not updated to reflect the modification.

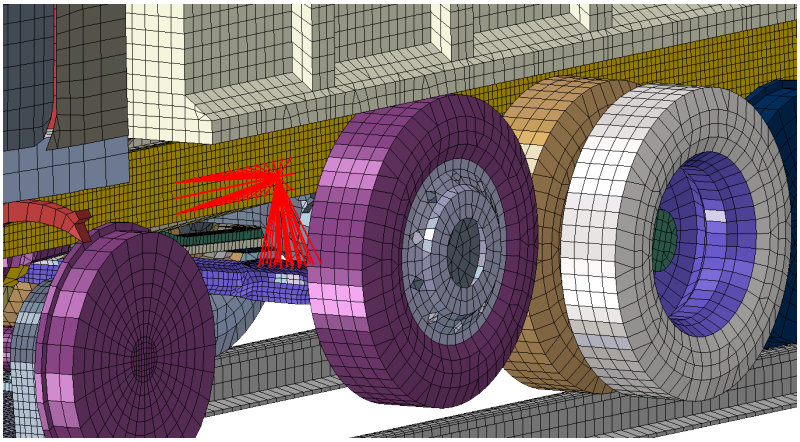

**Figure K 7. Drop Axle MPCs**

Figure K 8 shows the tie constraints used to connect the square channels to the dump body and the ballast to the square channels and dump floor. The team also tied chains from the front two ballast blocks to the tailgate; however, these were not represented in the FE model because they were not needed for sufficient restraint in the model and would have added unnecessary complexity.

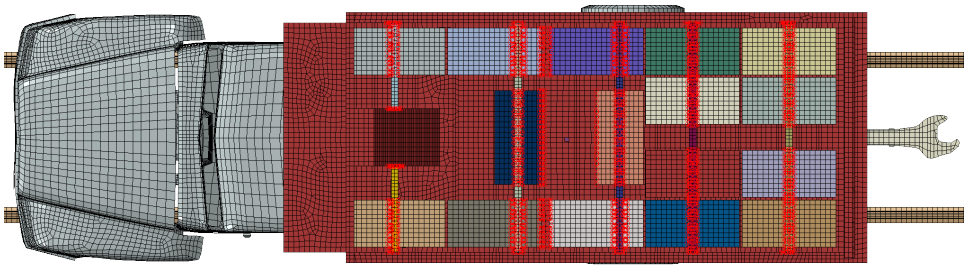

**Figure K 8. Ballast Restraint Ties**

Figure K 9 shows the tie constraints between the dump body and tailgate and between the coupler and rear bumper.

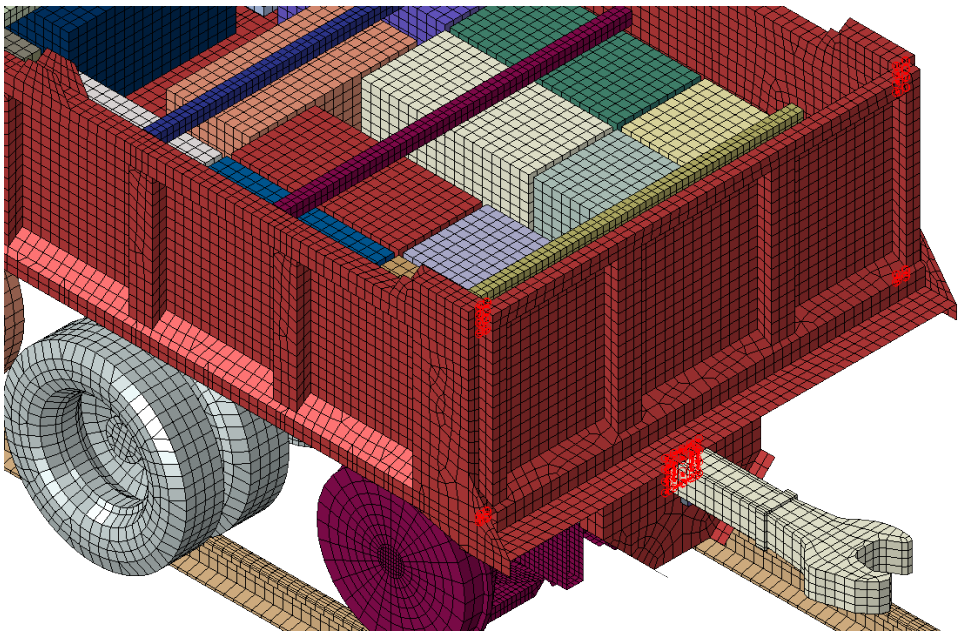

**Figure K 9. Dump Body Tailgate and Coupler Ties**

The dump body rested on an approximately 1/4 inch thick steel pad which was welded to the truck frame. Figure K 10 shows tie constraints between the pad and hitch plate and the truck frame.

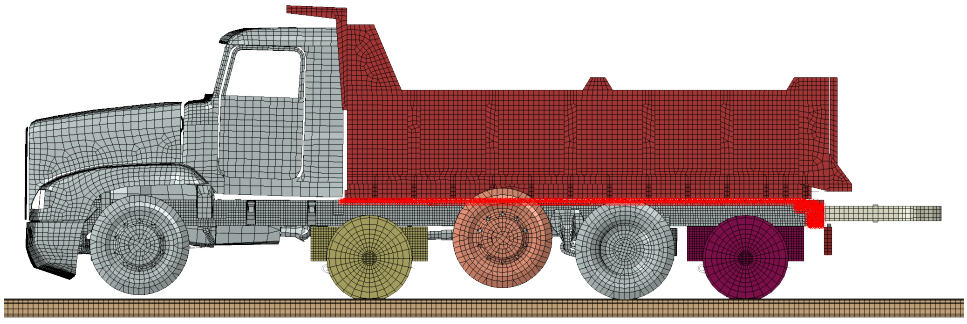

**Figure K 10. Dump Body Pad to Frame Ties**

After completion of the FE model, the team made four ~12 inch (0.305 m) length welds between the dump body and dump truck frame on the left and right dump truck longitudinal underframe

c-channels near the front and rear of the dump body to prevent upward motion of the dump body (refer to Section 2.3.1 in the Main Report). These additional restraints were not included in the model because they were added after modeling of the dump truck had been completed.

Figure K 11 shows the discrete connectors and constraints used to represent the rear hinges of the dump body. MPC constraints (colored in red) from the rear bumper were applied to two control reference points representing the pins. Hinge connectors (colored in green) were attached from the reference point to the dump body. Discrete elements were chosen for the hinges to limit the complexity of the model.

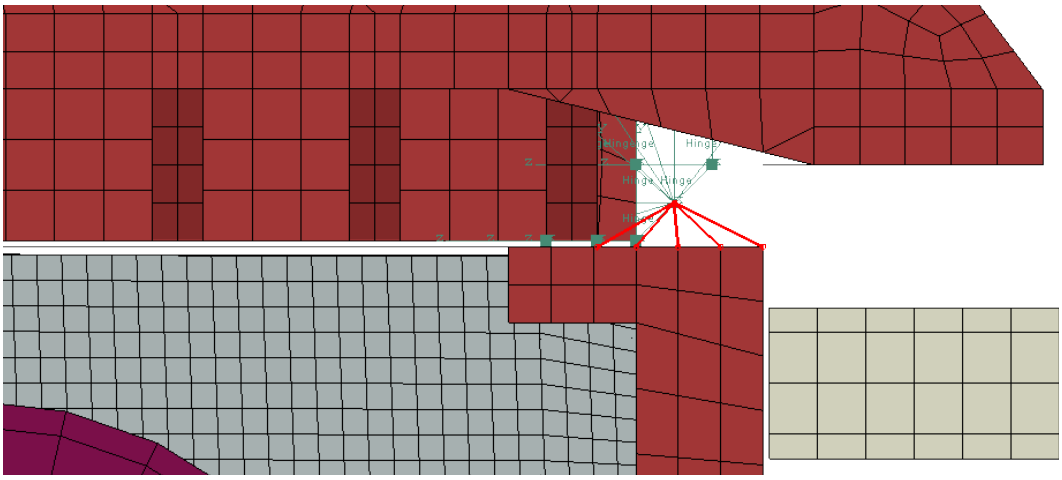

**Figure K 11. Dump Body Rear Hinge MPCs and Connectors**

The base truck model in LS-DYNA included accelerometers represented as rigid cubes measuring 40 mm. These accelerometers were translated to Abaqus and included in the final model. Additional accelerometers (highlighted in red) were placed at the CG of the modified dump truck located inside the dump bed and at the rear bumper, as shown in Figure K 12.

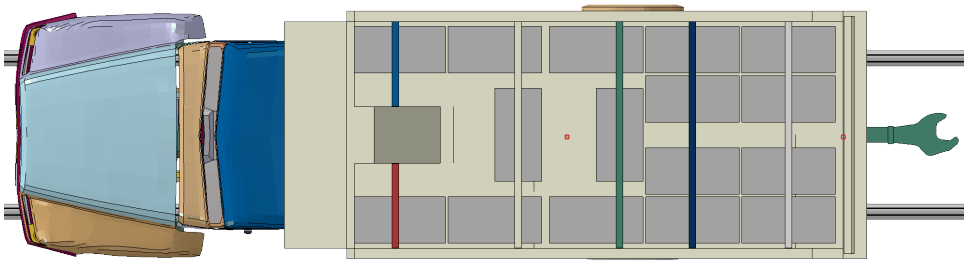

**Figure K 12. Tri-axial Accelerometer Locations at CG and Rear**

Figure K 13 shows the hinge connection between the top of the hydraulic piston and the dump body. A rigid body constraint was assigned to the solid elements at the top of the hydraulic piston and the reference point of the rigid body was connected to nodes on the dump body through hinge connectors.

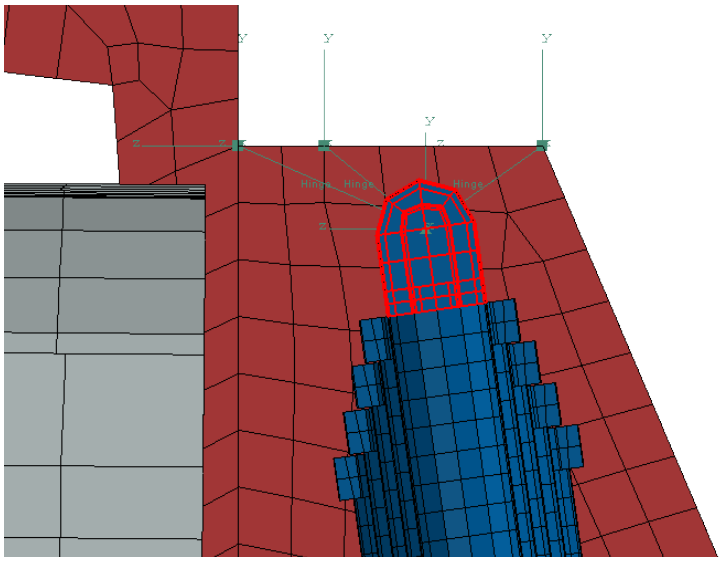

**Figure K 13. Hydraulic Piston Top Hinge Rigid Body and Connectors**

Figure K 14 shows the hinge connection between the bottom of the hydraulic piston and supporting structure. A rigid body constraint was assigned to the solid elements at the bottom of the hydraulic piston and the reference point of the rigid body was connected to nodes on the supporting structure through hinge connectors.

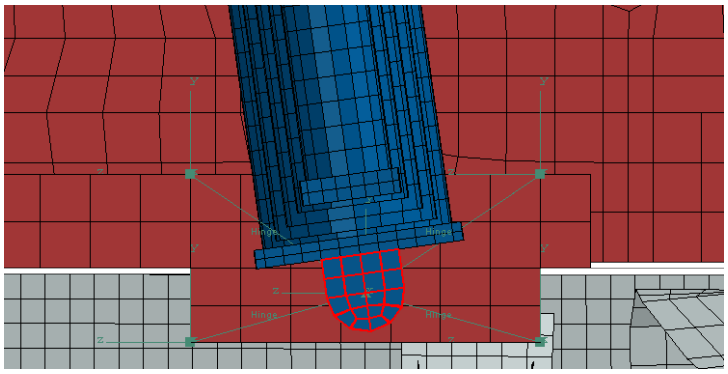

**Figure K 14. Hydraulic Piston Bottom Hinge Rigid Body and Connectors**

Figure K 15 shows the tie constraints between the truck underframe (not shown) and rectangular channels holding the leaf springs on the rail wheelset.

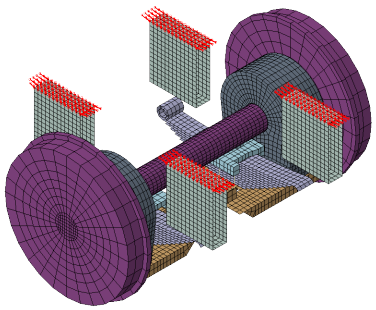

**Figure K 15. Wheelset Ties to Dump Truck Frame**

Figure K 16 shows the rigid body constraints on the rail wheelset.

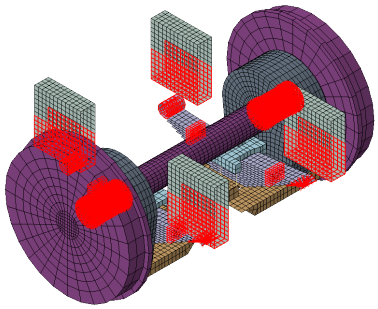

**Figure K 16. Wheelset Rigid Body Constraints**

Figure K 17 shows the hinge connectors (colored in black) for the leaf springs and axle. A section view is included to visualize one of the two hinge connectors on the axle.

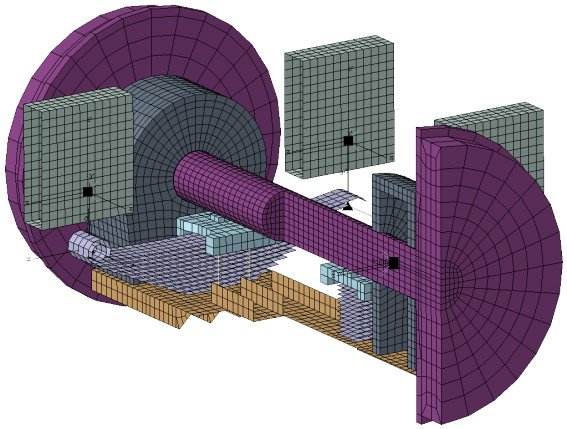

**Figure K 17. Wheelset Hinge Connectors (Section View)**

The additional features added to the base truck needed to have section and material definitions applied, including the dump body, rail wheelsets, ballast, and ballast restraints. Material testing was not conducted on any of the components in the dump truck. A material card from the base truck model representing mild steel with a 39 ksi yield strength (refer to Figure K 18) was used to define material properties for the steel features added to the model. A thickness of 1/4 inch was applied to the sheathing and framing of the dump body resulting in a weight of 5,600 lb.

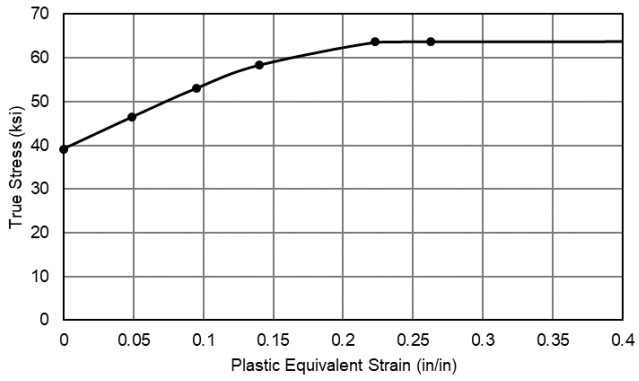


**Figure K 18. Steel Plasticity in Dump Truck FE Model**

Detailed geometry information was available for the rail wheelsets and ballast restraints, and it was used to determine material thicknesses. However, information on material specifications was not available for those components so the same 39 ksi steel material card from the base truck model also was applied.

The ballast blocks were specified as rigid, and a translational mass and rotary inertia were specified for each of the 16 blocks. The inertial properties are summarized in Table K 1. The blocks measured 36 x 18 x 18 inches.

**Table K 1. Rigid Ballast Block Properties of Inertia**

| Property | Value |
|---|---|
| Isotropic Translational Mass | 8.28825 $in^{-1} \cdot lbf \cdot s^2$ |
| Rotary Inertia (Along Length) | 447.565 $lbf \cdot in \cdot s^2$ |
| Rotary Inertia (Along Thickness and Width) | 1118.91 $lbf \cdot in \cdot s^2$ |

## References


[1] SAE International (2022). Instrumentation for Impact Test - Part 1: Electronic Instrumentation, Standard J211/1_202208. SAE, Warrendale, PA.

[2] MatWeb (n.d.). ASTM A500 Steel, grade B, shaped structural tubing. Accessed 30 September 2022.

[3] Kirkpatrick, S. W. (2010). Detailed Puncture Analyses of Various Tank Car Designs - Final Report - Revision 1. Applied Research Associates, Mountain View, CA.

[4] MatWeb (n.d.). ASTM A36 Steel, plate. Accessed 30 September 2022.

[5] MatWeb (n.d.). AISI 1045 Steel, cold drawn, high temperature stress relieved, 50-75 mm (2-3 in) round. Accessed 30 September 2022.

[6] SSAB (2022). ASTM A517 Grade E. Accessed 30 September 2022.

[7] Wilson, N., Carolan, M., Trevithick, S., & Eshraghi, S. (2021). Side Impact Test of a DOT-113 Surrogate Tank Car with Water (Report No. DOT/FRA/ORD-21/35). Federal Railroad Administration, Washington, DC.

[8] Trevithick, S., Carolan, M., & Eshraghi, S. (2020). Side Impact Test and Analyses of a DOT-111 Tank Car (Report No. DOT/FRA/ORD-15/30). Federal Railroad Administration, Washington, DC.

[9] Association of American Railroads (2011). AAR Manual of Standards and Recommended Practices M-107/M-208, Wheels and Axles. Washington, DC.

[10] Liu, X. (2015). Finite Element Modeling Study Report - Casselton, North Dakota - December 30, 2013. National Transportation Safety Board, Washington, DC.

[11] F. Xia (2002). The Dynamics of the Three-piece Freight Truck. Ph.D. Thesis, Informatics and Mathematical Modelling, Technical University of Denmark, DTU, Lyngby.

[12] Przybylinski, P. G., & Anderson, G. B. (1980). Engineering Data Characterizing the Fleet of U.S. Railway Rolling Stock. Volume II, Methodology and data (Report No. FRA/ORD 81/75.2). Federal Railroad Administration, Washington, DC.

[13] Southern Pacific Transportation Group Technical Research and Development Team (1978). Freight Car Truck Design Optimization: Vol. II - Phase I Final Report (Report No. FRA/ORD-78/12.II). Federal Railroad Administration, Washington, DC.

[14] Forbes, J. W., Hematian, J., & Bis, T. (2014). Rail Road Car Truck and Fitting Therefor. United States Patent 8113126.

[15] Wabtec Corporation. Truck Systems Springs Manual. Accessed 4 August 2022.

[16] Caldwell, R., Ladubec, C., Krzyzanowski, M., Liu, Y., & Caldwell, N. (2009). Investigation of Multiple Tank Car Rollover Derailments Related to Double Shelf Couplers and its Solutions. Transport Canada, Ottawa, ON.

[17] A. Stucki Company, "Compact Column Side Bearing," [Online]. Available: https://stucki.com/product/compact-column-side-bearing/. [Accessed 19 December 2022]

[18] Wabtec, "Wabtec Freight Car Components & Services Catalog - Truck Systems - Side Bearings," [Online]. Available: https://www.wabteccorp.com/freight-car-side-bearing-part-numbers?inline. [Accessed 19 December 2022]

[19] American Railway Engineering and Maintenance-of-Way Association (1999). AREMA Manual for Railway Engineering. AREMA, Lanham, Maryland.

[20] Jeong, D. Y., Woelke, P. B., Nied, H. F., DuPont, J. N., Kizildemir, S., Fletcher, F. B., & Hutchinson, J. W. (2019). Defect Growth Characterization in Modern Rail Steels. *ASME/IEEE 2019 Joint Rail Conference*, Snowbird, UT.

[21] LBFoster (n.d.). CXT (R) Concrete Ties - 200S-13 Tie. Accessed 1 February 2022.

[22] Hetényi, M. (1946). Beams on Elastic Foundation. Ann Arbor: University of Michigan Press.

[23] Talamini, B., Jeong, D. Y., & Gordon, J. (2007). Estimation of the Fatigue Life of Railroad Joint Bars. *2007 ASME/IEEE Joint Rail Conference & Internal Combustion Engine Spring Technical Conference*, Pueblo, CO.

[24] Bedford A., & Fowler, W. (2002). Engineering Mechanics - Statics (Third Edition). Upper Saddle River, NJ: Prentice Hall.

[25] Jeong, D., Samavedam, G., & Kish, A. (1986). Determination of Track Lateral Resistance from Lateral Pull Tests. Federal Railroad Administration, Washington, DC.

[26] Kish, A. (2011). On the Fundamentals of Track Lateral Resistance. *AREMA 2011 Annual Conference*, Minneapolis, MN.

[27] Jeong, D. Y. (2013). Analyses for Lateral Deflection of Railroad Track under Quasi-static Loading. *Proceedings of the ASME 2013 Rail Transportation Division Fall Technical Conference*, Altoona, PA.

[28] The Engineering Toolbox (n.d.) Air - Density and Specific Volume vs. Altitude. Accessed 17 March 2020.

[29] United States Geological Survey (USGS) (2002). Geographic Names Information System (GNIS) Detail - City of Pueblo. Accessed 18 January 2022.

[30] Association of American Railroads (2020, draft). Manual of Standards and Recommended Practices - Interoperable Fuel Tenders for Locomotives (M-1004). Association of American Railroads, Washington, DC.

[31] Lemmon, E. W., Bell, I. H., Huber, M. L., & McLinden, M. O. (2023). Thermophysical Properties of Fluid Systems. *NIST Chemistry WebBook, NIST Standard Reference Database Number 69*, P. J. Linstrom and W. G. Mallard, Eds., National Institute of Standards and Technology.

[32] National Transportation Research Center, Inc. FEM Models for Semitrailer Trucks.

[33] Plaxico, C., Kennedy, J., Simunovic, S., & Zisi, N. (n.d.) Enhanced Finite Element Analysis Crash Model of Tractor-Trailers (Phase A). National Transportation Research Center, Inc.

[34] Plaxico, C., Miele, C., Kennedy, J., Simunovic, S., & Zisi, N. (2009). Finite Element Analysis Crash Model of Tractor-Trailers (Phase B). National Transportation Research Center, Inc.

[35] Miele, C., Stephens, D., Plaxico, C., & Simunovic, S. (2010). Enhanced Finite Element Analysis Crash Model of Tractor-Trailers (Phase C). National Transportation Research Center, Inc.

[36] Miele, C., & Plaxico, C. (n.d.) Tractor-Semitrailer FE Model User's Manual / Release Notes. National Transportation Research Center, Inc.

[37] Livermore Software Technology Corporation (LSTC) (2022). LS-DYNA® Theory Manual.

## Abbreviations and Acronyms

| ACRONYM | DEFINITION |
|---|---|
| ASTM | American Society for Testing and Materials (former) |
| AAR | Association of American Railroads |
| ARA | Applied Research Associates |
| AREMA | American Railway Engineering and Maintenance-of-Way Association |
| BEF | Beam on Elastic Foundation |
| CCSB | Constant Contact Side Bearing |
| DOF | Degrees of Freedom |
| DOT | Department of Transportation |
| FRA | Federal Railroad Administration |
| FEA | Finite Element Analysis |
| FE | Finite Element |
| GN2 | Gaseous Nitrogen |
| LNG | Liquefied Natural Gas |
| LN2 | Liquid Nitrogen |
| MBD | Multibody Dynamics |
| MPC | Multi-Point Constraint |
| NCAC | National Crash Analysis Center |
| NGFT | Natural Gas Fuel Tender |
| NTCRI | National Transportation Research Center, Inc. |
| ORNL | Oak Ridge National Laboratory |
| PRV | Pressure Relief Valve |
| SAE | Society of Automotive Engineers (former) |
| STPT | Single Tie Push Test |
| TAG | Technical Advisory Group |
| TTC | Transportation Technology Center |
| TTI | Texas A&M Transportation Institute |
| UTK | University of Tennessee at Knoxville |